LBL--28449

DE90 011613

# Tunable Far Infrared Laser Spectroscopy of van der Waals Bonds: $Ar-NH_3$

Dz-Hung Gwo

(Ph.D. Thesis)

Department of Chemistry

University of California

and

Materials and Chemical Sciences Division

Lawrence Berkeley Laboratory

Berkeley, California 94720

November 1989

**DISCLAIMER**

This report was prepared as an account of work sponsored by an agency of the United States Government. Neither the United States Government nor any agency thereof, nor any of their employees, makes any warranty, express or implied, or assumes any legal liability or responsibility for the accuracy, completeness, or usefulness of any information, apparatus, product, or process disclosed, or represents that its use would not infringe privately owned rights. Reference herein to any specific commercial product, process, or service by trade name, trademark, manufacturer, or otherwise does not necessarily constitute or imply its endorsement, recommendation, or favoring by the United States Government or any agency thereof. The views and opinions of authors expressed herein do not necessarily state or reflect those of the United States Government or any agency thereof.

MASTER

DISTRIBUTION OF THIS DOCUMENT IS UNLIMITED

# ACKNOWLEDGMENT

This research has been supported by the Director, Office of Energy Research, Office of Basic Energy Sciences, Chemical Sciences Division of the U.S. Department of Energy under Contract No. DE-AC03-76SF00098.

# Tunable Far Infrared Laser Spectroscopy of van der Waals Bonds: Ar-$NH_3$

Dz-Hung Gwo

## ABSTRACT

Hyperfine resolved vibration-rotation-tunneling spectra of Ar-$NH_3$ and $(NH_3)_2$, generated in a planar supersonic jet, have been measured with the Berkeley tunable far infrared laser spectrometer. Among the seven *rotationally* assigned bands, one band belongs to Ar-$NH_3$, and the other six belong to $(NH_3)_2$.

To facilitate the intermolecular vibrational assignment for Ar-$NH_3$, a dynamics study aided by a permutation-inversion group theoretical treatment is performed on the *rovibrational* levels. The rovibrational quantum number correlation between the free internal rotor limit and the semi-rigid limit is established to provide a basic physical picture of the evolution of intermolecular vibrational component states ($K_a$ manifolds). An anomalous vibronically (not just rovibronically) allowed *unique Q branch* vibrational band structure is predicted to exist for a near prolate binary complex containing an inverting subunit.

According to the model developed in this work, the observed band of Ar-$NH_3$ centered at 26.470633(17) $cm^{-1}$ can correlate only to either (1) the fundamental dimeric stretching band for the $A_2$ states with the $NH_3$ inversional quantum number $v_i$=1, or (2) the $K_a$=0 ← 0 subband of the lowest internal-rotation-inversion difference band. Although the

estimated nuclear quadrupole coupling constant favors a tentative assignment in terms of the first possibility, a definitive assignment will require more far infrared data and a dynamical model incorporating a potential surface.

## Acknowledgements

I would like to thank my research director, Rich Saykally, for taking me as the first foreign student in his group, also for his guidance and encouragement over the past 6.3 years. I feel lucky to have been working for such a wonderful person who is "cool" outside but warm inside. His keen judgement in selecting both research topics and experimental techniques is an important lesson I hope to learn.

Doug and Ruth, my first experiment mentors in the States, deserve special thanks for patiently teaching me Stark spectroscopy. Surely that was not an easy job especially while my listening comprehension in English was still terribly poor. Other Stark fellows, David and Jim (UG) had helped me in many aspects of improving the experiment. David, in particular, made considerable efforts with me to do CPR on the dying Stark machine and extract its surplus value.

I am sincerely grateful to Kerry and Ron for kindly accepting me, as a refugee from the finally trashed Stark experiment, to work on the tunable FIR spectrometer. Without their enthusiastic assistance, I would not have been able to finish the thesis work so "early". With Martina, the wonderful experience of keeping the TFIR spectrometer running for 100+ hours continuously is also unforgettable. Bill was a helpful scanning partner; delightful conversations with him are remedy for lab fatigue.

My officemates Chris, Jeff, Andy and Jim Coe also deserve thanks for providing a good environment when I needed to work on the drawing board. Chris was a fantastic discussion partner, who can get excited by almost any question. Jeff was considerate; for example, he never

smokes in the office. In the lab, Jeff is addicted only to laughing gas, which made him pass out (but never laugh or pass out with a smiling face). It was also nice to have Andy, an early bird, whose showing up could remind me of going home to sleep.

Of course, the Saykally group represents something more. The already-doctor Mike has been entertaining to the group all the time; I hope there are youngsters who can take over the job. I am also pleased that Ken has become the first American who can write my Chinese name correctly; he must be good at topology. Eric is the right person to hang out with in the lab. And Charlie has been one of the most pleasant people I have ever seen. I think the only poor guy in the group is Mark, who is always a victim of Martin's joking; anyway I'll give Mark a guarantee lesson on whistling before I leave. The good personality of Susan and Neil will also be in my mind. Traditionally the group has excellent postdocs; Rene, Les, Geoff, Jim Coe and Jim Heath, I really hope to learn more from you all.

I would also like to thank several senior scientists not in the Saykally group. Dr. Jon Hougen for being like my private tutor on group theory. Dr. Andrew Peet for teaching me his recently developed collocation calculation method in detail. Dr. Jeremy Hutson for helping me better understand the Coriolis interactions involved in vdW molecules. Visiting Prof. Takeshi Oka for instructions and hands-on working on hardware over ten hours a day for nearly a month on the FIR/RF double resonance experiment.

Now, I get to say Dou-Hsia to Liang Mama for Zu-Bong for me in the past few months. To Wen, you are just about the best friend I

could have, thanks for the good time we have shared together. Also Hsie-Hsie my parents and grandmother not only for their steadfast support in all aspects but also for remembering me in their daily prayers to God. (Nainai, Baba, Mama: Hong-Hong yung-yuen ai ni-men.) Finally, my most sincere thanks go to the Heavenly Father for every single day I have had.

# Table of Contents

Chapter 1 Page

A Review of the Study of Small van der Waals Complexes ..... 1

1.1 Theoretical Approaches ..... 4

1.1.1 Perturbation Theories ..... 5

1.1.1.1 Polarization Perturbation ..... 5

1.1.1.2 Exchange Perturbation ..... 10

1.1.2 Supermolecular ab initio Calculations ..... 11

1.1.3 Group Theoretical Studies ..... 13

1.2 Semiempirical Studies ..... 19

1.2.1 Useful Experimental Data ..... 20

1.2.1.1 Data from Molecular Beam Studies ..... 20

1.2.1.2 Data from Spectroscopy ..... 22

1.2.2 Available Intermolecular Potentials ..... 26

1.3 Demonstrative Achievement of High Resolution FIR Spectroscopy: Ar-HCl Potential Surface ..... 34

References ..... 36

Chapter 2

Berkeley Tunable Far-Infrared/Planar Jet Laser Spectrometer 45

2.1 Spectrometer ..... 45

2.2 Lock-in Stabilization of the cw $CO_2$ Laser ..... 50

2.2.1 Principles of Offset Lock-in Stabilization ..... 52

2.2.1.1 Conventional Lock-in Stabilization ..... 52

2.2.1.2 Concepts for the New Designs ..... 55

2.2.1.2.1 Mathematical Simulation of a Lock-in Amplifier .. 56

2.2.1.2.2 Limitations of the Modulation-Amplitude-Controlled Scheme ..... 62

2.2.1.2.3 Geometric Arguments for the Response-Modification Schemes ..... 64

2.2.1.2.3 (A) 1f Modification — Slanting the Baseline of the Characteristic Curve ..... 64

2.2.1.2.3 (B) Decoupling the Effect of Gain on the Locking Position ..... 71

2.2.1.2.3 (C) 2f Demodulation — A Complement to 1f Modification ..... 74

2.2.2 Architecture of the Offset Lock-in Stabilization System ..... 79

2.2.2.1 ac Offset Scheme ..... 81

2.2.2.2 dc Offset Scheme ..... 85

2.2.3 Application to the cw $CO_2$ Laser Stabilization ..... 87

2.2.3.1 Actual Stabilization System ..... 87

2.2.3.2 Operation ..... 97

2.2.3.3 Performance ..... 104

References ..... 106

Chapter 3

Far-Infrared Vibration-Rotation-Tunneling Spectroscopy of Ar-$^{14}NH_3$ ..... 108

3.1 Introduction ..... 108

3.2 Experimental ..... 115

3.3 Spectrum Rotational Assignment and Analysis ..... 115

3.4 Group Theoretical Preparation for Vibrational Assignments ..... 117

3.4.1 Coordinate Definitions ..... 121

3.4.2 Coordinate Transformations ..... 126

3.4.2.1 Effect of Permutation (without *) on $R_{Ar}$ ..... 126

3.4.2.2 Effect of Permutation-Inversion (PI) on $R_{Ar}$ ..... 126

3.4.2.3 Effect of the * Operation on $R_i$ (i=N, 1, 2, 3) .... 128

3.4.2.4 Effects of the (23) and (23)* Class Operations on $R_i$ (i=N, 1, 2, 3) ..... 132

3.4.2.5 Effects of the (123) and (123)* Class Operations on $R_i$ (i=N, 1, 2, 3) ..... 138

3.4.3 Summary of Coordinate Transformations ..... 142

3.4.4 Transformation Properties of the Rotational Basis Functions ..... 148

3.4.4.1 $NH_3$ Subunit Symmetric Top Rotational Basis Functions ..... 148

3.4.4.2 Pseudo-Diatomic Frame Rotational Basis Functions .. 148

3.4.5 Transformation Properties of the $NH_3$ Subunit Inversional Wave Functions ..... 151

3.5 Zero-Order Energy for the Free Internal Rotor Limit ... 153

3.5.1 Derivation of the Kinetic Energy Expression ..... 153

3.5.2 Summary of the Kinetic Expression ..... 160

3.5.3 Potential Energy ..... 161

3.5.4 Total Energy ..... 163

3.6 The Unperturbed Case ..... 166

3.6.1 Zero-Order Intermolecular Vibrational Level Diagram . 166

3.6.2 Rotational Energy Level Manifold of a Zero-Order Intermolecular Vibrational State ..... 172

3.6.3 Selection Rules ..... 176

3.6.3.1 Optical Selection Rules ..... 176

3.6.3.2 Inter-State Interaction Selection Rules ..... 177

3.6.4 Intermolecular Vibrational Transitions in the Free Internal Rotor Limit ..... 178

3.7 Perturbed Cases ..... 181

3.7.1 Highly Near Prolate Top ..... 183

3.7.2 $K_a$ Rotational Manifolds as Evolving Units under $C_{3v}(M)$ between the Two Limits ..... 186

3.7.3 Splittings of Zero-Order Intermolecular Vibrational States into $K_a$ Vibrational Component States under $C_{3v}(M)$ ..... 192

3.7.4 $K_a$ Correlation under $C_{3v}(M)$ between the Two Limits .. 201

3.7.5 $K_a$ Correlation under $D_{3h}(M)$ between the Two Limits .. 218

3.7.6 Intermolecular Vibrational Transitions ..... 225

3.8 Intermolecular-Vibrational Assignment of Observed Spectrum ..... 237

References ..... 251

Chapter 4

Concluding Remarks ..... 255

References ..... 260

Appendices

Table 1, $D_{3h}(M)$ Character Table. ..... 261

Table 2, $D_{3h}(M)$ Symmetry Species Multiplication Table. ..... 261

Table 3, $C_{3v}(M)$ Character Table. ..... 262

Table 4, $C_{3v}(M)$-$D_{3h}(M)$ Symmetry Species Correlation. ..... 262

Table 5, Rotationally Unassigned Spectral Lines. ..... 263

# Chapter 1

## A Review of the Study of Small van der Waals Complexes

The interactions involved in chemistry may be roughly classified into covalent and noncovalent (ionic and intermolecular) ones. The borderline between them cannot be clearly defined. The covalent interaction results in the formation and dissociation *of* molecules. On the other hand, the noncovalent interactions cause the associations and dissociations *between* molecules. (Here, "molecules" in a general sense also include atomic, polyatomic ions and closed-shell atoms.)

Various names have been given to intermolecular interactions, viz., weak, physical (in contrast to "strong" and "chemical" used to describe covalent interactions) and van der Waals (vdW). However, because "weak" interaction is confusing with that involved in nuclear $\beta$ decay, and "physical" interaction implies something too general and thus misleading, we, following the suggestion by Hobza and Zahradnik [1], prefer "vdW interactions" as the proper name for the intermolecular interaction. The molecular clusters held by vdW interactions will therefore be called "vdW complexes".

From this connotation, vdW interactions are then involved in almost all chemical and physical phenomena in which more than one purely covalent system are implicated. Systems ranging from molecular dimers to condensed phases, and processes from molecular inelastic collision energy transfer, molecular photofragmentation, and solvation, to phase transitions and interphase interactions are all

related to vdW interactions. The ubiquity of the intermolecular vdW interactions makes the study of them fundamentally important. Due to their simplicity, the study of small vdW complexes such as dimers and trimers, i.e. the smallest possible pieces of condensed phases, naturally becomes a convenient starting point for the investigation of vdW interactions.

In terms of electronic configuration of the constituent molecules, small vdW complexes include vdW ions, vdW radicals, and vdW molecules. In terms of binding energy, vdW complexes range from strong ionic vdW complexes such as $H_2O{\cdot}Na^+$ [2-4] to weakly bound molecules such as $He_2$ [5]. In other words, their binding energy can be close to that of a typical covalent bond (40-200 kcal/mole) [6], or as low as a tenth of a kcal/mole. Among the various possible vdW molecules, the hydrogen-bonded (H-bonded) vdW molecules are a special class with binding energies of a few kcal/mole, for example, about 5 kcal/mole for $(H_2O)_2$ [7,8]. The binding energies of the "true" vdW molecules are usually 1 kcal/mole or less [5].

Due to their generally smaller stabilities and consequently shallower binding potential surfaces, vdW complexes have larger amplitude and more anharmonic intermolecular vibrations and tunneling motions. For example, the HCl diatomic subunit of the linear Ar-HCl complex is estimated to exhibit an approximately $40^\circ$ vibrational amplitude in the first intermolecular vibrational ($\Sigma$ bend) state of Ar-HCl [9-11]. And the two HF subunits in the slightly L-shaped H-bonded $(HF)_2$ complex exhibit donor-acceptor role interchange tunneling motion [12].

Under the Born-Oppenheimer approximation that the electrons take no time adjusting their motions to follow the nuclear motions, the potential energy of a molecular system is a function only of the nuclear configuration. This implies that the nuclei can "sense" and move on a potential energy surface of well defined geometry, which contains all the structural and dynamical information of the system. Therefore, the study of vdW interactions is equivalent to the study of the geometries of the intermolecular potential energy surfaces (abbreviated as "potential surfaces" in the following). The foci of the study have thus been experimentally measure, theoretically account for, and predict such geometries.

The theoretical study has two mainstreams, viz., the perturbation theories, and ab initio calculations [1]. The former provides insights to the various physical contributions to the vdW interaction. The latter serves as theoretical methods to directly predict the geometries of the potential surfaces. On the other hand, the experimental mainstream [13,14] has recently been dominated by spectroscopy thanks to its capability of probing the intermolecular nuclear motions which are direct manifestations of the potential surfaces.

In spite of having a solid quantum mechanical foundation, the state-of-the-art theoretical studies have serious difficulties in accurately predicting the potential surface for vdW dimer system with more than four electrons [15,16]. On the contrary, experimental measurements, spectroscopy in particular, become more and more powerful tools to probe the potential surfaces. A famous example is

the semiempirical determination of the potential surface for Ar-HCl by inverting only spectroscopic data [17]. Hopefully, the semiempirical potential surfaces can be accumulated enough someday to resuscitate the theoretical studies.

Several excellent review articles on theoretical and experimental approaches to vdW interactions have been published recently [1,13,14,18-22]. In the following two sections presented is a brief summary of only the basic ideas involved in pure theories (first principles) (Section 1.1), and semiempirical studies (Section 1.2) in the investigation of vdW complexes.

## 1.1 Theoretical Approaches

It has been well known that the four major contributions to vdW interactions can be classified as electrostatic, induction, dispersion, and exchange repulsion energies [13,22]. The first three of these are long range attractive interactions, while the exchange repulsion dominates at short range. The potential surfaces result from the combinations of these long and short range interactions.

The long range interactions are, according to the theory of electrostatics, proportional to sums of certain powers of 1/R, where R is the inter-subunit distance [23]. Among them, the electrostatic and induction interactions [24] have classical analogues, whereas the dispersion interaction is purely quantum mechanical in nature. The dispersion energy [25] is due to the intermolecular electron correlation effects arising from the interaction between the fluctuating instantaneous multipole moments. The quantum mechanical

exchange repulsion results from the charge overlap and the Pauli exclusion effects between the electron clouds of interacting molecules, and drops exponentially with R.

This partitioning of vdW interaction into the above four individual contributions originates from the exchange perturbation theory (Section 1.1.1.2) treatment. The four parts are individually well defined only at long range, where the mixed interaction terms generated by the perturbation treatment are negligibly small. the In other words, the partitioning is arbitrary to some extent.

All the aforementioned fundamental theoretical understandings of the vdW interactions were laid down in the first few decades of the century [22]. Briefly reviewed will be only the fundamental ideas and basic problems of the current theoretical efforts which mainly include perturbation theories (Section 1.1.1) and supermolecular ab initio calculations (Section 1.1.2). Being still in the stage of "mathematical games" and thus of little practical use, more sophisticated theoretical treatments extended from these fundamental ideas will not be discussed. Also reviewed are the fundamental ideas of group theoretical studies (Section 1.1.3), which have been mathematically the most straightforward and, in terms of physical insights, most important theoretical treatments so far. This is true particularly for H-bonded systems.

### 1.1.1 Perturbation Theories

#### 1.1.1.1 Polarization Perturbation

In the standard perturbation treatment of a vdW dimer, the sum of

the two subunit Hamiltonians constitutes the zero-order Hamiltonian. All the intermolecular interaction operators are then collectively treated as the perturbation. Consequently, the simplest zero-order wave functions are the direct products of the orthonormal wave functions of the two individual Hamiltonians. Since each electron is associated with one or the other subunit in the wave function expression (and therefore is "polarized"), this method is also called "the polarization approximation".

It is noted that these wave functions are not antisymmetrized with respect to inter-subunit exchange of electrons as required by the Pauli exclusion principle. Thus, as an intrinsic problem, it fails to generate the short range exchange repulsion energies [26-28]. However, this method is successful in providing interaction energies in the long range region, where the non-antisymmetric zero-order wave function should be a good approximation.

The polarization approximation is one of the fundamental formalisms used to calculate individual contributions to the intermolecular binding energy. This becomes clear when the perturbation energies of the first and second orders ($E^{(1)}$ and $E^{(2)}$) are written explicitly as [22,29]

$$E^{(1)} = \langle\Phi(A)\Phi(B)|V_{int}|\Phi(A)\Phi(B)\rangle, \qquad (1.1.1.1\text{-}1)$$

$$E^{(2)} = -\sum_{B'\neq B} \frac{|\langle\Phi(A)\Phi(B)|V_{int}|\Phi(A)\Phi(B')\rangle|^2}{\epsilon(B') - \epsilon(B)} - \sum_{A'\neq A} \frac{|\langle\Phi(A)\Phi(B)|V_{int}|\Phi(A')\Phi(B)\rangle|^2}{\epsilon(A') - \epsilon(A)}$$

$$- \sum_{B' \neq B} \sum_{A' \neq A} \frac{|\langle\Phi(A)\Phi(B)|V_{int}|\Phi(A')\Phi(B')\rangle|^2}{[\epsilon(A') - \epsilon(A)] + [\epsilon(B') - \epsilon(B)]} \qquad (1.1.1.1\text{-}2)$$

where $V_{int}$ is the sum of all intermolecular interaction operators, $|\Phi(A)\Phi(B)\rangle$'s are the direct product wave functions for the dimer with subunits a, b in $|\Phi(A)\rangle$ and $|\Phi(B)\rangle$ states, respectively, and $\epsilon(A)$ and $\epsilon(B)$ etc. are the corresponding energy eigenvalues of the free subunit states.

The two most widely used forms for $V_{int}$ have been the multipole expansion and partial wave expansion of the exact interaction operator.

The multipole expansion is an approximation which is asymptotically correct for infinite inter-subunit distance R. According to the wave functions being coupled in Equation (1.1.1.1-1) and (1.1.1.1-2), this expansion assigns straightforward physical meanings to $E^{(1)}$, $E^{(2)}$ in the limit of infinite R. For example, $E^{(1)}$ is obviously the electrostatic energy. The first two terms of the $E^{(2)}$ expression are the induction energies, and the last term of the $E^{(2)}$ expression is the dispersion energy. But, for finite R, as required for actual dimers, this expansion makes the second and higher order terms divergent. Moreover, it does not account for the short range charge overlap effects [30,31].

In order to obtain the missing charge overlap effects while keeping the various interactions obtained in the multipole expansion convergent, the partial wave expansion of the interaction operator can be used [32-36]. For example, in the simplest case of an atom-atom

system, the expansion of a given energy contribution can be written as [22]

$$E = \sum_{l_a=0} \sum_{l_b=0} \sum_{m=-\min[l_a,l_b]}^{\min[l_a,l_b]} \epsilon(l_a,l_b,m)$$

where $l_a$ and $l_b$ are the angular momentum quantum numbers of subunit a and b with respect to laboratory space, and m is the projection angular momentum. These individual components, $\epsilon(l_a,l_b,m)$, may be correlated to the multipole expansion terms $E^{(i)}$ by multiplying $E^{(i)}$ with the scaling functions, which are generally R and relative orientation dependent. For the divergent $E^{(2)}$ and higher order terms in the multipole expansion, these functions have damping effects. Also predicted in $E^{(1)}$ and $E^{(2)}$ by the partial wave expansion are some extra "spherical" partial wave components such as $\epsilon(0,0,0)$, $\epsilon(l_a,0,0)$, and $\epsilon(0,l_b,0)$ which have no such connection with the multipole expansion. Since no exchange effects have been included, these short range components can be attributed only to charge overlap effects. It is noted that there is no definitive reference with which to distinguish the short range charge overlap effects from induction and dispersion energies because $E^{(2)}$ is divergent in the limiting case of infinite R (in the multipole expansion).

According to the above expressions for $E^{(1)}$ and $E^{(2)}$, it is realized that, in practical calculations within the polarization approximation, the exact wave functions of the free subunits are essential.

The SCF wave functions are one-electron functions, which neglect the intra-subunit electron correlations. The correlation energy

within a classical molecule is on the order of 1 eV per electron (23 kcal/mole) [37], and usually orders of magnitude higher than any vdW bonds. Even if the inter-subunit electron correlation energy is only one per cent of that of the intra-subunit, electron correlation still contributes a nonnegligible fraction to the intermolecular force. Not properly taking account of such large intra-subunit correlation energies, the SCF wave functions are not expected to accurately produce the small inter-subunit correlation energies. This is usually a serious problem in treating certain vdW molecules where the dominant interaction is the dispersion energy, which is intrinsically due to electron correlation.

A tremendous amount of effort has been made to calculate the individual contributions, based upon these relatively crude approximations. The main scheme has been the double perturbation theory [38-42], which estimates some intra-subunit correlation effects [38]. How physically meaningful these mathematical results are still remains an important question. There are two major difficulties inherent in the polarization approximation scheme: (1) in terms of formalism, all the exchange effects are neglected, and (2) in terms of application, accurate zero-order wave functions are unavailable. It should also be stressed that even if the exact zero-order wave functions are available, the calculation does not yield a physically correct result because the zero-order wave functions are not antisymmetrized. In other words, it is a theoretical framework, providing an incomplete physical picture, rather than a practical method to accurately calculate any individual contribution.

1.1.1.2 Exchange Perturbation

In order to include the exchange effects in the perturbation treatment, there have been two kinds of symmetry adaptation schemes, viz., the "weak" and "strong" adaptations. In the strong adaptation, the antisymmetry is introduced starting from the first order energy. In the weak adaptation, it starts from the second; in other words, the first order expression is still obtained within the polarization approximation.

As a simple example of symmetry adaptation, the first order energy of the strong adaptation can be written as [22]

$$E^{(1)} = \frac{\langle \Phi(A)\Phi(B) | V_{int} A | \Phi(A)\Phi(B) \rangle}{\langle \Phi(A)\Phi(B) | V_{int} | \Phi(A)\Phi(B) \rangle}$$

where A is the standard total antisymmetrization operator for the complex. (It is emphasized that A is for all fermions involved: electrons, protons etc. For example, A for $H_2^+$ must produce the exchange antisymmetry between the two protons.) This expression can then be changed algebraically into two parts: (1) the electrostatic interaction, as previously obtained in the polarization approximation, and (2) its exchange counterpart, the first order exchange repulsion energy. Similarly in the second order term, after either a strong or weak adaptation, there exist not only the induction and dispersion energies, available in the polarization approximation, but also the exchange induction, and exchange dispersion energies. As expected, these exchange counterparts are all short range interactions.

The weak adaptation is physically incorrect because it does not consider the antisymmetry for the first perturbation term. It exists only due to some historic interest for theoretical comparisons. For instance, it is found that the weak adaptation fails, but the strong one succeeds, to produce reasonable induction and exchange induction contributions at the SCF level of the theory between small closed-shell atoms [43-45].

The strong adaptation scheme is able to further predict the existence of short range exchange counterparts of the three basic contributions simultaneously. However, this is a success only in terms of formalism, but not of practical application yet still because of the previously mentioned limitation of the SCF wave functions.

### 1.1.2 Supermolecular ab initio Calculations

Currently most of the pure ab initio calculations for small vdW systems are designed to calculate the energy difference ($\Delta E$), defined as

$$\Delta E = E_{ab} - (\epsilon(A) + \epsilon(B)) \qquad (1.1.2\text{-}1)$$

where $E_{ab}$ is the energy of the vdW complex, $\epsilon(A)$ and $\epsilon(B)$ are the energies of its constituent subunit A and B [1,13,22]. In other words, ab initio calculations are performed for the subunits and the "supermolecule" complex itself, respectively. Because this involves direct ab initio calculations and no individual contributions to the vdW interaction can thus be studied, this scheme is often described as a "brute force" one.

There are many benefits available from this scheme: (1) convergence problems of the aforementioned perturbation treatments are avoided, (2) inter-subsystem electron exchange effects are inherent in ab initio calculations. However, these benefits have been overshadowed by several disadvantages: (1) correlation inaccuracy arising from the SCF wave functions, (2) basis set superposition error (BSSE).

Most supermolecular ab initio calculations are also performed at the straightforward and inexpensive SCF level. Since, as mentioned in Section 1.1.1.1, any SCF calculation will fail to properly include the intra-subunit correlations and the "supermolecular" dispersion, corrections are thus required. Basically there have been three kinds of corrections: (1) semiempirical corrections, (2) perturbation theory corrections (Section 1.1.1), and (3) configuration interaction (CI) corrections. Of course, semiempirical corrections already represent a failure of the theoretical methodology, and are thus avoided by purists. The double perturbation treatments can take account of certain intra-subunit correlations [38]. But since the double perturbation treatments are also based on the SCF wave functions, the very concept of the correction must be seriously questioned. Thus these perturbation treatments are, in some sense, "blind" corrections. On the other hand, there has been no reasonable agreement between the experimental data and the results of the various expensive CI schemes, except for the very small systems such as He-$H_2$ [15,16]. One of the obvious problems of a truncated CI expansion is that the limiting energy of an infinitely separated supermolecule is unequal to the sum

of the subunit energies [46].

In supermolecular calculations for a vdW dimer, the respective subunits experience a lower energy in the enlarged dimer basis set because the basis functions of one subunit increase flexibility of the basis set for the other. This mathematical artifact results in an extra attractive contribution, which is usually named BSSE. This phenomenon is particularly serious for the cases of weak dimers using small basis sets [47,48]. Mostly BSSE is corrected for by the counterpoise method [49], in which the calculations for respective subunits are performed in the presence of the basis functions of the other subunit in the same relative position as in the dimer. Of course, if a very large basis set is someday allowed by the computer, BSSE will no longer be significant. This ideal has already been achieved for some small vdW systems at the SCF level [50].

According to Equation (1.1.2-1), this method requires a subtraction between energies (i.e. $E_{ab}$ and $(\epsilon(A) + \epsilon(B))$) that are many orders of magnitude larger than the vdW interaction energy ($\Delta E$). However, according to the aforementioned basis set problems, none of $E_{ab}$ and $(\epsilon(A) + \epsilon(B))$ can be calculated with an accuracy smaller than or even close to that of $\Delta E$. Therefore the supermolecular calculations have been practically not quite useful.

Recently, considerable improvement on the ab initio route has been made by Dykstra *et al* [51]. However, it still needs more extensive examination before .

### 1.1.3 Group Theoretical Studies

In view of the fact that the above numerical calculations are difficult that only crude results can be obtained from them, it is pragmatic to extract some relevant results purely from symmetry considerations. There are two kinds of symmetry groups that are most important for small isolated molecular systems, viz., the point groups and permutation-inversion (PI) groups [52]. For vdW complexes containing more than one nucleus of a given kind, it is the PI groups that are most useful in the state symmetry labelling and in the application of the labelling to understand intermolecular processes; generally the point group is of little use.

The molecular point group, based on the symmetry of the well defined equilibrium structure of a system, consists of elements that properly and improperly rotate [53] the molecular *vibronic* (not rovibronic) variables. (Reflections ($\sigma$'s), inversion (i), and improper rotations (S's) are all examples of improper rotations [54].) Since all the symmetry elements, such as rotation axes and reflection planes, used by the point group are defined in the rotating, and thus noninertial, molecule-fixed coordinate system, the corresponding symmetry operations should not act on the system rotational coordinates. If they do, all the noninertial forces (centrifugal and Coriolis forces) resulting from the noninertial rotating coordinate system would be altered by such symmetry operations. Since the system energy is thus changed, these symmetry operations cannot commute with the *rovibronic* Hamiltonian. Therefore the symmetry species of the molecular point group can be used to label and classify only the low-lying *vibronic* states of semi-rigid molecules, which have well

defined equilibrium structures.

The specific PI group used for a molecular system is named the molecular-symmetry (MS) group. The MS group, based on the experimentally observed feasibility of the molecular motions corresponding to the possible group elements, consists of three kinds of elements apart from the identity operation: (1) permutations among the experimentally indistinguishable nuclei, (2) parity (space-fixed) inversion of the spatial coordinates (polar vectors [55]) of all electron(s) and nuclei within the system, (All spin coordinates are left unchanged because they are axial vectors [55].) (3) the mixed-product operation of such permutation and space-fixed inversion. (It is noted that any permutation commutes with the inversion operation.)

In terms of the Hamiltonian expression, each PI operation of the MS group affects one or a set of certain rovibronic variables. Generally, the kinetic motions of different rovibronic variables interact with one another through the potential energy coupling terms, which are totally symmetric functions of the corresponding rovibronic variables. In other words, the zero-order states of the same symmetry under the MS group formed by direct multilplication of the zero-order wave functions corresponding to the motions involved can interact among themselves such that the zero-order energy level distribution is perturbed.

More generally, recalling that every term in the Hamiltonian of an isolated system must be totally symmetric, for the interaction building block $\langle i|V|j\rangle$ to be nonzero the state $|i\rangle$ and $|j\rangle$ must have

the same symmetry. Adding terms of rovibronic variable(s) that can be affected by any PI operation of the current MS group to the Hamiltonian will result in a *shifting* of the energy levels, but *not splittings*. One of the most important application of the MS group is thus to eliminate any extraneous numerical calculations for potential couplings between basis functions of different symmetry species [52]. If the added term is a function of the rovibronic variable(s) that cannot be affected by the current MS group operation but by other PI operation(s), then energy level *splittings* will occur, and the MS group needs to be enlarged to include the required new PI operation(s).

However, due to the limited number of nuclei in the system the MS group has an upper limit for its size, which is the "complete nuclear permutation inversion" (CNPI) group. The CNPI group is a PI group purely based on the complete chemical formula of the system; according to the formula, all conceivable combinations of all-particle inversion and nuclear permutations are included as elements. Once the MS group has reached its limit, the CNPI group, all further added terms can cause only energy level shiftings, but no splittings.

According to the definitions of the MS group, its PI operations (elements) have effects on all the spatial rovibronic (not just vibronic) coordinates, but leave the total energy and Hamiltonian unchanged. As a result, the symmetry species of the MS group can be used to classify the rovibronic states, in which several kinds of motions, even tunneling motions, could be highly mixed. This is the crucial advantage of the MS group over the point group. This is also

why the MS group is referred to as a "true" symmetry group, whereas the point group is an "approximate" symmetry group [52].

A comparison between the effects of a point group operation ($\sigma$ reflection) and a PI operation ((23)) on the total energy of the system is made in Figure 1.1.3 for an equilateral triangle molecule. In the upper diagram (a), keeping the system rotational coordinate intact, the point group $\sigma$ reflection of the vibrational (vibronic) coordinates changes the Coriolis force on each circularly "vibrating" nucleus. According to its definition, the Coriolis force on each nucleus is in the direction of $v \times \omega$, where $v$ is the instantaneous velocity of each nucleus with respect to the rotating molecule-fixed coordinate system, and $\omega$ is the angular velocity vector of the rotating system with respect to the laboratory space. Classically speaking, after the reflection, the Coriolis force decreases the restoring force and thus lower the vibrational energy of each vibrating nucleus. In the lower diagram (b), the (23) operation on the rovibrational (rovibronic) coordinate obviously has no effect on the system energy.

Usually weakly bound complexes do not have a single well defined equilibrium structure, as required by the point group treatment. In addition, since the potential barriers among their large amplitude motions are small, the various inter- and even intra-subunit dynamical (rovibronic) coordinates are usually coupled together, and various tunneling motions might occur. The MS group treatment can better exhibit its advantages for such systems, for it can provide many physical insights before accurate numerical calculations are

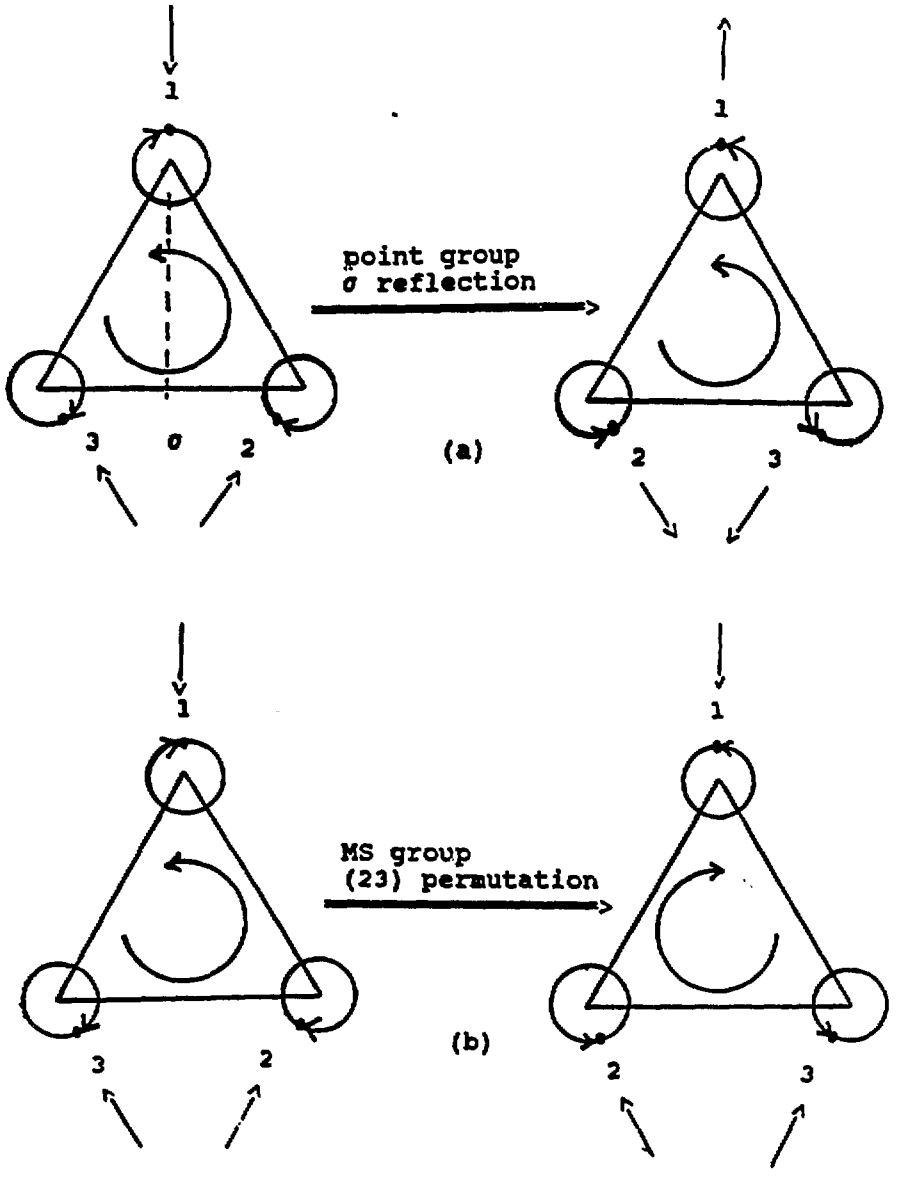


Figure 1.1.3
A comparison between the effects of a point group $\sigma$ reflection and a MS group (23) permutation on a rotating (as indicated as the circular arrow in the middle of each molecule) triatomic molecule with equilateral triangle equilibrium structure. All the nuclei are circularly vibrating as indicated. The directions of the Coriolis force are indicated as straight arrows.

unavailable. In Chapter 3 is presented the application of the MS group theory to FIR spectra of the Ar-$NH_3$ complex studied in this thesis work.

## 1.2 Semiempirical Studies

Semiempirical potential surfaces are obtained by fitting experimental data to parameterized functional forms. Such surfaces are characterized by two features: (1) the parameterization provides the flexibility to fit the experimental data which usually sample the intermediate regions (basically the lower part of the potential well), which are most difficult for current theories, (2) the functional forms can be designed to follow the necessary theoretical constraints in the regions which have not been accessed by experiments (usually long and short ranges). As more experimental data sampling additional regions of configuration space are available, more theoretical constraints will be withdrawn from such potential surface syntheses. In other words, the ultimate goal is to obtain purely experimental potential surfaces.

It is crucial that semiempirical potential surfaces are available especially when their theoretical counterparts cannot be put into practical use. This is because they can serve as (1) ever-improving standards or goals for the theoretical studies and (2) starting points for various applied calculations, in which only the geometries of the potential surfaces are required. As a result, extensive and intensive experimental studies probing the vdW systems have been undertaken for many years with the ultimate goal of producing such potential

surfaces.

### 1.2.1 Useful Experimental Data

Since vdW interactions are involved in almost all chemical phenomena involving two and more classical molecular subunits, various types of experimental data contain information about the potential surfaces [13,56]. For the purpose of semiempirically synthesizing potential surfaces, the value of the data depends upon (1) if an economical data-to-potential inversion scheme is available, and (2) if the data is detailed enough to make the resulting potential surfaces contain the most detailed information, such as intermolecular anisotropy. By such criteria, two types of data have been shown to be superior, viz., molecular beam scattering data, and spectroscopic data, which will be briefly discussed below. (Little information on the anisotropy is contained in measurements of virial coefficients. The information extracted from transport and relaxation properties are generally expensive for heavier molecules [13].)

#### 1.2.1.1 Data from Molecular Beam Studies

In molecular beam experiments, the total elastic cross sections (measured as a function of collision energy) give information mainly on the spherically symmetric part of the potential, while the inelastic (state-to-state) cross sections characterize the anisotropic as well as spherical aspects [57]. However, due to the quality of the experimental data, inversion of the anisotropy has not been extensively employed to date. Some anisotropy information on the

repulsive part of the potential is reflected in the damping of quantum diffraction oscillations of differential or integral cross sections. Since such oscillations are possible only for collision systems with small reduced mass, such as those involving He, its generalization to heavier systems is difficult. On the other hand, certain information on the anisotropy of the well part of the potential is reflected in the damping of the rainbow oscillations [57], which are more obvious for heavier systems. But this type of information is not sensitive enough to the many intricate features on the usually multidimensional potential hypersurface. As a result, in terms of obtaining anisotropy, molecular beam studies are practical only for light dimeric systems involving $H_2$ or He. However, this is complementary to the spectroscopic studies because the complexes containing He or $H_2$ are difficult to generate due to their weak binding energies. Of course, it is complementary in a more general sense that, in terms of the geometry of the potential surfaces, the molecular beam scattering data is more sensitive to the repulsive part, and the spectroscopic data mainly to the "well" part of the potential surface.

A general problem characteristic of the molecular beam study is that the data reduction usually does not yield a potential surface more conclusively than that obtained from spectroscopic data. This is because the least squares fit, an inexpensive routine for spectroscopic data, is still relatively impractical for scattering data. However, the scattering data always serve as tests for trial potential surfaces synthesized using other data, particularly spectroscopic data.

1.2.1.2 Data from Spectroscopy

Since the distribution of intermolecular eigenstates is a direct and detailed manifestation of the topology of the potential "well", spectroscopy has dominated the study of small vdW systems in recent years. In terms of spectral region, the microwave (<1 $cm^{-1}$), infrared (IR: 1000 to a few thousand $cm^{-1}$), and particularly far infrared (FIR: 10 to a few hundred $cm^{-1}$) have been the most valuable. In terms of sample source, the most popular two are: free jets (or molecular beams) and bulk gases. (Although low temperature (<30 K) rare gas matrices have also been popular sample sources, they are impractical in determining the intermolecular eigenstates because the matrix perturbations are on the same order as the intermolecular binding energies of interest.)

Due to the extremely low effective temperatures obtained in molecular beams and free jets, the lower states involved in the spectroscopic transitions are usually within the lowest ground intermolecular vibrational state of the vdW complex. (Here, the "lowest" is emphasized because different intermolecular potential wells are associated with all high frequency vibrations of the classical subunits.) The use of free jets (or molecular beams) can thus greatly reduce the "hot band" spectral congestion caused by the relative high temperature bulk gases [58], and thus simplify the spectrum assignment.

Currently the most useful combinations between the spectral range and the sample source are: microwave-free-jet, FIR-free-jet,

IR-free-jet, and IR-bulk-gas. Basically, the microwave-free-jet spectroscopy probes mostly the lowest ground intermolecular vibrational states, which sample the bottom (near equilibrium) part of the lowest potential wells. Thus far it has been so prolific, with approximately 100 complexes having been studied [14], that it is the lowest parts of intermolecular potential surfaces that are now better understood. The FIR-free-jet spectroscopy measures not only the lowest ground but also the excited intermolecular vibrational states, which sample much more of the potential wells. Due to the large anharmonicity of the intermolecular potential wells, intermolecular vibrational transitions generally have favorable Franck-Condon factors. In order to investigate the global feature of the lowest potential well without any "contamination" by the high frequency vibrations of the subunit(s), the FIR-free-jet spectroscopy has obviously become the most promising tool. As revealed in the "satellite" combination bands (hot bands), the IR spectroscopy accesses the intermolecular vibrational states associated with high frequency vibrations of the classical subunit(s), and thus samples the lowest and some higher intermolecular potential wells simultaneously. It thus provides the dependence of the vdW interaction on the subunit vibrational coordinate. As a result, all these experiments complement themselves. The above discussion by no means implies that the congested "hot band" data provided by bulk gas samples are relatively useless; starting with the free jet experiments is simply an easier and logical approach.

The most useful spectroscopic constants, extracted from the

1kHz-resolution microwave experiments, are rotational constants, dipole moments, and nuclear quadrupole coupling constants. (Of course, other higher order spectroscopic constants such centrifugal distortion constants are also important to test trial potentials.) On the other hand, in the state-of-the-art FIR and IR experiments, the nuclear quadrupole coupling constants are not always available due to the MHz-resolution obtained [14].

Generally speaking, the spectroscopically measured molecular constants of an intermolecular vibrational state of one isotopomer are not enough to determine the structure of that state conclusively. Since the electronic structure of each subunit is generally only slightly distorted by the weak vdW interaction, the structural determination can usually be reduced to the determinations of inter-subunit distance (R) and relative orientation (e.g. three Euler angles for binary complexes). This approximation greatly decreases the number of structural variables and thus the number of isotopomers that have to be studied by microwave spectroscopy for the purpose of structural determination. Since the vdW complexes generally have large amplitude motions, the ground vibrationally averaged structures thus determined generally are quite different from the equilibrium structures, as opposed to the case of semirigid molecules. For weakly bound complexes, the area on the potential surface sampled by the equivalent large amplitude motion is different among the isotopomers; the area sampled by an intermolecular vibrational state of a lighter isotopomer includes and thus is larger than the area by the corresponding state of a heavier isotopomer. Different isotopomers

exhibit different vibrationally averaged structures. The microwave studies for a few isotopomers, if available, thus serve as a practical way to determine whether large amplitude motions occur in the ground intermolecular vibrational states. For a relatively rigid complex, the averaged structures of the isotopomers of the ground intermolecular vibrational state can also be used to extrapolate to the equilibrium structure.

Within the approximation that the subunits remain unperturbed, the inter-subunit orientation can also be obtained from the measurement of the dipole moments and nuclear quadrupole coupling constants of the complex. This is valuable especially when the isotopic substitution study is impractical or not available. For example, classically speaking, in a dimer of dipolar molecules, the measured dipole moment of the complex is the projection of the vectorial sum of the two individual dipole moments on the principal axis of the complex. But the actual measured value, with induction and higher order effects neglected, is an expectation of the dipole projection over the sampled potential surface [59], which needs to be determined. Similarly, the nuclear quadrupole coupling constants, available when the complex contains nucleus with spin $I \geq 1$, also involve the expectation values of the cosine square of the relative orientation angles [59]. Therefore, unless the complex is rigid, the measured dipole moment and nuclear quadrupole coupling constants should *not* be inverted to give the inter-subunit equilibrium orientations directly, but rather serve as values that need be reproduced by trial potential surfaces.

### 1.2.2 Available Intermolecular Potentials

In the wide variety of existing vdW complexes ranging from "true" vdW molecules to vdW ions, the study of potential surface has so far been focused mainly on small neutral atom-molecule and molecule-molecule vdW systems. The binding energies of such systems fall within the range of a few kcal/mole or less. So far the potential surface of He-$H_2$ is the only case successfully studied by ab initio calculations. No theoretical calculation seems generally promising for other simple vdW complexes with more electrons at least in the near future. Currently, semiempirical syntheses of potential surfaces are playing more important roles.

Most of the existing semiempirical potential surfaces have been obtained for complexes with binding energy less than 1 kcal/mole. The reason is that, for weakly bound complexes, it is easier to obtain a large fraction of the intermolecular energy level distribution, and thus the global features of the potential surface. Since the potential surfaces of many relatively stronger systems, such as H-bonded dimers, still cannot be synthesized due to inadequacy of available experimental data, in these cases it is advantageous to organize the obtained energy level distributions with physical insights. An important approach is fit the distribution to a parameterized energy eigenvalue expression derived from a parameterized secular equation corresponding to an effective Hamiltonian. The basic idea can be elucidated in the following example. The resulting energy (E) level distribution of a two-level

system containing state $|1\rangle$ and $|2\rangle$ perturbed by a Hamiltonian operator P can be obtained by solving the following secular equation:

$$\begin{vmatrix} \langle 1|P|1\rangle - E & \langle 1|P|2\rangle \\ \langle 2|P|1\rangle & \langle 2|P|2\rangle - E \end{vmatrix} = \begin{vmatrix} a-E & c \\ c & b-E \end{vmatrix} = 0.$$

Conversely, empirically fitting the parameter (c; a and b are assumed to be known.) corresponds to measuring the Hamiltonian matrix element ($\langle 1|P|2\rangle$). In other words, even when the explicit expression of the perturbation operator (P) is unknown, some physical insights of the Hamiltonian are still available. For large and complicated secular calculations for vdW systems, the use of MS group symmetry consideration can eliminate many off-diagonal terms. Great simplification is thus achieved in Hougen's classic work on $(H_2O)_2$ [60]. As to the Hamiltonian itself, such a method usually assumes the "high barrier limit", in which the complex is as semi-rigid as a normal classical molecule, and all tunneling motions are perturbations treated as above. Therefore it is intrinsically better for relatively strongly bound complexes.

Table 1.2.2 is a list of the potential surfaces obtained in recent years. They are divided into several classes, each of which has basically a chronological listing of the potentials belonging to different complexes; the later the potential appears, the better it is. Most of them are semiempirical, but few theoretical ones (e.g. the CEPA potential for He-$N_2$) are also included if their semiempirical potential surfaces exist. These theoretical potential surfaces are either unsuccessful or experimentally unconfirmed. Also listed are

Table 1.2.2 A list of semiempirical and theoretical potential surfaces of prototypical vdW dimers. Also included are the data types used in the semiempirical syntheses and various experimental tests. (Abbreviation list is shown below the table.)

| (data used) | (potential) | (test(s)(g/b:good/bad)) |
|---|---|---|
| inert gas-$H_2$: | | |
| | Ar-$H_2$, Ar-$D_2$ | |
| partially resolved near IR [65] | (-)[a] [66,67] | |
| above data semiempirical $C_6$, He-Ar potential, | $BC_3$(6,8) [68] | $H_2$,Ar scat(g) [69] trnsp(g) [70] nucl hypf(b) [71-73] $D_2$,Ar scat(b) [74,75] |
| above data, except low rsln IR, low T mix near IR [76] | $TT_3$(6,8) [77] (w/ new disp damp. extended to Kr-$H_2$, X-$H_2$) | rotationally inelastic scat(g) [74] mixed virl coeff(g) [78,79] trnsp, rlx(g) [80,81] |
| inert gas-HCl: | | |
| | Ar-HCl | |
| MW, RF [82,83] | HWK [84] (single min near Ar-HCl configuration) | HCl pres broad(b) [85] |
| HCl rot pres broad [85] | (-) [85,86] | |
| above data, mixed 2nd virl coeff [87] | M3 [88] (bottom similar to HWK, more anisotropic wall, featureless around Ar-ClH region) | HCl pres broad(g) |
| | Ne-HCl | |
| MW [89] (enough for complete angular range) | M5 [89] (2nd min near Ne-ClH) | |

| | | |
|---|---|---|
| | Ar-HCl | |
| above data | M5 [89] (constrained 2nd min near Ar-ClH, as predicted by semiempirical and ab initio calc. [90-92] extended to Kr-HCl, Xe-HCl) | $H_2$,Ar scat(g;better than M3) [93,94], near IR(g) [95] FIR(g) [9-11,96-99] (FIR-->2nd min conclusively [100]) |
| above data | M6 [101] | |
| **inert gas-HF:** | | |
| | X-HF, (X= Ar, Kr, Xe) | |
| MW [102-106] (no data sensitive to X-FH region) | (-) [107] (accurate near X-HF equil structure) | near IR(b) (expecting well deeper by 10-20 $cm^{-1}$ [108]) |
| | HF-HF | |
| MW,RF [109,110] | (-) [111] (accurate around the min) | |
| near IR [112,113] (not used) | | |
| | [ab initio] (high level) [114,115] | |
| **inert gas-$N_2$ and -$O_2$:** | | |
| | He-$N_2$ | |
| total DCS [116] | KSK [116] (anisotropy too weak) | rot rlx(b) |
| (semiempirical) | KKM3 [117] (anisotropy increased) HTT [118], HFD1 [119] HFD2 [119] (extended to Ar-$N_2$, Ne-$N_2$) (all bad) | scat(b) virl coeff(b) trnsp(b) SBE cross section(b) [120,121] |

| | | |
|---|---|---|
| | [CEPA] [122] (too shallow. short range might be approximately close) | vib rlx(b) |
| (semiempirical) | (-) [123] (isotropic part) | |
| | M3SV [124] | (generally bad) |
| | $He-O_2$ | |
| total DCS [116] relative, absolute ICS [125] | (-) [125] (isotropic) | |
| above data, (in)elastic DCS [126] | (-) [126] (anisotropic, fine structure predicted [127]) | (no test) |
| | $Ar-O_2$ | |
| high energy ICS, glory scat, low rsln IR [128] | (-) [128] (fine structure, RF Zeeman spec predicted [129,130]) | |
| above data, new DCS [131] | (-) [131] (extended to $Ar-N_2$) | Zeeman spec [132] (better than the 1st) |
| inert gas-linear polyatomic molecule: | | |
| | $He-CO_2$, $He-N_2O$, $He-C_2N_2$ | |
| total DCS, following only for $He-CO_2$: 2nd virl coeff, viscosity, diffusion coeff, ICS [133] | (-) [133] (all anisotropic. good short range for $He-CO_2$) | |

| | | |
|---|---|---|
| | $He-CO_2$ | |
| above data, pres broad, other trnsp [134] | (-) [134] | differential energy loss spec for rotationally inelastic collision(b) [135] (-->anisotropy of its repulsive part needs modification) |
| | $He-CO_2$, $He-C_2H_2$, He-OCS | |
| above data, better total DCS [136] | (-) [136] | ($He-CO_2$ too weakly bound, no spec available) |
| | $Ar-CO_2$ | |
| MW, 2nd virl coeff, mean-square torque [137] | (-) [137] (strong well anisotropy, good min region; T-shape equil structure. elsewhere uncertain) | total DCS(b) [138] (-->small well anisotropy) |
| | $Xe-CO_2$ | |
| MB differential energy loss spec [139] | (-) [139] (large well anisotropy) | |
| inert gas-$SF_6$: | | |
| | $Ar-SF_6$, $Kr-SF_6$ | |
| total DCS (rainbow oscillation) diffusion coeff, viscosity, 2nd virl coeff [140] | (-) [140] (well anisotropy better determined than for $He-SF_6$. nearly isotropic. equil structure has 3-fold axis) | |
| | $He-SF_6$, $Ne-SF_6$ | |
| total DCS (diffraction oscillation), diffusion coeff, viscosity, 2nd virl coeff 140] | (-) [141] (repulsive wall anisotropy better determined than for $Ar-SF_6$, $Kr-SF_6$ nearly isotropic. equil structure has 3-fold axis) | |

| inert gas-$CH_4$: | | |
|---|---|---|
| | $Ar-CH_4$ | |
| total DCS [142] | {-} [142] | |
| | $Ne-CH_4$, $Ar-CH_4$ | |
| above data, viscosity, 2nd virl coeff [143] | {-} [143] (isotropic) | |
| | $Ar-CH_4$ | |
| MB differential energy loss spec [144] | {-} [144] (equil structure has 3-fold axis) | |
| | $He-CH_4$ | |
| SCF, multipole expansion [145] | {-} [146] (anisotropic) | MB ICS (g) and rotationally inelastic CS (b:near repulsive region) with resolved diffraction oscillations, energy loss spec (b) [146] |

Abbreviations:

calc: calculation(s) coeff: coefficient
CS: cross section
disp damp: dispersion damping function
DCS: differential cross section
equil: equilibrium ICS: integral cross section
MB: molecular beam min: minimum
MW: microwave spectra
nucl hypf: nuclear hyperfine constants
pres broad: pressure broadening
rlx: relaxation data rot: rotation
rsln: resolution scat: scattering data,
SCF: self-consistent field calculation
spec: spectrum T: temperature
trnsp: transportation properties
vib: vibrational virl: virial

[a] {-}: no specific name for the potential
[b] [name]: no specific name for the potential, but the theoretical method is indicated by the name bracketed.

the types of experimental data used in the synthesis of the potential surface, and post-synthesis tests. Strong interactions obviously exist between the experimental measurements and the syntheses of potential. A general fact is that spectroscopy *always* provides the best data for the synthesis (e.g. the conclusive determination for Ar-HCl, purely based on FIR spectra), while other methods provide reasonable post-synthesis testing data. A synthesis without including high resolution spectroscopic data is usually a failure (e.g. the use of only low resolution IR spectroscopic data causes the failure of the $BC_3(6,8)$ potential for $Ar\text{-}H_2$). For very isotropic systems (e.g. Ne-HCl), microwave data can sample all angular coordinates on the potential, while for anisotropic systems (e.g. Ar-HCl), including FIR or IR data is a necessity.

Among the various small prototypical vdW complexes, such as indicated in Table 1.2.2, so far only $Ar\text{-}H_2$, Ne-HCl and Ar-HCl have semiempirical potential surfaces determined conclusively for most of the "intermediate" range in the well. Similar semiempirical potential surfaces have been synthesized for their heavier inert gas analogues. However, in order to be confirmed, these extended syntheses, for which less spectroscopic data are used, require more experimental examinations, particularly FIR and IR spectroscopy. Of course, including those in this table, all other prototypical systems need to be measured spectroscopically to accurately establish their potential surfaces. Although the semiempirical synthesis is still in its infancy in terms of the number of conclusive potential surfaces obtained, it is becoming a promising "industry".

## 1.3 Demonstrative Achievement of High Resolution FIR Spectroscopy: Ar-HCl Potential Surface

Spectroscopy measurements, particularly in the FIR, have become an important method for the semiempirical syntheses of potential surfaces. Such a key role played by the high resolution FIR spectroscopy was first demonstrated in its probing of Ar-HCl, the prototypical anisotropic vdW complex, which has attracted most extensive experimental studies [9,61].

Hutson and Howard semiempirically synthesized several potential surfaces for Ar-HCl by performing a simultaneous least squares fit in different parameterized functional forms (basically Maitland-Smith forms) to several types of data, including molecular beam scattering, HCl rotational line broadening, second virial coefficients and molecular beam electric resonance (MBER) spectra. In terms of fitting, two equally good potential surfaces, labelled as M3 and M5, were then obtained. The major difference between the two surfaces is in the number of potential minima. The M3 potential has only one minimum at the Ar-HCl linear configuration. However, the M5 potential has a secondary minimum at Ar-ClH linear configuration. This implies that all the above experimental data together are inadequate to determine the global topological features of the potential.

Later our research group measured the FIR Stark spectra of the first three intermolecular vibrational states of Ar-HCl, viz., the lowest $\Sigma$ bend, $\Sigma$ stretch and $\Pi$ bend state distributed from 25–34 $cm^{-1}$ [10,11,61-64], with ~MHz resolution. Employing these FIR measurements

along with the ground state microwave data from MBER, Hutson fitted a new double minimum potential (M6)*, which is well determined in most of the attractive part. [17] The question of a single minimum or double minima was then answered very clearly. This represents a breakthrough in the determination of the intermolecular potential surfaces because only spectroscopic data are included in the fit. [61,9]

Based upon such inherent superiority of the high resolution FIR spectroscopic data to other non-spectroscopic data, it is desirable to extend these measurements to more complicated vdW complexes using tunable FIR direct absorption spectroscopy. It is noted in Table 1.2.2 that, except for the unlisted atom-atom systems, only the potential surfaces for atom-diatom systems have ever been determined successfully. In terms of both geometric and spectroscopic complexity, as well as physical interest, it is logical to study an atom-symmetric-top system as the next step in the process. Consequently, the Ar-$NH_3$ complex, which is clearly one of the best candidates, becomes the target of this thesis work.

References

1. P. Hobza and R. Zahradnik, Chem. Rev. 88, 871 (1988).

2. I. Dzidic and P. Kebarle, J. Phys. Chem. 74, 1466 (1970).

3. H. Kistenmacher, H. Popkie and E. Clementi, J. Chem. Phys. 61, 799 (1974).

4. T.P. Lybrand and P.A. Kollman, J. Chem. Phys. 83, 2923 (1985).

5. J.M. Farrar, T.P. Schafer, and Y.T. Lee in 'Transport Phenomena' (J. Kestin, ed.), A.I.P. Conference Proceedings No.11 (1973).

6. J.E. Huheey, 'Inorganic Chemistry', 2nd ed. (Harper & Row Publishers, New York, 1978), p.842.

7. T.R. Dyke, K.M. Mack, and J.S. Muenter, J. Chem. Phys. 66, 498 (1977).

8. L.A. Curtiss and J.A. Popple, J. Mol. Spectrosc. 55, 1 (1975).

9. R.L. Robinson, Ph.D. Dissertation, University of California, Berkeley (1987).

10. R.L. Robinson, D.-H. Gwo, D. Ray and R.J. Saykally, J. Chem. Phys. 86, 5211 (1987).

11. R.L. Robinson, D.-H. Gwo, D. Ray and R.J. Saykally, Mol. Phys. 63, No.6, 1021 (1988).

12. A.S. Pine, W.J. Lafferty, B.J. Howard, J. Chem. Phys. 81, 2939 (1984).

13. A.D. Buckingham, P.W. Fowler, and J.M. Hutson, Chem. Rev. 88, 963 (1988).

14. D.J. Nesbitt, Chem. Rev. 88, 843 (1988).

15. W. Myer, P.C. Hariharan, W. Kutzelnigg, J. Chem. Phys. 73, 1880 (1980).

16. J. Schaefer, W.E. Kohler, Physica A, 129, 469 (1985).

17. R.J. Saykally, Accounts of Chem. Research, 22, 295 (1989) and references therein.

18. M.P. Casassa, Chem. Rev. 88, 815 (1988).

19. L.A. Curtiss and M. Blander, Chem. Rev. 88, 827 (1988).

20. A.E. Reed, L.A. Curtiss, and F. Weinhold, Chem. Rev. 88, 899 (1988).

21. C.J. van Oss, M.K. Chaudhury, and R.J Good, Chem. Rev. 88, 927 (1988).

22. G. Chalasinski and M. Gutowski, Chem. Rev. 88, 943 (1988).

23. J.D. Jackson, 'Classical Electrodynamics', 2nd ed. (John Wiley and Sons, New York, 1975).

24. P.W. Atkins, 'Physical Chemistry' (W.H. Freeman and Co., San Francisco, 1982).

25. F. London, Trans. Faraday Soc. 33, 8 (1937).

26. P. Claverie, Int. J. Quant. Chem. 5, 273 (1971).

27. P. Claverie, In 'Intermolecular Interactions: From Diatomics to Biopolymers', B. Pullman, ed. (Wiley, New York, 1978).

28. W. Kutzelnigg, J. Chem. Phys. 73, 343. (1980).

29. W.J. Meath, Am. J. Phys. 40, 21 (1972).

30. A. Dalgarno, J.T. Lewis, Proc. R. Soc. London, Ser.A, A233, 70 (1955).

31. R.H. Young, Int. J. Quant. Chem. 9, 47 (1975).

32. H. Kreek, W.J. Meath, J. Chem. Phys. 50, 2289 (1969).

33. J.O. Hirschfelder, C.F. Curtiss, R.B. Bird, 'Molecular Theory of Gases and Liquids' (Wiley, New York, 1964).

34. R. Buehler, J.O. Hirschfelder, Phys. Rev. 83, 628 (1951).

35. R. Buehler, J.O. Hirschfelder, Phys. Rev. 85, 149 (1952).

36. K.C. Ng, W.J. Meath, A.R. Allnatt, Mol. Phys. 32, 177 (1976).

37. R.S. Berry, S.A. Rice, and J. Ross, 'Physical Chemistry' (John Wiley and Sons, New York, 1980).

38. B. Jeziorsky, W. Kolos, Int. J. Quant. Chem. XII, Suppl 1, 91 (1977).

39. K. Szalewics, B. Jeziorsky, Mol. Phys. 38, 191 (1979).

40. S. Rybak, K. Szalewics, B. Jeziorsky, and M. Jaszunski, J. Chem. Phys. 86, 5652 (1987).

41. S. Rybak, Ph.D. thesis, University of Warsaw (1988).

42. G. Chalasinski, Mol. Phys. 49, 1353 (1983).

43. G. Chalasinski, B. Jeziorski, Theor. Chim. Acta, 46, 277 (1977).

44. G. Chalasinski, B. Jeziorski, Mol. Phys. 32, 81 (1976).

45. M. Jaszunski, Mol. Phys. 39, 77 (1980).

46. J.H. van Lenthe, J.G.C.M. van Duijneveldt-van de Rijdt, F.B. van Duijneveldt, Adv. Chem. Phys. 69, 521 (1987).

47. P.W. Fowler, A.D. Buckingham, Mol. Phys. 50, 1349 (1983).

48. M. Losonczy, J.W. Moscowitz, F.H. Stillinger, J. Chem. Phys. 61, 2438 (1974).

49. S.F. Boys, F. Bernardi, Mol. Phys. 19, 553 (1970).

50. M. Gutowski, J. van Lenthe, J. Verbeek, F.B. van Duijneveldt, G. Chalasinski, Chem. Phys. Lett. 124, 370 (1986).

51. C.E. Dykstra, Acc. Chem. Res. 21, 355 (1988).

52. P.R. Bunker, 'Molecular Symmetry and Spectroscopy' (Academic Press, New York, 1979).

53. J.T. Hougen, "Methane Symmetry Operations". MTP International Review of Science, Physical Chemistry (Editor: D.A. Ramsy), Series Two, Vol.3 Spectroscopy (Butterworth, London, 1976).

54. J.B. Marion, 'Classical Dynamics of Particles and Systems', 2nd ed. (Academic Press, New York, 1970)

55. G. Arfken, 'Mathematical Methods for Physicists' (Academic Press, New York, 1966)

56. M. Rigby, E.B. Smith, W.A. Wakeham, G.C. Maitland, 'The Forces between Molecules' (Clarendon Press, Oxford, 1986).

57. R.B. Bernstein, 'Chemical Dynamics via Molecular Beam and Laser Techniques' (Clarendon Press, Oxford, 1982).

58. A.S. Pine, J. Opt. Soc. Am. 64, 1683 (1974); 66, 97 (1976).

59. D.D. Nelson, Jr., G.T. Fraser, K.I. Peterson, K. Zhao, W. Klemperer, F.J. Lovas, R.D. Suenram, J. Chem. Phys. 85, 5512 (1986), and references therein.

60. L.H. Cordert and J.T. Hougen, J. Mol. Spectrosc. 130, 86 (1988), and references therein.

61. D. Ray, Ph.D. Dissertation, University of California, Berkeley (1985), and references therein.

62. D. Ray, R.L. Robinson, D.-H. Gwo, R.J. Saykally, J. Chem. Phys. 84, 1171 (1986).

63. R.L. Robinson, D. Ray, D.-H. Gwo, R.J. Saykally, J. Chem. Phys. 87, 5149 (1987).

64. R.L. Robinson, D.-H. Gwo, R.J. Saykally, J. Chem. Phys. 87, 5156 (1987).

65. A.R.W. McKellar, H.L. Welsh, J. Chem. Phys. 55, 595 (1971).

53. J.T. Hougen, "Methane Symmetry Operations". MTP International Review of Science, Physical Chemistry (Editor: D.A. Ramsy), Series Two, Vol.3 Spectroscopy (Butterworth, London, 1976).

54. J.B. Marion, 'Classical Dynamics of Particles and Systems', 2nd ed. (Academic Press, New York, 1970)

55. G. Arfken, 'Mathematical Methods for Physicists' (Academic Press, New York, 1966)

56. M. Rigby, E.B. Smith, W.A. Wakeham, G.C. Maitland, 'The Forces between Molecules' (Clarendon Press, Oxford, 1986).

57. R.B. Bernstein, 'Chemical Dynamics via Molecular Beam and Laser Techniques' (Clarendon Press, Oxford, 1982).

58. A.S. Pine, J. Opt. Soc. Am. 64, 1683 (1974); 66, 97 (1976).

59. D.D. Nelson, Jr., G.T. Fraser, K.I. Peterson, K. Zhao, W. Klemperer, F.J. Lovas, R.D. Suenram, J. Chem. Phys. 85, 5512 (1986), and references therein.

60. L.H. Cordert and J.T. Hougen, J. Mol. Spectrosc. 130, 86 (1988), and references therein.

61. D. Ray, Ph.D. Dissertation, University of California, Berkeley (1985), and references therein.

62. D. Ray, R.L. Robinson, D.-H. Gwo, R.J. Saykally, J. Chem. Phys. 84, 1171 (1986).

63. R.L. Robinson, D. Ray, D.-H. Gwo, R.J. Saykally, J. Chem. Phys. 87, 5149 (1987).

64. R.L. Robinson, D.-H. Gwo, R.J. Saykally, J. Chem. Phys. 87, 5156 (1987).

65. A.R.W. McKellar, H.L. Welsh, J. Chem. Phys. 55, 595 (1971).

87. B. Schramm, U. Leuchs, Ber. Bunsenges. Phys. Chem. 83, 847 (1979).

88. J.M. Hutson, B.J. Howard, Mol. Phys. 43, 493 (1981).

89. J.M. Hutson, B.J. Howard, Mol. Phys. 45, 769 (1982), and references therein.

90. C. Douketis, J.M. Hutson, B.J. Orr, G. Scoles, Mol. Phys. 52, 763 (1984).

91. J.H. van Lenthe, T. van Dam, F.B. van Duijneveldt, L.M.J. Kroon-Battenburg, J. Faraday Symp. Chem. Soc. 19, 125 (1984).

92. J. Andzelm, S. Huzinaga, M. Klobukowski, E. Radzio Chem. Phys. 100, 1 (1985).

93. U. Buck, J. Schleusener, J. Chem. Phys. 75, 2470 (1981).

94. U. Buck, Faraday Discuss. Chem. Soc. 73, 308 (1982).

95. B.J. Howard, A.S. Pine, Chem. Phys. Lett. 122, 1 (1985).

96. M.D. Marshall, A. Charo, H.O Leung, W. Klemperer, J. Chem. Phys. 83, 4924 (1985).

97. D. Ray, R.L. Robinson, D.-H. Gwo, R.J. Saykally, J. Chem. Phys. 84, 1171 (1986).

98. R.L. Robinson, D. Ray, D.-H. Gwo, R.J. Saykally, J. Chem. Phys. 87, 5149 (1987).

99. R.L. Robinson, D.-H. Gwo, R.J. Saykally, J. Chem. Phys. 87, 5156 (1987).

100. J.M. Hutson, J. Chem. Soc., Faraday Trans. 2, 82, 1163 (1986).

101. J.M. Hutson, J. Chem. Phys. 89, 4550 (1988).

102. S.J. Harris, S.E. Novick, W. Klemperer, J. Chem. Phys. 60, 3028 (1074).

103. T.A. Dixon, C.H. Joyner, F.A. Baiocchi, W. Klemperer, J. Chem.

Phys. 74, 6539 (1981).

104. F.A. Baiocchi, T.A. Dixon, C.H. Joyner, W. Klemperer, J. Chem. Phys. 75, 2014 (1981).

105. M.R. Keenan, L.W. Buxton, T.J. Balle, W.H. Flygare, J. Chem. Phys. 74, 2133 (1981).

106. L.W. Buxton, E.J. Campbell, M.R. Keenan, T.J. Balle, W.H. Flygare, Chem. Phys. 54, 173 (1981).

107. J.M. Hutson, B.J. Howard, Mol. Phys. 45, 791 (1982).

108. G.T. Fraser, A.S. Pine, J. Chem. Phys. 85, 2502 (1986).

109. T.R. Dyke, B.J. Howard, W. Klemperer, J. Chem. Phys. 56, 2442 (1972).

110. B.J. Howard, T.R. Dyke, W. Klemperer, J. Chem. Phys. 81, 5224 (1984).

111. A.E. Barton, B.J. Howard, Faraday Discuss. Chem. Soc. 73, 45 (1982).

112. A.S. Pine, W.J. Lafferty, J. Chem. Phys. 78, 2154 (1983).

113. A.S. Pine, W.J. Lafferty, B.J. Howard, J. Chem. Phys. 81, 2939 (1984).

114. D.W. Michael, C.E. Dykstra, J.M. Lisy, J. Chem. Phys. 81, 5998 (1984).

115. M.J. Redmon, J.S. Binkley, J. Chem. Phys. 87, 969 (1987).

116. M. Keil, J.T. Slankas, A. Kupperman, J. Chem. Phys. 70, 541 (1979), and references therein.

117. W.-K. Liu, F.R. McCourt, D.E. Fitz, D.J. Kouri, J. Chem. Phys. 75, 1496 (1981).

118. P. Habitz, K.T. Tang, J.P. Toennies, Chem. Phys. Lett. 85, 461

(1982).

119. R.R. Fuchs, F.R.W. McCourt, A.J. Thakkar, F. Grein, J. Phys. Chem. 88, 2036 (1984).

120. M. Faubel, K.H. Kohl, J.P. Toennies, K.T. Tang, Y.Y. Yung, Faraday Discuss. Chem. Soc. 73, 205 (1982).

121. F.R. McCourt, R.R. Fuchs, A.J. Thakkar, J. Chem. Phys. 80, 5561 (1984).

122. A.J. Banks, D.C. Clary, H.-J. Werner, J. Chem. Phys. 84, 3788 (1986).

123. R. Candori, F. Pirani, F. Vecchiocattivi, F.A. Gianturco, U.T. Lamanna, G. Petrella, Chem. Phys. 92, 345 (1985).

124. F.A. Gianturco, M. Venanzi, R. Candori, F. Pirani, F. Vecchiocattivi, A.S. Dickinson, M.S. Lee, Chem. Phys. 109, 417 (1986).

125. F. Battaglia, F.A. Gianturco, P. Casavecchia, F. Pirani, F. Vecchiocattivi, Faraday Discuss. Chem. Soc. 73, 257 (1982).

126. M. Faubel, K.H. Kohl, J.P. Toennies, F.A. Gianturco, J. Chem. Phys. 78, 5629 (1983), and references therein.

127. J. Tennyson, A. van der Avoird, Chem. Phys. Lett. 105, 49 (1984).

128. F. Pirani, F. Vecchiocattivi, Chem. Phys. 59, 387 (1981), and references therein.

129. V. Mingelgrin, R.G. Gordon, J. Chem. Phys. 70, 3828 (1979).

130. J. Tennyson, J. Mettes, Chem. Phys. 76, 195 (1983).

131. R. Candori, F. Pirani, F. Vecchiocattivi, Chem. Phys. Lett. 102, 412 (1983), and references therein.

132. J. Mettes, B. Heymen, P. Verhoeve, J. Reuss, D.C. Laine, G.

Brocks, Chem. Phys. 92, 9 (1985).

133. G.A. Parker, M. Keil, A. Kupperman, J. Chem. Phys. 78, 1145 (1983).

134. M. Keil, G.A. Parker, J. Chem. Phys. 82, 1947 (1985).

135. U. Buck, H. Meyer, M. Tolle, R. Schinke, Chem. Phys. 104, 345 (1986).

136. I. Danielson, K.M. McLeod, M. Keil, J. Chem. Phys. 87, 239 (1987).

137. A.M. Hough, B.J. Howard, J. Chem. Soc., Faraday Trans. 2, 83, 173, 191 (1987), and references therein.

138. G. Rotzoll, A. Lubbert, J. Chem. Phys. 71, 2275 (1979).

139. U. Buck, F. Huisken, D. Otten, R. Schinke, Chem. Phys. Lett. 101, 126 (1983).

140. R.T. Pack, J.J. Valentini, J.B. Cross, J. Chem. Phys. 77, 5486 (1982)

141. R.T. Pack, E. Piper, G.A. Pfeffer, J.P. Toennies, J. Chem. Phys. 80, 4940 (1984).

142. U. Buck, J. Schleusen ner, D.J. Malik, D. Secrest, J. Chem. Phys. 74, 1707 (1981).

143. M.J. O'Loughlin, B.P. Reid, R.K. Sparks, J. Chem. Phys. 83, 5647 (1985), and references therein.

144. U. Buck, A. Kohlhase, A. Phillips, D. Secrest, Chem. Phys. Lett. 98, 199 (1983).

145. R. Ahlrichs, R. Penco, and G. Scoles, Chem. Phys. 19, 119 (1979).

146. U. Buck, K.H. Kohl, A. Kohlhase, M. Faubel, V. Staemmler, Mol. Phys. 55, 1255 (1985).

# Chapter 2

## Berkeley Tunable Far-Infrared/Planar Jet Laser Spectrometer

### 2.1 Spectrometer

The Tunable far infrared (FIR) laser system and the supersonic planar jet configuration have been described in previous papers [1-4] and Laughlin's dissertation [5], and will be discussed only briefly in the following.

The schematic diagram of the spectrometer is shown in Figure 2.1. The tunable monochromatic FIR radiation used is generated by mixing the output of an optically pumped, selectable fixed frequency FIR molecular gas laser (shop built) with that of a YIG-tuned microwave oscillator (HP 8673B) system. A discharge pumped $CO_2$ mid-infrared laser (Apollo 150), with maximum power 150 W, serves to longitudinally pump the FIR laser. The $CO_2$ laser is line tunable, among approximately 100 different $CO_2$ vibration-rotation transitions, using a grating at one end of the laser cavity. The zero order beam from the grating is sent to a spectrum analyzer (Optics Engineering) to identify the pump laser line. Over 60 different simple organic molecules, including their deutero-derivatives, can be pumped to produce over 2000 discrete FIR laser frequencies from 10-200 $cm^{-1}$ [6]. In this work, HCOOH was used to produce the 692.9513 GHz, 761.6087 GHz, and 564.3857 GHz laser lines, and DCOOD for the 787.7565 GHz laser line. The FIR laser output, with FWHM approximately 100 kHz, is directed through a polarizing Michelson diplexer into a cornercube in

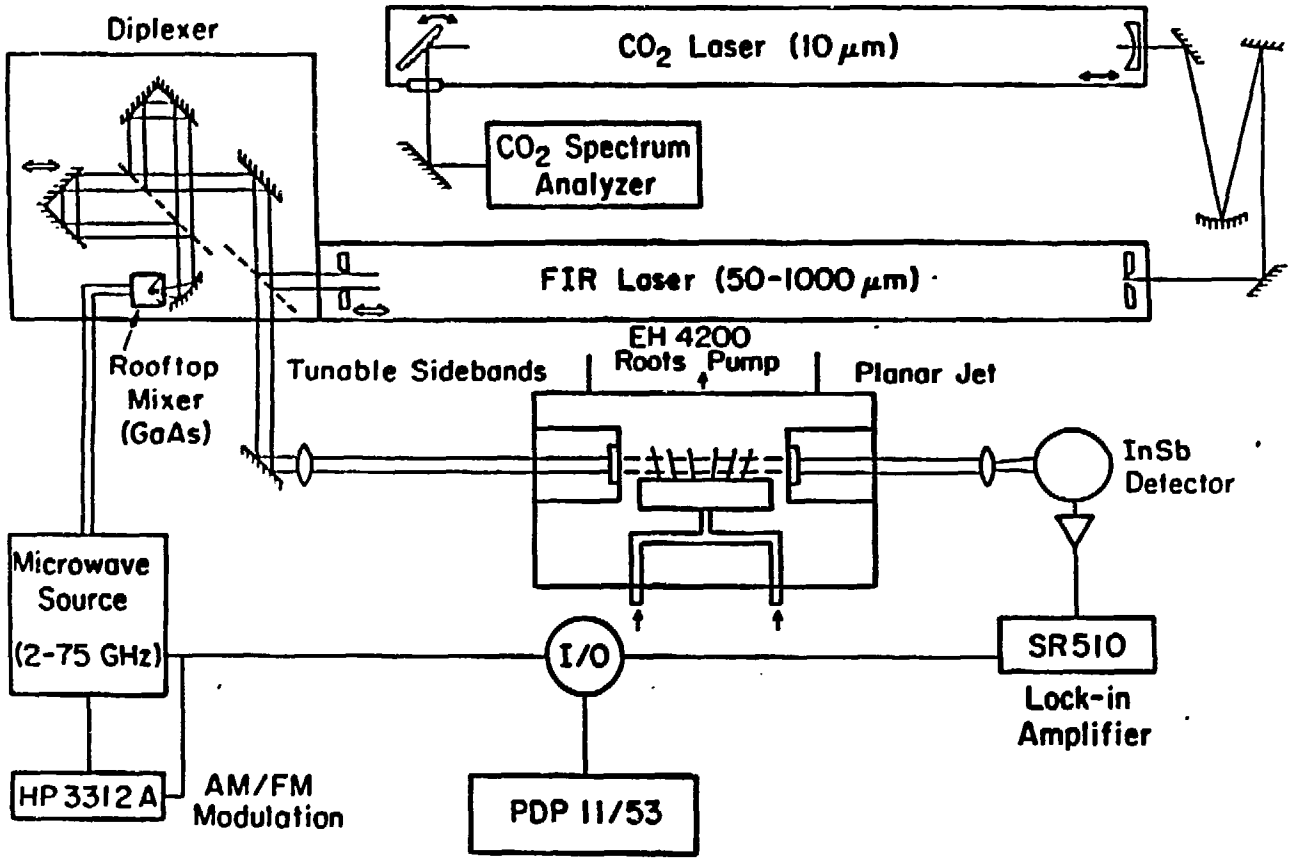


Figure 2.1
Schematic of the Berkeley Tunable Far-Infrared/Planar Jet Laser Spectrometer.

which a GaAs Schottky barrier diode together with a contacting 0.001 in. diameter whisker antenna are mounted. The FIR laser radiation is thus coupled onto the diode through the antenna. In the meantime, tunable microwave radiation is also coupled onto the diode either through the whisker mount or through the post on which the diode is located. The microwave tuning range from 2-26 GHz from the microwave oscillator is extended to 2 to 75 GHz by using frequency doublers (Spacek Ka2X, Honeywell V2200N) combined with a travelling wave tube amplifier (Hughes 8001H12). Due to the nonlinearity of the voltage vs. current characteristic curve of the diode, the fixed frequency FIR and tunable microwave radiation are mixed, and the resultant tunable FIR sidebands are generated at the sum and difference of the FIR laser and the microwave frequencies. Consequently, tunable first order FIR sidebands are produced from 2-75 GHz on either side of the FIR laser line. In other words, a 5 $cm^{-1}$ tunability is carried by each fixed frequency FIR laser line. Both the FIR carrier, viz., the laser frequency component, and the sidebands radiate from the cornercube back through the diplexer, which then separates the sidebands from the much more intense carrier. In the 30 $cm^{-1}$ region, the resultant total power of the two sidebands is approximately 100-200 $\mu W$ on the strongest FIR laser lines. Both sidebands are collimated together and sent through the planar supersonic jet expansion in which the van der Waals (vdW) complexes are generated due to the well known cooling effect. The absorption signals are detected with a liquid helium cooled InSb hot electron bolometer (Cochise Instruments) with typical sensitivities of $10^{-12}$-$10^{-13}$ $W/Hz^{1/2}$. Accordingly, a power/noise

ratio exceeding $10^5$ for an integration time of one second can be obtained. The microwave radiation and thus the FIR sidebands are frequency modulated at 100 kHz with a frequency deviation 125 kHz. The absorption signals from the bolometer are lock-in (SR 519) demodulated at twice the modulation frequency. A minicomputer (Digital PDP11/53) is used to help control the scanning and store the data.

When the transition moment is about 1 Debye, the stronger transitions absorb at least 0.1% of the sideband power. According to the estimated power/noise ratio this implies that the best signal to noise is expected to be larger than 1000. Since both sidebands pass through the expansion, which one that causes an absorption must be determined. By slightly changing the FIR laser frequency to the red, for example, i.e. slightly increasing the laser cavity length, the upper sideband absorption will require a higher microwave frequency, however the lower sideband a lower microwave frequency. In other words, by "pulling" the FIR laser the shift direction of the absorption peak with respect to the scanning microwave frequency identifies the sideband. Of course, the FIR laser can also be pulled to the blue, with opposite peak shifts. The FIR laser has to be reset to the peak of its gain curve after the laser pulling. However, because the FIR laser is not locked, such resetting actually dominates the uncertainties in the absolute measurements of the absorption frequencies. This uncertainty is estimated to be about 0.5-1.0 MHz. Nuclear quadrupole hyperfine structures generally appear in one scan, typically 10 MHz, and is not affected by the laser pulling. The

uncertainties in the quadrupole constants is mainly due to the spectrum resolution; the hyperfine structures are only partially resolved for Ar-$NH_3$.

The planar supersonic jet expansion is generated by passing a gas mixture through a 1.5"×0.001" stainless steel slit housed in a large vacuum chamber. The vacuum is maintained by a 2850 cfm roots blower (Edwards EH4200) backed with two 175 cfm mechanical pumps (Edwards E2M275) in parallel. Limited by the 40'x8" PVC pipe connecting the vacuum chamber and the roots blower, the effective pumping speed is estimated to be 1600 cfm. Typical operating conditions are 700±200 Torr behind the slit nozzle with a chamber background pressure approximately 90±20 mTorr. The gas mixture generally consists of a molecular species of interest seeded in a carrier gas (such as a noble gas), which could also be a constituent of the vdW complexes. For example, 1-3% $NH_3$-in-Ar mixtures are used in the studies of Ar-$NH_3$ and $(NH_3)_2$. To avoid too many higher molecular clusters, higher percentage is not used. The planar expansion has two major advantages over the pinhole expansion: (1) the detection sensitivity is greatly increased by increasing the effective pathlength and the total number of sampled vdW complexes, (2) Doppler linewidth is reduced by a factor of one order of magnitude due to the "alignment" effect of the planar flow.

The sub-Doppler line width make many rotational fine structures and part of nuclear hyperfine structures to be resolved even in FIR. Typical linewidth ranges from 200-400 kHz. Since the frequency modulation deviation is 125 kHz, which is smaller than the measured

linewidth, the artefact broadening due to the modulation scheme is negligible to a first approximation (see Figure 2.2.1.2.3-5 in Section 2.2.1.2.3). According to the total densities of about $10^{15}$ $cm^{-3}$ in the probed region of the expansion estimated in similar experiments on Ar-$H_2O$ [7], the pressure broadening should contribute less than 100 kHz to the linewidth. In addition, the time-of-fight broadening is estimated to be 75 kHz. These estimations indicate that the residual Doppler broadening effect dominates the linewidth.

## 2.2 Lock-in Stabilization of the cw $CO_2$ Laser

The frequency stability of the FIR laser depends mostly upon that of the pump $CO_2$ laser [8]. The stabilization of the $CO_2$ laser is thus important to the operation efficiency of the spectrometer as well as accuracy of the measured FIR spectral frequencies. The two most popular methods for locking the $CO_2$ laser have been: (1) frequency locking with an etalon, and (2) power locking with a lock-in stabilizer, such as Lansing lock-in stabilizer (Model 80.215).

The etalon frequency locking uses the transmission of the $CO_2$ laser output through an etalon with its mirror spacing thermally stabilized to establish high frequency precision. The etalon spacing is ramped over a short distance centered at its mean value. The dithered transmission is then detected and inverted electronically into a feedback signal to the piezoelectric translator (PZT) which controls the $CO_2$ laser cavity length to within one wave length of the laser. In other words, the $CO_2$ laser is locked at the frequency corresponding to the mean etalon mirror spacing. This scheme, using a

Burleigh etalon (Model #CFT-500IR), has proven effective elsewhere with a measured drift in the FIR output frequency of approximately 100 kHz/hour [8,9]. However, despite its critical requirement for alignment to avoid multimode transmission, the major disadvantage is cost; the etalon alone is about $15,000.

The power locking with a conventional lock-in stabilizer involves the modulation of the laser PZT and the demodulation of the corresponding electronic signal of the detected dithered laser output power into a dc correction which is fed back to the PZT. Since the $CO_2$ laser output power is a strong function of its output frequency (determined by the cavity length), it is the frequency corresponding to the maximum output power that is locked. However, this locking scheme also has its drawbacks; the maximum power operating point is generally close to the most noisy spot, due to certain resonances (few hundred kHz and up) of the lasing gas electric discharge, moreover, it is usually not at the $CO_2$ frequency optimum for optically pumping the FIR laser.

As a result, a new and versatile offset locking scheme for the cw $CO_2$ laser has been designed and put into practical use on the spectrometer. Typical drift in the FIR output frequency achieved by this method is approximately 75 kHz/hour, which is better than obtained from the expensive etalon locking scheme. Since the locked operating point can be set selectively to almost anywhere on the $CO_2$ laser output power profile (as a function of its laser frequency), the noisy spots can basically be avoided to greatly facilitate the spectrometer operation.

### 2.2.1 Principles of Offset Lock-in Stabilization

Here the design concepts for an electronic offset lock-in stabilization system will be introduced. Being generally applicable to any dc-controlled system with a sufficiently short response time constant to allow the modulation, the principles of the new scheme will be explained with terminology that is not specific to the laser system. But when appropriate the corresponding terminology for laser systems will also be incorporated.

The new designs are modifications to the conventional lock-in stabilization scheme. They help to stabilize a dc-controlled system at any point on its characteristic curve (system output, a physical variable as a function of input dc voltage), as opposed to conventional lock-in stabilization, which locks only at one of the local extrema (maxima or minima). As a starting point for modification, the basic principle of conventional lock-in stabilization will be briefly reviewed. The new design will then be explained with some geometrical arguments.

#### 2.2.1.1 Conventional Lock-in Stabilization

A conventional lock-in stabilizer consists basically of three parts: (1) a lf lock-in amplifier, which generates the modulation sine wave and demodulates the periodic response of the dc-controlled system, when necessary, into a correction dc voltage, (2) a dc power supply, which provides the controlling dc bias voltage for the system before the correction, and (3) a voltage adder, which superimposes the

correction dc and the power supply bias voltages together to form a corrected controlling dc voltage that maintains the average output of the system.

The graphical example, shown in Figure 2.2.1.1, further demonstrates the mechanism. Without losing generality, the characteristic curve of the system to be stabilized is assumed to be a Gaussian function of the controlling dc bias. In the case of a laser system, this could be the output power profile as a function of the dc-bias-controlled cavity length or of the corresponding laser frequency. Suppose that the bias is originally intended to be set at the maximum (point M in Figure 2.2.1.1) of the curve, but the operating point drifts to the left (point L) of the maximum. According to the periodic response (trace 1) of the system at point L, the stabilizer generates a correction dc voltage (trace 1') to the existing dc bias (at point L) to force the operating point back toward the maximum, at which the periodic response of the system generates no dc correction (trace m'). For the case of drifting to the right of the maximum, a similar but opposite returning dc correction can be obtained because the periodic response of the system is basically 180° out of phase with respect to on the left. The stabilization at the maximum can therefore be achieved. The disappearance of the dc correction at the maximum is due to the fact that the dc output of a 1f lock-in amplifier is proportional to the amplitude of the fundamental modulation frequency (1f) component in its input with the signed proportionality constant controlled by the lock-in phase setting. However the fundamental frequency of the system output at

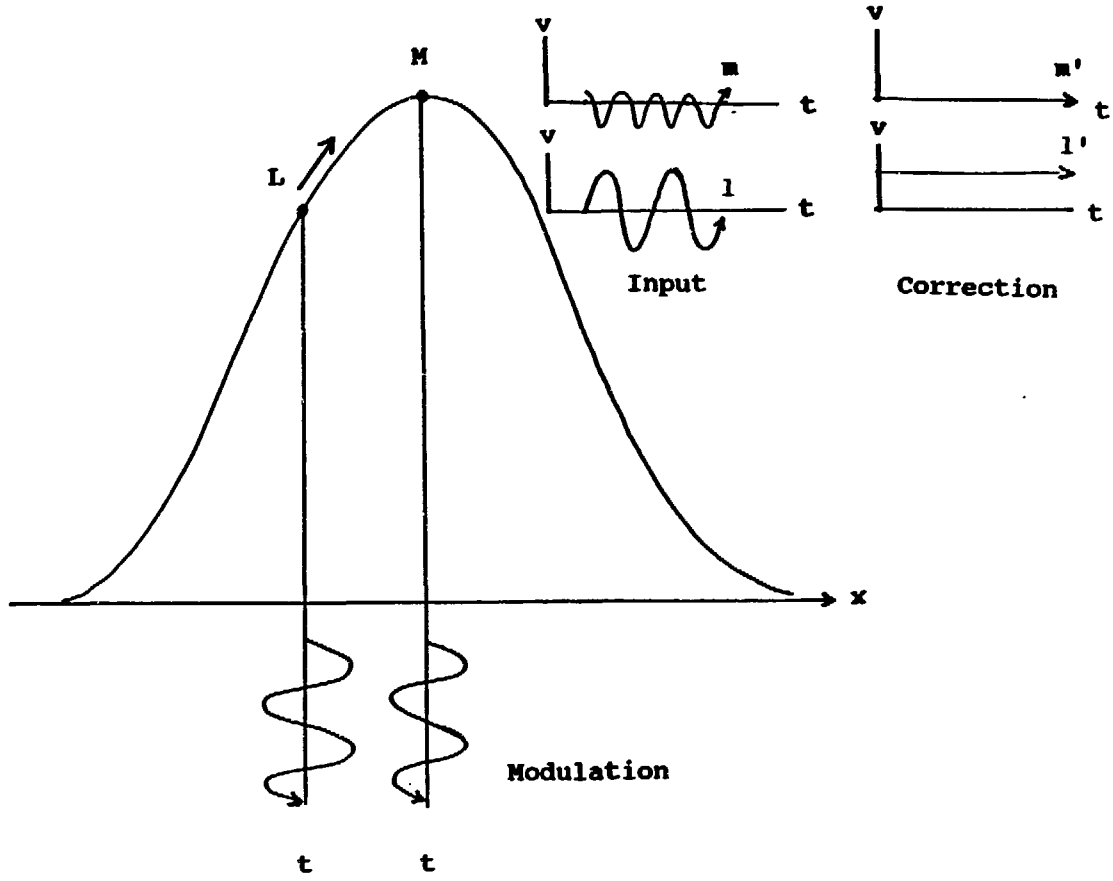


Figure 2.2.1.1
Mechanism of conventional 1f lock-in stabilizer.

the maximum of the symmetric Gaussian function is the second harmonic of the modulation frequency. Here, the term locally "symmetric" should be emphasized because only in such cases is the maximum the same as the locked point, as will be further demonstrated in Section 2.2.1.2. If it is locally asymmetric, a shift is generally expected between the locked point and the local extremum. (The stabilization at a local minimum is analogous except that the demodulation phase of the lock-in amplifier needs to be 180° out of phase, as opposed to that for a local maximum, in order to switch the signs of the dc correction.)

Briefly speaking, a conventional lock-in stabilizer can be considered as a local-extremum locator, within a shift, on the characteristic curve of a dc-controlled system. The key role is played by the demodulation of the lf lock-in amplifier which can be thought of as a lf (fundamental) frequency amplitude extractor with adjustable proportionality. It should also be particularly noted that it is where the dc correction switches sign that a locking can take place. (A more mathematical .cture of conventional lock-in stabilization is available in Section 2.2.1.2.1 and 2.2.1.2.2.)

### 2.2.1.2 Concepts for the New Designs

It will be shown that offset locking using a lock-in stabilizer can be achieved either by adjusting the modulation amplitude or by modifying the response from the system to be controlled. The amplitude-controlled offset locking scheme has its intrinsic limitations. However, the response-modification scheme is flexible

and versatile.

In order to provide a mathematical language for the discussion, simulations of a lock-in amplifier in the 1f and 2f mode will be proposed first.

#### 2.2.1.2.1 Mathematical Simulation of a Lock-in Amplifier

It is beneficial to take a detailed look at the function of a lock-in amplifier [10]. The key component of a standard lock-in amplifier is its demodulator, which inverts the amplitudes of the input frequency components only at certain multiples of the modulation frequency (1f) into corresponding dc voltages that constitute the demodulator output. The inversion proportionality at each multiple of 1f is dependent on (1) the demodulation mode (1f or 2f), (2) the multiple value considered, and (3) the demodulation phase. For example, the 1f demodulation of a third harmonic, shown in Figure 2.2.1.2.1, generally generates a nonzero dc voltage, which is modulation phase dependent with a period of $2\pi/3$ and 6 sign switching phase per $2\pi$. It can be shown that in the 1f mode the demodulator inverts the amplitudes of all odd multiples of 1f, including the fundamental frequency, into dc voltages, whereas in the 2f mode the same applies to all even multiples of 1f. However, some standard lock-in amplifiers have an input frequency filter, which, when the amplifier is set in the 1f and 2f mode, passes only the 1f and 2f component, respectively, among the multiples of 1f. (A high Q or very narrow bandwidth is unnecessary for the filter because in terms of frequency component the demodulator can be considered as an extremely

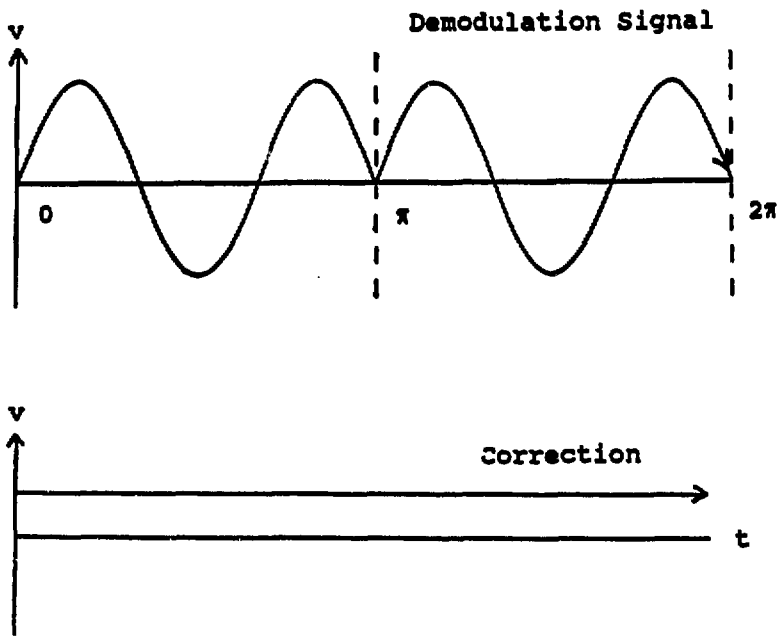


Figure 2.2.1.2.1
Phase-optimized 1f demodulation of a third harmonic.

narrow "gridpass" invertor.) Such a combination of the input filter and the demodulator makes the lock-in amplifier in the 1f mode generates a dc voltage proportional to the amplitudes only of the input fundamental frequency. Similarly, such a lock-in amplifier in the 2f mode generates a dc proportional to the amplitude of the input second harmonic.

Being an amplitude extractor for the 1f or 2f component of the input temporal signal, the functions of a lock-in amplifier can be simulated as being proportional to the following linear integral transformations (within a proportionality, which are linearly dependent on the phase-independent gain of the lock-in amplifier): in 1f mode,

$$L_1^A f(x) =$$

$$F_1'(x,A,\phi) = \int_0^{\omega t=2\pi} [f(x + A\cos(\omega t)) \cos(\omega t + \phi)]\, d(\omega t), \qquad (2.2.1.2.1\text{-}1)$$

in the 2f mode,

$$L_2^A f(x) =$$

$$F_2'(x,A,\phi) = \int_0^{\omega t=2\pi} [f(x + A\cos(\omega t)) \cos(2\omega t + \phi)]\, d(\omega t), \qquad (2.2.1.2.1\text{-}2)$$

where $L_1^A$ and $L_2^A$ are the corresponding linear operators, f(x) stands for the characteristic curve of the system being measured, A is one-half of the modulation depth, $\omega$ is the modulation frequency in

radians/second, the dummy variable t is the time in seconds, and $\phi$ is the relative phase setting. (Here, $F_1'$ and $F_2'$ are *not* derivatives of $F_1$ and $F_2$.) $L_1^A$ and $L_2^A$ are linear basically because integration is a linear operation. In both integral transformations, the modulation is accounted for by incorporating $A\cos(\omega t)$ as an additional part of the independent variable, x, of f(x) in the integrand, whereas the idealized demodulation at 1f and 2f, with no electronic gain involved, is given by the $\cos(\omega t+\phi)$ and $\cos(2\omega t+\phi)$ as multiplicative factors of the integrands.

Such integral expressions for demodulation can be deduced by using the orthogonality among all $\cos(n\omega t)$'s and $\sin(n\omega t)$'s, with n being any nonnegative integer [11]. Both integral transformations can be considered as the "inner product" of the modulated function, $f(x+A\cos(\omega t))$, with the demodulation references, i.e., $\cos(\omega t+\phi)$ and $\cos(2\omega t+\phi)$, respectively. In other words, these two integral transformations can be further thought of as the "projections" of $f(x+A\cos(\omega t))$ onto the "unit vector" functions, $\cos(\omega t+\phi)$ and $\cos(2\omega t+\phi)$. Consequently, Equations (2.2.1.2.1-1) and (2.2.1.2.1-2) are fully justified for simulating the lock-in amplifier as an amplitude extractor for 1f and 2f component of the input temporal signal.

Because the integrations are taken over $\omega t$ for one full cycle ($2\pi$) both transformations correspond to an infinitely long time constant for the lock-in amplifier. As a result, both $F_1'$ and $F_2'$ are functions of x and the two panel-adjustable variables, $\phi$, A. Using the Taylor expansion for $f(x+A\cos(\omega t)$ in polynomials of $A\cos(\omega t)$,

along with the aforementioned orthogonality, the expressions (2.2.1.2.1-1) and (2.2.1.2.1-1) can be rewritten as

$$F_1'(x,A,\phi) = 2\pi \cos\phi \; F_1(x,A) \qquad (2.2.1.2.1\text{-}3)$$

where

$$F_1(x,A) = \frac{1}{2\pi} \int_0^{\omega t = 2\pi} [f(x + A\cos(\omega t)) \cos(\omega t)] \, d(\omega t), \qquad (2.2.1.2.1\text{-}3a)$$

and

$$F_2'(x,A,\phi) = 2\pi \cos\phi \; F_2(x,A) \qquad (2.2.1.2.1\text{-}4)$$

where

$$F_2(x,A) = \frac{1}{2\pi} \int_0^{\omega t = 2\pi} [f(x + A\cos(\omega t)) \cos(2\omega t)] \, d(\omega t), \qquad (2.2.1.2.1\text{-}4a)$$

respectively, which indicate that $\phi$ affects only the signed gain and therefore the sign of the lock-in output functions. If $F_1(x,A)$ and $F_2(x,A)$ are further defined as the lock-in output functions with the phase dependent gain ($\cos\phi$) and the phase independent gain (G) both equal to one, then the lock-in output functions $S_1(x,A,\phi,G)$ and $S_2(x,A,\phi,G)$ in the 1f and 2f mode, respectively, can be generally be written as

$$S_1(x,A,\phi,G) = G \cos\phi \; F_1(x,A) \qquad (2.2.1.2.1\text{-}5)$$

and

$$S_2(x,A,\phi,G) = G \cos\phi \; F_2(x,A). \qquad (2.2.1.2.1\text{-}6)$$

In other words, apart from the signed gain, the geometry of the lock-in outputs, $F_1$ and $F_2$ (abbreviations of $F_1(x,A)$ and $F_2(x,A)$) defined in Equations (2.2.1.2.1-3a) and (2.2.1.2.1-4a), and thus the places where they switch signs are basically determined by both the modulation amplitude A and the characteristic curve f(x). However, it is impossible to separate the individual effects of A and f(x) on the geometry of $F_1$ or $F_2$. This can be shown more explicitly by the Taylor expansions of $F_1$ and $F_2$ in polynomials of A:

$$F_1(x,A) = \sum_{n=1}^{\infty} \left[ C_{2n-1} \cdot \frac{d^{(2n-1)} f(x)}{dx^{(2n-1)}} \cdot A^{2n-1} \right] \qquad (2.2.1.2.1\text{-}7)$$

where

$$C_{2n-1} = \frac{1}{2^n (n-1)!\,n!} \qquad (2.2.1.2.1\text{-}7a)$$

and

$$F_2(x,A) = \sum_{n=1}^{\infty} \left[ C_{2n} \cdot \frac{d^{(2n)} f(x)}{dx^{(2n)}} \cdot A^{2n} \right] \qquad (2.2.1.2.1\text{-}8)$$

where

$$C_{2n} = \frac{1}{2^{2n} (n-1)!\,(n+1)!}. \qquad (2.2.1.2.1\text{-}8a)$$

All terms in these expressions are cross terms between A raised to some power and a derivative of f(x).

2.2.1.2.2 Limitations of the Modulation-Amplitude-Controlled Scheme

Since $F_1(x,A)$ and $F_2(x,A)$ are functions of A, it might seem possible that the offset locking can be achieved simply by adjusting the modulation amplitude with conventional lf lock-in stabilization. However, this is not always feasible, as will be explained in the following.

Any function, g(x), can be decomposed into an even, $f_e(x-a)$, and odd part, $f_o(x-a)$, with respect to any position at x=a, viz.,

$$g(x)= f(x-a)= \frac{f(x-a) + f(-(x-a))}{2} + \frac{f(x-a) - f(-(x-a))}{2}$$

$$= f_e(x-a) + f_o(x-a). \qquad (2.2.1.2.2\text{-}1)$$

With the geometry unaffected, Expression (2.2.1.2.1-3a) for $F_1$ can then be rewritten as

$$F_1(x-s,A)= \sum_{n=1}^{\infty}\left[ C_{2n-1}\cdot\frac{d^{(2n-1)}[f_e(x-s)+f_o(x-s)]}{dx^{(2n-1)}}\cdot A^{2n-1} \right]$$

(2.2.1.2.2-2)

with the origin shifted to one of the local extrema of f(x) at x=s. It is noted that it is the even part, $f_e(x-s)$, of f(x-s) that contributes the oddness of $F_1$ about x=s, whereas the odd part, $f_o(x-s)$, that contributes the evenness of $F_1$. The reason is that an odd order, (2n-1), differentiation switches the parity about x=s.

The limitations of the amplitude-controlled offset locking at 1f will be shown for the cases with locally symmetric and asymmetric extrema, respectively. Here, the "local" is defined to be the modulated region [s-A,s+A] at the extremum (x=s). The local functions and their symmetry will then be dependent on the modulation amplitude A. In addition, within the local region, the only extremum will be located at x=s.

For the case with locally symmetric extremum, the corresponding local $f_o(x-s)$ vanishes completely, but at least one local odd $\frac{d^{(2n-1)}f_e(x-s)}{dx^{(2n-1)}}$ function exists. As a result, as long as the value of A constrains all the local $\frac{d^{(2n-1)}f_o(x-s)}{dx^{(2n-1)}}$ derivatives to remain zero, x=s is always a point where $F_1$ switches sign; no continuous offset locking starting from x=s is possible. As a trivial example, in the case of a symmetric characteristic curve such as a Gaussian function, adjustment of the modulation amplitude completely fails to shift the locked point from its maximum.

However, for the case with a locally asymmetric extremum, at least a local $\frac{d^{(2n-1)}f_e(x-s)}{dx^{(2n-1)}}$ becomes nonzero. According to Equation (2.2.1.2.2-2), the necessary condition for x=s to be a sign-switching point, i.e. $F_1=0$ at x=s, is now violated. If there is a transition from being locally symmetric to asymmetric with continuously increasing value of A, the disappearance of sign-switching at x=s implies only that such a sign-switching point has shifted continuously

to its neighborhood already. In other words, for many cases, there will be a threshold value for A to be effective in such offset locking. Being system-dependent, such threshold of A could be so large that it might become an intolerable perturbation to the system. In addition, the shift direction of the locked point will be controlled basically by the geometry of f(x) instead of A.

Such system-dependent limitations definitely need to be avoided in a versatile offset locking scheme. Consequently, in terms of the expressions for $F_1(x,A)$ and $F_2(x,A)$, a modification of f(x) is the only remaining choice for offset locking with lock-in stabilization. (A similar discussion, using Equations (2.2.1.2.1-6) and (2.2.1.2.2-1), can be made for a 2f lock-in stabilization and similar system-dependent limitations for amplitude-controlled offset locking are to be obtained.)

#### 2.2.1.2.3 Geometric Arguments for the Response-Modification Schemes

##### 2.2.1.2.3 (A) 1f Modification — Slanting the Baseline of the Characteristic Curve

Previously, f(x) was referred to as the characteristic curve of the system. In the following discussion, the true characteristic curve will be denoted by T(x), as opposed to the effective (modified) characteristic curve f(x) "seen" by the lock-in amplifier of stabilization system.

For most practical applications, the modulation amplitude A is made small enough to reduce the unwanted perturbation due to the modulation itself or to reflect the true characteristic response T(x)

of the system as much as possible. Usually A is thus smaller than the typical widths of the features of T(x) and thus of f(x), i.e. $A \ll 1$. In addition, the coefficients, $C_{2n-1}$ and $C_{2n}$, decay fast for higher order terms in the expansions (Equations (2.2.1.2.1-7) and 2.2.1.2.1-8)) for both $F_1$ and $F_2$. This is indicated by the numerical values of the first few coefficients listed in Table 2.2.1.2.3. Therefore, for most applications, the leading term of the expansions for $F_1$ and $F_2$ should be a good first order approximation, viz.,

$$F_1(x,A) \propto \frac{df(x)}{dx} \cdot A \qquad (2.2.1.2.3\text{-}1)$$

$$F_2(x,A) \propto \frac{d^{(2)}f(x)}{dx^{(2)}} \cdot A^2. \qquad (2.2.1.2.3\text{-}2)$$

Without getting into an involved mathematical analysis, the major physical insights for the response-modification scheme can be extracted from the behavior of the derivatives of f(x) using this approximation.

Because conventional 1f lock-in stabilization fails to offset-lock the system continuously from an extremum about which the characteristic curve is locally symmetric, it is interesting to take a look at the behavior of a Gaussian function located on straight baselines of different slopes, as shown in Figure 2.2.1.2.3-1 (a)-(d), along with the corresponding first derivative curves in Figure 2.2.1.2.3-2 (a')-(d'). In (a), an Gaussian function G(x−s) centered at x=s is depicted. In (b), the symmetric G(x−s) is distorted with its maximum shifted toward a newly generated minimum by a slightly

Table 2.2.1.2.3

The numerical values of the first few coefficients, $C_{2n-1}$ and $C_{2n}$, in the expansions (Equations (2.2.1.2.1-7) and 2.2.1.2.1-8) for both $F_1$ and $F_2$.

| n | $C_{2n-1}$ | $C_{2n}$ |
|---|---|---|
| 1 | 0.500000 | 0.125000 |
| 2 | 0.125000 | 0.010417 |
| 3 | 0.007813 | 0.000326 |
| 4 | 0.000011 | 0.000005 |

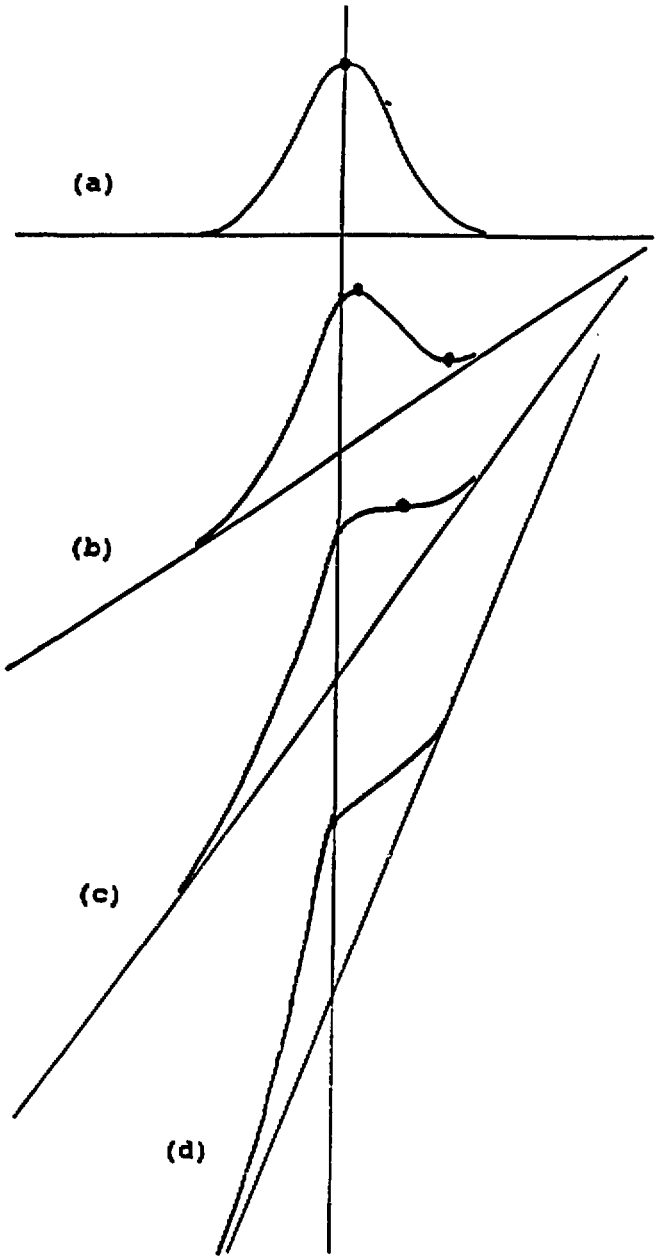


Figure 2.2.1.2.3-1 (a)-(d)
Behaviors of a Gaussian function located on straight baselines of different slopes.

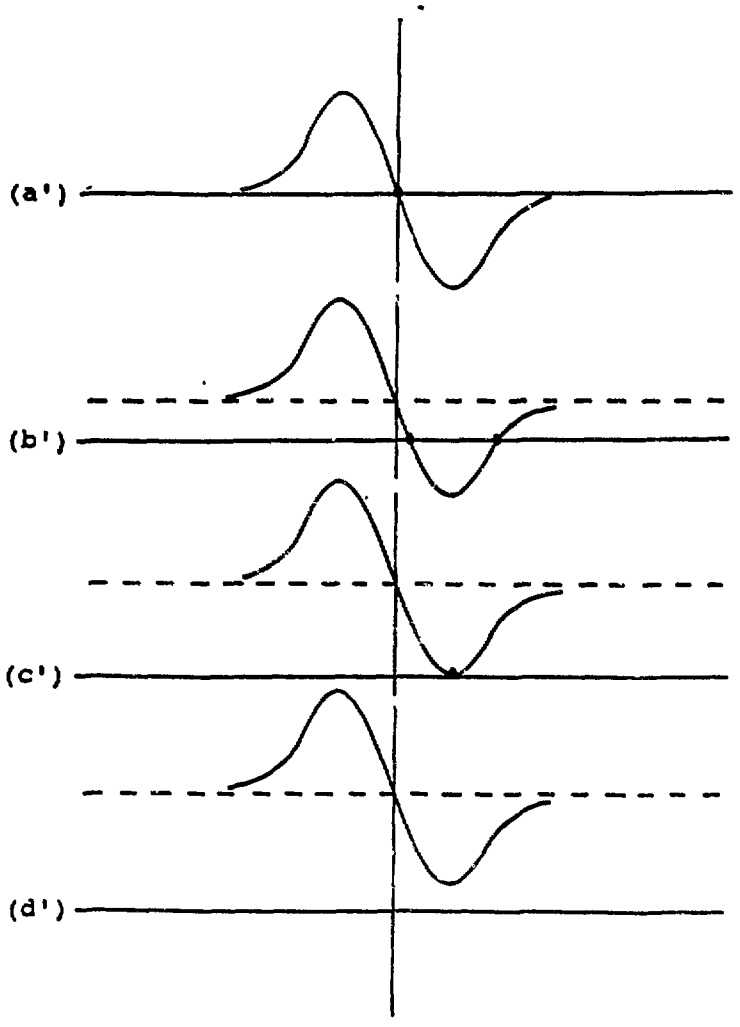


Figure 2.2.1.2.3-2 (a')-(d')
The corresponding first derivative curves of Figure 2.2.1.2.3-1 (a)-(d).

slanted baseline m(x−s) with slope m. Such a phenomenon can be confirmed by Figure 2.2.1.2.3-2 (b'), in which the two intersections between the derivative curve and the x axis correspond to the two extrema in (b). It is noted that the height of the horizontal baseline in (b') and thus the positions of the extrema can be controlled by the slope m of the slanted baseline in (b). However, when the slope is increased, as shown in Figure 2.2.1.2.3-1 (a)-(d), the maximum and minimum will first approach each other, then coalesce into an inflection point, and finally disappear. A similar phenomenon can be imagined if the slope of the baseline is increased negatively. As a result, as long as the slope is under our control, the existence and direction of the offset locking with conventional lock-in stabilization should be no longer limited by the requirement for local asymmetry about an extremum of the true characteristic curve T(x).

With the true characteristic curve T(x) left unmodified, the next question is how to create such an effective baseline with adjustable slope to "cheat" the conventional lock-in stabilizer. The "cheating" characteristic curve f(x) can be expressed as

$$f(x) = T(x) + m(x - s) \qquad (2.2.1.2.3\text{-}3)$$

where x=s is the position of one of the extrema of T(x), from which offset locking is to be performed. It will be shown that the s is not critical in the expression of the baseline later. The corresponding temporal response at a specific position $x=x_o$ due to a modulating sine wave with amplitude A can then be obtained by replacing x with $x_o+A\cos(\omega t)$, i.e.

$$f(x_o + A\cos(\omega t)) = T(x_o + A\cos(\omega t)) + m(x_o + A\cos(\omega t) - s). \tag{2.2.1.2.3-4}$$

This equation suggests that, by adding a slanted baseline, the only modifications are the two Fourier components of the original temporal response, viz., the "dc" and fundamental frequency component. Being never detected by a lock-in amplifier, the change in "dc", $m(x_o-s)$, is not of concern. Interestingly, it is noted that the change in the amplitude of the fundamental frequency component, which is to be detected, is a function of the slope m of the baseline, as indicated by the $mA\cos(\omega t)$ term. Conversely, also in a more operational sense, the slope m ($=A'/A$) can be controlled practically by superimposing an in-phase and amplitude preselected sine wave, $A'\cos(\omega t)$, at the modulation frequency onto the true temporal response $T(x_o+A\cos(\omega t))$ from the system while $x_o$ is changing. (Here, $180^o$ out of phase is also considered as "in phase" because it corresponds to a negative amplitude.) If the intended offset locked point is located at $x=s'$, this slope-controlling sine wave must exactly annihilate the fundamental frequency component of the true system temporal response $T(x+A\cos(\omega t))$ at $x=s'$; the value of $F_1(x,A)$ corresponding to the effective (cheating) characteristic curve $f(x)=T(x)+m(x-s)$ at $x=s'$ must be zero, so that no corresponding dc correction is generated. However, the lack of a dc correction at a nonextremum point still does not ensure that offset locking can occur. The dynamical requirement for locking at $x=s'$ is that $x=s'$ must be a sign switching point for the $F_1(x,A)$ in order to provide the returning dc corrections of

opposite signs in the opposite neighborhoods of x=s'. As a result, such schemes fail to offset lock the system at the places where $F_1(x,A)$ are the extrema. According to Expressions (2.2.1.2.3-1), this requirement suggests that the effective $\frac{df(x)}{dx}$ should switch sign at the limiting position of the locked point as A asymptotically approaching to zero. In other words, the limiting locked point can never be an inflection point of f(x). Here, the inflection points are also those of T(x) because the effective slanted straight baseline has no effect on their position(s).

Since (1) the lock-in amplifier is in the 1f mode, and (2) the preset input reference for generating a dc correction is served by an added cheating sine wave, such a scheme will be named "1f ac modification". As opposed to this scheme, "1f dc modification" is the scheme in which a direct dc reference corresponding to the sine wave reference is employed to bias the lock-in amplifier output in the stabilization. Basically, both 1f ac and dc modification result in the same offset stabilization, and will be called "1f modification" in the following.

2.2.1.2.3 (B) Decoupling the Effect of Gain on the Locking Position

Special care must be taken for the 1f dc modification. With the f(x) substituted by the expression (Equation (2.2.1.2.3-3)) of the effective characteristic curve (one with slanted straight baseline), the expansion for $F_1(x,A)$ (Equation (2.2.1.2.1-7)) becomes

$$F_1(x,A) = F_{1T}(x,A) + mA/2 \qquad (2.2.1.2.3\text{-}4)$$

where $F_{1T}(x,A)$ has the same expression as the $F_1(x,A)$ in Equation (2.2.1.2.1-7) with f(x) replaced by T(x), and therefore is the original $F_1(x,A)$ corresponding to the true characteristic curve T(x). With Equations (2.2.1.2.3-4) and (2.2.1.2.1-5) combined, the corresponding output dc correction curve ($S_1(x,A,G,\phi)$) of the lock-in stabilizer can be expressed as

$$S_1(x,A,G,\phi) = G \cos\phi \, [F_{1T}(x,A) + mA/2]. \qquad (2.2.1.2.3\text{-}5)$$

Here, the mA/2 term can be thought of as either a preset reference dc or the dc resulting from a preset reference sine wave. Although mA/2 is dependent on A, since any reference ac or dc signal can be actually adjusted, mA/2 can be denoted by a single variable $R_p$ to emphasize its role as an independent variable in the operational sense. Equation (2.2.1.2.3-5) can thus be rewritten as

$$S_1(x,A,G,\phi) = G \cos\phi \, [F_{1T}(x,A) + R_p]. \qquad (2.2.1.2.3\text{-}6)$$

For a locking position to exist, there are two requirements for $S_1(x,A,G,\phi)$ along the x axis direction: (1) $S_1$ must switch sign at this position, and (2) the slope of $S_1$ at this position must have the right sign for the correction to converge into rather than diverge from this position. According to Equation (2.2.1.2.3-6), such sign switching is determined only by the bracketed part, and the sign of the slope of $S_1$ is determined by that of the product of $\cos\phi$ and the bracketed part. (G's of most lock-in systems are positive.) The "candidate" locking positions thus include the correction convergent

as well as correction divergent points because their convergent-divergent roles can be switched simply by switching the sign of the lock-in panel-controlled parameter $\cos\phi$. (It is noted that the panel phase reading ($\phi'$) is generally unequal to the $\phi$ value in this discussion. However, there exists the one-to-one relationship between them.)

In terms of actual operation, once the modulation amplitude A (and thus $F_{1T}(x,A)$ are determined), the preset reference signal $R_p$ (ac or dc) alone controls *all* the candidate offset locking positions. On the other hand, as indicated by the $G\cos\phi F_{1T}(x,A)$ term, with A fixed first, the net gain $G\cos\phi$ independently controls the slope of $S_1$, which reflects the correction efficiencies about the candidate locking points. In other words, once A and the sign of $\cos\phi$ are fixed, the correction convergent position(s), if exists, and the stabilization efficiency around it are respectively controlled by the preset reference signal $R_p$ and the net gain ($G\cos\phi$).

Since, as indicated by Equations (2.2.1.2.1-7) and (2.2.1.2.1-8), A is always inevitably involved with every aspect of the output performance in any lock-in system, no attempt will be made to decouple the effect of A from those of G, $\phi$, and $R_p$ on the locking position and stabilization efficiency. Therefore, for both ac and dc modification scheme, Equation (2.2.1.2.3-6) represents the ideal that requires the reference signal be synchronously tuned with the net gain.

The feature that different independent parameters are used to control different performance variables automatically accompanies the lf *ac* modification because it must be performed before the lock-in

stabilization stage. In order to preserve this feature for the 1f *dc* modification, that must be performed after the lock-in demodulation stage, the reference dc ($G\cos\phi R_p$) has to be synchronously tuned with both $\cos\phi$ and G. Here, "both" must be emphasized; otherwise, the effects of the net gain ($G\cos\phi$) and the reference dc on the locking position and the stabilization efficiency will be mixed up. This can be shown by the following example, a slightly modified version of Equation (2.2.1.2.3-6),

$$S_1(x,A,G,\phi) = G\cos\phi\, F_{1T}(x,A) + G\,R_p$$
$$= G\,[\cos\phi\, F_{1T}(x,A) + R_p] \qquad (2.2.1.2.3\text{-}7)$$

in which the reference dc ($GR_p$) is synchronously tuned only with G, but not $\cos\phi$. Apparently, the locking position is determined not only by the preset reference dc ($R_p$) but also by $\phi$ in this case. This requirement can also be illustrated by the examples in Figure 2.2.1.2.3-3. Similarly, if there are more than one gain-tunable stages, denoted by their gains $G_i$ (i= 1, 2, etc.), then the reference dc should be synchronously tunable with each of the $G_i$.

2.2.1.2.3 (C) 2f Demodulation — A Complement to 1f Modification

The corresponding 2f ac and dc modification can be imagined analogously following the discussion for 1f modification schemes, and will not be discussed in detail. Two major and conceivable differences for 2f modifications are: (1) if ac modification is used, an in phase and amplitude adjustable second harmonic, $A''\cos(2\omega t)$, of the modulation frequency can serve as an ac input reference, (2) it is

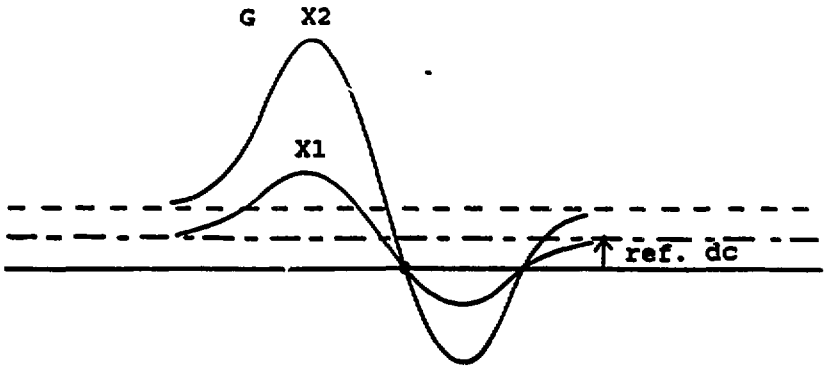


(1.a) $G\cos\phi[F_1(x,A) + R_p]$

Same locking position.
Different stabilization efficiency.

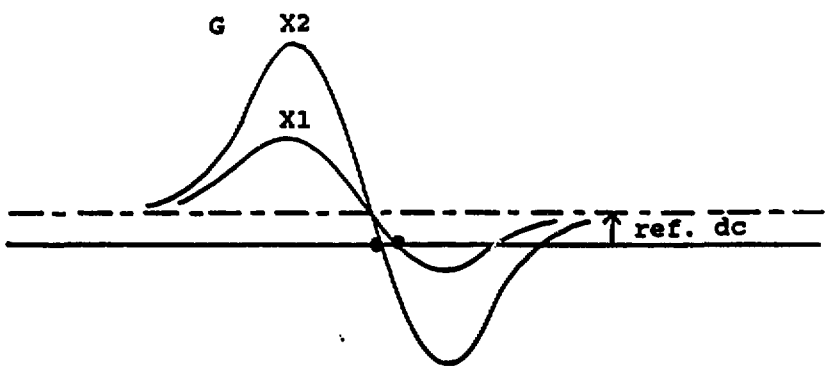


(1.b) $G\cos\phi F_1(x,A) + R_p$

Different locking position.
Different stabilization efficiency.

Figure 2.2.1.2.3-3
Differences between synchronous and nonsynchronous tuning of the post-demodulation reference dc ($R_p$) with the pre-demodulation net gain ($G\cos\phi$).

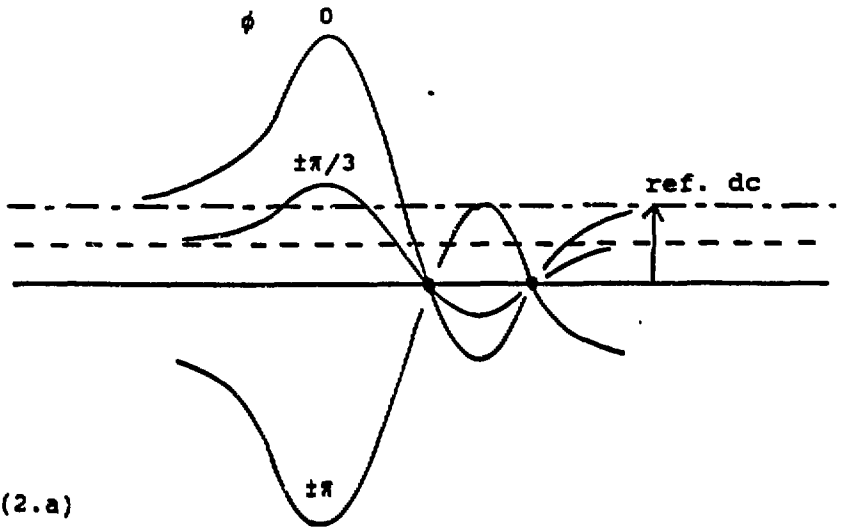


(2.a)

$G\cos\phi[F_1(x,A) + R_p]$

Same locking position, when cosφ keeps the same sign.
Different stabilization efficiency.

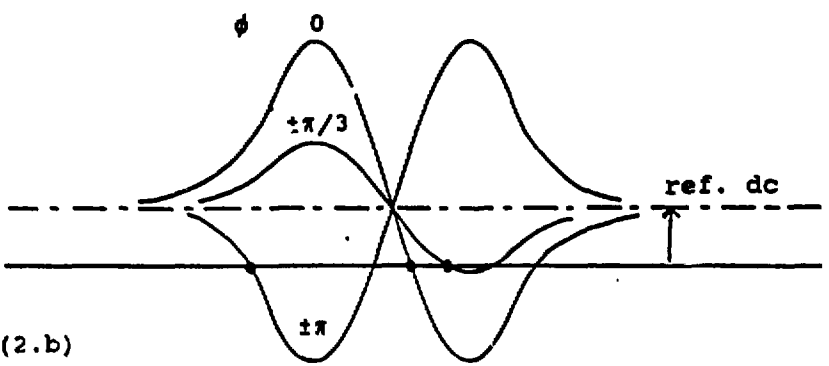


(2.b)

$G\cos\phi F_1(x,A) + R_p$

Different locking position, if existing, for different cosφ.
Different stabilization efficiency.

Figure 2.2.1.2.3-3 (Continued)

where $F_2(x,A)$ crosses the x axis that can be locked (It never offset locks the system at the extrema of $F_2(x,A)$).

Although lf modification schemes are, in principle, capable of offset locking the system almost everywhere on a typical physical characteristic curve, there do exist places where such schemes fail. Apart from the theoretical example of the inflection points of f(x) or T(x) in the small amplitude limit, a practical problem is illustrated in Figure 2.2.1.2.3-4, in which the $F_1(x,A)$ corresponding to the effective characteristic curve f(x) has two nearby intersections $x_1$ and $x_2$, with the x axis, where the offset locking is allowed. Since the proper lock-in phase settings for offset locking the system at $x_1$ and $x_2$ are $180^o$ out of phase, the offset locking can occur only at one intersection at a time. The directions of the corresponding dc corrections in regions $R_1$, $R_2$ and $R_3$, separated by $x_1$ and $x_2$ are represented by the arrows shown below the x axis. An effective offset locking is indicated by a head-on contact of two such adjacent arrows (solid). For example, in the case of locking the system at $x=x_1$, it is noted that the effective stabilization can take place only in regions $R_1$ and $R_2$; once the system drifts to region $R_3$, the operating point will be pushed to the right and eventually out of the picture to seek for another lockable position, which may not exist. Generally speaking, the stabilization range terminates at the first point where $F_1(x,A)$ "crosses" (not just intersects) the x axis on either side of the intended locked point, which is also such a crossing point. The actual problem is that if two such crossing points are too close together, as in the current example, then the effective dynamic range

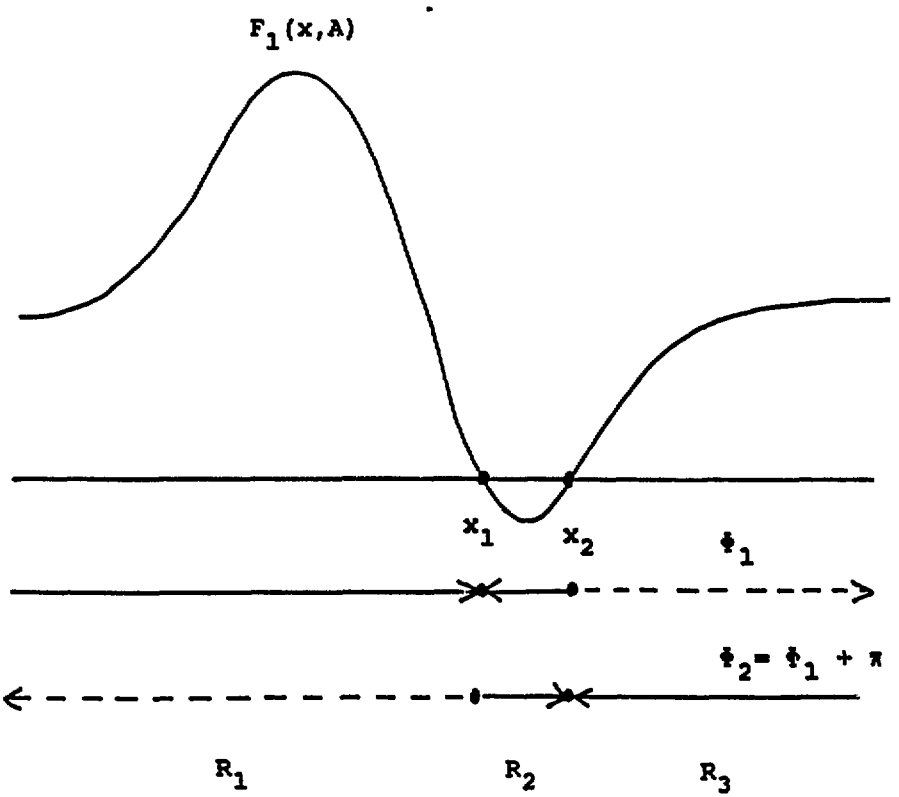


Figure 2.2.1.2.3-4
A practical problem, in which the $F_1(x,A)$ corresponding to the effective characteristic curve $f(x)$ has two nearby intersections $x_1$ and $x_2$ with the x axis.

for either crossing point to become the intended locked point will be seriously limited.

This problem can be solved by complementing the 1f modification scheme with the 2f lock-in stabilization. The reason is that where $F_1(x,A)$ is an extremum or equivalently where 1f modification fails is usually near where $F_2(x,A)$ crosses the x axis (not just equal to zero), as indicated in Figure 2.2.1.2.3-5 in which many $F_1(x,A)$'s and $F_2(x,A)$'s corresponding to different modulation amplitude A for a Gaussian characteristic curve are depicted together. This is apparent by considering the small amplitude limit, in which any sign switching point of $F_2(x,A)$ is exactly an extremum of $F_1(x,A)$. Since most of the offset locking can be achieved by 1f modification, in order to complement it, we employ only 2f lock-in stabilization, not 2f modification schemes. Of course, using both 1f and 2f modification schemes is an "overkill".

### 2.2.2 Architecture of the Offset Lock-in Stabilization System

Based upon the above geometric arguments, in addition to the conventional 1f lock-in stabilization capability, a versatile offset lock-in stabilization scheme should have the following two selectable basic functions: (1) the 1f ac or dc modification and (2) the 2f lock-in demodulation. In other words, there are two possible combinations, i.e. either with the 1f ac or 1f dc modification incorporated. They will be named the "ac offset scheme" and "dc offset scheme", respectively.

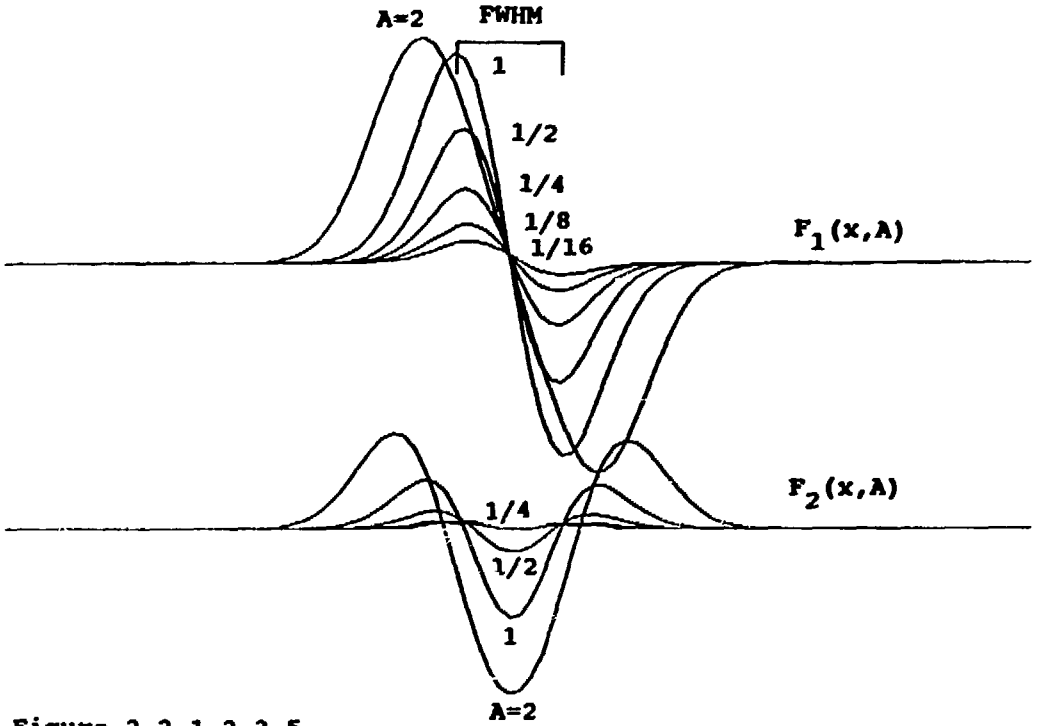


Figure 2.2.1.2.3-5
$F_1(x,A)$'s and $F_2(x,A)$'s corresponding to different modulation amplitude A for a Gaussian characteristic curve. The modulation amplitudes indicated are in unit of the FWHM of the Gaussian function. The computer graphics are based upon Equations (2.2.1.2.1-3a) and (2.2.1.2.1-4a). (A: modulation amplitude. FWHM: full-width-at-half-maximum)

2.2.2.1 ac Offset Scheme

The ac offset scheme, as shown in Figure 2.2.2.1, consists of two parts: (1) the system response modification circuit and (2) the lock-in stabilizer, which is capable of both 1f and 2f mode (as opposed to the conventional lock-in stabilizer which operates only in the 1f mode). Since the stabilizer involved is still conventional in terms of the arrangement of its principal components (enclosed in the dashed line in Figure 2.2.2.1), only the system response modification circuit will be briefly discussed.

The modification circuit has two signal channels summed up by a voltage adder (VA1 in Figure 2.2.2.1), which leads to the input of the lock-in stabilizer, i.e., the input of the built-in lock-in amplifier. These two channels are: (A) the detector channel and (B) the reference channel.

The purpose of the detector channel is to extract only the 1f component in the system temporal response. This elimination of all harmonics of 1f is unnecessary for the lock-in stabilization stage; however, this is necessary for signal processing which relies on visually recognizing 1f. This channel consists of a voltage gain tuner, followed by a frequency filter centered at 1f. The gain tuner should be set at a value which is small enough to not saturate the following electronic stages but large enough for monitoring (at $M_A$) and processing purpose. This is the reason why the gain tuner had better be capable of both amplification and attenuation (unless the detector signal level is known beforehand, as in the case of offset locking the $CO_2$ laser). As to the frequency filter, its type (such as

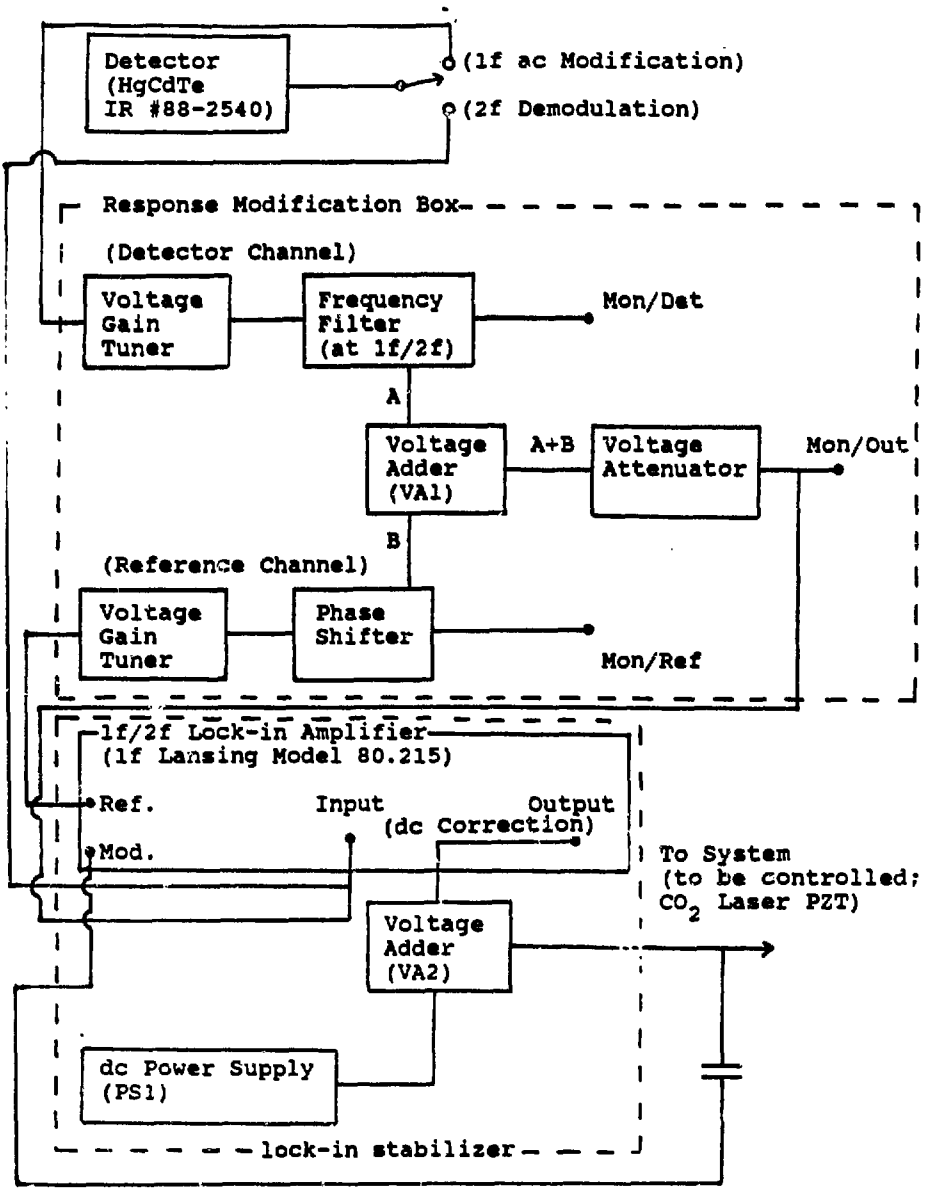


Figure 2.2.2.1
Block diagram for the 1f ac modification plus 2f demodulation scheme.

lowpass or bandpass, Butterworth or Chebyshev [12], etc.) and specifications (such as bandwidth and pole-number [12]) are not critical in the design. This is because the major filtering of the offset stabilization scheme is conducted by the lock-in stabilizer instead, as indicated by the following two facts: (1) due to the modulation on a generally nonlinear system characteristic curve at a constant frequency 1f, the system temporal response is basically a linear combination of the 1f component plus its harmonics with the amplitude distribution evolving with time while the modulation center varies, and should, in principle, be free of other frequency components, (2) the lock-in amplifier (in the 1f mode) in the lock-in stabilizer is theoretically a single frequency component (1f) invertor. Therefore, for monitoring and processing the 1f component, the only requirements for the filter are: (1) its bandwidth covers only the 1f component among 1f and the harmonics, (2) the Bode plot [12], gain vs. frequency, and consequently the corresponding phase vs. frequency plot of the filter should be flat around the 1f frequency, so that no amplitude envelope "ringing" and phase fluctuation effect might occur due to the practical slight change in the 1f component. Since the lock-in amplifier is a phase sensitive detector, such phase fluctuations could cause serious problem in locking stability. The second requirement implies that if a bandpass filter centered at 1f is used, a high Q value should be avoided; if a lowpass filter is used, the −3dB point should not be too close to the 1f frequency.

On the other hand, the reference channel is to generate a reference sine wave for the 1f component extracted by the detector

channel to annihilate. If the input of this channel is directed from a pure sine wave generator, such as the built-in modulation oscillator of the lock-in stabilizer, this channel should consist of a voltage gain tuner and an in-series phase shifter. The phase shifter should have a tuning range a little over 360°, so that a local continuous tuning is possible about any phase reading. If the input of this channel is provided by a periodic non-sine wave (e.g. square wave) generator, then a frequency filter centered at 1f will be necessary to extract a pure sine wave form at 1f. For similar reasons, the requirements for this filter should be the same as those for the one in the detector channel.

Both channels are directed to the inputs of a voltage adder (VA1 in Figure 2.2.2.1), which is followed by a voltage attenuator. Since the reference sine wave is equivalent to the negative wave form of the 1f component of the system response at the intended offset locked point, the adder actually subtracts this 1f component from the post-filter only remaining frequency component, the 1f component, of the detector temporal response. Here an voltage attenuator rather than a more versatile gain tuner is used. The reason is that there usually exists an input voltage amplifier (not attenuator) in most lock-in amplifiers. This voltage attenuator along with the built-in input amplifier of the lock-in stabilizer can control the signal level to be demodulated, and therefore can affect the dc correction efficiency of the stabilizer. Since the correction efficiency should be high enough to correct any system fluctuation in time and low enough to avoid "overshooting" in correction, this post-adder voltage

gain tuning is critical in terms of locking stability. Because the signal level could have been raised up by the two gain tuners of the detector and reference channel, extra attenuation factor might be needed in the design. Ideally, the minimum attenuation factor should be at least enough to compensate the maximum amplification factors of the two gain tuners.

Of course, all the modification circuit should be bypassed when the 2f demodulation is in use.

### 2.2.2.2 dc Offset Scheme

The dc offset scheme, shown in Figure 2.2.2.2, is also based on a standard lock-in stabilizer. For 1f dc modification, a voltage adder (VA2), which sums up the lock-in correction and the reference dc, is incorporated between the output of the lock-in amplifier and the voltage adder (VA1) of the lock-in stabilizer. The preset reference dc, which corresponds to $R_p$ in Equation (2.2.1.2.3-6) within a proportionality constant, is provided by a tunable voltage power supply (PS2). In order to be synchronously tuned by the net gain of the lock-in stabilizer, the preset reference dc is then directed to a lock-in-gain-controlled (G-controlled) and an in-series lock-in-phase-controlled ($\phi$-controlled) voltage gain tuner before being added to the lock-in correction signal.

The gain (G) tuning on a typical lock-in amplifier is generally unipolar. This makes the G-controlled gain tuner unipolar. On the other hand, according to Equation (2.2.1.2.1-5), the $\phi$-controlled gain tuner should be linearly controlled by the value either of $\cos\phi$ or of

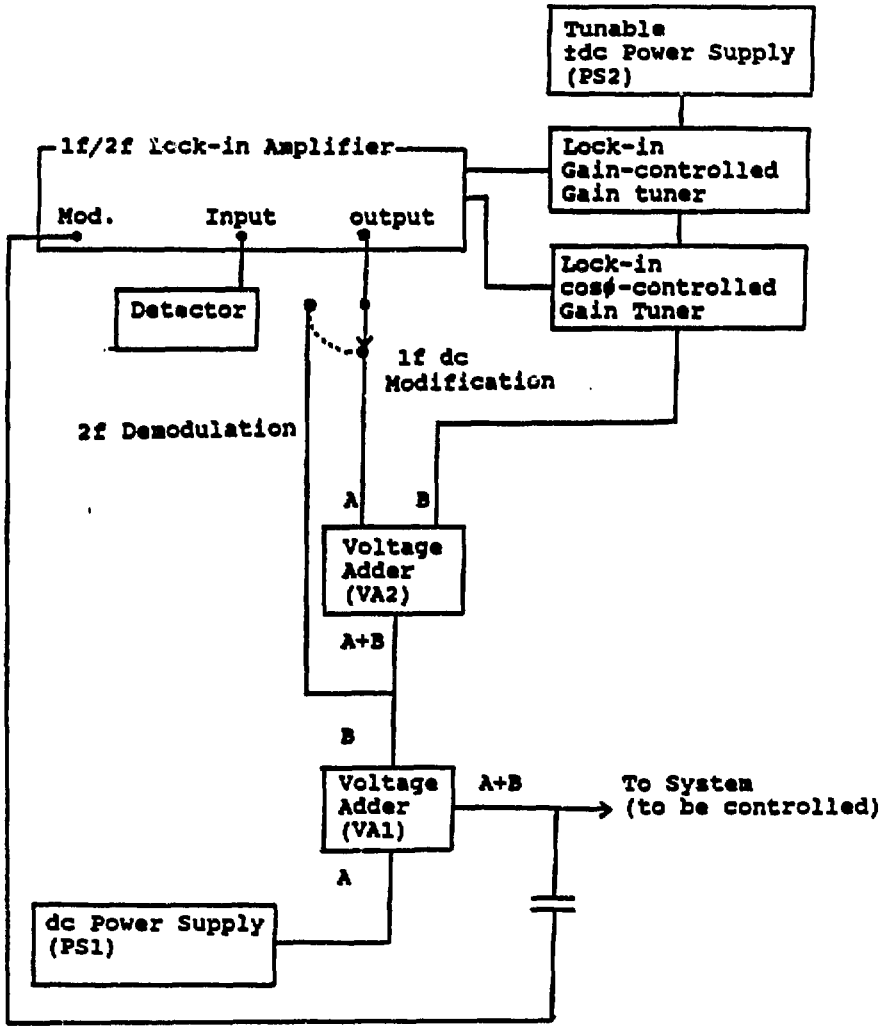


Figure 2.2.2.2
Block diagram for the 1f *dc* modification plus 2f demodulation scheme.

$|\cos\phi|$. For the case of $\cos\phi$, since the polarity of the tuned reference dc (not the preset one) can be determined simply by the lock-in phase ($\phi$) adjustment, the tunable PS2 power supply need be only unipolar. In other words, PS2 must be a bipolar one for the case of $|\cos\phi|$. However, since $\phi$ is usually optimized to be $\pm\pi$ (not the actual $\phi$ reading on the lock-in panel) first in terms of actual operation, it is always more convenient to render the sign switching capability to a bipolar PS2.

Similarly to the ac offset scheme, when 2f demodulation is in use, the above modification circuit for the lock-in correction must be detoured.

### 2.2.3 Application to the cw $CO_2$ Laser Stabilization

#### 2.2.3.1 Actual Stabilization System

Since (1) no attempt was made to modify a commercial 1f lock-in stabilizer, as required by the G-controlled and $\phi$-controlled gain tuner in the dc offset scheme and (2) it is always more convenient and efficient to monitor ac signal on an oscilloscope than dc signal on a voltmeter, we adopted the ac offset scheme to offset lock the $CO_2$ laser. It seems that few people are interested in locking a dc-controlled systems around their inflection points. Currently no commercial lock-in stabilizer with both 1f and 2f mode exists. The 2f demodulation capability was therefore not included in the prototype stabilization system (Figure 2.2.2.1).

The grating zero order beam of the $CO_2$ laser, used for laser line identification, is now directed to a liquid nitrogen cooled HgCdTe

detector (Infrared #88-2549). (Caution: Never ever use the detector to detect the laser first order output, which is usually stronger than 100W and more than enough to burn the detector.) The detector built-in preamp signal is then processed with the response modification circuit. The modification circuit, including the detector channel, the reference channel, the voltage adder (VA1), and the post-adder attenuator are all built in one box, the actual circuit schematic of which is shown in Figures 2.2.3.1-1 (a)-(e). The "cheated" lock-in stabilizer is Lansing Model 80.215 with the modulation frequency factory-preset at 518 Hz. The circuit for connecting the lock-in stabilizer to the PZT of the $CO_2$ laser is put in a separate box with proper protection circuit (Figure 2.2.3.1-2) suggested by the Lansing instruction manual.

Since the modification circuit (Figure 2.2.3.1-1) was homebuilt, some comments for the circuit design will be made briefly. But no explanation of the detailed electronic mechanism will be given, because basically only standard operational amplifier (op amp) circuits are employed [12,13]. The function of each electronic stage will simply be noted below the corresponding part of the circuit diagram in Figure 2.2.3.1-1 (a)-(c).

The input signal of the reference channel is derived from the Monitor Sync connector (on FP/L), which is a 20 v pk-to-pk 518 Hz sine wave source. (FP/L stands for "front panel of Lansing".) Such a large amplitude makes that only attenuation is required in the reference channel. Because the dc level associated with this sine wave is negligibly small, this input is dc coupled. The first stage

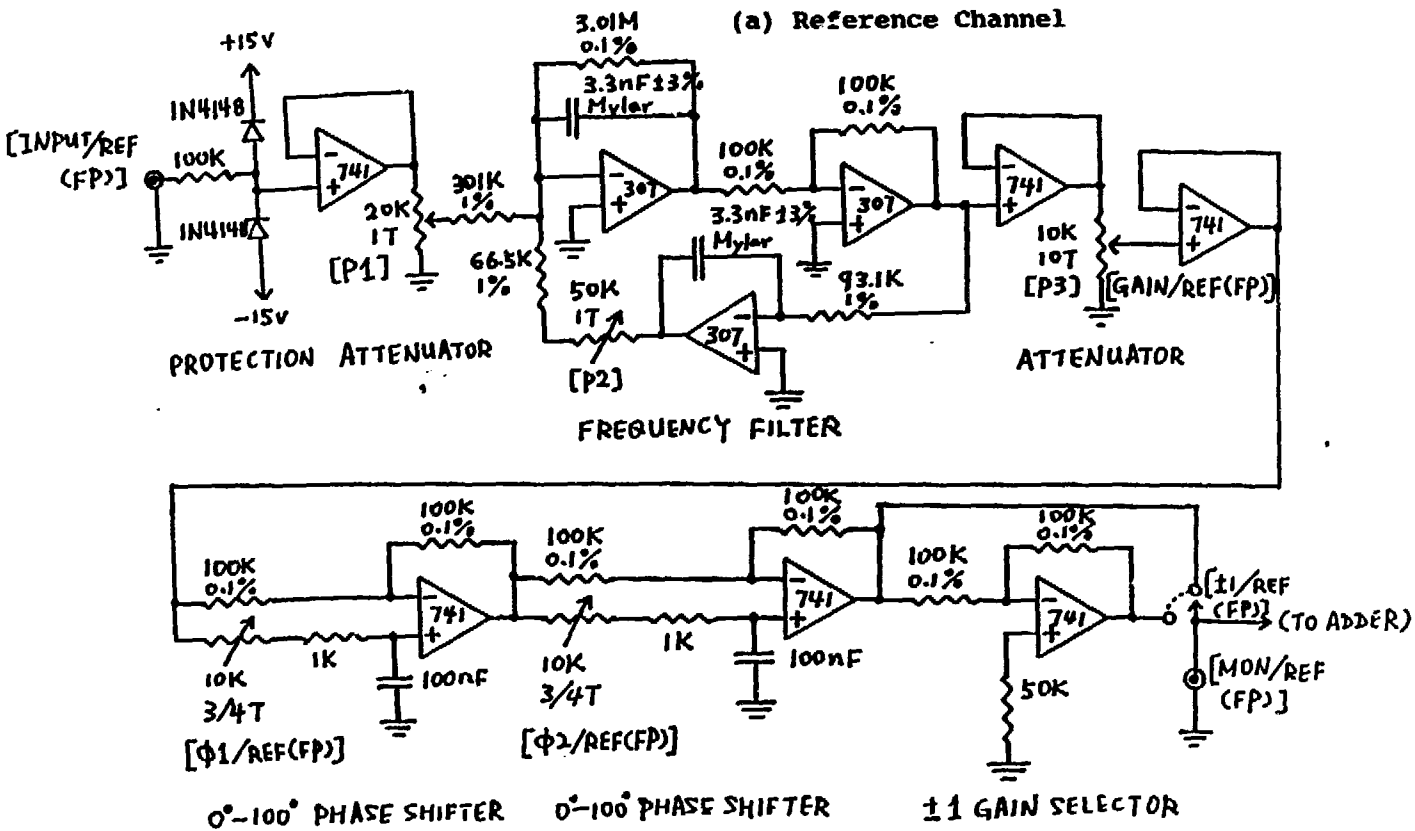


Figure 2.2.3.1-1
Circuit schematic of the response modification box: (a) reference channel, (b) detector channel, (c) reference and detector channel adder, (d) power system, (e) front panel layout.

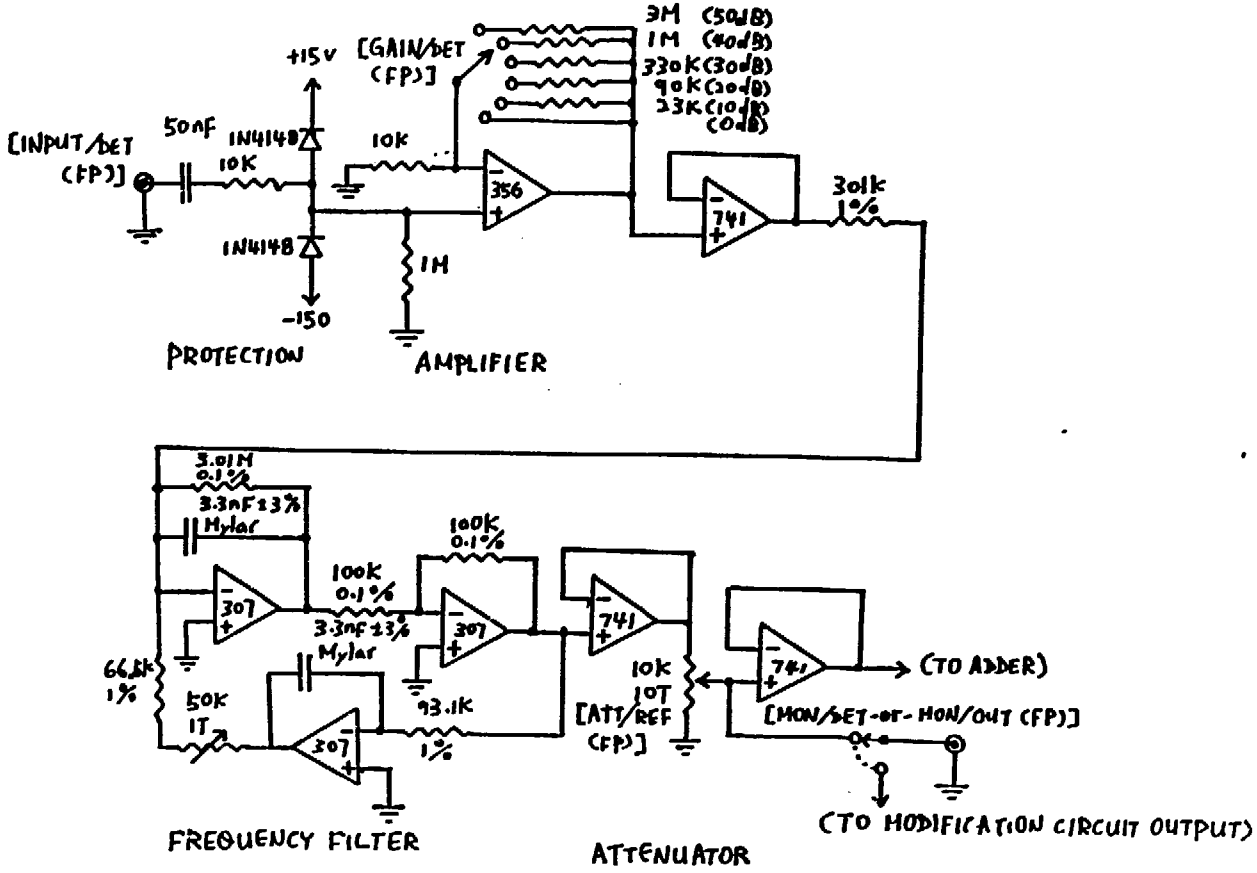


Figure 2.2.3.1-1 (Continued) (b) Detector Channel

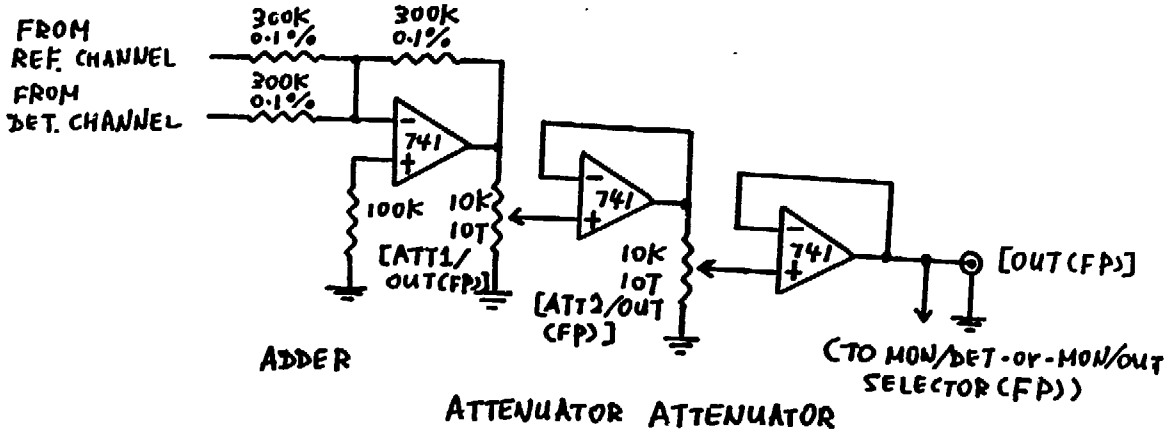


Figure 2.2.3.1-1 (Continued) (c) Reference and Detector Channel Adder

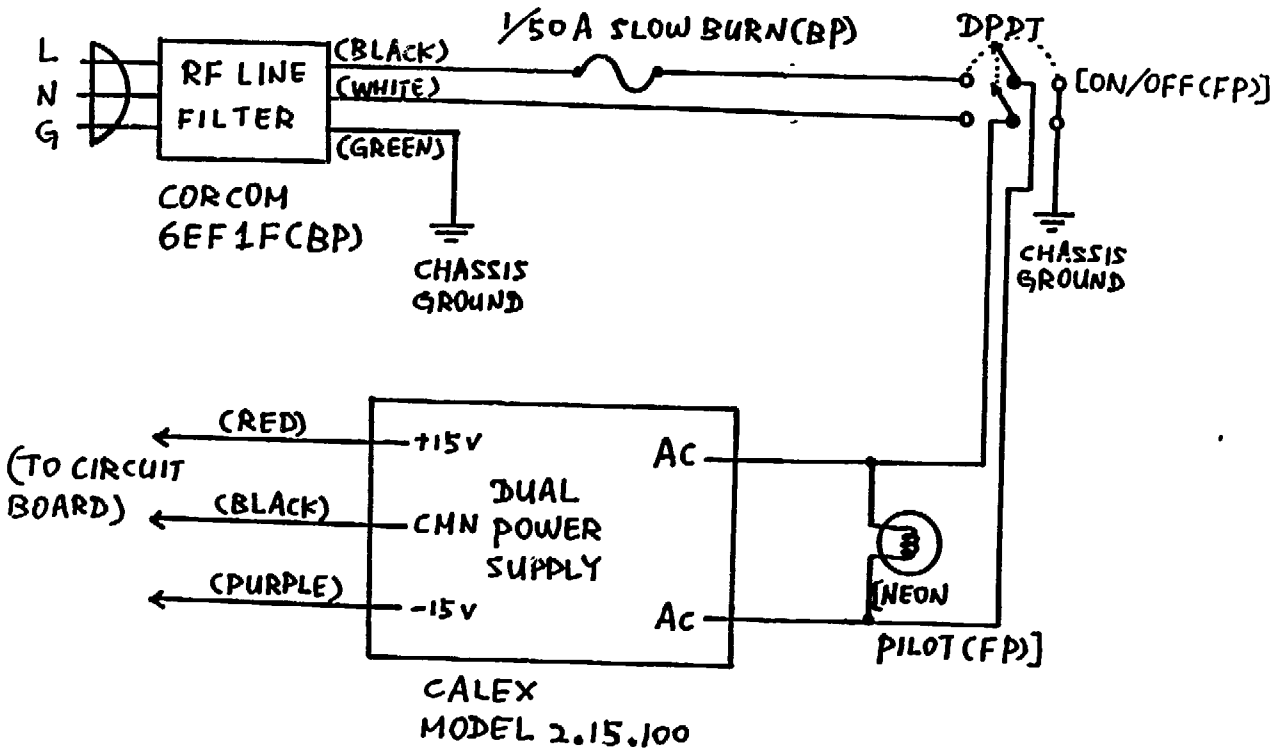


Figure 2.2.3.1-1 (Continued) (d) Power System

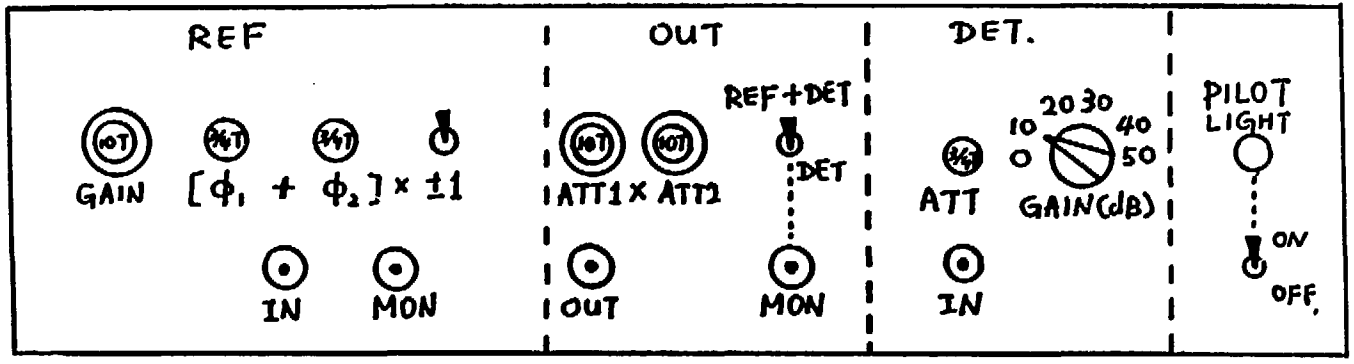


Figure 2.2.3.1-1 (Continued) (e) Front Panel Layout

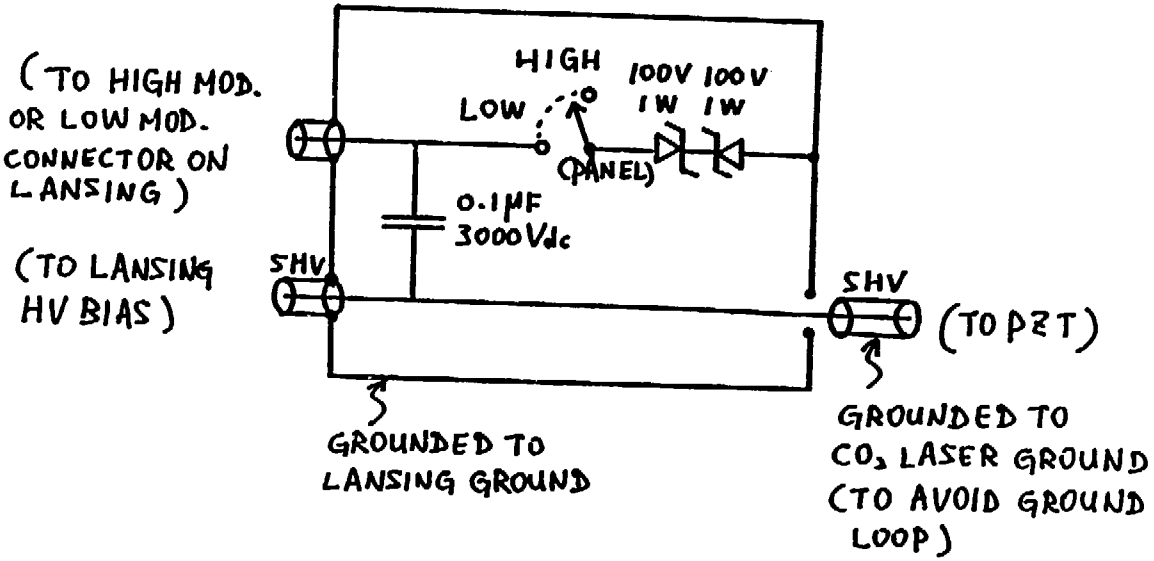


**Figure 2.2.3.1-2**
**Circuit connecting the lock-in stabilizer to the PZT of the $CO_2$ laser.**

of the reference channel, consisting of a current limiting resister and a ±15+0.7 v diode-pair voltage catcher [12], is to protect the following stages and the ±15 v circuit power supply. This large amplitude input is attenuated with an on-board pot (P1) to ensure that no voltage saturation occurs in this channel, particularly in the next frequency filtering stage. The linearity of the voltage pot tuning is provided by (1) its preceding op amp voltage follower, which raises up the input impedance of the pot by orders of magnitude, and (2) the relatively large input impedance of the following filtering stage, which is at least an order of magnitude larger than the pot resistance rating. (Since the only purpose of all the voltage followers in the circuit is for voltage transfer impedance matching to avoid nonlinear interactions between consecutive linear stages such as in the current case, all the rest voltage followers will be neglected in the discussion.) The 518 Hz bandpass filtering stage is incorporated to "purify" the signal from the Monitor Sync connector (on FP/L), which is at least contaminated by a small third harmonic of the fundamental 518 Hz component.

The pure sine wave thus obtained is further attenuated and then phase shifted to become the required *reference* sine wave. The attenuation is adjusted with a 10T voltage pot (P3), which is panel-controlled (Gain/Ref knob on FP/M). ("M" stands for the modification box.) The phase shifting is achieved by three in-series stages: the first two are $0^{\circ}$-$100^{\circ}$ shifters, the third one is a ±1 gain selector (±1/Ref toggle switch on FP/M). The net shifting range of $\phi$ is thus $[-200^{\circ}, +200^{\circ}]$, which is, as required, *over* $360^{\circ}$. Ideally, the

two $0^{\circ}$–$100^{\circ}$ shifters can be controlled synchronously by a single high resolution pot. However, in this prototype circuit two separate panel-controlled low resolution pots ($\phi_1$/Ref and $\phi_2$/Ref knob on FP/M) are used instead for this purpose.

The detector channel also has a protection input stage, similar to that of the reference channel. But now the input is *ac* coupled. The reason is that the small signal from the detector preamp generally needs to be amplified, and any dc component associated with the preamp output, if not eliminated first, could cause the saturation-clipping of the ac signal either within or after the amplification stage. (This ac coupling feature was important particularly when the offset stabilization scheme was tested on different IR detectors.) The amplification stage is panel-controlled (Gain/Det selector on FP/M, 6 position) from 0–50 dB by 10 dB step size. The continuous tuning between these fixed amplification factors is achieved with the attenuator after the 518 Hz bandpass filtering stage. In terms of actual operation, this continuous tuning between the selectable discrete gain is unimportant because (1) the amplitude of the reference sine wave can always be continuously adjusted to match that of the detector channel sine wave, amplified (discretely) only for oscilloscope monitoring, (2) the stabilization efficiency, affected by the signal level before the lock-in demodulation stage, can always be throttled by the post-adder attenuation and the lock-in input amplification. The incorporation of this attenuation is only for a quick circuit test which employs the 20 v pk-to-pk sine wave, provided by the Monitor Sync connector (on FP/L) (the only sine wave source in

this stabilization system), as the inputs of both the detector and reference channel.

2.2.3.2 Operation

Introduced in the following is an efficient offset locking procedure, which gives not only the least interactions among the controlling parameters (knobs and switches) but also the best offset locking quality. Although the introduction of the procedure looks long due to the accompanied reasonings, the procedure itself is only a 10 minute job. To facilitate the discussion, the panel layout is shown in Figure 2.2.3.1-1 (e).

Step (1) Set up the system as specified in Figure 2.2.2.1. Connect an oscilloscope (Scope A) to the Monitor Signal connector (BNC on FP/L), and set the Monitor selector (on FP/L) to the Demod (demodulation) position. Connect a dual trace oscilloscope (Scope B) to the Mon/Ref and Mon/Det connector (BNC's on FP/M). (Set the Mon/Out-or-Mon/Det selector (toggle switch on FP/M) to the Mon/Det position.)

Step (2) Turn the Att/Det knob (on FP/M) all way up. (This is a knob only for circuit testing.) For monitoring convenience as will be shown later, the triggering phases of the two traces on Scope B are suggested to be set to differ by 180°, and the gains of the two traces had better be always the same. Monitor Scope B to check if the reference channel signal is a sine wave free of distortion. If distortion can be visually recognized, adjust pots P1 and P2 on CB/M. ("CB" stands for circuit board.)

Step (3) Set a PZT modulation amplitude. Usually, a modulation amplitude at about 10 v is an empirically reasonable starting point. Lansing has two modulation signal outputs: the Low Mod (0-15 v) and High Mod (0-150 v) SHV BNC connectors on BP/L. (BP stands for back panel.) Now the Low Mod connector should be used for better tuning resolution. Since this amplitude is not directly monitored, its adjustment is achieved by turning the Mod Amplitude control (recessed pot on FP/L) to approximately 2/3 of the full tuning range from zero.

Step (4) Determine the $CO_2$ laser PZT bias to be locked. Set the Function selector (on FP/L) to the Manual position, and then adjust the Bias (0.2-1.6 kv) knob (on FP/L) until an optimal (a compromised) FIR laser performance is obtained in terms of its output power, mode quality, and the noise level. It is noted that the $CO_2$ laser, on whatever the laser line, usually has a noisy spot close to where it has the maximum power. Therefore, to obtain enough locking stability, the bias at the maximum power should be avoided in this initial setting. (This is part of the reason to offset lock the $CO_2$ laser. If a spot with a little higher power than this preset value is really needed, a fine readjustment of the bias by tuning the reference sine wave amplitude is available in step (8) (Case (8c))). Two longitudinal $CO_2$ laser modes are within the PZT bias tuning; there always exist two equivalent optimal biases, separated approximately by 0.5-0.7 kv, depending on the aging of the PZT. It is suggested that we select the lower value one. (Because the stabilization usually drives the locking PZT bias to higher values to compensate the thermal expansion of the laser cavity, this selection will provide more

clearance for locking bias drifting.) The voltage separation between the two longitudinal modes should be remembered as a reference for step (9) (Lansing Mode Jump).

Step (5) Annihilate the 1f component of the detector channel. Adjust the Gain/Ref, $\phi$1/Ref, $\phi$2/Ref knobs and ±1/Ref selector (on FP/M) to make the two sine waves (from the Mon/Ref and Mon/Det connector) monitored on the dual trace oscilloscope have the same amplitude but $180^{\circ}$ out of phase with each other. This corresponds to exactly overlapping these two traces on the oscilloscope. (Remember the trace settings for Scope B in step (1).) For better matching between these two sine waves, if allowed by the noise level, this adjustment can begin with a larger gain of the detector channel, controlled with the Gain/Det selector (on FP/M). (Of course, the annihilation can also be monitored at Mon/Out (on FP/M). But this does not provide the relative deviation of the detector channel signal from the reference sine wave.)

Step (6) Optimize the lock-in demodulation phase ($\phi_d$). This can be achieved by (a) disconnecting the detector signal from and putting a 50 Ω BNC terminator on the detector channel input (Input/Det connector on FP/M), and (b) using the phase matched and fluctuation free reference sine wave alone to optimize the corresponding Lansing Demod signal on Scope A by adjusting the +λ toggle switch (on FP/L), which adds $\pi$ to $\phi_d$, and the $0^{\circ}$-$180^{\circ}$ Phase control (recessed pot on FP/L). (Here, the "+λ", given by the Lansing Company, is a name that does not make sense to the author.) Generally, the Demod signal with $\phi_d$ uncorrected is a 2f periodic wave train with the functional form

$A_d \sin(2\pi ft)$ within the interval $t:[\phi_d/(2\pi f),(\phi_d+\pi)/(2\pi f)]$ as one period. Here, $A_d$ is the amplitude of the Demod signal. Apart from the gain, the optimal Lansing Demod signal, which provides the highest lock-in correction efficiency, should be either the $-|\sin(2\pi ft)|$ or $|\sin(2\pi ft)|$ wave train. (Of course, the worst Demod signal is with $\pm\sin(2\pi ft)$ within $t:[-1/(4f),+1/(4f)]$ as one period because it can not be inverted into any dc correction.) It is noted that the lock-in demodulation phase uncertainty thus obtained should be to within 0 *or* $\pi$. Now, reconnect the detector preamp signal to the Input/Det connector.

Step (7) <u>Try to lock</u> the $CO_2$ laser. Turn the Function selector (on FP/L) from the Manual to the Set position and then to the Stab position.

Step (8) <u>Confirm</u> if the locking does occur. In terms of the PZT bias, shown on the panel meter of Lansing, there could be three cases: (8a) the bias starts drifting away from the preset value in one direction, (8b) the bias starts oscillating about the preset value, (8c) there is no obvious change in the bias.

Case (8a), a failure, can also be revealed by that the 2f periodic Demod signal (on Scope A) starts evolving with a nonzero dc component. For this case, there are two possible causes (if no mistakes has been made in steps (1)-(7)). The first passible cause is that the demodulation phase needs to be changed by $\pi$. We can thus return the Function selector (on FP/L) back to Manual, and restart it from step (4) (the bias optimization). Since the PZT bias does not drift much in such a short time, the new optimal bias should be close

to the original one. But in step (6) (the demodulation phase optimization) only to change the $+\lambda$ toggle switch (on FP/L) setting is required. If drifting still happens after step (7), then the cause could be that the preset PZT bias is too close to one of the extrema of the $F_1(x,A)$. We return the Function selector (on FP/L) to Manual again, then vary the Bias control (on FP/L) about the preset position while monitoring Scope B. If the amplitude of the detector channel sine wave (on Scope B) as a function of the PZT bias is found to have a maximum around the preset bias position, this cause is then confirmed. In such a situation, because the 2f demodulation capability is not incorporated in the current stabilization scheme, the only resort is to select a new, nonoptimal, but lockable preset PZT bias which still provides reasonably good optically pumping for the FIR laser. Since typical PZT modulation amplitude is much smaller than the typical width of the feature of the $CO_2$ laser gain profile (the characteristic curve f(x)) as a function of the PZT bias, usually little shifting(s) of the extremum (extrema) of the corresponding $F_1(x,A)$ can be made by increasing the modulation amplitude A. (See Equation (2.2.1.2.3-1).) Therefore, it is suggested that we restart it from step (4) to avoid the extremum, instead of step (3) to change the modulation amplitude.

Case (8b) implies a bad quality locking with dominant *periodic* "overshooting" corrections. This overshooting oscillation is because the signal level before the lock-in demodulation stage is too large; a large positive correction always needs to be followed by a large negative correction, and vice versa. This case can also be revealed

by Scope A and B simultaneously: the amplitude $A_d$ of the Demod signal $A_d|\sin(2\pi ft)|$ on Scope A will oscillates between the two signs; the amplitude of the detector channel sine wave on Scope B will oscillate about that of the reference channel sine wave. (Remember the trace settings for Scope B in step (1).) This situation can be improved by decreasing either (i) the gain before the demodulation stage or (ii) the PZT modulation amplitude until the dominant periodic oscillation begins to disappear and a smaller random bias fluctuation, if observable, about the preset PZT bias starts to dominate. To decrease the pre-demodulation gain, it is suggested to adjust *only* the Att/Out knobs on FP/M and the Input Gain on FP/L, and to leave the gains of both detector and reference channel unchanged. When decreasing the pre-demodulation gain, there should not be any accompanied change in the preset PZT bias, the center of the oscillation or fluctuation. Such a accompanied change could imply that the resultant dc correction has been too small to lock the $CO_2$ laser in time. If this happens, an in-time increase in the gain could save it; otherwise, it is required to restart it from step (4) all over again. Strictly speaking, the lowering of the modulation amplitude A should not be used to remove this oscillation because the lf lock-in stabilization correction output function $S_1(x,A,\phi,G)$ is a nonlinear function of A; a change in A could cause a change in the offset locking bias. (See Section 2.2.1.2.2) However, when A is small, the change in A might not have such a sensitive effect on the locking bias. Actually, this sensitivity can be easily tested by monitoring the FIR laser performance as a function of A.

Case (8c) implies the offset stabilization is either a success, or a failure with an obscurely slow PZT bias drifting. This can be tested by (i) slightly changing the PZT bias with the Bias control (on FP/L) or (ii) slightly varying the amplitude of the reference sine wave on Scope B with the Gain/Ref knob (on FP/M). If it is a successful locking, in test (i), with the manually bias varying as a perturbation, the laser will return to the preset operating position; in test (ii), the system will "chase" to match the new reference setting. Actually, the latter is a better practice because it also helps to reoptimize the PZT bias, particularly when it takes a while to do steps (5)-(7). If the locking is successful, it is fun to see how efficiently the detector channel sine wave follows the reference sine wave being manually varied. But do not make the amplitude of the reference sine wave too much larger than the preset value because otherwise the locking stability might be reduced (See Section 2.2.1.2.3 (C).) or the locking position might even disappear (See Section 2.2.1.2.3 (A).)

Step (9) Set up the Lansing <u>Mode Jump</u>. Because, as previously explained, the locking bias almost always drifts toward higher voltages, the bias will start getting trapped upon reaching its limiting value at 1.6 kv. In this situation, generally, the Demod signal on Scope A will have a dc component, and the two traces on Scope B will not exactly overlap. To avoid such a fake locking in the PZT bias, it is suggested to use the Mode Jump of Lansing. (See Lock-in Stabilizer Model 80.215 Instruction Manual.) In principle, the step size of the Mode Jump should be close to one longitudinal

mode step so that their difference can be automatically compensated by the stabilization. (Here, the "mode step" is the voltage separation, obtained in step (4), between two equivalent operating points of two adjacent longitudinal modes). Any chosen step size should be tested with the *Manual* Mode Jump as following while the $CO_2$ laser is being locked. The jump should be triggered in the direction that can accommodate the step size. After a short while, if needed, the PZT bias should be either relocked at certain value or trapped at 0.2 kv or 1.6 kv, a limiting position. (It is possible that the bias will be locked with the same reference sine wave at an *inequivalent* operating point of the original or adjacent longitudinal mode.) Further correction for the step size will be required until the corresponding Manual Mode Jump can result in relocking the bias at the equivalent operating point of the adjacent longitudinal mode. Once the step size is determined, set the Mode Jump from Manual to Automatic. (Of course, it is even better if the step size corresponds to two longitudinal mode steps because the number of the Mode Jumps, which are interference to spectrum scanning, can be reduced by 50% in any cases. However, in order to test such a large step size, we need to wait until the locked bias drifts to the positions close to either end of the Bias range.)

#### 2.2.3.3 Performance

This ac offset scheme for the $CO_2$ laser has been successfully tested on over a dozen $CO_2$-laser-pumped FIR laser lines. (Mostly were tested on the FIR Laser Electric Resonance spectrometer [14,15], which

is worse in terms of laser power and noise level of both the CO2 and FIR lasers. According to the resultant FIR laser performance, this technique can actually quintuple the number of laser lines available on that experiment.) So far no optimal $CO_2$ pumping line has been found close to the inflection point of its gain profile, where the 1f modification is difficult and the 2f demodulation is needed. In each case, without any stabilization control readjusted, the stabilization lasted as long as the cooling of the IR detector or as long as the operator's interest. In other words, once the stabilization scheme is set up correctly (in about 10 minutes), at least ten hour locking is guaranteed. The FIR frequency drift rate is approximately 75 kHz/hour, which is a little better than the best available from an etalon locking scheme [8,9]. However, the cost of the response modification box, less than $100, is more than two orders of magnitude cheaper than that for a qualified etalon.

References

1. K.B. Laughlin, G.A. Blake, R.C. Cohen, D.C. Hovde, and R.J. Saykally, Philos. Trans. R. Soc. London Ser. A 324, 97 (1987).

2. K.L. Busarow, G.A. Blake, K.B. Laughlin, R.C. Cohen, Y.T. Lee, and R.J. Saykally, Chem. Phys. Lett., 141, 289 (1987).

3. K.L. Busarow, G.A. Blake, K.B. Laughlin, R.C. Cohen, Y.T. Lee, and R.J. Saykally, J. Chem. Phys., 89, 1268 (1987).

4. G.A. Blake, K.L. Busarow, R.C. Cohen, K.B. Laughlin, Y.T. Lee, and R.J. Saykally, J. Chem. Phys. 89, 6577 (1988).

5. K.B. Laughlin, Ph.D Dissertation, University of California, Berkeley (1988).

6. M. Ignuscio, G. Moruzzi, K.M. Evenson, and D.A Jennings, J. Appl. Phys. 60, R161 (1986).

7. R.C. Cohen, K.L. Busarow, K.B. Laughlin, G.A. Blake, M. Havenith, Y.T. Lee, and R.J. Saykally, J. Chem. Phys. 89, 4494 (1988).

8. J. Farhoomand and H.M. Pickett, Int. J. Infrared and Millimeter Waves 8(5), 441 (1987).

9. G.A. Koepf, H.R. Fetterman and N. McAvoy, Int. J. Infrared and Millimeter Waves 1(4), 597 (1980).

10. For example, Instruction Manual of Lansing Model 80.215 Lock-in Stabilizer (Lansing Research Corporation), and Instruction Manual of Precision Lock-in Amplifier Model PAR124A, (Princeton Applied Research Corporation).

11. G. Arfken, 'Mathematical Methods for Physicists' (Academic Press, New York, 1966).

12. J. Millman, 'Microelectronics' (MaGraw-Hill, New York, 1979).

13. P. Horowitz and W. Hill, 'The Art of Electronics' (Cambridge, New York, 1980).

14. D. Ray, Ph.D. Dissertation, University of California, Berkeley (1985).

15. R.L. Robinson, Ph.D. Dissertation, University of California, Berkeley (1987).

# Chapter 3

## Far Infrared Vibration-Rotation-Tunneling Spectroscopy of Ar-$^{14}NH_3$

### 3.1 Introduction

The establishment of general rules governing vdW interactions on a molecular level is essential in understanding condensed phases and inter-phase interactions. Although various small vdW complexes have been studied, only few general rules have so far been deduced. Unexpectedly, detailed spectroscopic studies of the gas phase $NH_3$-containing binary complexes have destroyed one such important rule.

One might think intuitively, according to the definition of hydrogen bond (H-bond) [1], that $NH_3$ can act not only as a H-bond donor but also as an acceptor, respectively due to the relatively strong electronegativity and the available electron lone pair of the N atom; in other words, $NH_3$ can in principle, be a Lewis acid (H-bond donor) as well as a Lewis base (H-bond acceptor) [2]. However, this guess has been experimentally found to be only partially correct. [3]

The role of $NH_3$ in binary vdW complexes that have been studied, mostly by microwave spectroscopy, can be classified into three types [3]. The first type consists of linearly H-bonded systems such as $H_3N$-HCN [4], $H_3N$-HCl [5], $H_3N$-HBr [6], $H_3N$-HOH [7], $H_3N$-HCCH [8], and $H_3N$-$HCF_3$ [9], in which the $NH_3$ subunit behaves clearly as a H-bond acceptor or Lewis base. In these cases, the partners of the $NH_3$ subunit ranges from strong (e.g. HCN) to extremely weak Lewis acids

(e.g. $CHF_3$). The second type contains the T-shaped complexes $H_3N$-$CO_2$ [10], and $H_3N$-$N_2O$ [11], which are non-H-bonding systems but in which the $NH_3$ subunit behaves as a Lewis base pointing its lone pair toward the middle of its linear partner. The third type are those in which the Lewis acid-base roles are indeterminate, such as CO-$NH_3$ [12], the free-internal-rotor system Ar-$NH_3$ [13-15], and the bent $(NH_3)_2$ [16,17]. Interestingly, all the subunits, viz., CO, Ar, and $NH_3$, involved in this type can form nearly linear H-bonds with HF, $H_2O$, except in the case of Ar-$H_2O$ [18] whose structure has not been determined conclusively. In other words, so far no experimental evidence has indicated that $NH_3$ can be a H-bond donor yet.

This is different from other prototypical H-bonding molecules, viz., the first row hydrides HF and $H_2O$, which can act as both H-bond donor and acceptor. As first pointed out by Nelson [3], this can be illustrated further by considering the vdW stereochemistry of the six binary complexes that can be formed by HF, $H_2$, and $NH_3$. If it is assumed that (1) the complexes have linear H-bonds with the basic H-bond acceptor pointing a lone pair of electrons toward its partner, and (2) the trend of donating H-bonds is: $NH_3 < H_2O < HF$, then, as shown in Figure 3.1-1, the predicted structures of five of these complexes are in essential agreement with experimental results, except in the case of $(NH_3)_2$. It is noted that $(NH_3)_2$ is the only complex, among the six, in which $NH_3$ needs to donate a H-bond, and also the only case that contradicts the prediction.

This strange behavior of $NH_3$ has attracted a great deal of experimental and theoretical interests as well as much controversy,

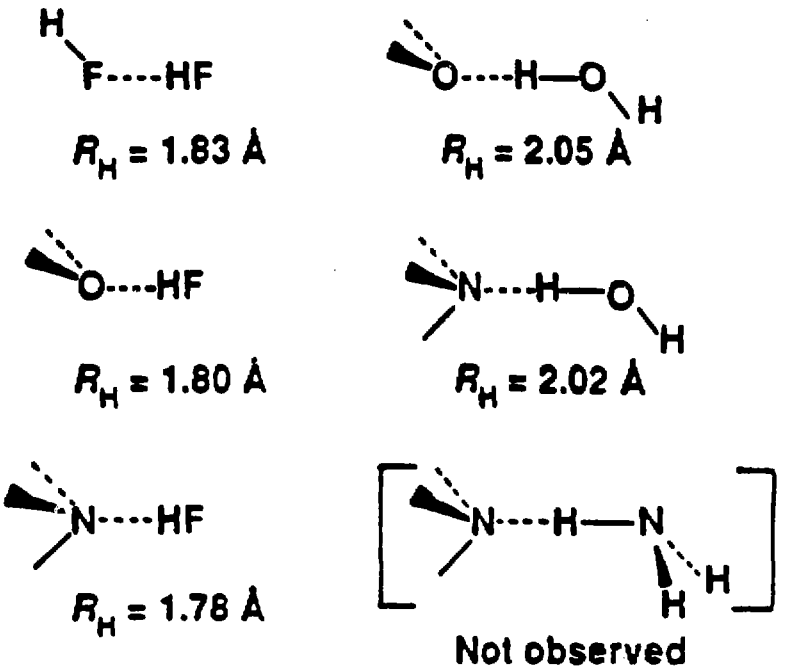


Figure 3.1-1
Linearly H-bonded structures of the binary complexes from the prototypical first row hydrides, HF, $H_2O$, $NH_3$. High-resolution spectroscopy has established these structures to be correct except in the case of $NH_3$ dimer. (From D.D. Nelson, Jr., G.T. Fraser, and W. Klemperer, Science 238, 1670 (1987).)

particularly over the structure of $(NH_3)_2$.

Many theoretical calculations [3,19] of the $(NH_3)_2$ potential surface either preassume or produce a nearly linear H-bonding structure (Figure 3.1-2(a)) as the global minimum, and in one calculation [20] a $C_{2h}$ centro-symmetric structure (Figure 3.1-2(c)) has been predicted to be a local minimum. However, recent microwave spectroscopic studies [16,17] of two intermolecular vibrational states of $(NH_3)_2$ and one of $(ND_3)_2$ by Klemperer and coworkers indicate that $(NH_3)_2$ has a bent *equilibrium* structure (Figure 3.1-2(b)), which is in conflict with almost all theoretical calculations. (Only the post-experiment theoretical "prediction" by Sagarik *et al.* [21] produces a similar structure.) Their two major experimental results are: (1) the ground intermolecular vibrational state shows rigidity, as confirmed by isotopic substitutions, and (2) the small dipole moment projection $\mu_a$, 0.75 D, are found along the a principal axis of the dimer. These imply that $\mu_a$ basically results from the vectorial addition of the two monomer dipole moments with a bent and relatively rigid configuration. Otherwise, if linear H-bond is assumed (and higher order electric interactions can be ignored), then this projection should be approximately 2 D instead. Consequently, this result rules out both the nearly linear (Figure 3.1-2(a)) and centrosymmetric (Figure 3.1-2(c)) H-bonded structure.

After these microwave studies, some theoreticians [22], instead of economically preassuming a nearly linear or a centrosymmetric structures, carried out a geometry optimization on the potential surface at the SCF level for $(NH_3)_2$ and other first and second row

(a)

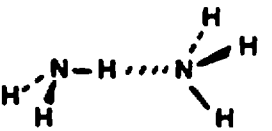

(b)

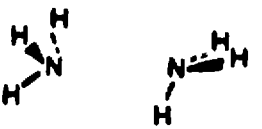

(c)

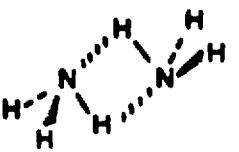

Figure 3.1-2
Possible structures of $(NH_3)_2$:

(a) theoretical (nearly) linear structure,
(b) experimentally observed bent structure, as an intermediate between the two theoretical structures shown in (a) and (c),
(c) theoretical centro-symmetric structure.
(Adapted from A.D. Buckingham, P.W. Fowler, J.M. Hutson, Chem. Rev. 88, 963 (1988).)

hydrides. They found that $(NH_3)_2$ is a rather special and extremely difficult case; when the basis set is small, a centro-symmetric structure is the global minimum, a nearly linear structure is a saddle point, whereas when the basis set is relatively large, there is a role switching between the two structures. Although other higher order calculations [20,23] were made, *no* agreement on the relative orientations of the equilibrium geometry and even the number of minima on the potential surface have been achieved. Certain calculation [20] showed that the conversion energy between the linear and centro-symmetric structures are extremely low that the predicted geometry is sensitive to the correlation energy calculated. All these indicate the difficulty of the structural prediction, and conflict with the existence of rigidity effects shown by the microwave studies. Theoreticians [24] therefore suggested that (1) the measured $\mu_a$ be interpreted as an average value due to large amplitude motions on the relatively flat multibarrier potential surface, and (2) many torsional motion couplings do not lead to spectroscopic splittings. Basically this implies that the $\mu_a$ measured by Klemperer cannot be interpreted in terms of a straightforward classical vector model, and the equilibrium structure thus derived could be incorrect. It is also shown that although $\mu_a$ is a strong function of the relative orientation between the two $NH_3$ subunits within an electrostatic model, approximately equally good structural reassignments can be made with one of the torsional angles varying from $0^o$-$60^o$. In terms of the apparent rigidity, the discrepancy between theories and experiments therefore remains.

Nelson *et al.* [25] then made a MS group theoretical study for the energy level splittings due to rotational-tunneling motions. This study illustrates that even when certain torsional tunnelings are allowed, the tunneling splittings could still be missing and a classical semirigid rotor type microwave spectrum *could* be observed.

So far, perhaps, the most meaningful theoretical results is that the $(NH_3)_2$ complex does provide a serious challenge to theoreticians. In order to understand these anomalous behaviors of $NH_3$, experimental studies of its potential surface are then required.

Because of the simplicity of the Ar atom as a featureless probe for the behavior of the $NH_3$ subunit, Ar-$NH_3$, instead of $(NH_3)_2$, clearly becomes the starting point for a detailed experimental study of the weak binding of $NH_3$. Due to the suggestion, by microwave spectroscopy [14,15], that $NH_3$ subunit of Ar-$NH_3$ is essentially an inverting, free internal rotor even in the ground intermolecular vibrational state, its potential surface is expected to be relatively isotropic. A further characterization of the global features and finer details of the potential surface becomes a more intriguing challenge. Since FIR spectroscopy directly samples the intermolecular vibrational states, which can then be inverted into the potential surface, we use the state-of-the-art tunable FIR laser technique described in Chapter 2 to probe the system.

In this work, we report a study of an intermolecular vibrational transition of Ar-$^{14}NH_3$ at 26.470633(17) $cm^{-1}$. The ground state of this band was studied previously by Nelson *et al.* and Lovas *et al.* using molecular beam electric resonance experiments and pulsed nozzle

Fourier transform microwave spectroscopy. [13] The obtained molecular constants of the upper vibrational state are also consistent with the nearly free internal rotor model. The molecular constants, the permutation-inversion group theory, the selection rules, and the quantum number correlation were all used to make a tentative assignment of this vibrational band and to extract information about the intermolecular potential surface.

## 3.2 Experimental

Used in the range from 21 to 28 $cm^{-1}$ on the tunable FIR/planar jet spectrometer were four fixed frequency FIR laser lines, i.e. 692.9514 GHz, 761.6083 GHz, 584.3882 GHz from HCOOH, and 787.7555 GHz from DCOOD [26]. About 350 transitions (see Appendix Table 5 for the approximately 250 rotationally unassigned lines) were observed over this region. A stick spectrum of these lines with observed intensities is shown in Figure 3.2. At least two different vdW species, viz., the Ar-$NH_3$ and $(NH_3)_2$ complexes, were observed in the supersonic expansion from a 700 Torr 3% $NH_3$-in-Ar mixture through a 1.5" long and 0.001" wide room temperature slit into a chamber at approximately 100 mTorr. Although most of the observed lines were catalogued using a 3% mixture, the signals of Ar-$NH_3$ and $(NH_3)_2$ can be improved threefold with 0.5% and 2% mixtures, respectively. The signal of Ar-$NH_3$ is in general about ten times stronger than that of $(NH_3)_2$, and has a maximum signal-to-noise ratio of about 200.

## 3.3 Spectrum Rotational Assignment and Analysis

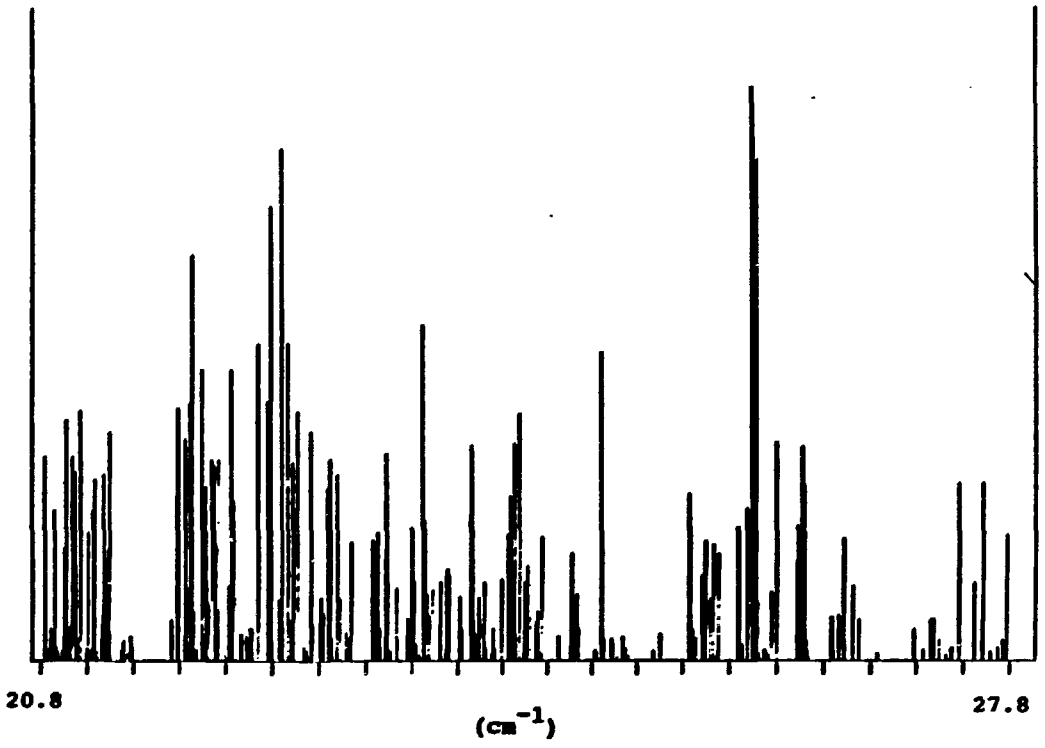


Figure 3.2
Computer reproduction of the far-ir spectrum observed in a 3% $NH_3$-in-Ar mix.

A $K_a$: 0 ← 0 subband of the near prolate Ar-$^{14}NH_3$ complex centered at 26.470633(17) $cm^{-1}$ was identified and shown to have the same lower state as that observed previously by microwave spectroscopy [13]. The observed subband structure is shown in Figure 3.3 as a stick spectrum. Twenty three transitions (Table 3.3-1) have been assigned to this subband. The results of the fit are given in Table 3.3-2. The standard deviation of the fit of six parameters to 23 lines is 1.1 MHz, which is consistent with the uncertainty due to laser frequency drift. The P(7) line at 751 GHz was obscured by the atmospheric water absorption at 752 GHz in the unpurged optical path. $^{14}N$ Nuclear hyperfine structure from the $^{14}N$ quadrupole interaction was only partially resolved for each of these spectral lines, as is evident in the P(2) line shown in Figure 3.3. In the fit, the upper state nuclear quadruple coupling constant ($eqQ_{aa}'$) was fit with the ground state constant ($eqQ_{aa}''$) fixed at the value from the microwave study, in which the hyperfine structure was much better resolved. Over ninety other far infrared lines in the 7 $cm^{-1}$ interval measured have been assigned as vibration-rotation-tunneling (VRT) transitions in $(NH_3)_2$. Their rotational analyses will be given separately in Reference 27.

### 3.4 Group Theoretical Preparation for Vibrational Assignments

The transformation properties of the nuclear coordinates of Ar-$NH_3$ under the permutation inversion (PI) operations of the $D_{3h}(M)$ molecular symmetry group (Appendix Table 1, character table) will be discussed first. The methodology of the coordinate transformation

Table 3.3-1
Observed $K_a$=0 ← 0 subband transitions of Ar-$NH_3$.

| TRANSITION | | | | | | | OBS. FREQ. | O-C |
|---|---|---|---|---|---|---|---|---|
| | $J'$ | $K_a'$ | $K_c'$ | ← $J''$ | $K_a''$ | $K_c''$ | (MHz) | (MHz) |
| 1. | 14 | 0 | 14 | 15 | 0 | 15 | 696307.0 | −0.6 |
| 2. | 13 | 0 | 13 | 14 | 0 | 14 | 703581.0 | 1.2 |
| 3. | 12 | 0 | 12 | 13 | 0 | 13 | 710717.0 | 0.1 |
| 4. | 11 | 0 | 11 | 12 | 0 | 12 | 717728.5 | −0.3 |
| 5. | 10 | 0 | 10 | 11 | 0 | 11 | 724623.0 | −0.1 |
| 6. | 9 | 0 | 9 | 10 | 0 | 10 | 731405.0 | −0.8 |
| 7. | 8 | 0 | 8 | 9 | 0 | 9 | 738080.5 | −0.7 |
| 8. | 7 | 0 | 7 | 8 | 0 | 8 | 744653.3 | 0.6 |
| 9. | 5 | 0 | 5 | 6 | 0 | 6 | 757492.3 | 1.4 |
| 10. | 4 | 0 | 4 | 5 | 0 | 5 | 763758.7 | −0.5 |
| 11. | 3 | 0 | 3 | 4 | 0 | 4 | 769926.4 | −0.4 |
| 12. | 2 | 0 | 2 | 3 | 0 | 3 | 775992.7 | −0.3 |
| 13. | 1 | 0 | 1 | 2 | 0 | 2 | 781957.7 | 1.0 |
| 14. | 0 | 0 | 0 | 1 | 0 | 1 | 787816.4 | 0.2 |
| 15. | 1 | 0 | 1 | 0 | 0 | 0 | 799215.0 | −0.1 |
| 16. | 2 | 0 | 2 | 1 | 0 | 1 | 804748.7 | −1.0 |
| 17. | 3 | 0 | 3 | 2 | 0 | 2 | 810170.0 | −1.0 |
| 18 | 4 | 0 | 4 | 3 | 0 | 3 | 815476.5 | 0.8 |
| 19. | 5 | 0 | 5 | 4 | 0 | 4 | 820661.7 | 1.5 |
| 20. | 6 | 0 | 6 | 5 | 0 | 5 | 825718.0 | −2.4 |
| 21. | 7 | 0 | 7 | 6 | 0 | 6 | 830652.9 | 1.3 |
| 22. | 9 | 0 | 9 | 8 | 0 | 8 | 840105.1 | 0.9 |
| 23. | 10 | 0 | 10 | 9 | 0 | 9 | 844610.8 | −0.8 |

Table 3.3-2
Spectroscopic constants (in MHz) of the observed VRT band of Ar-$NH_3$. The uncertainties in the parentheses are two standard deviations.

The observed band[a]

| | Lower state: | Ground state:[b] |
|---|---|---|
| $(B''+C'')/2$ | 2876.927(94) | 2876.849(2) |
| $D_J''$ | 0.08644(27) | 0.0887(2) |
| $eqQ_{aa}''$ | ... | 0.350(8) |
| | Upper state: | |
| $(B'+C')/2$ | 2822.87(11) | |
| $D_J'$ | 0.10225(48) | |
| $H_J'$ | $-30.5(16) \times 10^{-6}$ | |
| $eqQ_{aa}'$ | $-0.8$[c] | |

[a]This work. Rotational constants are determined in a simultaneous fit of both the upper and lower states.

[b]Reference [13].

[c]The upper state $^{14}N$ nuclear quadruple coupling constants were obtained by fixing the lower state constants at the values from microwave spectroscopy.

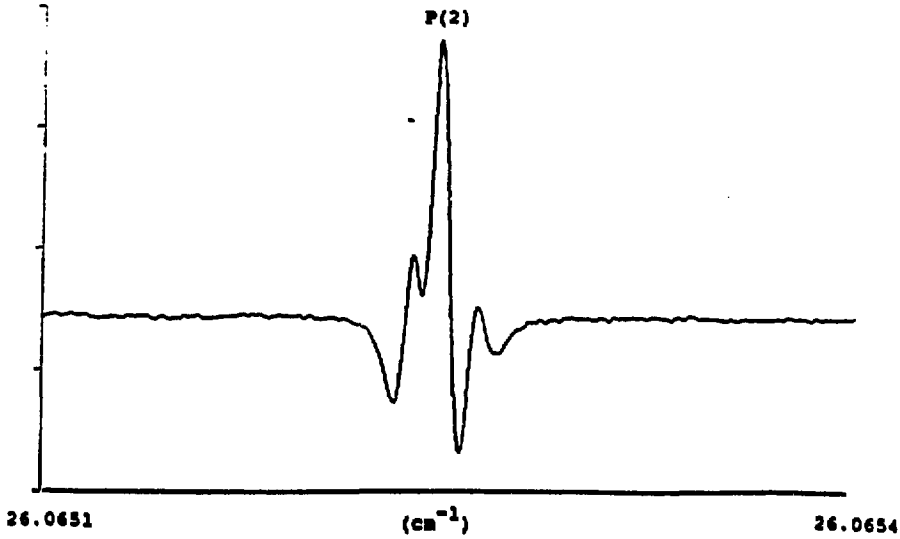


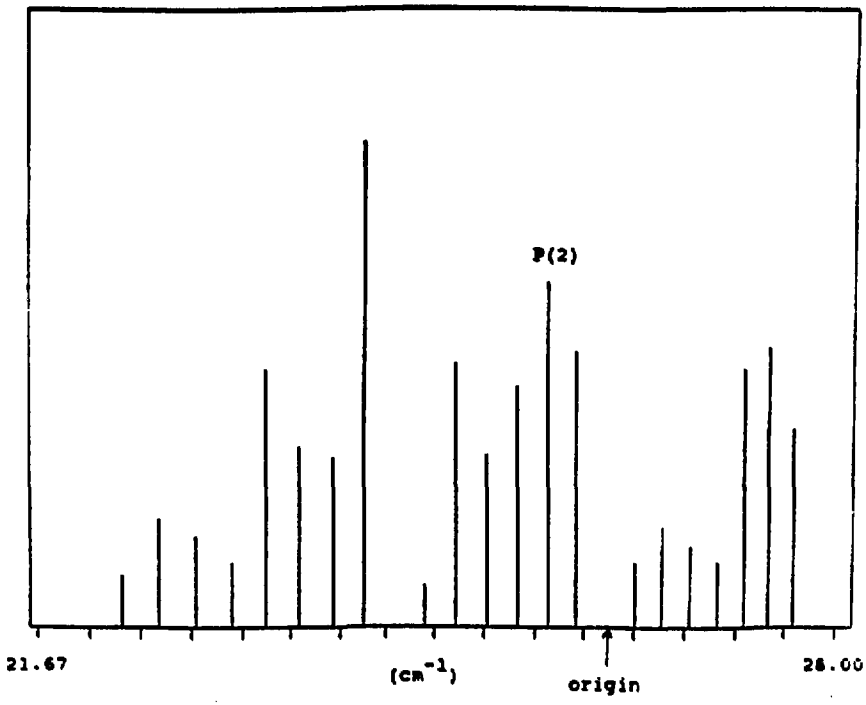


Figure 3.3
Upper: A 10 MHz scan showing P(2) of the 26.47 cm$^{-1}$ band of Ar-$NH_3$, with $^{14}N$ nuclear hyperfine structure partially resolved.
Lower: A stick spectrum of the intermolecular vibrational band with the actual observed intensities indicated.

employed was first introduced by J. Hougen [28]. The transformation properties of the rotational wave functions and inversion coordinate will also be derived.

### 3.4.1 Coordinate Definitions

The $NH_3$ subunit-fixed Cartesian coordinate system is defined in Figure 3.4.1-1. Its origin is the center of mass of the subunit. If the $C_3$ symmetry is assumed for the $NH_3$ subunit, then the three axes can be specified as follows:

- $y_s$: parallel to the plane defined by the equilibrium positions of the three hydrogens, and in the direction of the vector pointing from the equilibrium position of H3 to that of H2,
- $x_s$: parallel to the plane defined by the equilibrium positions of the three hydrogens, and pointing toward H1,
- $z_s$: determined by the right-hand rule from $x_s$ and $y_s$ axes, and is collinear with the $C_3$ symmetry axis of $NH_3$.

The atomic coordinates, $R_i$ (i=Ar, N, 1, 2, and 3), with respect to the laboratory-fixed coordinate system are defined as follows:

$$R_{Ar} = R_{cm} + S^{-1}(\pi/2,\theta_d,\phi_d)[-(m_s/M)Rk]$$
$$= R_{cm} + S_d^{-1}[-(m_s/M)Rk] \qquad (S_d^{-1} = S^{-1}(\chi_d,\theta_d,\phi_d),\ \chi_d=\pi/2); \tag{3.4.1-1}$$
$$R_{i\neq Ar} = R_{cm} + S^{-1}(\pi/2,\theta_d,\phi_d)[(m_{Ar}/M)Rk]$$
$$+ S^{-1}(\chi_s,\theta_s,\phi_s)[a_i^{o}(\gamma) + d_i(\gamma)]$$

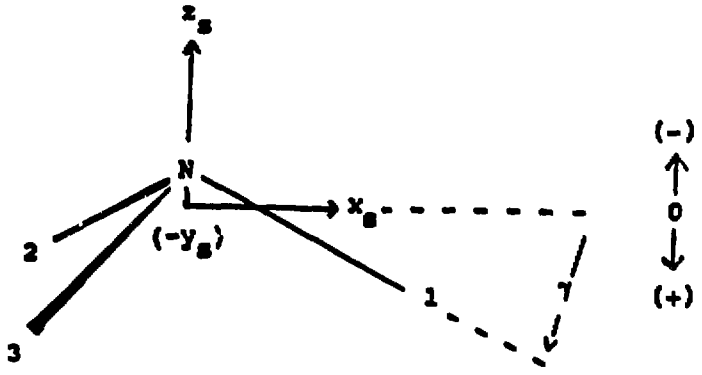


Figure 3.4.1-1
Definition of the $NH_3$ subunit-fixed Cartesian coordinate system, and the angle coordinate ($\gamma$) of the $NH_3$ inversion motion. $\gamma$ is the angle between the positive $x_s$ axis and the vector pointing from the equilibrium position of N to that of H1. $\gamma$ has the same sign as the $z_s$ coordinate of the equilibrium position of N.

$$= R_{cm} + S_d^{-1}[(m_{Ar}/M)Rk] + S_s^{-1}[a_i^{o}(\gamma) + d_i(\gamma)], \quad (S_s^{-1} = S^{-1}(\chi_s, \theta_s, \phi_s)) \tag{3.4.1-2}$$

in which

$R_i$: position vector of atom i (i=Ar, N, 1, 2, 3) or the center of mass of the complex (i=cm) with respect to the laboratory-fixed coordinate system,

S: rotation matrices, following the convention of Wilson, Decius and Cross [29],

$$S(\chi,\theta,\phi) = \begin{array}{c} \\ x \\ y \\ z \end{array} \begin{array}{c} \begin{array}{ccc} X & Y & Z \end{array} \\ \begin{bmatrix} c\chi c\theta c\phi - s\chi s\phi & c\chi c\theta s\phi + s\chi c\phi & -c\chi s\theta \\ -s\chi c\theta c\phi - c\chi s\phi & -s\chi c\theta s\phi + c\chi c\phi & s\chi s\theta \\ s\theta c\phi & s\theta s\phi & c\theta \end{bmatrix} \end{array}, \tag{3.4.1-3}$$

where c=cosine, s=sine. The X, Y, Z correspond to the Cartesian coordinates of the laboratory-fixed system; the x, y, z are the Cartesian coordinates of the rotating body-fixed system. $S_d^{-1}$ describes the orientation of the Ar-$NH_3$ pseudo-diatomic frame with respect to the laboratory-fixed coordinate system. $\chi_d$ is chosen arbitrarily to be $\pi/2$. Similarly, $S_s^{-1}$ describes the orientation of the $NH_3$ subunit with respect to the laboratory space with $\theta_s$, $\phi_s$ fixing the $C_3$ axis of $NH_3$, and $\chi_s$ the rotation about the $C_3$ axis.

$m_s$: mass of the $NH_3$ subunit,

$m_{Ar}$: mass of Ar atom,

M: total mass of the Ar-$NH_3$ complex,

R: distance between the Ar atom and the center of mass of the

$NH_3$ subunit, (see Figure 3.4.1-2)

k: unit vector pointing from the Ar atom to the center of mass of the $NH_3$ subunit, (see Figure 3.4.1-2)

$\gamma$: $NH_3$ inversion coordinate, defined in Figure 3.4.1-1. $\gamma$ is the angle between the positive $x_s$ axis and the vector pointing from the equilibrium position of N to that of H1. $\gamma$ has the same sign as the $z_s$ coordinate of the "equilibrium" position of N (see below).

$a_i^o(\gamma)$: equilibrium position vector of atom i in the $NH_3$ subunit with respect to the subunit-fixed coordinate system; a vector function of $\gamma$, defined as

$$a_i^o(-\gamma) = \begin{bmatrix} x_i^o(-\gamma) \\ y_i^o(-\gamma) \\ z_i^o(-\gamma) \end{bmatrix} = \begin{bmatrix} +x_i^o(+\gamma) \\ +y_i^o(+\gamma) \\ -z_i^o(+\gamma) \end{bmatrix}.$$

The large amplitude $NH_3$ inversion displacement is inherent in such an "equilibrium" position vector. Therefore, it is the equilibrium position only when $\gamma$ is held at a constant. Since it is a vector function of $\gamma$, its length, $|a_i^o(\gamma)|$, may vary with the inversional motion.

$d_i(\gamma)$: *noninversional* Displacement vector of atom i of the $NH_3$ subunit with respect to the subunit-fixed coordinate system; defined similarly as $a_i^o(\gamma)$ as

$$d_i(-\gamma) = \begin{bmatrix} d_{xi}(-\gamma) \\ d_{yi}(-\gamma) \\ d_{zi}(-\gamma) \end{bmatrix} = \begin{bmatrix} +d_{xi}(+\gamma) \\ +d_{yi}(+\gamma) \\ -d_{zi}(+\gamma) \end{bmatrix}.$$

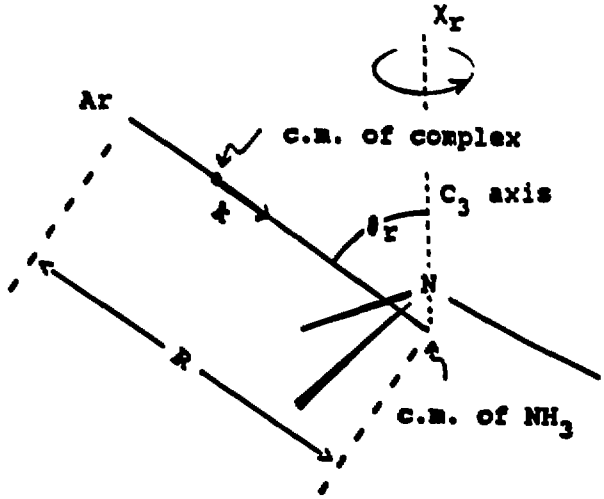


Figure 3.4.1-2
Definitions of distance R, unit vector k, and Eulerian angles $\theta_r$, $\chi_r$ for Ar-$NH_3$. (c.m.: center of mass.) $\theta_r$ will be simplified as $\theta$ from Section 3.6.1.

Since both $a_i^{\circ}(\gamma)$ and $d_i(\gamma)$ are polar vectors [30], they have similar defining expressions in terms of $\gamma$.

### 3.4.2 Coordinate Transformations

#### 3.4.2.1 Effect of Permutation (without *) on $R_{Ar}$

Since any permutation among the three H's has no effect on $R_{Ar}$, it is straightforward that

$$R_{Ar} \longrightarrow R_{cm} + S^{-1}(\pi/2,\theta_d,\phi_d)[(m_{Ar}/M)Rk]$$
$$= \text{original } R_{Ar}. \qquad (3.4.2.1)$$

#### 3.4.2.2 Effect of Permutation-Inversion (PI) on $R_{Ar}$

Apparently, the net effect on $R_{Ar}$ of any PI operation with * explicitly involved will be the same as that of the * operation itself. Therefore,

$$R_{Ar} \xrightarrow{*} -R_{cm} + [S^{-1}(\pi/2,\theta_d,\phi_d)(-N_d^{-1})][-(m_s/M)R]N_d k)$$
$$= -(\text{original } R_{Ar}), \qquad (3.4.2.2\text{-}1)$$

where

$$N_d = N_d^{-1} = \begin{bmatrix} +1 & 0 & 0 \\ 0 & -1 & 0 \\ 0 & 0 & +1 \end{bmatrix} \qquad (3.4.2.2\text{-}2)$$

and

$$k = \begin{bmatrix} 0 \\ 0 \\ 1 \end{bmatrix}. \qquad (3.4.2.2\text{-}3)$$

Here, k is a unit vector for the displacement vector used in the pseudo-diatomic model; it has the same coordinate expression with

respect to the pseudo-diatomic frame coordinate system before and after the * operation.

Equation (3.4.2.2-2) can be derived as follows: Using the convention of Wilson, Decius and Cross, with $\chi_d=\pi/2$, we get

$$S_d^{-1}= S^{-1}(\pi/2,\theta_d,\phi_d)= \begin{bmatrix} -S\phi_d & -C\theta_d C\phi_d & S\theta_d C\phi_d \\ C\phi_d & -C\theta_d S\phi_d & S\theta_d S\phi_d \\ 0 & S\theta_d & C\theta_d \end{bmatrix}. \qquad (3.4.2.2\text{-}4)$$

On the other hand, $[S^{-1}(\pi/2,\theta_d,\phi_d)(-N_d^{-1})]$ $(=[-S_d^{-1}N_d^{-1}])$ in Equation (3.4.2.2-1) is the equivalent proper rotation [31] of the * operation with respect to the laboratory-fixed coordinate system. By doing the following substitutions in Equation (3.4.2.2-4) for $S_d^{-1}$,

$$\theta_d \longrightarrow \pi - \theta_d,$$
$$\phi_d \longrightarrow \pi + \phi_d,$$

its explicit form can thus be obtained as

$$[-S_d^{-1}N_d^{-1}]= \begin{bmatrix} +S\phi_d & -C\theta_d C\phi_d & -S\theta_d C\phi_d \\ -C\phi_d & -C\theta_d S\phi_d & -S\theta_d S\phi_d \\ 0 & +S\theta_d & -C\theta_d \end{bmatrix}. \qquad (3.4.2.2\text{-}5)$$

Because

$$\begin{aligned} N_d^{-1} &= -S_d[-S_d^{-1}N_d^{-1}] \\ &= (-1)[S_d^{-1}]^t[-S_d^{-1}N_d^{-1}], \qquad (3.4.2.2\text{-}6) \\ &(\because S_d^{-1} \text{ and } S_d \text{ are orthonormal, } S_d^{-1}=S_d^t), \end{aligned}$$

with the use of Equations (3.4.2.2-4) and (3.4.2.2-5) for $S_d^{-1}$ and $[S_d^{-1}N_d^{-1}]$, the explicit expression for $N_d^{-1}$ (Equation (3.4.2.2-2))

can then be verified.

Geometrically, Figure 3.4.2.2 serves as a visual verification for the explicit expression of the rotation operation $[-N_d]$ (see Equation 3.4.2.2-2), which represents a rotation of the pseudo-diatomic frame about its y axis by $180^o$.

### 3.4.2.3 Effect of the * Operation on $R_i$ (i= N, 1, 2, 3) (Figure 3.4.2.3)

The transformation of the $NH_3$ nuclear coordinates under the * operation is as follows:

$$\begin{aligned} R_i \xrightarrow{*} & -R_{cm} + [S_d^{-1}(-N_d^{-1})][N_d(m_{Ar}/M)Rk] \\ & + [S_s^{-1}(-N_{s*}^{-1})][a_i^o(-\gamma) + d_i(-\gamma)] \\ = & -R_{cm} - [S_d^{-1}N_d^{-1}][N_d(m_{Ar}/M)Rk] \\ & - [S_s^{-1}N_{s*}^{-1}][N_{s*}(a_i^o(+\gamma) + d_i(+\gamma))] \\ = & -(\text{original } R_i), \end{aligned} \qquad (3.4.2.3\text{-}1)$$

where

$N_d$ and k: same as derived previously for $R_{Ar}$,

$N_{s*}$: equivalent *improper* rotation [31] of the * operation with respect to subunit-fixed coordinate system, with its explicit expression being

$$N_{s*} = \begin{bmatrix} +1 & 0 & 0 \\ 0 & +1 & 0 \\ 0 & 0 & -1 \end{bmatrix}, \qquad (3.4.2.3\text{-}2)$$

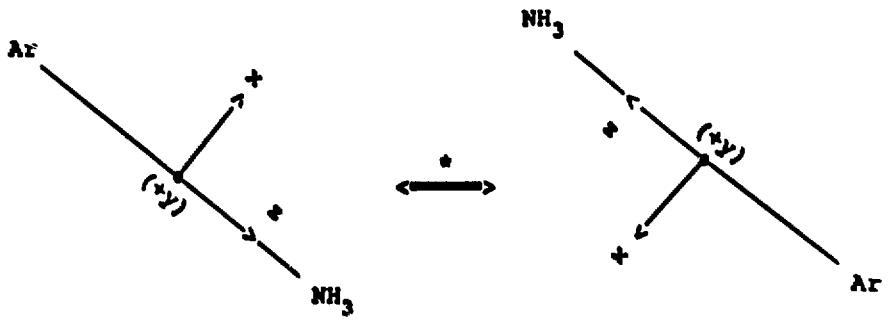


Figure 3.4.2.2
Effect of the * operation on the pseudo-diatomic frame coordinate system.

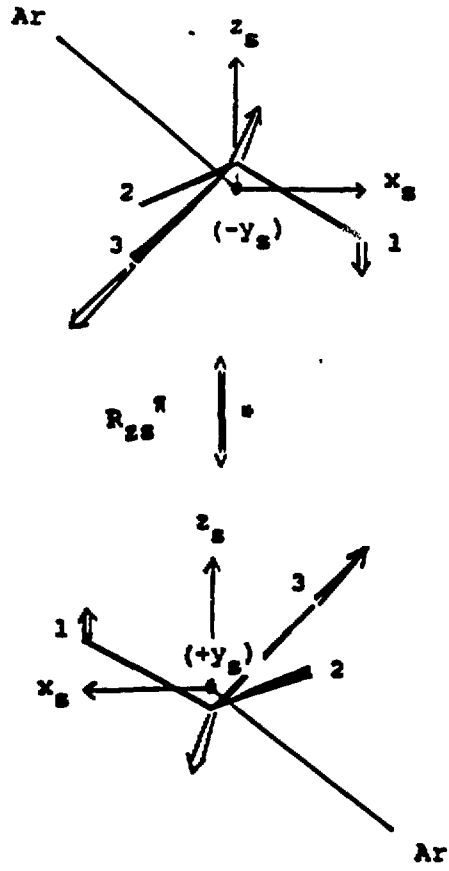


Figure 3.4.2.3
Effect of the * operation on $R_i$ (i= N, 1, 2, 3).

(The determinant values of +1 and −1 are characteristic of proper and improper rotation matrices, respectively.)

$a_i^{\circ}(-\gamma)$ and $d_i(-\gamma)$: new equilibrium position and displacement vector of atom i with respect to the new subunit-fixed coordinate system after the * operation.

Equation (3.4.2.3-1) can be verified as follows: The first two terms, referring to the center of mass of the $NH_3$ subunit, can be obtained similarly as in the previous case of the * operation on $R_{Ar}$. The third term can be justified with Figure 3.4.2.3, which shows the equivalent proper rotation, with respect to the laboratory-fixed system, of the $NH_3$ subunit-fixed coordinate system causes a rotation about $z_s$ axis by 180°, i.e.

$$S^{-1}(\chi_s,\theta_s,\phi_s) \xrightarrow[{[R_{zs}{}^{\pi}]}]{*} S^{-1}(\chi_s,\theta_s,\phi_s)(-N_{s*}{}^{-1}) \qquad (3.4.2.3\text{-}3)$$

$$(= S^{-1}(\chi_s+\pi,\theta_s,\phi_s)),$$

where $[R_{zs}{}^{\pi}]$ and $N_{s*}{}^{-1}$ are the corresponding proper and improper rotation, with

$$[R_{zs}{}^{\pi}] = [R_{zs}{}^{\pi}]^{-1} \; (= -N_{s*} = -N_{s*}{}^{-1}) = \begin{bmatrix} -1 & 0 & 0 \\ 0 & -1 & 0 \\ 0 & 0 & +1 \end{bmatrix}.$$

It is also apparent, from Figure 3.4.2.3, that $a_i^{\circ}(+\gamma)$ and $d_i(+\gamma)$ are changed into

$$a_i^{\circ}(-\gamma) \; (= N_{s*}a_i^{\circ}(+\gamma)) \qquad (3.4.2.3\text{-}4)$$

and

$$d_i(-\gamma)\ (= N_{s*}d_i(+\gamma)). \qquad (3.4.2.3\text{-}5)$$

As a result of Equations (3.4.2.3-2) through (3.4.2.3-5), Equation (3.4.2.3-1) is justified.

### 3.4.2.4 Effects of the (23) and (23)* Class Operations on $R_i$ (i=N, 1, 2, 3) (Figure 3.4.2.4-1)

The individual equivalent proper rotations for the pseudo-diatomic frame under the (23) pair permutation and the * parity inversion can be expressed as

$$S^{-1}(\pi/2,\theta_d,\phi_d) \xrightarrow[{[R^o]}]{(23)} S_d^{-1} \xrightarrow[{[R_y^{\pi}]}]{*} S_d^{-1}(-N_d^{-1}).$$

Similarly, those for the $NH_3$ subunit-fixed coordinate system are

$$S^{-1}(\chi_s,\theta_s,\phi_s) \xrightarrow[{[R_{xs}^{\pi}]}]{(23)} S_s^{-1}M_{(23)}^{-1}$$

$$\xrightarrow[{[R_{zs}^{\pi}]}]{*} S_s^{-1}M_{(23)}^{-1}(-N_{s*}^{-1})$$

$$(= S_s^{-1}[R_{ys}^{\pi}]^{-1}),$$

where

$$M_{(23)}^{-1} = \begin{bmatrix} +1 & 0 & 0 \\ 0 & -1 & 0 \\ 0 & 0 & -1 \end{bmatrix} (= M_{(23)})$$

and

$$N_{s*} = -[R_{zs}^{\pi}] = \begin{bmatrix} +1 & 0 & 0 \\ 0 & +1 & 0 \\ 0 & 0 & -1 \end{bmatrix}.$$

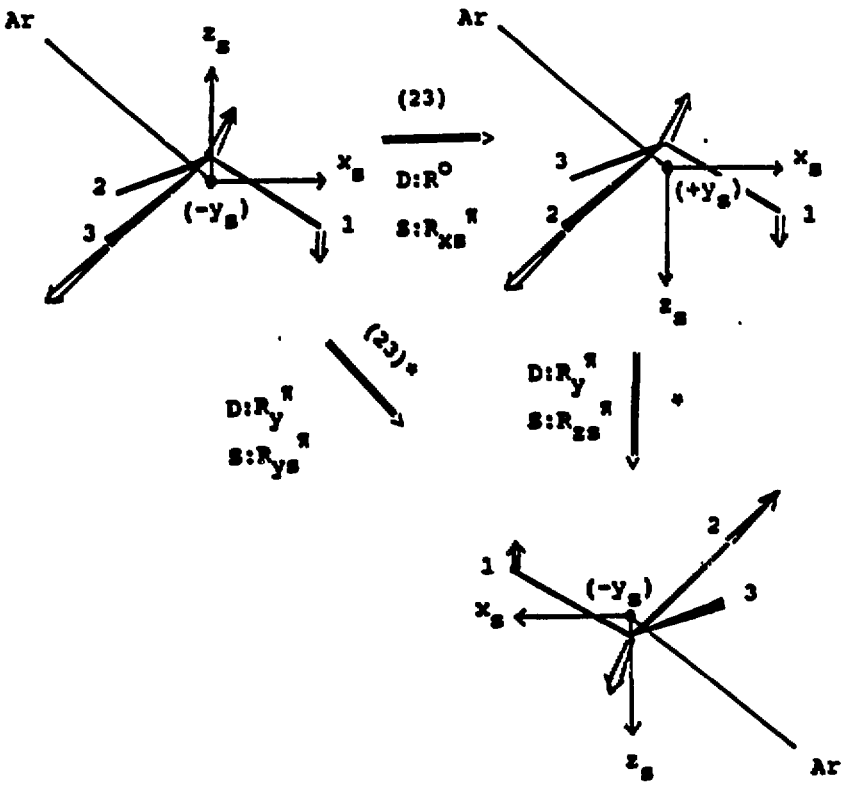


Figure 3.4.2.4-1
Effect of the (23) and (23)* operation on $R_i$ (i= N, 1, 2, 3). (D: pseudo-diatomic. : subunit.)

Here, $M_{(23)}$ and $N_{s*}$ are proper and improper rotation matrix, respectively. We will keep using M for proper matrices, and N for improper matrices in the following. (It is noted that (23) corresponds to an improper rotation under $C_{3v}(M)$, while to a proper rotation under $D_{3h}(M)$.)

The change in the equilibrium position of each nuclear coordinate od $NH_3$ is derived as follows:

N:

$$a_N^{\circ}(+\gamma) = \begin{bmatrix} 0 \\ 0 \\ z_N^{\circ}(+\gamma) \end{bmatrix} \xrightarrow{(23)} M_{(23)} a_N^{\circ}(+\gamma)$$

$$\left(= \begin{bmatrix} 0 \\ 0 \\ -z_N^{\circ}(+\gamma) \end{bmatrix} = a_N^{\circ}(-\gamma)\right)$$

$$\xrightarrow{*} N_{s*} M_{(23)} a_N^{\circ}(+\gamma) = M_{(23)} a_N^{\circ}(-\gamma)$$

($N_{s*}$ and $M_{(23)}$ are both diagonal, therefore they commute.)

$$(= N_{s*} a_N^{\circ}(-\gamma) = a_N^{\circ}(+\gamma)),$$

H1:

$$a_1^{\circ}(+\gamma) = \begin{bmatrix} x_1^{\circ}(+\gamma) \\ 0 \\ z_1^{\circ}(+\gamma) \end{bmatrix} \xrightarrow{(23)} M_{(23)} a_1^{\circ}(+\gamma)$$

$$(= \begin{bmatrix} x_1{}^{o}(+\gamma) \\ 0 \\ -z_1{}^{o}(+\gamma) \end{bmatrix}$$

$$= a_1{}^{o}(-\gamma))$$

$$\xrightarrow{*} M_{(23)}a_1{}^{o}(-\gamma)$$

$$(= N_{s*}a_1{}^{o}(-\gamma)$$

$$= a_1{}^{o}(+\gamma)),$$

H2:

$$a_2{}^{o}(+\gamma) \xrightarrow{(23)} M_{(23)}a_3{}^{o}(+\gamma)$$

$$(= \begin{bmatrix} +x_3{}^{o}(+\gamma) \\ -y_3{}^{o}(+\gamma) \\ -z_3{}^{o}(+\gamma) \end{bmatrix})$$

$$\xrightarrow{*} N_{s*}M_{(23)}a_3{}^{o}(+\gamma)$$

$$= M_{(23)}a_3{}^{o}(-\gamma),$$

H3: (Do a (23) permutation in the above $a_2{}^{o}(+\gamma)$ expression.)

$$a_3{}^{o}(+\gamma) \xrightarrow{(23)} M_{(23)}a_2{}^{o}(+\gamma)$$

$$\xrightarrow{*} M_{(23)}a_2{}^{o}(-\gamma).$$

In other words, the expressions for the changes in the equilibrium positions are of the following form:

$$a_i{}^{o}(+\gamma) \xrightarrow{(23)} M_{(23)}a_j{}^{o}(+\gamma) \qquad (3.4.2.4)$$

$$\xrightarrow{*} M_{(23)}a_j{}^{o}(-\gamma)$$

where $i=j$ or $i\neq j$ depends on if atom i is involved in the permutation operation or not. Other simpler forms are available only when the $C_{3v}$ point group symmetry of the $NH_3$ subunit is introduced.

Since $a^o$'s and d's are both physical vectors, the general expression for them are similar; the transformation of $d_i$ under (23) and (23)* should be Expression (3.4.2.4) with all $a_i{}^o$'s replaced by $d_i$. Because there is no equilibrium geometric restrictions on d's as on $a^o$'s, d's generally do not map simply into $d_i(\pm\gamma)$. For example, for N atom,

$$d_N(+\gamma) \xrightarrow{(23)} M_{(23)}d_N(+\gamma)$$

$$\xrightarrow{*} N_{s*}M_{(23)}d_N(+\gamma) = M_{(23)}d_N(-\gamma),$$

and for H2,

$$d_2(+\gamma) \xrightarrow{(23)} M_{(23)}d_3(+\gamma) \xrightarrow{*} M_{(23)}d_3(-\gamma).$$

The effects of the (23) and (23)* operation on $R_i$ (i=N, 1, 2, 3) can then be summarized as follows:

$$R_N \xrightarrow{(23)} R_{cm} + S_d{}^{-1}[(m_{Ar}/M)Rk]$$
$$+ [S_s{}^{-1}M_{(23)}{}^{-1}][a_N{}^o(-\gamma) + M_{(23)}d_N(+\gamma)]$$
$$= \text{original } R_N,$$

$$R_1 \xrightarrow{(23)} R_{cm} + S_d{}^{-1}[(m_{Ar}/M)Rk]$$
$$+ [S_s{}^{-1}M_{(23)}{}^{-1}][a_1{}^o(-\gamma) + M_{(23)}d_1(+\gamma)]$$
$$= \text{original } R_1,$$

$$R_2 \xrightarrow{(23)} R_{cm} + S_d^{-1}[(m_{Ar}/M)Rk]$$
$$+ [S_s^{-1}M_{(23)}^{-1}][M_{(23)}a_3^{\,o}(+\gamma) + M_{(23)}d_3(+\gamma)]$$
$$= \text{original } R_3,$$

$$R_3 \xrightarrow{(23)} \text{original } R_2$$

(Same expression as that for $R_2$ under (23), but with subscripts 2, 3 switched),

$$R_N \xrightarrow{(23)*} -R_{cm} + [S_d^{-1}(-N_d^{-1})][N_d(m_{Ar}/M)Rk]$$
$$+ [S_s^{-1}M_{(23)}^{-1}(-N_{s*}^{-1})][a_N^{\,o}(+\gamma) + M_{(23)}d_N(-\gamma)]$$
$$= -R_{cm} - S_d^{-1}(m_{Ar}/M)Rk$$
$$- S_s^{-1}M_{(23)}^{-1}N_{s*}^{-1}[N_{s*}M_{(23)}(a_N^{\,o}(+\gamma) + d_N(+\gamma)]$$
$$= -(\text{original } R_N),$$

$$R_1 \xrightarrow{(23)*} -(\text{original } R_1)$$

(same expressions as those for $R_N$ under (23)*, but with subscript N replaced with 1),

$$R_2 \xrightarrow{(23)*} -R_{cm} + [S_d^{-1}(-N_d^{-1})][N_d(m_{Ar}/M)Rk]$$
$$+ [S_s^{-1}M_{(23)}^{-1}(-N_{s*}^{-1})][M_{(23)}a_3^{\,o}(-\gamma)$$
$$+ M_{(23)}d_3(-\gamma)]$$
$$= -R_{cm} - S_d^{-1}(m_{Ar}/M)Rk$$
$$- S_s^{-1}M_{(23)}^{-1}N_{s*}^{-1}[N_{s*}M_{(23)}(a_3^{\,o}(+\gamma) + d_3(+\gamma)]$$
$$= -(\text{original } R_3),$$

$$R_3 \xrightarrow{(23)*} -(\text{original } R_2)$$

(same expressions as those for $R_2$ under (23)*, but with subscripts 2, 3 switched).

The effects of the (13), (13)*, (12), and (12)* operation on $R_i$ (i=N, 1, 2, 3) can be derived with the same scheme. The proper rotation matrices, $M_{(13)}$ and $M_{(12)}$, are given in Table 3.4.3-1. Due to the fact that their rotation axes are not collinear with any Cartesian coordinate axis of the $NH_3$ subunit-fixed system as in the case of $M_{(23)}$, both of them are nondiagonal. (See Figure 3.4.2.4-2 for the cases of (13) and (13)*.) However, they are symmetric, and therefore, like $M_{(23)}$, can commute with $N_{s*}$ (diagonal).

### 3.4.2.5 Effects of the (123) and (123)* Class Operations on $R_i$ (i=N, 1, 2, 3) (Figure 3.4.2.5)

The individual equivalent proper rotations for the pseudo-diatomic frame under the (123) cyclic permutation and the * parity inversion can be expressed as

$$S^{-1}(\pi/2,\theta_d,\phi_d) \xrightarrow[{[R^o]}]{(123)} S_d^{-1} \xrightarrow[{[R_y^{\pi}]}]{*} S_d^{-1}(-N_d^{-1}).$$

Similarly, those for the $NH_3$ subunit-fixed coordinate system are

$$S^{-1}(\chi_s,\theta_s,\phi_s) \xrightarrow[{[R_{zs}^{(2/3)\pi}]}]{(123)} S_s^{-1}M^{-1}_{(123)}$$

$$\xrightarrow[{[R_{zs}^{\pi}]}]{*} S_s^{-1}M^{-1}_{(123)}(-N_{s*}^{-1}),$$

where

$$M_{(123)} = S((2/3)\pi,0,0) = \begin{bmatrix} -1/2 & +\sqrt{3}/2 & 0 \\ -\sqrt{3}/2 & -1/2 & 0 \\ 0 & 0 & +1 \end{bmatrix}.$$

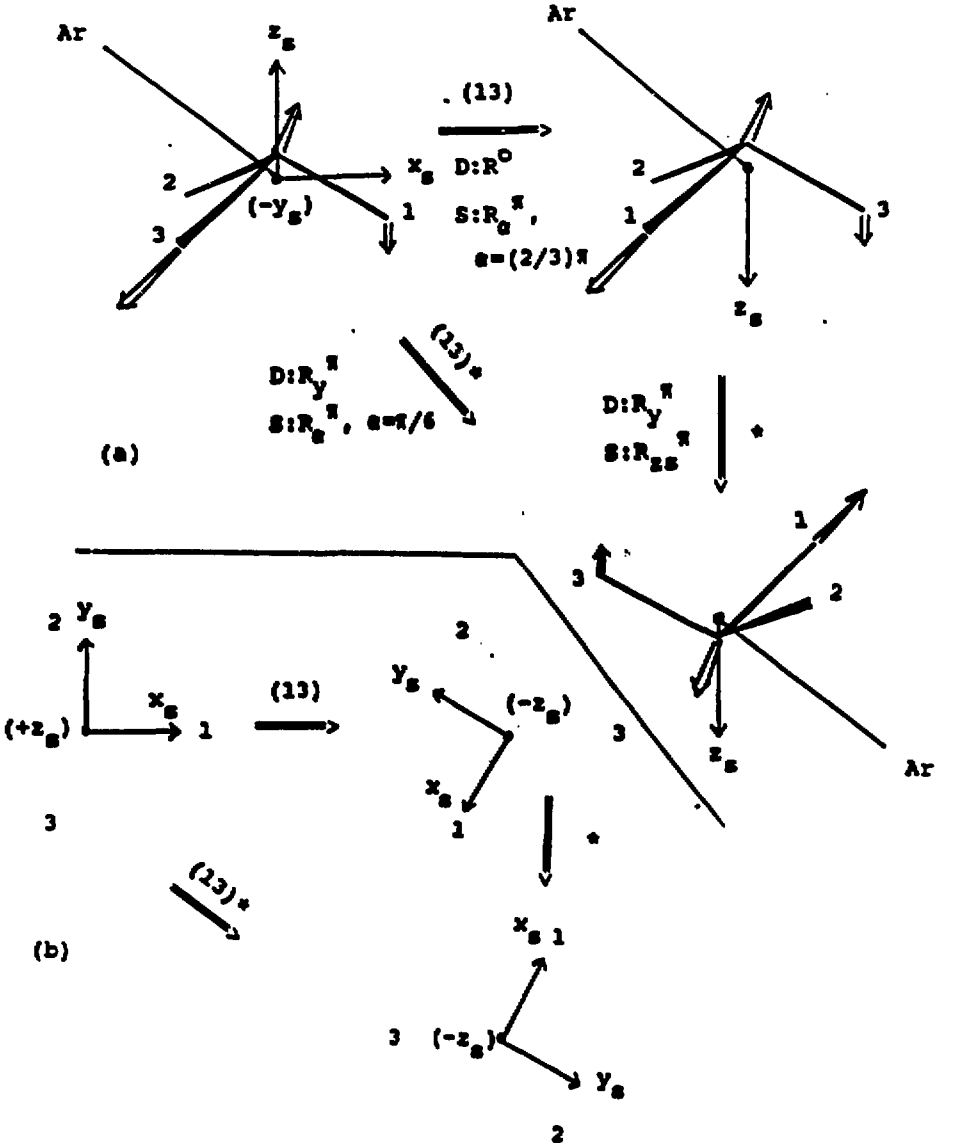


Figure 3.4.2.4-2
(a) Effect of the (13) and (13)* operation on $R_i$ (i= N, 1, 2, 3).
(D: pseudo-diatomic. S: subunit.)
(b) Top view of the $NH_3$ subunits in (a).

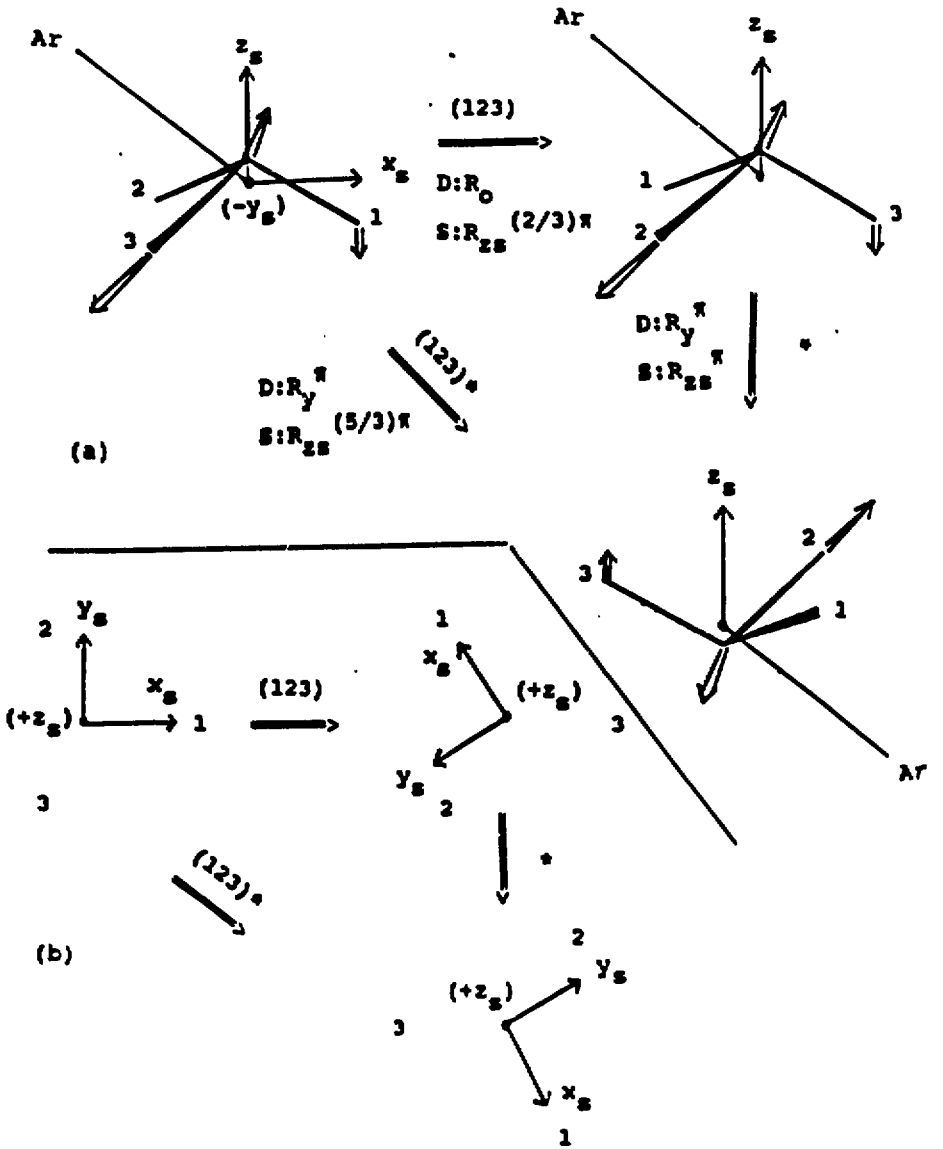


Figure 3.4.2.5
(a) Effect of the (123) and (123)* operation on $R_i$ (i= N, 1, 2, 3).
(D: pseudo-diatomic. S: subunit.)
(b) Top view of the $NH_3$ subunits in (a).

The effects of the (123) and (123)* operation on $R_i$ (i=N, 1, 2, 3) are summarized as follows:

$$R_N \xrightarrow{(123)} R_{cm} + S_d^{-1}[(m_{Ar}/M)Rk] + S_s^{-1}M_{(123)}^{-1}[a_N^{\circ}(+\gamma) + M_{(123)}d_N(+\gamma)]$$
$$= \text{original } R_N;$$

$$R_1 \xrightarrow{(123)} R_{cm} + S_d^{-1}[(m_{Ar}/M)Rk] + S_s^{-1}M_{(123)}^{-1}[M_{(123)}a_2^{\circ}(+\gamma) + M_{(123)}d_2(+\gamma)]$$
$$= \text{original } R_2;$$

$$R_2 \xrightarrow{(123)} \text{original } R_3$$

(same expression as for $R_1$ under (123), but with subscript 1 replaced by 2, 2 by 3);

similar to $R_2$ under (123),

$$R_3 \xrightarrow{(123)} \text{original } R_1;$$

$$R_N \xrightarrow{(123)*} -R_{cm} + [S_d^{-1}(-N_d^{-1})][N_d(m_{Ar}/M)Rk] + [S_s^{-1}M_{(123)}^{-1}(-N_{s*}^{-1})][a_N^{\circ}(-\gamma) + N_{s*}M_{(123)}d_N(+\gamma)]$$
$$= -(\text{original } R_N);$$

$$R_1 \xrightarrow{(123)*} -R_{cm} + [S_d^{-1}(-N_d^{-1})][N_d(m_{Ar}/M)Rk] + [S_s^{-1}M_{(123)}^{-1}(-N_{s*}^{-1})][N_{s*}M_{(123)}a_2^{\circ}(+\gamma) + N_{s*}M_{(123)}d_2(+\gamma)]$$
$$= -(\text{original } R_2);$$

$R_2 \xrightarrow{(123)*} -(\text{original } R_3)$ ·

(same expression as for $R_1$ under (123)*, but with subscript 1 replaced by 2, 2 by 3);

similar to $R_2$ under (123)*,

$R_3 \xrightarrow{(123)*} -(\text{original } R_1)$.

The effects of the (132) and (132)* operation on $R_i$, (i=N, 1, 2, 3) can be obtained similarly.

### 3.4.3 Summary of Coordinate Transformations

The equivalent proper rotation matrices for all the PI operations are listed in Table 3.4.3-1. The equivalent rotations, the corresponding transformations of the Eulerian angles and the $NH_3$ inversion coordinate are listed in Table 3.4.3-2. It is noted that there are two sets of Eulerian angles, one for the pseudo-diatomic frame, one for the $NH_3$ subunit; they are the same as those for the diatomic system and for the unperturbed $NH_3$ monomer, respectively.

The equivalent motions (or motion) for each PI operation, shown in Table 3.4.3-3, can be obtained unambiguously from Table 3.4.3-2. Basically, all PI operations (with and without *), except for the identity operation E, involve the $NH_3$ internal rotation. The pair permutation (with or without *) causes an internal rotation along an axis normal to the $C_3$ axis, the cyclic permutation (with or without *) causes such a rotation along the $C_3$ axis. The end-over-end

Table 3.4.3-1
The equivalent proper rotation matrices for all the PI operations of the $D_{3h}(M)$ group for Ar-$NH_3$.

$$(-N_d) = S(\pi,\pi,\pi)^{a} = \begin{bmatrix} -1 & 0 & 0 \\ 0 & +1 & 0 \\ 0 & 0 & -1 \end{bmatrix}$$

$$M_E = S(0,0,0) = \begin{bmatrix} +1 & 0 & 0 \\ 0 & +1 & 0 \\ 0 & 0 & +1 \end{bmatrix}$$

$$M_{(23)} = S(0,\pi,\pi) = \begin{bmatrix} +1 & 0 & 0 \\ 0 & -1 & 0 \\ 0 & 0 & -1 \end{bmatrix}$$

$$M_{(13)} = S((2/3)\pi,\pi,\pi) = \begin{bmatrix} -1/2 & -\sqrt{3}/2 & 0 \\ -\sqrt{3}/2 & +1/2 & 0 \\ 0 & 0 & -1 \end{bmatrix}$$

$$M_{(12)} = S((4/3)\pi,\pi,\pi) = \begin{bmatrix} -1/2 & +\sqrt{3}/2 & 0 \\ +\sqrt{3}/2 & +1/2 & 0 \\ 0 & 0 & -1 \end{bmatrix}$$

$$M_{(123)} = S((2/3)\pi,0,0) = \begin{bmatrix} -1/2 & +\sqrt{3}/2 & 0 \\ -\sqrt{3}/2 & -1/2 & 0 \\ 0 & 0 & +1 \end{bmatrix}$$

$$M_{(132)} = S((4/3)\pi,0,0) = \begin{bmatrix} -1/2 & -\sqrt{3}/2 & 0 \\ +\sqrt{3}/2 & -1/2 & 0 \\ 0 & 0 & +1 \end{bmatrix}$$

[a]The rotation matrix S follows the convention of Wilson, Decius and Cross [29]. Its variables are expressed in the format as $S(\chi,\theta,\phi)$.

Table 3.4.3-1 (continued)

$$M_{E*} = (-N_{s*})M_E = S(\pi,0,0)S(0,0,0) = S(\pi,0,0) = \begin{bmatrix} -1 & 0 & 0 \\ 0 & -1 & 0 \\ 0 & 0 & +1 \end{bmatrix}$$

$$M_{(23)*} = (-N_{s*})M_{(23)} = S(\pi,0,0)S(0,\pi,\pi) = S(\pi,\pi,\pi)$$

$$= \begin{bmatrix} -1 & 0 & 0 \\ 0 & +1 & 0 \\ 0 & 0 & -1 \end{bmatrix}$$

$$M_{(13)*} = (-N_{s*})M_{(13)} = S(\pi,0,0)S((2/3)\pi,\pi,\pi) = S((5/3)\pi,\pi,\pi)$$

$$= \begin{bmatrix} +1/2 & +\sqrt{3}/2 & 0 \\ +\sqrt{3}/2 & -1/2 & 0 \\ 0 & 0 & -1 \end{bmatrix}$$

$$M_{(12)*} = (-N_{s*})M_{(12)} = S(\pi,0,0)S((4/3)\pi,\pi,\pi) = S(\pi/3,\pi,\pi)$$

$$= \begin{bmatrix} +1/2 & -\sqrt{3}/2 & 0 \\ -\sqrt{3}/2 & -1/2 & 0 \\ 0 & 0 & -1 \end{bmatrix}$$

$$M_{(123)*} = (-N_{s*})M_{(123)} = S(\pi,0,0)S((2/3)\pi,0,0) = S((5/3)\pi,0,0)$$

$$= \begin{bmatrix} +1/2 & -\sqrt{3}/2 & 0 \\ +\sqrt{3}/2 & +1/2 & 0 \\ 0 & 0 & +1 \end{bmatrix}$$

$$M_{(132)*} = (-N_{s*})M_{(132)} = S(\pi,0,0)S((4/3)\pi,0,0) = S(\pi/3,0,0)$$

$$= \begin{bmatrix} +1/2 & +\sqrt{3}/2 & 0 \\ -\sqrt{3}/2 & +1/2 & 0 \\ 0 & 0 & +1 \end{bmatrix}$$

Table 3.4.3-2
The equivalent rotations, the explicit transformations of the Eulerian angles and the $NH_3$ inversion coordinate for Ar-$NH_3$ under the $D_{3h}(M)$ group operations.

| PI Op. | E | (23) | (13) | (12) | (123) | (132) |
|---|---|---|---|---|---|---|
| Frame Rot. | $R^o$ | $R^o$ | $R^o$ | $R^o$ | $R^o$ | $R^o$ |
| New | | | | | | |
| $\chi_d$ | $\pi/2$ | $\pi/2$ | $\pi/2$ | $\pi/2$ | $\pi/2$ | $\pi/2$ |
| $\theta_d$ | $\theta_d$ | $\theta_d$ | $\theta_d$ | $\theta_d$ | $\theta_d$ | $\theta_d$ |
| $\phi_d$ | $\phi_d$ | $\phi_d$ | $\phi_d$ | $\phi_d$ | $\phi_d$ | $\phi_d$ |
| $NH_3$ rot. | $R^o$ | $R_{xs}^{\pi}$ | $R_{(2/3)\pi}^{\pi}$ | $R_{\pi/3}^{\pi}$ | $R_{zs}^{(2/3)\pi}$ | $R_{zs}^{(4/3)\pi}$ |
| New | | | | | | |
| $\chi_s$ | $\chi_s$ | $-\chi_s$ | $-(4/3)\pi-\chi_s$ | $-(2/3)\pi-\chi_s$ | $(2/3)\pi+\chi_s$ | $(4/3)\pi+\chi_s$ |
| $\theta_s$ | $\theta_s$ | $\pi-\theta_s$ | $\pi-\theta_s$ | $\pi-\theta_s$ | $\theta_s$ | $\theta_s$ |
| $\phi_s$ | $\phi_s$ | $\pi+\phi_s$ | $\pi+\phi_s$ | $\pi+\phi_s$ | $\phi_s$ | $\phi_s$ |
| $NH_3$ Inv. | $\gamma$ | $-\gamma$ | $-\gamma$ | $-\gamma$ | $+\gamma$ | $+\gamma$ |

Table 3.4.3-2 (continued)

| PI Op. | E* | (23)* | (13)* | (12)* | (123)* | (132)* |
|---|---|---|---|---|---|---|
| Frame Rot. | $R_y^{\pi}$ | $R_y^{\pi}$ | $R_y^{\pi}$ | $R_y^{\pi}$ | $R_y^{\pi}$ | $R_y^{\pi}$ |
| New | | | | | | |
| $\chi_d$ | $\pi/2$ | $\pi/2$ | $\pi/2$ | $\pi/2$ | $\pi/2$ | $\pi/2$ |
| $\theta_d$ | $\pi-\theta_d$ | $\pi-\theta_d$ | $\pi-\theta_d$ | $\pi-\theta_d$ | $\pi-\theta_d$ | $\pi-\theta_d$ |
| $\phi_d$ | $\pi+\phi_d$ | $\pi+\phi_d$ | $\pi+\phi_d$ | $\pi+\phi_d$ | $\pi+\phi_d$ | $\pi+\phi_d$ |
| $NH_3$ Rot. | $R_{zs}^{\pi}$ | $R_{ys}^{\pi}$ | $R_{\pi/6}^{\pi}$ | $R_{(5/6)\pi}$ | $R_{zs}^{(5/3)\pi}$ | $R_{zs}^{\pi/3}$ |
| New | | | | | | |
| $\chi_s$ | $\pi+\chi_s$ | $\pi-\chi_s$ | $-(\pi/3)-\chi_s$ | $\pi/3-\chi_s$ | $(5/3)\pi+\chi_s$ | $\pi/3+\chi_s$ |
| $\theta_s$ | $\theta_s$ | $\pi-\theta_s$ | $\pi-\theta_s$ | $\pi-\theta_s$ | $\theta_s$ | $\theta_s$ |
| $\phi_s$ | $\phi_s$ | $\pi+\phi_s$ | $\pi+\phi_s$ | $\pi+\phi_s$ | $\phi_s$ | $\phi_s$ |
| $NH_3$ Inv. | $-\gamma$ | $+\gamma$ | $+\gamma$ | $+\gamma$ | $-\gamma$ | $-\gamma$ |

Table 3.4.3-3
The equivalent motion(s) for each class of the PI operations under the $D_{3h}(M)$ group for Ar-$NH_3$.

| Class in $D_{3h}(M)$ | Equivalent Motion(s) of Frame | $NH_3$ subunit | | |
|---|---|---|---|---|
| | e-o-e rotation | internal rotation | | inversion |
| | | normal to $C_3$ | along $C_3$ | |
| E | | | | |
| (123) | | | ×(2π/3)[a] | |
| (23) | | ×(π) | | × |
| E* | ×(π) | | ×(π) | × |
| (123)* | ×(π) | | ×(2π/3) | × |
| (23)* | ×(π) | ×(π) | | |

[a]The number in parenthesis is the rotational angle.

(abbreviated as e-o-e in the following) rotation is generated only by parity inversion *. Because both the * and the pair permutation are rotation sense-reversing, both can invert the $NH_3$ subunit. As a result, when both are involved in a PI operation, for example, (23)*, the inversion coordinate will remain intact.

### 3.4.4 Transformation Properties of the Rotational Basis Functions

By direct substitution of the Eulerian angle transformations of Table 3.4.3-2 in the standard symmetric top rotational basis functions $|J,m,k\rangle$ [32], the transformation properties of the rotational basis functions of the $NH_3$ internal rotor and the pseudo-diatomic frame can then be determined.

#### 3.4.4.1 $NH_3$ Subunit Symmetric Top Rotational Basis Functions

The transformation properties of the $NH_3$ subunit symmetric top rotational basis functions, $|j,m_j,k\rangle$, are summarized in Table 3.4.4.1-1. If we use $|j,m_j,k_c\rangle$ and $|j,m_j,-k_c\rangle$ as a basis, we can thus readily obtain the symmetry species for the $NH_3$ internal rotation as a function of $j$ and $k_c$ (Table 3.4.4.1-2). (Here, we reserve $K$ to represent the projection angular momentum along the a principal axis of the complex. Therefore, instead of the conventional symbol $K$, $k_c$ is used.)

#### 3.4.4.2 Pseudo-Diatomic Frame Rotational Basis Functions

Since any geometrically linear system can be treated as a special case of symmetric top with the symmetric top quantum number $k$ equal to

Table 3.4.4.1-1
The transformation properties of the symmetric top rotational basis functions of the $NH_3$ internal rotor.

| $D_{3h}(M)$ class | Equivalent rotation of $NH_3$ subunit | $\|j,m_j,k_c\rangle$[a] | $\|j,m_j,-k_c\rangle$[b] |
|---|---|---|---|
| E | $R^{o}$ | $\|j,m_j,k_c\rangle$ | $\|j,m_j,-k_c\rangle$ |
| (123) | $R_{zs}^{(2/3)\pi}$ | $\exp(ik_c(2/3)\pi)\|j,m_j,k_c\rangle$ | $\exp(ik_c(-2/3)\pi)\|j,m_j,-k_c\rangle$ |
| (23) | $R_{xs}^{\pi}$ | $(-1)^j\|j,m_j,-k_c\rangle$ | $(-1)^j\|j,m_j,k_c\rangle$ |
| E* | $R_{zs}^{\pi}$ | $(-1)^{k_c}\|j,m_j,k_c\rangle$ | $(-1)^{k_c}\|j,m_j,-k_c\rangle$ |
| (123)* | $R_{zs}^{(5/3)\pi}$ | $\exp(i(-2/3)\pi k_c)\|j,m_j,k_c\rangle$ | $\exp(i(2/3)\pi k_c)\|j,m_j,-k_c\rangle$ |
| (23)* | $R_{ys}^{\pi}$ | $(-1)^{j+k_c}\|j,m_j,-k_c\rangle$ | $(-1)^{j+k_c}\|j,m_j,k_c\rangle$ |

[a]The quantum numbers are arranged in the order of $|J,m,k\rangle$.

[b]$k_c$ is assumed to be nonnegative integer.

Table 3.4.4.1-2
The $NH_3$ subunit internal rotational symmetry species under $D_{3h}(M)$ as a function of $j$ and $k_c$ quantum number.

| $k_c$ | | Symmetry species under $D_{3h}(M)$ |
|---|---|---|
| 0 | even $j$ | $A_1'$ |
| | odd $j$ | $A_2'$ |
| 1, 6n±1[a] | | E" |
| 2, 6n±2 | | E' |
| 6n±3 | | $A_1'' \oplus A_2''$ |
| 6n | | $A_1' \oplus A_2'$ |

[a]n: positive integer.

zero, we use $|l,m_l,0>$ to represent the rotational basis function of the pseudo-diatomic frame. Here, $l$ and $m_l$ are the angular momentum and its corresponding projection with respect to the laboratory-fixed coordinate system. According to either Table 3.4.4.1-1 or -2, the resultant transformation properties are shown in Table 3.4.4.2. Because only the parity inversion * can affect the pseudo-diatomic Euler angles, the only transformation effect on the basis functions is a multiplicative factor $(-1)^l$, as expected for any diatomic molecule. This makes the pseudo-diatomic rotational basis function transform as totally symmetric $A_1'$ under the $D_{3h}(M)$ group for even $l$, and as $A_1''$ for odd $l$. In other words, the only symmetry effect of the pseudo-diatomic rotational basis function is parity reversal ($' \leftrightarrow ''$) for odd $l$.

### 3.4.5 Transformation Properties of the $NH_3$ Subunit Inversional Wave Functions

Free $NH_3$ is well known to have a double well potential along the inversion coordinate. Due to the fact that the potential function is symmetric with respect to the origin of the inversional coordinate, $\gamma$, all inversional wave functions with even $v_i$ ($NH_3$ inversional quantum number) are symmetric, i.e. $|v_i(-\gamma)>=+|v_i(+\gamma)>$, and functions with odd $v_i$ are antisymmetric, i.e. $|v_i(-\gamma)>=-|v_i(+\gamma)>$. In other words, the molecular symmetry group, $D_{3h}(M)$, of Ar-$NH_3$ has no effect on the inversional wave functions with even $v_i$. This makes the even $v_i$ functions have $A_1'$ symmetry. On the other hand, the odd $v_i$ wave functions all transform as $\gamma$ which, according to the transformation

Table 3.4.4.2
The transformation properties of the rotational basis functions of the pseudo-diatomic frame.

| $D_{3h}(M)$ class | Equivalent rotation of frame | $\|l,m_l,0\rangle$[a] |
|---|---|---|
| E | $R^0$ | $\|l,m_l,0\rangle$ |
| (123) | $R^0$ | $\|l,m_l,0\rangle$ |
| (23) | $R^0$ | $\|l,m_l,0\rangle$ |
| E* | $R_y^{\pi}$ | $(-1)^l\|l,m_l,0\rangle$ |
| (123)* | $R_y^{\pi}$ | $(-1)^l\|l,m_l,0\rangle$ |
| (23)* | $R_y^{\pi}$ | $(-1)^l\|l,m_l,0\rangle$ |

[a]The quantum numbers are arranged in the order of $|J,m,k\rangle$. $l$ and $m_l$ are the angular momentum and its projection of the pseudo-diatomic frame with respect to the laboratory-fixed coordinate system, and $k$ is assumed to be zero as required for any linear system.

properties of $\gamma$, shown in Table 3.4.3-2, transforms as $A_2''$.

## 3.5 Zero-Order Energy for the Free Internal Rotor Limit

In order to provide the basis for the construction of the zero-order energy level diagram, the kinetic energy expression will be derived in detail, and the interactions among different kinetic motions through the intermolecular potential (the ultimate goal and a principal unknown) will also be discussed qualitatively.

### 3.5.1 Derivation of the Kinetic Energy Expression

If we assume that all the atomic mass $m_i$, including electron(s) and nucleus, is located at each nucleus (Assumption 1), then the kinetic energy $T_o$, can be expressed as

$$2T_o = \sum_i m_i \dot{R}_i^t \dot{R}_i \qquad (3.5.1\text{-}1)$$

where the summation is taken over all the atoms in the complex (i=Ar, N, 1, 2, 3). Since (1) we are concerned only with the ground vibronic state and the first inversional state ($v_i$=1 or $v_2$=0$^-$ [33]) of the $NH_3$ subunit and (2) the large amplitude inversion displacements are already inherent in $a_i^o(\gamma)$, the displacement vectors $d_i(\gamma)$, which describe all the *non*inversional vibrations, can be eliminated in the following calculation (Assumption 2). But it is remembered that $|a_i^o(\gamma)|$ is dependent on $\gamma$, and therefore, the N-H bond length is still allowed to stretch during the $NH_3$ inversional motion. However, this is the stretching involved in the definition of the equilibrium

position $a_i^o(\gamma)$, and should not be mixed up with the N-H stretching vibration, accounted for by $d_i(\gamma)$. In other words, Equation (3.4.1-2) is simplified to be

$$R_{i\neq Ar} = R_{cm} + S_d^{-1}[(m_{Ar}/M)Rk] + S_s^{-1}a_i^o(\gamma). \qquad (3.5.1\text{-}2)$$

Substituting the equations (3.4.1-1) and (3.5.1-2) for the position vectors $R_i$'s with respect to the laboratory-fixed coordinate system, we can rewrite $2T_o$ as

$$\begin{aligned}
2T_o = & \sum_i m_i \dot{R}_{cm}{}^t \dot{R}_{cm} && \text{(part 1)}\\
& + [\mu_d R^2(\dot{S}_d^{-1}k)^t(\dot{S}_d^{-1}k) + 2\mu_d R\dot{R}(\dot{S}_d^{-1}k)^t(S_d^{-1}k) \\
& \qquad + \mu_d \dot{R}^2(S_d^{-1}k)^t(S_d^{-1}k)] && \text{(part 2)}\\
& + \sum_j m_j[\dot{S}_s^{-1}a_j^o(\gamma) + S_s^{-1}\dot{a}_j^o(\gamma)]^t[\dot{S}_s^{-1}a_j^o(\gamma) \\
& \qquad + S_s^{-1}\dot{a}_j^o(\gamma)] && \text{(part 3)}\\
& + 2\sum_j m_j[\dot{S}_s^{-1}a_j^o(\gamma) + S_s^{-1}\dot{a}_j^o(\gamma)]^t[\dot{R}_{cm} \\
& \qquad + (m_{Ar}/M)R\dot{S}_d^{-1}k + (m_{Ar}/M)\dot{R}S_d^{-1}k] && \text{(part 4)}\\
& && (3.5.1\text{-}3)
\end{aligned}$$

where the summation over i is taken for all the atoms in the complex, the two summations over j are taken over for the atoms in the $NH_3$ subunit. And $\mu_d$ is defined to be $m_{Ar}m_s/M$, the reduced mass of the pseudo-diatomic frame. (Since the time derivative ($\dot{}$) operation commutes with the transpose and the inverse operations, the symbols used in the equation do not take care of the order of operations among

them.)

The expression of $2T_o$ is arranged into four parts. With the use of the center of mass conditions for the $NH_3$ subunit, i.e.

$$\sum_j m_j a_j^{\,o}(\gamma) = 0$$

and consequently

$$\sum_j m_j \dot{a}_j^{\,o}(\gamma) = 0.$$

Part 4 thus vanishes. Part 1 corresponds to the kinetic energy of the center of mass of the Ar-$NH_3$ complex.

Part 2 corresponds to the internal kinetic energy of the pseudo-diatomic frame. This becomes obvious when Part 2 is abbreviated as

$$\mu_d[R\dot{S}_d^{-1}k + \dot{R}S_d^{-1}k]^2$$

or

$$\mu_d[d(RS_d^{-1}k)/dt]^2.$$

Because $(S_d^{-1}k)$ must be perpendicular to its tangent velocity, $(\dot{S}_d^{-1}k)$, due to the rotation, it is noted that

$$(\dot{S}_d^{-1}k)^t(S_d^{-1}k) = 0$$

and therefore the second term of Part 2 vanishes. On the other hand, $(S_d^{-1}k)^t(S_d^{-1}k)$ in the third term of this part is equal to one. This can be understood by thinking of it as the inner product between the rotated unit vector, $(S_d^{-1}k)$, and itself. This can also be verified

algebraically as follows:

$$
\begin{aligned}
(S_d^{-1}k)^t(S_d^{-1}k) &= k^t(S_d^{-1})^t(S_d^{-1}k) \\
&= k^t S_d(S_d^{-1}k) \qquad (\because S_d \text{ is orthonormal.}) \\
&= k^t k \\
&= 1.
\end{aligned}
$$

Consequently, the internal kinetic energy of the frame is just a sum of two terms:

(1) the dimeric e-o-e rotational energy, $\mu_d R^2(\dot{S}_d^{-1}k)^t(\dot{S}_d^{-1}k)$, and

(2) the dimeric stretching energy, $\mu_d \dot{R}^2$.

Part 3 of the $2T_o$ expression can be rewritten as

$$\sum_j m_j[d(S_s^{-1}a_j^o(\gamma))/dt]^t[d(S_s^{-1}a_j^o(\gamma))/dt].$$

Since in (1) the summation is taken over the atoms in the $NH_3$ subunit, and (2) $[d(S_s^{-1}a_j^o(\gamma))/dt]$ is the velocity of atom j with respect to the $NH_3$ subunit-fixed coordinate system, it is recognized that Part 3 corresponds to the $NH_3$ internal kinetic energy. To elucidate its physical meaning, Part 3 is further expanded as

$$
\begin{aligned}
&\sum_j m_j[\dot{S}_s^{-1}a_j^o(\gamma) + S_s^{-1}\dot{a}_j^o(\gamma)]^t[\dot{S}_s^{-1}a_j^o(\gamma) + S_s^{-1}\dot{a}_j^o(\gamma)] \\
&= \sum_j m_j[(a_j^o(\gamma))^t(\dot{S}_s^{-1})^t + (\dot{a}_j^o(\gamma))^t(S_s^{-1})^t] \\
&\qquad [\dot{S}_s^{-1}a_j^o(\gamma) + S_s^{-1}\dot{a}_j^o(\gamma)]
\end{aligned}
$$

$$= \sum_j m_j (a_j{}^o(\gamma))^t (\dot{S}_s{}^{-1})^t \dot{S}_s{}^{-1} a_j{}^o(\gamma)$$

$$+ \sum_j m_j (\dot{a}_j{}^o(\gamma))^t (S_s{}^{-1})^t S_s{}^{-1} \dot{a}_j{}^o(\gamma)$$

$$+ \sum_j m_j (a_j{}^o(\gamma))^t (\dot{S}_s{}^{-1})^t S_s{}^{-1} \dot{a}_j{}^o(\gamma)$$

$$+ \sum_j m_j (\dot{a}_j{}^o(\gamma))^t (S_s{}^{-1})^t \dot{S}_s{}^{-1} a_j{}^o(\gamma). \qquad (3.5.1\text{-}4)$$

Each term will be examined in the following.

By inserting the matrix product $S_s{}^t S_s$, which equals the identity matrix, in the first term of the right hand side of Equation (3.5.1-4), this term becomes

$$\sum_j m_j (a_j{}^o(\gamma))^t (\dot{S}_s{}^{-1})^t \dot{S}_s{}^{-1} a_j{}^o(\gamma)$$

$$= \sum_j m_j [(a_j{}^o(\gamma))^t (\dot{S}_s{}^{-1})^t S_s{}^t][S_s \dot{S}_s{}^{-1} a_j{}^o(\gamma)]$$

$$= \sum_j m_j [S_s \dot{S}_s{}^{-1} a_j{}^o(\gamma)]^t [S_s \dot{S}_s{}^{-1} a_j{}^o(\gamma)]. \qquad (3.5.1\text{-}5)$$

Let us consider the physical significance of the column matrix $[S_s \dot{S}_s{}^{-1} a_j{}^o(\gamma)]$ in the above equation. (The following calculation, up to Equation (3.5.1-9) is in parallel with a treatment for rigid molecules given in Reference 33, p.31-32.) Since $S_s$ is orthonormal,

$$S_s S_s{}^t = E \text{ (identity matrix)}. \qquad (3.5.1\text{-}6)$$

If time derivatives are taken on both sides of Equation (3.5.1-6), it becomes

$$\dot{S}_s S_s^{\,t} + S_s \dot{S}_s^{\,t} = 0.$$

Therefore,

$$S_s \dot{S}_s^{\,t} = -\dot{S}_s S_s^{\,t}$$
$$= -(S_s \dot{S}_s^{\,t})^t.$$

In other words, the product matrix $S_s \dot{S}_s^{\,t}$ is antisymmetric, and can be written in the following form:

$$S_s \dot{S}_s^{\,t} = \begin{bmatrix} 0 & -\omega_{zs} & \omega_{ys} \\ \omega_{zs} & 0 & -\omega_{xs} \\ -\omega_{ys} & \omega_{xs} & 0 \end{bmatrix}. \qquad (3.5.1\text{-}7)$$

With the definition of the rotational matrix S, Equation 3.4.1-3, it follows from the above equation that

$$\omega_{xs} = \sin\chi_s \cdot \dot{\theta}_s - \sin\theta_s \cos\chi_s \cdot \dot{\phi}_s,$$

$$\omega_{ys} = \cos\chi_s \cdot \dot{\theta}_s + \sin\theta_s \sin\chi_s \cdot \dot{\phi}_s,$$

$$\omega_{zs} = \cos\theta_s \cdot \dot{\phi}_s + \dot{\chi}_s. \qquad (3.5.1\text{-}8)$$

Thus the $\omega_{xs}$, $\omega_{ys}$, $\omega_{zs}$ are recognized (according to Reference 29, p.281-2) to be the Cartesian components (with respect to the $NH_3$ subunit-fixed system) of the total angular velocity $\omega_s$ of the $NH_3$ subunit-fixed system. With Equations (3.5.1-7) and (3.5.1-8), it can be verified that

$$[S_s \dot{S}_s^{-1} a_j^{\,o}(\gamma)] = \omega_s \times a_j^{\,o}(\gamma). \qquad (3.5.1\text{-}9)$$

$[S_s\dot{S}_s^{-1}a_j^{o}(\gamma)]$ is then known to be the velocity of atom j with respect to the laboratory-fixed system. Therefore, with the expression in Equation (3.5.1-5), the first term is realized to correspond to the rotation of the $NH_3$ subunit.

The second term of the right hand side of Equation (3.5.1-4) can also be simplified as

$$\sum_j m_j(\dot{a}_j^{o}(\gamma))^t(S_s^{-1})^t S_s^{-1}\dot{a}_j^{o}(\gamma)$$
$$= \sum_j m_j(\dot{a}_j^{o}(\gamma))^t(\dot{a}_j^{o}(\gamma)). \qquad (3.5.1\text{-}10)$$

The result indicates that this term corresponds to the $NH_3$ inversional motion. Since $C_{3v}$ symmetry is assumed for the $NH_3$ subunit (If the perturbation due to Ar is negligible. (Assumption 3)), all three $a_j^{o}(\gamma)$'s of the three H's are confined in the three $\sigma$ planes of $NH_3$, and $a_N^{o}(\gamma)$ is on the $C_3$ axis. Thus, with Assumptions 2 and 3, they are allowed to move only symmetrically and synchronously, as specified by j and the common variable $\gamma$. This is the reason why $(\dot{a}_j^{o}(\gamma))$ on the right hand side of Equation (3.5.1-10) can only be the inversional velocity.

Because the inner product is commutative, the last two terms in Equation (3.5.1-4) are equal to each other. We will consider only the third term, which can be rewritten as

$$\sum_j m_j(a_j^{o}(\gamma))^t(\dot{S}_s^{-1})^t S_s^{-1}\dot{a}_j^{o}(\gamma)$$
$$= \sum_j m_j[S_s\dot{S}_s^{-1}a_j^{o}(\gamma)]^t\dot{a}_j^{o}(\gamma)$$

$$= \sum_j m_j [\omega_s \times a_j^{\circ}(\gamma)]^t \dot{a}_j^{\circ}(\gamma) \qquad \text{(Equation (3.5.1-9) is used.)}$$

$$= \sum_j m_j [a_j^{\circ}(\gamma) \times \dot{a}_j^{\circ}(\gamma)]^t \omega_s .$$

When expanded more explicitly, the last expression becomes

$$m_N [a_N^{\circ}(\gamma) \times \dot{a}_N^{\circ}(\gamma)]^t \omega_s + m_H \sum_k [a_k^{\circ}(\gamma) \times \dot{a}_k^{\circ}(\gamma)]^t \omega_s$$

where the summation is taken over the three H's. Since $\dot{a}_N^{\circ}(\gamma)$ and $a_N^{\circ}(\gamma)$ are collinear with each other along the $C_3$ axis, their cross product and, therefore, the first term vanish. Due to the $C_3$ symmetry among the three H's, the vectorial summation in the second term becomes a null vector. This can be visualized by thinking that all three cross products, $[a_k^{\circ}(\gamma) \times \dot{a}_k^{\circ}(\gamma)]$, are on a plane perpendicular to the $C_3$ axis, and can be mapped into one another by the $C_3$ rotations. Thus the second term also vanishes.

As a result, in the total kinetic energy expression, there is no inner product between $[\dot{S}_s^{-1} a_j^{\circ}(\gamma)]$ and $[S_s^{-1} \dot{a}_j^{\circ}(\gamma)]$. Since these are the velocities due to the $NH_3$ internal rotation and inversion, respectively, it implies that under our assumptions there is *no* Coriolis coupling between the two motions. However, when the $NH_3$ subunit is partially deuterated and therefore loses its $C_{3v}$ symmetry, such a Coriolis coupling term will appear.

### 3.5.2 Summary of the Kinetic Expression

The assumptions used in the derivation of the total kinetic energy expression of the complex are summarized below:

(1) All the atomic mass, including electron(s) and nucleus, is concentrated at each respective nucleus.

(2) The $NH_3$ subunit can access only its ground vibronic state and the first inversional state ($v_i$=1 or $v_2$=$0^-$). The displacement vectors, $d_i(\gamma)$, are therefore not considered.

(3) The perturbation due to Ar is negligible. $C_{3v}$ symmetry is assumed for the equilibrium geometry of the $NH_3$ subunit.

Since we are not interested in the center of mass kinetic energy of the complex, the internal kinetic energy (T) defined as

$$2T = 2T_o - \sum_i m_i(\dot{R}_{cm})^t\dot{R}_{cm}$$

will be used in the subsequent discussions.

In summary, 2T can then be written as

$$2T = \mu_d\dot{R}^2 + \mu_d R^2(\dot{S}_d^{-1}k)^t(\dot{S}_d^{-1}k) + \sum_j m_j(a_j^o(\gamma))^t(\dot{S}_s^{-1})^t\dot{S}_s^{-1}a_j^o(\gamma) + \sum_j m_j(\dot{a}_j^o(\gamma))^t(\dot{a}_j^o(\gamma)). \quad (3.5.2)$$

The four terms, in the order of their appearance in the above expression, correspond to:

(1) dimeric stretching vibration (stretch),

(2) dimeric end-over-end rotation (e-o-e rot.),

(3) $NH_3$ subunit internal rotation (int. rot.), and

(4) $NH_3$ inversional motion (inv.).

### 3.5.3 Potential Energy

When not in the free internal rotor limit, the potential energy $V(R,\gamma,\chi_r,\theta_r)$ of the complex is a function of the dimeric stretching coordinate (R), $NH_3$ inversional coordinate ($\gamma$), and subunit relative orientation coordinates (Eulerian angles $\chi_r$, $\theta_r$, but not $\phi_r$). (See Figure 3.4.1-2.) Here, $\chi_r$, $\theta_r$, $\phi_r$ are defined by the following rotational matrix relation:

$$S(\chi_r,\theta_r,\phi_r) = S(\chi_s,\theta_s,\phi_s)\ S^{-1}(\pi/2,\theta_d,\phi_d). \qquad (3.5.3\text{-}1)$$

That the potential is a function of two, instead of three, Eulerian angles is due to the symmetry of the Ar atom with respect to the a-principal axis, connecting the Ar atom and the center of mass of the $NH_3$ subunit.

In the *free internal rotor* limit, the $NH_3$ subunit experiences an isotropic potential, which is not a function of the relative Eulerian angles ($\chi_r$ and $\theta_r$). (Assumption a) However, the isotropic potential still needs to be a function of R and $\gamma$ to maintain (1) the formation of the dimer and (2) the inversional vibration of the $NH_3$ subunit. In other words,

$$V(R,\gamma,\chi_r,\theta_r) \longrightarrow V_{fr}(R,\gamma), \qquad (3.5.3\text{-}2)$$

(in the free internal rotor limit)

When the corresponding frequencies of the dimeric stretching vibration and $NH_3$ inversion differ by at least an order of magnitude, an adiabatic approximation can be applied, and the zero-order $V_{fr}(R,\gamma)$ can further be separated into two parts, i.e.

$$V_{fr}(R,\gamma) \longrightarrow V_s^{\,o}(R) + V_i^{\,o}(\gamma) \qquad (3.5.3\text{-}3)$$

where $V_s^o(R)$ is the zero-order dimeric stretching potential and $V_i^o(\gamma)$ is the zero-order $NH_3$ double-well inversion potential. (Assumption b)

Since the predicted stretching frequency (approximately 35 $cm^{-1}$ [13]) and the inversion frequency (approximately 0.7 $cm^{-1}$) do differ by more than an order of magnitude, Expression (3.5.3-3) will be used to construct the zero-order energy level diagram.

### 3.5.4 Total Energy

Although there is no explicit cross term among the four motions in the kinetic expression (Equation (3.5.2)), they do share certain common variables, as summarized below:

(1) stretch : R,

(2) e-o-e rot.: R, $\theta_d$, $\phi_d$,

(3) int. rot. : $\chi_s$, $\theta_s$, (or $\theta_d$, $\phi_d$, $\chi_r$, $\theta_r$), $\gamma$,

(4) inv. : $\gamma$.

The introduction of the intermolecular potential $V(R,\gamma,\chi_r,\theta_r)$ will then couple these four motions together. For example, the dimeric stretching vibration and e-o-e rotation are directly coupled through the stretching coordinate (R), and similarly, the $NH_3$ internal rotation and inversion directly couple through the inversion coordinate ($\gamma$). It is noted that since the potential is not a function of $\theta_d$ and $\phi_d$, the e-o-e and $NH_3$ internal rotation are not directly coupled through any rotational coordinate, but rather *indirectly* through R and $\gamma$. In other words, the Coriolis coupling

between the e-o-e and $NH_3$ internal rotation, which makes $K_a$ no longer an exact good quantum number, results from the potential coupling through R and $\gamma$. (Here, $K_a$ is the conventional symbol for the projection magnitude of the total angular momentum J on the a principal axis of the complex.) Basically, the better the potential can be approximated by Equation (3.5.3-3), the better the $K_a$ quantum number is.

When the potential can be approximated by Equation (3.5.3-3), the stretching vibration and e-o-e rotation have a zero-order coupling through $V_s^{\circ}(R)$; on the other hand, the $NH_3$ internal rotation and $NH_3$ inversion through $V_i^{\circ}(\gamma)$. In this zero-order picture, the total energy (E) of the complex can then be organized as follows:

$$E \approx [T_{stretch}(R) + V_s^{\circ}(R) + T_{e\text{-}o\text{-}e}(R;\theta_d,\phi_d)] + [T_{int.rot.}(\theta_d,\phi_d;\chi_r,\theta_r;\gamma) + T_{inv.}(\gamma) + V_i^{\circ}(\gamma)] \qquad (3.5.4\text{-}1)$$

where the four T terms correspond to half of the four kinetic terms in Equation (3.5.2), respectively. It is noted that the last three terms correspond to the energy of free inverting-rotating $NH_3$.

Since the corresponding stretching vibration frequency is actually on the order of a few tens $cm^{-1}$, as opposed to the e-o-e rotational constant on the order of a few GHz, the coupling between the stretching vibration and e-o-e rotation through $V_s^{\circ}(R)$ should be small. ("Assumption" c) As a result, $T_{e\text{-}o\text{-}e}(R;\theta_d,\phi_d)$ can be approximated by $T_{e\text{-}o\text{-}e}(R_{av};\theta_d,\phi_d)$ $(=T'_{e\text{-}o\text{-}e}(\theta_d,\phi_d))$ with variable R replaced by its vibrationally averaged value $R_{av}$; the first two terms in Equation (3.5.4-1) can thus be grouped together and treated as the

dimeric stretching vibration energy ($E_{stretch}$). On the other hand, because the low lying rotation-inversion energy level distribution of the free $NH_3$ has been well known, there is no need to decouple the internal rotation from the inversion to obtain a zero-order energy level diagram. However, in order to facilitate the derivation of the symmetry species of the zero-order wave function, the variable $\gamma$ of $T_{int.rot.}$ will be replaced by its inversionally averaged value $\gamma_{av}$ (i.e. $T_{int.rot.}(\theta_d,\phi_d;\chi_r,\theta_r;\gamma)$ becomes $T_{int.rot.}(\theta_d,\phi_d;\chi_r,\theta_r;\gamma_{av})=T'_{int.rot.}(\chi_s,\theta_s,\phi_s=\phi_d)$) to indicate a decoupling between the internal rotation and the inversion. (Assumption (d)) Therefore, the sum of the last two terms will become the pure inversional energy ($E_{inv.}$). In other words, Equation (3.5.4-1) in this limit can be written as

$$E= E_{stretch}(R) + T'_{e\text{-}o\text{-}e}(\theta_d,\phi_d) + \\ + T'_{int.rot.}(\chi_s,\theta_s,\phi_s=\phi_d) + E_{inv.}(\gamma), \qquad (3.5.4\text{-}2)$$

which constitutes the construction basis of the free internal rotor limit zero-order picture. As a direct result, the zero-order wave function is therefore a product of those corresponding to these four motions.

Apart from the assumptions used in the derivation of the kinetic energy expression (summarized in Section 3.5.2), four other assumptions employed in reaching Equation (3.5.4-2) are summarized as follows:

(a) The $NH_3$ subunit is in the free internal rotor limit.

(b) The corresponding stretching vibration frequency is at least

an order of magnitude higher than the corresponding $NH_3$ inversion frequency.

(c) The corresponding stretching vibration frequency is at least an order of magnitude higher than the corresponding complex e-o-e rotation frequency.

(d) No coupling is assumed between the internal rotation and the inversion.

Here, assumptions (a)-(c) have supporting experimental evidence; however, assumption (d) is only an artifact. It is these assumptions or, equivalently, Equation (3.5.4-2) that we imply by "zero-order". The free internal rotor assumption alone does *not* fully account for "zero-order".

As an aside, the *isotropic* potential, generally expressed by Equation (3.5.3-2)), in *the free internal rotor limit* does not necessarily have its R and $\gamma$ coordinate well decoupled; it is the *ideal zero-order* potential, expressed by Equation (3.5.3-3), that can make $K_a$ an exact good quantum number.

## 3.6 The Unperturbed Case

### 3.6.1 Zero-Order Intermolecular Vibrational Level Diagram

From the microwave spectrum of the ground state [13-15], it was established that the complex is very close to the free rotor limit. This was deduced mainly from two observations: (1) inconsistent calculated values obtained for the polar angle ($\theta$) derived from the measured $\langle P_1(\cos\theta)\rangle$ and $\langle P_2(\cos\theta)\rangle$, respectively, (2) an extremely

long Ar-$NH_3$ bond distance (3.8723 Å), which is longer than any conceivable combination of vdW radii if the Ar atom is in one of the dihedral planes of the $NH_3$ subunit with two closer H's at equal distance. (To simplify the notation, $\phi_r$ defined in Section 3.5.3 will be replaced with $\phi$ from now on.) In order to provide the basic language for describing the nearly free internal rotor system and to facilitate the intermolecular vibrational assignment of the spectrum, the zero-order intermolecular vibrational energy level diagram for the complex is required.

Since the inversional motion of the $NH_3$ subunit has apparently been observed in the microwave spectrum of the ground intermolecular vibrational state of the complex [13-15], the molecular symmetry group required to describe the dynamics of the complex is $D_{3h}(M)$ (Appendix Table 1, character table), the group of the $NH_3$ monomer [32]. This is apparent either from the detailed discussion in Section 3.4 or simply by considering the fact that $D_{3h}(M)$ permutation inversion group is the maximum group (complete nuclear permutation inversion (CNPI) group) allowed in terms of its chemical formula, and none of its subgroups have an operation corresponding to an $NH_3$ inversional motion [32,33].

Based upon Equation (3.5.4-2), two main features of the zero-order picture are thus: (1) the total energy of the complex is given by the summation over the four different motions, (2) the zero-order wave function is just the product of the wave functions representing these four motions, which then clearly establishes the physical meaning of each zero-order energy state. This last result is used below to deduce the symmetry species under the $D_{3h}(M)$ group for

each zero-order state. Since the molecular symmetry group is employed, the symmetry species of any zero-order rovibronic wave function should be the same as that of the corresponding true wave function which the zero-order function can continuously evolve into.

The zero-order energy level diagram for the low lying intermolecular vibrational states constructed according to the above arguments is shown in Figure 3.6.1. It is arranged into four columns, each of which represents a set of the lowest internal rotational states of the $NH_3$ subunit with different combinations of the dimeric stretching and $NH_3$ inversional quantum number, denoted by $v_s$ and $v_i$, respectively. The internal rotational energy levels shown in each column are arranged in the conventional order for an oblate symmetric top, with levels grouped into stacks of different $k_c$ values [34]. Here, if $J$ is the angular momentum quantum number of the $NH_3$ subunit with respect to a space-fixed coordinate system, $k_c$ is the absolute value of the projection of the angular momentum j along the $C_3$ axis of $NH_3$. The relative heights among the four columns are determined by the associated stretching and inversion energies. In other words, column two ($(v_s;v_i)=(1;0)$) is higher than column one ($(v_s;v_i)=(0;0)$) by an energy corresponding to the dimeric stretching frequency, which has not been determined conclusively by experiment. Similarly, the two columns on the right, both with one additional quantum in the inversional mode, are replicate of columns one and two, but shifted upward by the $NH_3$ inversional frequency (about 24 GHz or 0.8 $cm^{-1}$ [35]).

Symmetry species of the $D_{3h}(M)$ group (Appendix Table 1, character

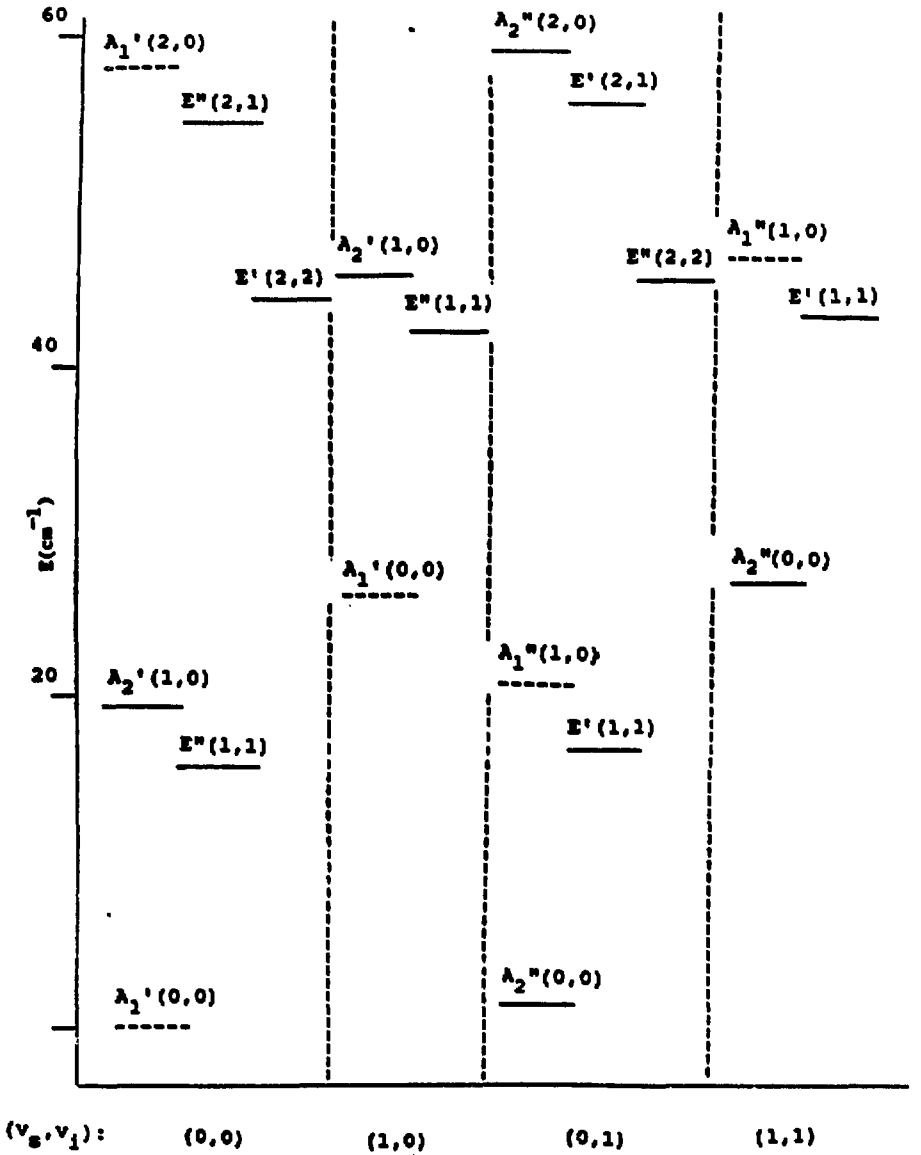


**Figure 3.6.1**
**Zero-order intermolecular vibrational energy level diagram for $Ar\text{-}NH_3$.**

Table 3.6.1
Smmetry species of the zero-order intermolecular vibrational states as a function of internal rotation and inversion quantum number.

| $k_c$ | | $v_i$ | |
|---|---|---|---|
| | | even | odd |
| 0 | even $j$ | $A_1'$ | $A_2''$ |
| | odd $j$ | $A_2'$ | $A_1''$ |
| 1, 6n±1[a] | | E" | E' |
| 2, 6n±2 | | E' | E" |
| 6n±3 | | $A_1'' \bullet A_2''$ | $A_2' \bullet A_1'$ |
| 6n | | $A_1' \bullet A_2'$ | $A_2'' \bullet A_1''$ |

[a]n: positive integer.

where $S_o$ represents the intermolecular *vibrational* symmetry species under the $D_{3h}(M)$ group, and $(v_s;v_i;j,k_c)$ are the dimeric stretching, subunit inversion, and subunit rotation quantum numbers as previously defined.

### 3.6.2 Rotational Energy Level Manifold of a Zero-Order Intermolecular Vibrational State

As a basic reference for the intermolecular vibrational band pattern expected for a dimer containing one *nearly* free internal *symmetric-top* rotor, we will first examine the general features of the rotational energy level manifolds of the zero-order intermolecular vibrational states.

In the free internal rotor limit, no coupling is assumed between the e-o-e rotation (l) and internal rotation (j). As a result, all zero-order intermolecular vibrational states have the same diatomic-like rotational energy level manifold, characterized by the same pseudo-diatomic rotational constant $(B+C)/2 \approx B$. Each rotational level of the manifold can thus be labelled unambiguously with the corresponding e-o-e rotational quantum number ($l$) as in Figure 3.6.2. In other words, $j$ is used to label the intermolecular *vibrational* state, or the corresponding whole rotational manifold, whereas $l$ is used to label the levels within the manifold.

To determine the symmetry of the total *rovibrational* wave function for each level of the rotational manifold, we multiply the intermolecular vibrational state symmetry (shown in Figure 3.6.1) by that of the e-o-e pseudo-diatomic rotational wave function, i.e.

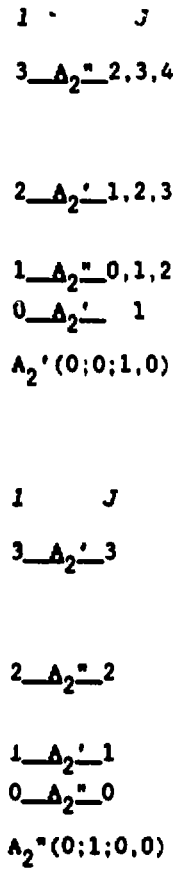


Figure 3.6.2
Schematic rovibrational level manifolds for the $A_2'(0;0;1,0)$ (upper) and $A_2''(0;1;0,0)$ state (lower).

$A_1'$ for even $l$ rovibrational levels,

$A_1''$ for odd $l$ rovibrational levels,

according to Section 3.4.4.2. In terms of symmetry species notation, the only effect of the e-o-e rotational wave function is thus a change of the superscript (' ⟷ ") on the intermolecular *vibrational* state symmetry only for all odd $l$ levels. In other words, both even and odd $l$ levels have the same symmetry species as that of the intermolecular vibrational state, except that the odd $l$ levels are of opposite parity.

Since (a) the total angular momentum $J$ (J=j+l) is a good quantum number even in the perturbed cases, where neither $l$ nor $j$ is, and (b) the usual $\Delta J$ optical dipole selection rules and the $\Delta J=0$ intermolecular interaction selection rule (see Section 3.6.3) should always hold, it is important to label each rotational level also with all possible associated $J$ values, such as in Figure 3.6.2. In addition to the degeneracy described by the intermolecular vibrational symmetry species (A, E, etc.), in terms of the number of associated $J$ values, all nonzero $l$ e-o-e rotational levels of any nonzero $j$ intermolecular *vibrational* state are *accidentally degenerate*, with $2l+1$ $J$-degeneracy when $l \leq j$ (i.e. $J=|j-l|$, $|j-l+1|$, $|j-l+2|$, $\cdots$, $j+l$) or $2j+1$ $J$-degeneracy as $l \geq j$. Here, the "degeneracy" includes only those which are to be broken by the anisotropic intermolecular potential, but *not* the spatial degeneracy of each $J$, which is not of concern. $k_c$ of the intermolecular vibrational state is not involved in this addition scheme because it is only an *internal* quantum number

of the $NH_3$ subunit. Consequently, in the free rotor limit, the $J$ labelling of the rotational manifold is determined only by $l$ and by the $j$ value of the intermolecular vibrational state, and is independent of both intermolecular vibrational state symmetry species and $k_c$.

In the present context, "accidentally degenerate" implies that the degeneracy of each zero-order e-o-e rotational level labelled with $l$ can be broken by the intermolecular potential anisotropy without affecting its original symmetry. Since, under one molecular symmetry group, an irreducible representation can never be a linear combination of irreducible representations of different symmetry species, the resultant *non*zero-order states must retain the same symmetry as that of their common original zero-order *level*. For example, a triply $J$-degenerate zero-order E", $l$=1 rotational level of a $j$=1 intermolecular vibrational state can split into three E" rotational states corresponding to $J$=0, 1, 2. In fact, this splitting should actually be considered as separate *shiftings* of three distinct E" states, instead of a *splitting* of a single triply degenerate E" state. This is consistent with the requirement that *no splitting*, but only *shifting* may occur for the zero-order states [32], when the proper molecular symmetry group is used. If there is no accidental degeneracy but splitting does occur, then a higher order group must be used. However, since in the present case the maximum group, i.e. the CNPI group, is in use, the $J$-degeneracy of the zero-order state must, therefore, be accidental.

It should also be noted that a given $J$=0 rovibrational state does

not necessarily have the same parity as its intermolecular vibrational state. In the j-l coupling scheme, the $J$=0 rotational state obviously correlates to $l$=$j$. Therefore, whether the $J$=0 rovibrational state has the same or opposite parity as the intermolecular vibrational symmetry species depends on whether the $j$ of the intermolecular vibrational state is even or odd. (Of course, the $l$=0 rovibrational state always has the same symmetry, including parity, as the corresponding intermolecular vibrational state.)

### 3.6.3 Selection Rules

#### 3.6.3.1 Optical Selection Rules

The optical selection rules under $D_{3h}(M)$ can be derived directly from its character table (Appendix Table 1) [32]. Since the $A_1''$ symmetry associated with the electric dipole operator corresponds purely to a parity switch, by considering the symmetry product for the transition moment, the rules can readily be "visualized" from the character table as follows:

$$A_1''(0) \leftrightarrow A_1'(0),$$
$$A_2''(12) \leftrightarrow A_2'(12),$$
$$E''(6) \leftrightarrow E'(6).$$

These imply that only the rovibrational states with *the same symmetry but* opposite parities can be connected by a single-photon transition. It is noted that the parity selection rule

$$' \leftrightarrow ''$$

is inherent in the above relations. Here, the numbers in parentheses are the proton nuclear spin statistical weights (Fermion statistics), indicating that all states of $A_1$ symmetry are forbidden, whatever the associated parity is. Of course, these rovibronic selection rules should always be used along with the single-photon selection rule, $\Delta J=0, \pm 1$, which is a requirement under the spatial three-dimensional pure rotation group [32], K(spatial), an intrinsic molecular symmetry group to any isolated molecule when no nuclear spin I is considered in the Hamiltonian. (It is emphasized that both $D_{3h}(M)$ and K(spatial) are *exact* molecular symmetry groups with respect to the *rovibronic* Hamiltonian, and should be distinguished from any *near* symmetry group, such as the $D_{3h}$ point group and molecular three-dimensional pure rotation group K(mol). [32])

According to the parity alternation feature of the rovibrational levels associated with each increment of *l* by one within a zero-order intermolecular vibrational state, the intermolecular *vibrational* selection rules are then simply:

$$A_2 \longleftrightarrow A_2$$
$$E \longleftrightarrow E.$$

Since the optical interaction between $A_2$ and E is forbidden, the relative positions of the $A_2$ states and E states can *never* be determined by absorption spectroscopy, except through the analysis of perturbations.

### 3.6.3.2 Inter-State Interaction Selection Rules

The potential operator (V) of an isolated system, free of external field, is required to be invariant and then totally symmetric under any feasible symmetry operation of $D_{3h}(M)$ and K(spatial). Consequently, a *necessary, but insufficient*, condition for the interaction matrix element $\langle 1|V|2\rangle$ in the perturbation theory to be nonzero is that states $|1\rangle$ and $|2\rangle$ must be of the same symmetry species under both groups. Since different total angular momentum quantum numbers (J, in the j-l coupling scheme) correspond to different symmetry species in K(spatial), the interacting states not only need to have exactly the *same symmetry species* in $D_{3h}(M)$, but also the *same J*. In other words, at whatever level of coupling in the wavefunctions, only states of the same $D_{3h}(M)$ symmetry and the same J can be mixed and thus "repelled" by one another when further intermolecular potential terms are introduced. [32,35]

In such a context, these general inter-*rovibrational-state* interaction selection rules have already covered both the Fermi resonance [34] and Jahn's Coriolis selection rules [34], which have less rigorous implications because the *vibronic near* symmetry species of the point group are employed instead.

### 3.6.4 Intermolecular Vibrational Transitions in the Free Internal Rotor Limit

To elucidate the intermolecular vibrational branches allowed in the free internal rotor limit, small characters n, o, p, q, r, s, t, etc. will be used to label them in terms of $\Delta l$, in the same way that P, Q, R are conventionally used for $\Delta J$, with $\Delta l=0$ corresponding to q

branch. For example, t branch corresponds to $\Delta l=+3$. As will be shown, even though $J$ is always a good quantum number in the j-l coupling scheme, $l$ is more convenient than $J$ for describing the rovibrational spectrum in the free internal rotor limit.

As an example, we consider the $A_2'(0;0;1,0) \leftarrow A_2''(0;1;0,0)$ intermolecular vibrational transition, which corresponds to a $NH_3$ inversion-rotational transition (see Figure 3.6.1; the schematic zero-order rotational manifolds are shown in Figure 3.6.2.) In the upper $A_2'(0;0;1,0)$ state, due to the j+l vectorial addition with $j=1$, each $l>0$ level of the rotational manifold is accidentally triply degenerate, with $J=l-1$, $l$ and $l+1$; the $l=0$ level is nondegenerate with $J=j=1$. Now, following the optical selection rules for parity and $J$, three branches can be obtained with $\Delta l=-2$, 0, and +2, respectively (i.e. o, q, s branches). (In this particular case, the parity selection rule is inherent in the $J$ selection rule. However, this by no means implies that the parity selection rule can be neglected; generally, both selection rules are necessary in the perturbed cases.) It is interesting that the P, Q, R branch transitions are now regrouped into a pattern of three new branches in the free internal rotor limit. The o-q-s to P-Q-R branch evolution between the two limits for this vibrational transition will be discussed in Section 3.7.6 on the perturbed cases. Because of the same relative spacings within both upper and lower rotational manifolds, the q branch consists of a single peak (superimposed lines) in the free internal rotor limit.

If other intermolecular vibrational transitions are examined

similarly, the $\Delta l$ selection rule in the free internal rotor limit can be readily deduced. In general, for an allowed intermolecular vibrational transition with $j_u$ and $j_l$ as the upper and lower state $j$, if the two intermolecular vibrational states are of the *same* parity, then all *odd* $\Delta l$ branches with $|\Delta l| \leq j_u + j_l + 1$ can exist; if of *opposite* parity, then all *even* $\Delta l$ branches with $|\Delta l| \leq j_u + j_l + 1$ are present. For example, the E'(0;0;2,2) ← E"(0;0;1,1) intermolecular vibrational transition should have m,o,q,s,u branches corresponding to $\Delta l = -4$, $-2$, 0, +2 and +4, respectively, because $j_u + j_l + 1 = 4$. However, E"(1;0;1,1) ← E"(0;0;1,1) should have n, p, r, t branches corresponding to $\Delta l = -3$, $-1$, +1, +3. It can be shown that the spectral line spacing of a $\Delta l$ branch is $2B|\Delta l|$, where $B$ is the pseudo-diatomic rotational constant, and the band center gap of a $\Delta l = \pm k$ ($k > 1$) branch pair is $2B[k^2 + k]$.

It can be verified that the existence of a q branch in the free internal rotor limit is an indication that the corresponding internal inversion-rotational transition is originally allowed for the *free* $NH_3$ *monomer*; if q is missing, then it is originally forbidden. Here, "allowed" or "forbidden" is defined in terms of the most unrestrictive selection rules, given in Section 3.6.3.1, under $D_{3h}(M)$ and K(spatial) for the $NH_3$ *monomer*, not of certain classical approximate selection rules which help to distinguish strong transitions from the rest. (For example, certain $NH_3$ transitions forbidden by the approximate rotation selection rule $\Delta k_c = 0$ are allowed by the rules given in Section 3.6.3.1. However, these "allowed forbidden" transitions are in principle weaker. [32])

It is also interesting to scrutinize a special case, the limiting

band pattern of the E'(0;1;1,1) ← E"(0;0;1,1) transition, which corresponds to a $NH_3$ monomer inversional motion. According to the $\Delta I$ selection rule, three branches, i.e. o, q, and s branches are expected. However, since the two zero-order intermolecular vibrational states are separated only by approximately 24 GHz [35], while the pseudo-diatomic rotational constant (B) is 2.8 GHz, one might ask how far the high $I$ transitions of the o branch can extend. Actually, in the zero-order rovibrational level diagram (Figure 3.6.4(a)), the upper and lower states are reversed for all high $I$ transitions starting with o(3). This results in a necessary o branch "reflection" bandhead at zero frequency (Figure 3.6.4(b)). Interestingly, this bandhead structure is *not* due to the usual noninertial effects. (Actually, as can be readily verified, this reflection effect occurs for any band structure that reaches zero frequency in both perturbed and unperturbed cases.) This is a special intermolecular vibrational transition also because there will be many inter-state interactions within the manifold of the two zero-order vibrational states when the anisotropic potential is introduced (see Section 3.7.6). This gives rise to an unusually complicated spectrum, as has been observed in microwave by Nelson *et al* [14,15], but is not yet theoretically understood.

### 3.7 Perturbed Cases

It will be shown that due to the near prolate top configuration of the complex the $K_a$ manifolds can be considered as the appropriate evolving units for the energy level correlation between the free

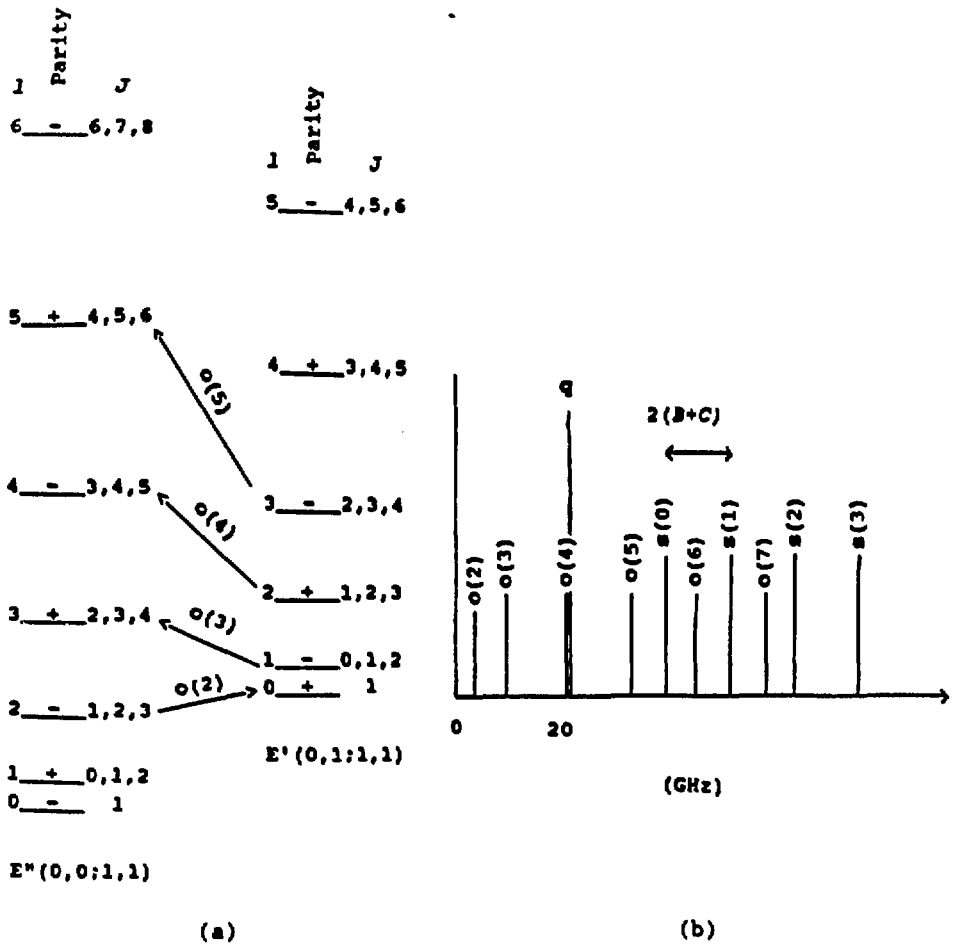


Figure 3.6.4
(a) the zero-order rovibrational level distributions for the E'(0;1;1,1) ← E"(0;0;1,1) inversional transition. The reversing of the upper and lower rovibrational states are indicated by arrows.
(b) the zero-order intermolecular vibrational band derived from (a) energy level distribution, showing a bandhead at zero frequency. (The intensities indicated are arbitrary.)

internal rotor limit and semi-rigid limit. The quantum number correlation between the two limits will then be established under both $C_{3v}(M)$ and $D_{3h}(M)$. Finally, the qualitative aspects of the intermolecular rovibrational transitions will be discussed.

### 3.7.1 Highly Near Prolate Top

Due to the small mass of the hydrogen atom, the Ar-$NH_3$ complex, approaching any rigid structure in the limit of high anisotropy, will be a *near* prolate top. (Of course, two trivial exceptions are when the $C_3$ axis of the $NH_3$ and a-principal axis of the complex are collinear; they are *exact* prolate tops.) This can be verified by considering the numerical values of the rotational constants, or of the corresponding principal moments of inertia, if a rigid model is assumed for the complex.

In order to simplify the derivation and the expression of the inertia tensor for the complex, the (right handed) Cartesian coordinate system is defined with its y and z axis (in the direction of k in Figure 3.4.1-2) in the plane spanned by the $C_3$ axis of the $NH_3$ and the a-principal axis of the complex. The inertia tensor (I) can then be shown to be

$$I = \begin{bmatrix} I_{b,s} + \mu R^2 & 0 & 0 \\ 0 & I_{b,s}C^2\theta + I_{c,s}S^2\theta + \mu R^2 & (I_{b,s} - I_{c,s})C\theta S\theta \\ 0 & (I_{b,s} - I_{c,s})C\theta S\theta & I_{b,s}S^2\theta + I_{c,s}C^2\theta \end{bmatrix} \tag{3.7-1}$$

where $I_{b,s}$ and $I_{c,s}$ are the moments of inertia of the $NH_3$ *monomer*, the subunit which is assumed to be unperturbed, along its b- and

c-principal axis; $\mu$ is the reduced mass of the pseudo-diatomic frame; R and $\theta$ are as previously defined; C and S denote cosine and sine.

Due to the $D_{\infty h}$ symmetry of the momental ellipsoid of the $NH_3$ monomer, in terms of $\theta$ (Figure 3.4.1-2), the inertia tensor I of the complex should be symmetric with respect to $\theta=0^\circ$ and $90^\circ$ (and thus $180^\circ$ and $270^\circ$), as also indicated by Equation (3.7-1). Since the principal moments of inertia, i.e. the three roots of the secular equation corresponding to the matrix in Equation (3.7-1), are either a constant or a *monotonic* function of $\theta$ within the range of $[0^\circ,90^\circ]$, the $I_i$'s (i=a, b and c) and the corresponding rotational constants for these two configurations ($\theta=0^\circ$, $90^\circ$) are thus the boundary values for the *rigid* model. The principal moments of inertia for all possible rigid configurations therefore vary in the following two set of limiting values:

| $\theta = 0^\circ$ | $\longrightarrow$ | $\theta = 90^\circ$ |
|---|---|---|
| ($\theta = 180^\circ$ | $\longleftarrow$ | ) |
| collinear configuration | | T-configuration |

| | | | |
|---|---|---|---|
| $I_a = I_{c,s}$ (3.7-2a) | $\xrightarrow{\text{decreasing}}$ | $I_a = I_{b,s}$ | (3.7-3a) |
| $I_b = I_{b,s} + \mu R^2$ (3.7-2b) | $\xrightarrow{\text{constant}}$ | $I_b = I_{b,s} + \mu R^2$ | (3.7-3b) |
| $I_c = I_{b,s} + \mu R^2$ (3.7-2c) | $\xrightarrow{\text{increasing}}$ | $I_c = I_{c,s} + \mu R^2$. | (3.7-3c) |

(Actually, for such special configurations with $\theta=0^\circ$ and $90^\circ$, these

expressions can be "visualized" directly from Figure 3.4.1-2 by using the parallel axis theorem for moment of inertia [31], without employing Equation (3.7-1).)

If R is substituted in the above expressions for $I_i$'s by the distance estimated from the microwave spectrum [13] (or from this work), the corresponding rotational constants can be estimated as follows:

for collinear configurations (two symmetric tops),

$A$= 189 GHz = 6.3 $cm^{-1}$,

$B$= $C$= 2.849 GHz;

for T-shaped configuration (the most asymmetric top),

$A$= 298 GHz = 9.9 $cm^{-1}$,

$B$= 2.849 GHz,

$C$= 2.834 GHz.

The corresponding asymmetry parameter $\kappa$ (=$(2B-A-C)/(A-C)$) [33,34] for the latter, the most asymmetric configuration possible, can be approximated by $[-1+2(B-C)/A]$, where $2(B-C)/A$ is only on the order of $10^{-4}$. (Here, because the large difference between the numerical uncertainty of $A$ and those of $B$ and $C$, no direct evaluation of $\kappa$ is made.) This indicates that the complex even at its most asymmetric configuration is still a *highly* near prolate top.

The typical change in vdW bond length (R) between the ground and the first few excited intermolecular vibrational states is within few percent [13,40]. In addition, in the expressions for $I_b$ and $I_c$ (Equations (3.7-2b,c) and (3.7-3b,c)), the $\mu R^2$ term is two orders of

magnitude more dominant than $I_{b,s}$ and $I_{c,s}$, which characterize the *internal rotation*. As a result, the feature of being a highly near prolate top in the rigid model can then be extended to any floppy model, in which the inter-subunit relative orientation, distance, and the $NH_3$ inversional coordinate are not fixed.

### 3.7.2 $K_a$ Rotational Manifolds as Evolving Units under $C_{3v}(M)$ between the Two Limits

Since the evolution of rovibrational levels between the free internal rotor limit (defined together with the zero-order limit in Section 3.6.2) and the semi-rigid limit is of concern, a clear definition is required for "semi-rigid". "Semi-rigid" means that only harmonic vibrations with infinitesimally small amplitudes are allowed. [29] Such a definition gives rise to two phenomena: (1) the vibrational motions can be separated from the overall rotations and (2) the independent vibrational normal modes can exist. The connotations for the $NH_3$ subunit and the overall complex need further clarification.

It is noted that, whether the semi-rigid $NH_3$ subunit has $C_{3v}$ *point group* symmetry or not, the $NH_3$ inversion, allowed by a semi-rigid *planar* $NH_3$, can never be achieved by a semi-rigid *nonplanar* $NH_3$ with an infinitesimally small amplitude in the inversional coordinate ($\gamma$). Consequently, in the semi-rigid limit, if the $NH_3$ subunit is planar, then the molecular symmetry group of both the subunit itself and the complex will be $D_{3h}(M)$; if it is nonplanar, the molecular symmetry group will be $C_{3v}(M)$. (Of course, the use of these

groups by no means implies that the complex is necessarily semi-rigid.)

In the following discussion, the "semi-rigid $NH_3$" is further defined to have $C_{3v}$ point group symmetry. This definition necessarily quenches the inversional motion completely, and makes the molecular symmetry group of the complex become $C_{3v}(M)$. However, in terms of the complex configuration, "$C_{3v}(M)$ semi-rigid", or generally "semi-rigid", needs to be distinguished from "$C_{3v}$ semi-rigid". The former implies an arbitrary semi-rigid relative configuration between the Ar and $C_{3v}$ semi-rigid $NH_3$ subunit; however, as a special case of the former, the latter further requires that the Ar atom be on the $C_3$ axis of the $NH_3$ subunit. Therefore, there are two different kinds of $C_{3v}$ semi-rigid configurations for the complex: one with the Ar atom attached directly to the N atom, the other to the plane formed by the three H's. (The following discussion makes no difference between these two kinds of $C_{3v}$ semi-rigid configurations.) An important result from these definitions is that whenever the complex is described as semi-rigid, the molecular symmetry group of the complex must be $C_{3v}(M)$, instead of $D_{3h}(M)$, because we do not consider the case in which the $NH_3$ has a semi-rigid planar structure.

According to Section 3.7.1, it is known that the feature of Ar-$NH_3$ being a highly near prolate top is insensitive to the rigidity of the complex. This makes the complex always similar to a diatomic molecule in many aspects. It is noted that in the j-l coupling scheme the absolute projection value $K_a$ of the total angular momentum $J(=j+l)$ onto the complex a principal axis is *basically* due to the internal

angular momentum j. Therefore, j and $K_a$ of the complex play the roles analogous to those of the diatomic electronic angular momentum L and its absolute projection value $\Lambda$ onto the diatomic figure axis, respectively. [36] More or less normal rotational level distribution is thus expected for each $K_a$; the rotational $J$-stack for each $K_a$ should be basically characterized by the pseudodiatomic rotational constant $B$, in a similar way that the $J$-stack for each $\Lambda$ is by the diatomic $B$ constant. It is also expected that different $K_a$'s can interact with each other and be mixed by the noninertial forces, i.e. the Coriolis and the centrifugal distortion forces, when the complex is rotating. However, according to the experience with diatomic molecules, we do not think such $K_a$ mixings are a dominant feature in a first approximation. In other words, $K_a$ should be a nearly good quantum number for this floppy but always highly near prolate top complex.

(Because $K_a$ is a quantum number purely of *rotational* motion, *not* of the $NH_3$ inversional motion which extends the molecular symmetry group from $C_{3v}(M)$ to $D_{3h}(M)$, we will keep the discussion first in terms of $C_{3v}(M)$.)

In terms of the energy level correlation between the two limiting cases each $K_a$ rotational manifold should constitute an evolving unit, as further supported by the following facts. As can be readily verified for any symmetric (and thus near symmetric) top, *no* rovibrational states in one $K_a$ rotational manifold of a *semi-rigid* vibrational state share *both* the same symmetry and same $J$. [32] Consequently, *within* such a manifold, there is no "internal repulsion"

to be *reduced* when the potential evolves toward the free internal rotor limit. It is noted that the two states corresponding to a doubly degenerate E (in $C_{3v}(M)$) rovibrational state do not interact with each other. Therefore, such two degenerate states are considered as *one* rovibrational state in the above statement. In addition, since the inter-subunit distances corresponding to any physically *reasonable* intermolecular potentials should be on the same order (few Å's), the rotational constant $B(\approx C)$ and thus the state density of each $K_a$ rotational manifold should be relatively insensitive to the potential variation. As a result, the rovibrational levels corresponding to a given $K_a$ are basically "held" together and evolve as a *unit* between the two limiting cases.

When the intermolecular anisotropy is raduced, the "repulsions" that give rise to the classical distribution of the semi-rigid vibrational states and the $K_a$ rotational manifolds therein can only be decreased. Furthermore, as expected from the physical significance of $K_a$ (the absolute projection value of j on the a principal axis), all $K_a$ should ultimately be in the framework of the free $NH_3$ rotational levels. As a result, when the complex is far from the semi-rigid limit, the distribution of the $K_a$ rotational manifolds correlating to a vibrational state in the semi-rigid limit can no longer be approximated by the well-known rotational energy ($E_{rot}$) expression for a semi-rigid near prolate top, [34]

$$E_{rot} = [(B + C)/2]J(J+1) + [A - (B + C)/2]K_a^2. \qquad (3.7.2)$$

In other words, the vibrational states in the semi-rigid limit fail to

evolve together as units between the two limits. This makes the structurally informative rotational $A$ constant unavailable through this equation. However, in the free internal rotor limit the distribution scale between the $K_a$ manifolds is two orders larger than that (the complex $B$ value) *within* each $K_a$ manifold. This makes the $K_a$ manifolds behave more like evolving *units*.

When the complex approaches the free internal rotor limit, there should be a higher chance for two $K_a$ rotational manifolds to intercross or interact with each other as functions of the potential evolution. The statement that the $K_a$ rotational manifolds evolve as units should be further clarified by considering such intercrossings. Accordingly, we examine the interaction between an $A_2$ $K_a$=0 and an $A_1 \oplus A_2$ $K_a$=1 rotational manifold, as depicted in Figure 3.7.2-1. Here, the symmetry species of the $K_a$ rotational manifold is defined to be the overall symmetry of the level(s) with the lowest $J(=K_a)$ in the manifold. It is found that, although there exist the deflections of the interacting rovibrational levels, each $K_a$ rotational manifold structure appears to "penetrate" the interaction region as an evolving unit before and after the interaction region. (It is noted that the $K_a$ values cannot be defined in the interaction (mixing) region.) More importantly, according to the standard textbook discussion on system of two interacting states [34,35], it can be inferred that it is not only the manifold structure but also the associated physical significance (wave functions) of each interacting $K_a$ rotational manifold that has the "penetrating capability"; the farther from the interaction region, the less each $K_a$ manifold is "contaminated" by its

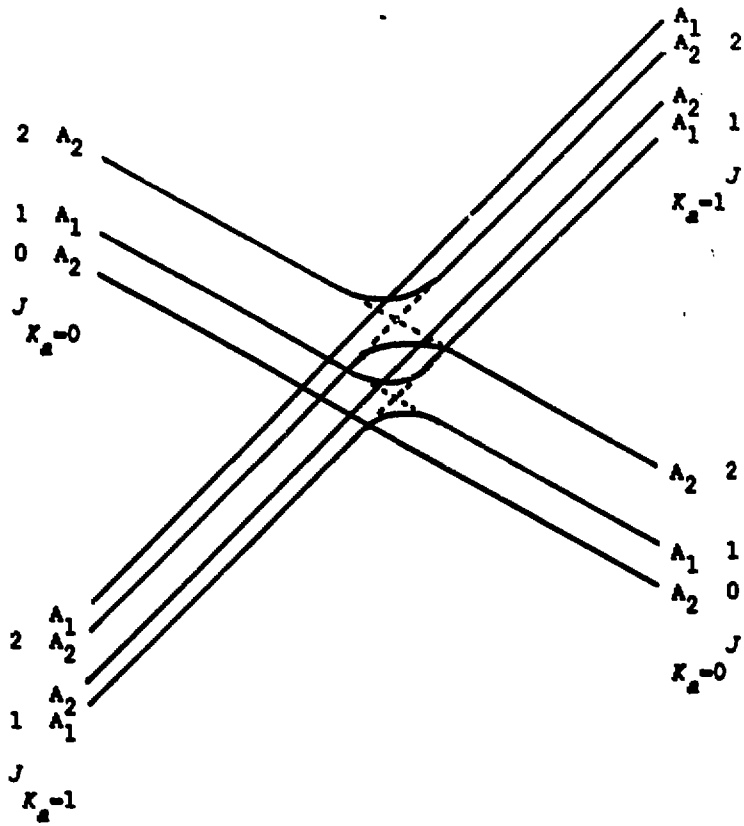


Figure 3.7.2-1
Schematic representation of the interaction between an $A_2$ $K_a$=0 and an $A_1 \otimes A_2$ $K_a$=1 rotational manifold under $C_{3v}(M)$. (The x axis corresponds to one of the variables that control the potential evolution.)

interacting partner. Similar observations can be made for the intercrossing between two $K_a$ manifolds with the same $K_a$ value and same symmetry. Although in this case *all* rotational levels in each manifold are deflected in the interaction region, the above remarks on the wave function "penetrating capability" still hold. In other words, treating the $K_a$ manifolds as the evolving units is based on the evolution of the associated wave functions rather than of their actual rovibrational levels.

All these facts suggest that a correlation diagram between the two limiting cases can be established with the $K_a$ rotational manifolds as the evolving units.

### 3.7.3 Splittings of Zero-Order Intermolecular Vibrational States into $K_a$ Vibrational Component States under $C_{3v}(M)$

Since, according to the $C_{3v}(M)$-$D_{3h}(M)$ symmetry species correlation table (Appendix Table 4) or the fact that $C_{3v}(M)$ is a subgroup of $D_{3h}(M)$, there will be further energy level splittings when the molecular symmetry group evolves from $C_{3v}(M)$ into $D_{3h}(M)$. Therefore, any further splitting complications can be considered to occur *within* each evolving unit, the $K_a$ rotational manifold, instead of between them.

Again we will derive the overall picture only under $C_{3v}(M)$ for the moment. As will be shown below, when the intermolecular potential is introduced, each zero-order intermolecular vibrational state which involves the $NH_3$ free *rotational* motion can split into several $K_a$ rotational manifolds, each of which correlates to a $K_a$ stack of a

*different* classical near prolate top vibrational state in the semi-rigid limit. In such a context, each $K_a$ rotational manifold can be considered as a *vibrational component* state with respect to either limit.

Now, we examine first the rotational manifolds of the zero-order intermolecular vibrational states in $C_{3v}(M)$. In such a case, the two columns on the left of the zero-order intermolecular vibrational level diagram, Figure 3.6.1, coalesce with the two on the right into two new columns corresponding to $(v_s,v_l)=(0,X)$ and $(1,X)$, where "X" is used to reflect that the $NH_3$ inversional motion is quenched and thus the associated quantum number becomes indeterminate. Consequently, each resultant vibrational level is labelled with *two* symmetry species in $D_{3h}(M)$, which correspond to *one* species in $C_{3v}(M)$ according to the symmetry species correlation (Appendix Table 4).

For example, the $A_2'(0;0;1,0)$ and $A_1''(0;1;1,0)$ state in $D_{3h}(M)$ becomes the $A_2(0;X;1,0)$ state in $C_{3v}(M)$. (The notation $S_o(v_s;v_l;J,k_c)$ for the zero-order intermolecular vibrational state is still preserved under $C_{3v}(M)$.) Similar two-to-one species relationship can be observed for each zero-order rovibrational level of the $A_2(0;X;1,0)$ vibrational state. Since its $J$ equals 1, based on the discussion in Section 3.6.4, each of its zero-order $l$ rovibrational level, except the $l=0$ level, is triply $J$-degenerate, with the associated $J=l-1$, $l$, $l+1$. As indicated in Figure 3.7.2-2, such accidental $J$-degeneracy of three states of the *same* symmetry will be removed basically due to the pairwise interactions between every other $l$ levels, according to the same-symmetry-same-J inter-state interaction selection rules (Section

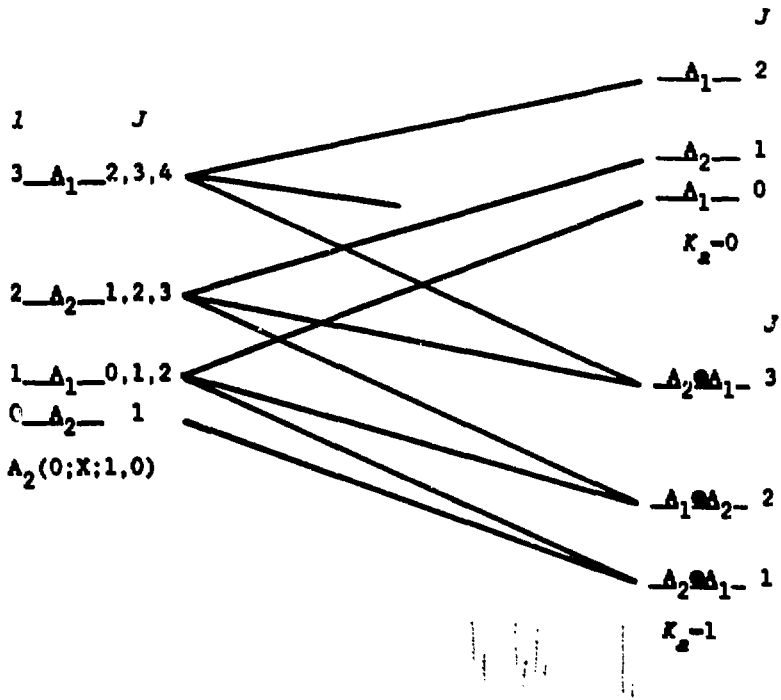


Figure 3.7.2-2
Schematic representation of the splitting of the $A_2(0;X;1,0)$ state into a $K_a$=0 and 1 component state by the anisotropy of the intermolecular potential.

3.6.3).

To simplify the discussion on the splittings of the $A_2(0;X;1,0)$ state, it is assumed that all other zero-order intermolecular vibrational states are located sufficiently far away and their influences on $A_2(0;X;1,0)$ can then be neglected. Since the vibrational state distribution is a *continuous* function of the potential evolution, this assumption will not hamper the generality of the result thus derived. Under this assumption, the *necessary* result according to the previously justified requirement that the $K_a$ rotational manifolds be the evolving units is as follows: As indicated in Figure 3.7.2-2, the triply degenerate zero-order rovibrational states with a given $l$ *shift* respectively into *rovibrational* states only of *two* $K_a$ *rotational manifolds*, viz., $J=l-1$ of a $K_a=0$ manifold and $J=l$, $l+1$ of a $K_a=1$ manifold; the only nondegenerate zero-order $l=0$ state becomes one of the two $J=1$ levels of the $K_a=1$ manifold. In other words, the $A_2(0;X;1,0)$ vibrational state can split into one $A_1$ $K_a=0$ and *one* $A_1 \oplus A_2$ $K_a=1$ rotational manifold. (It is remembered that the semi-rigid $K_a=1$ (or more generally >0) stacks should have symmetry which is totally two dimensional.) Similarly, the $E(0;X;1,1)$ state can be shown to split into one E $K_a=0$ manifold and *two* E $K_a=1$ manifolds.

Even according to the schematic correlation in Figure 3.7.2-2 whose rotational stacks are all drawn to scale with $BJ(J+1)$, it is apparent that generally there is a *necessary* distortion associated with each $K_a$ manifold approaching the free internal rotor limit. (This is "necessary" distortion because we have already assumed the

influence due to the $K_a$ manifolds (or manifold) correlating to other zero-order intermolecular vibrational states is negligibly small.) To the first approximation, the only distortion-free $K_a$ manifold should be that of the zero-order intermolecular *ground* vibrational state $A_1(0;X;0,0)$. Although the $K_a$ manifolds are described as distorted in the free internal rotor limit, actually the distortion is in the opposite direction. It is remembered that the $J$-level regularity within and the independence among the semi-rigid $K_a$ manifolds are the limiting phenomena due to the limiting anisotropic intermolecular potential; the "normal" $K_a$ manifolds in the semi-rigid limit actually result from the distortion of the accidentally degenerate and apparently "distorted" *zero-order* $K_a$ manifolds.

If similar examinations are made for other zero-order intermolecular vibrational states under $C_{3v}(M)$, the rules of their splittings can be summarized in Table 3.7.3. The symmetry species of each $K_a$ vibrational component state used in this table is still as previously defined in Section 3.7.2. For example, the $K_a$=1 component state in Figure 3.7.2-2 has $A_1 \otimes A_2$ symmetry, which corresponds to the two nondegenerate rovibrational states of $J$=1 in the manifold. Consequently, the symmetry species dimension of the $K_a$ vibrational component state is the same as that of the *overall* species of the rovibrational state(s) corresponding to each $J$ within the manifold. (As an afterthought, by counting the number and the symmetry species dimensions of the $K_a$ component states in Table 3.7.3, it can be found that the degeneracies due to both $K_a$ and $k_c$ have been fully accounted

Table 3.7.3
The correlation between the zero-order intermolecular vibrational states and their $K_a$ vibrational component state(s) (or the $K_a$ rotational manifolds).

| zero-order vibrational state | ⟶ number and symmetry of $K_a$=0 manifold(s) | $K_a$≠0 ($K_a$:[1,$J$]) manifold(s) |
|---|---|---|
| $A_1$ ($k_c$=0, even $J$) | one $A_1$[a] | one ($A_1$ ⊕ $A_2$) |
| $A_2$ ($k_c$=0, odd $J$) | one $A_1$ | one ($A_1$ ⊕ $A_2$) |
| E ($k_c$=1, 3n±1)[b] | one E | two E's |
| ($A_1$ ⊕ $A_2$) ($k_c$=3n) | one $A_1$<br>one $A_2$ | two ($A_1$ ⊕ $A_2$)'s |

[a]The symmetry species refers to that (those) of the level(s) of the lowest $J$ in the rotational manifold.
[b]n: positive integer.

for.)

It is noted that for any $K_a$ rotational manifold with a symmetry species associated with subscript, i.e. the $A_1$, $A_2$, or $A_1 \oplus A_2$ $K_a$ manifold there is always a subscript alternation feature for the rotational symmetry species associated with each increment of $J$ by one. Of course, no subscript alternation can be made for the $K_a$ manifolds with E symmetry. Therefore, as long as the symmetry of the $K_a$ manifold is known, the symmetry species of any $J$ in the manifold can be quickly figured out. Although this rule might seem trivial under $C_{3v}(M)$, it is such simplicity that justifies the convenience of the use of the $K_a$ manifold symmetry thus defined.

The splittings of the zero-order intermolecular vibrational states into different $K_a$ manifolds can also be justified in terms of the $C_{3v}(M)$ symmetry species of the free $NH_3$ *rotational* states. By first assuming that the e-o-e rotation is quenched and only the $NH_3$ subunit is allowed to rotate, we recognize that the $NH_3$ subunit is in an intermolecular potential with $C_\infty$ symmetry about the complex a axis. In terms of symmetry, this phenomenon is therefore equivalent to the Stark effect [35] of the free $NH_3$ (without inversion yet). Consequently, each *parity-undefined* ($j \neq 0, k_c$) $NH_3$ rotational state will result in $2j+1$ "*first order* Stark component states", corresponding to its $2j+1$ possible projections ($m_J$'s) on the complex a axis; however, each *parity-defined* ($j \neq 0, k_c$) state will result in $j+1$ "*second order* Stark component states", corresponding to the $j+1$ possible absolute projection values ($|m_J|$'s). In order to determine the associated parity, the $C_{3v}(M)$-$D_{3h}(M)$ symmetry correlation table can then be used.

It is found that $A_1$ correlates only to positive parity, $A_2$ only to negative parity, and E to both (parity-undefined). As a result, each $(j,k_c=0)$ state splits into $j+1$ component states; all $(j,k_c>0)$ states into $2j+1$ component states. When the e-o-e rotation is "turned on", each of these component states will correlate to a $K_a$ rotational manifold. This result is then in agreement with Table 3.7.3.

The relative positions of the $K_a$ manifolds originating from a zero-order intermolecular vibrational state depend on the geometry of the intermolecular potential function. Since no particular functional form has yet been assumed for the potential, the relative position of the $K_a=0$ and $K_a=1$ component state, shown in Figure 3.7.2-2, is arbitrary. However, by using the correspondence principle, qualitative arguments on the ordering of the $K_a=0$ and $K_a=1$ component state can be made for the special case of the $A_2(0;X;1,0)$ state with $k_c=0$, when in the *slightly* perturbed cases. (Here, "slightly" implies that the dominant interaction is still between these two component states.) If the equilibrium configuration is T-shaped between the $NH_3$ $C_3$ axis and the complex a-principal axis (for example, when the Legendre $P_2(\cos\theta)$ [37], instead of other $P_n(\cos\theta)$ with $n\neq2$, dominates the potential), then the $K_a=1$ state is more likely to be lower than the $K_a=0$ state. This can be understood by considering the corresponding *classical* motions of the $K_a=0$ and $K_a=1$ state, shown in Figures 3.7.3 (a1) and (a2). Since $k_c=0$ in the $A_2(0;X;1,0)$ state, the $j=1$ can be ascribed to an internal libration or rotation about an axis perpendicular to the $C_3$ axis. The corresponding internal rotation of the $K_a=1$ state always senses the minimum of the classical potential,

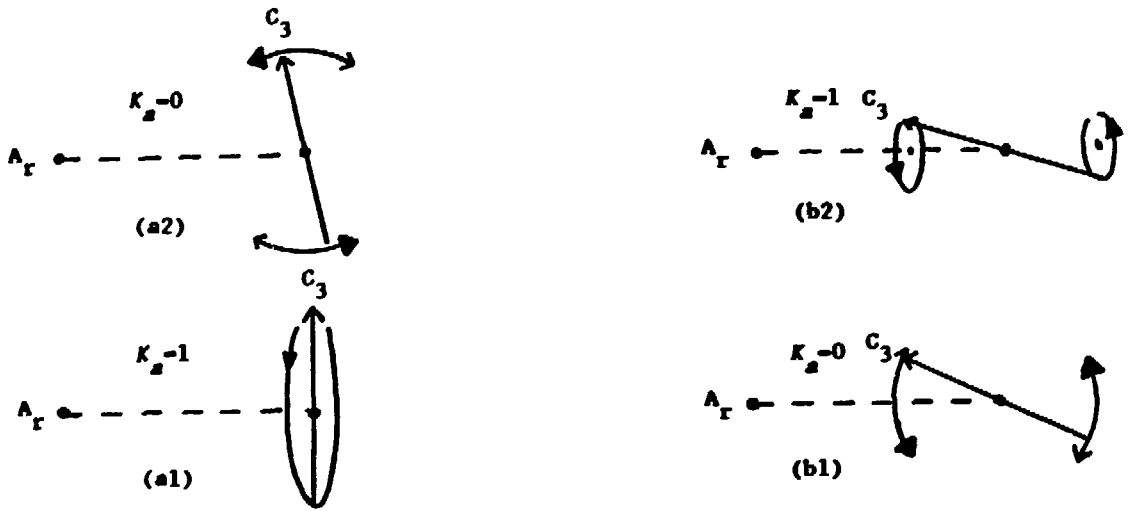


Figure 3.7.3
Corresponding classical motions of the $K_a$=0 and 1 component state of the $A_2(0;X;1,0)$ intermolecular vibrational state:
(a1) and (a2) correspond to the $K_a$=1 and 0 motions, respectively, when the complex has a T-shaped equilibrium configuration, shown in (a).
(b1) and (b2) correspond to the $K_a$=0 and 1 motions, respectively, when the complex has a linear equilibrium configuration, shown in (b).

as opposed to that of the $K_a$=0 state which passes at least two internal rotation barriers per cycle of the internal rotation. As a result, the $K_a$=1 state is lower than the $K_a$=0 state. Similar arguments can be applied to the case when the $C_3$ and a-principal axis are collinear in the equilibrium structure (for example, the Legendre $P_1(\cos\theta_r)$ dominates the potential). As indicated in Figures 3.7.3 (b1) and (b2), only the $K_a$=0 motion can probe the potential minimum, which the motion corresponding to $K_a$=1 never experiences. Therefore, the relative position between the $K_a$=0 and 1 state is reversed. (However, when the state is complicated by nonzero $k_c$, which represents a classical internal rotation about the $C_3$ axis, the above qualitative arguments cannot be generalized easily.)

### 3.7.4 $K_a$ Correlation under $C_{3v}(M)$ between the Two Limits

Since, along the whole path of a correlation between any two limits, there is only one single point that is physically existent, establishing such an evolution type correlation is merely a construction that provides more insights to the complex. The numerical models which assume different evolution paths for the potential produce different evolutions of the state distribution. Any such numerical models are acceptable as long as they can account for the state distributions at the following three places: the two limiting cases defined and the position corresponding to the actual complex. Therefore, generally it is the *qualitative* aspects, rather than the *quantitative* aspects, of the evolution type correlation that are more significant. Due to this reason, the correlation in this

section will be made only in terms of the quantum numbers belonging to the two limiting cases along with the symmetry species of the molecular symmetry group, which is temporarily assumed to be $C_{3v}(M)$. In other words, the correlation to be discussed is mainly to indicate the physical significance connections between the states in the two limits. A state (quantum number) correlation *table*, instead of the state correlation *curves*, will be constructed.

Because the two limiting cases do not belong to the real world, they need be artificially but reasonably defined, as already done for the free internal rotor limit, before any correlation can be made. Now, it is time to define the semi-rigid limit for the complex. In this limit, Ar and $NH_3$ can be *assumed* to combine together in various ways with different semi-rigid configurations, vibrational frequencies, etc.. However, since it is the quantum number correlation that is to be constructed, any quantitative specification, such as the semi-rigid vibrational frequencies, becomes unnecessary. In order to facilitate the physical meaning assignment to the semi-rigid energy levels, as will be shown below, the only specification required is the complex configuration.

Within the semi-rigid limit, the energy level distribution is still a continuous function of the variation of the *internal* potential. In other words, the state correlation can also be established, at least in principle, for any two semi-rigid configurations. Because in this limit the vibrations are well separated from the overall rotations, such correlations should have the vibrational states, or, equivalently, the corresponding near

prolate top rovibrational manifolds, as the largest evolving units, each of which can be characterized by the $K_a$ quantum numbers and the associated rotational constants [34]. This fact allows us to select *any* semi-rigid configuration as the reference point to be correlated directly to the free internal rotor limit. If we are interested in any other semi-rigid configuration, for example, the one corresponding to the minimum of the actual intermolecular potential, then a secondary correlation starting from the reference semi-rigid configuration can always be established *within* the semi-rigid limit. In such a secondary correlation, the classical discussions on the Fermi resonance and Coriolis interactions between different semi-rigid vibrational states should apply. Since such secondary correlation is, in principle, always feasible, and is a relatively well understood topic, without losing any generality, we will focus the discussion only on the simplest correlation between the free internal rotor limit and the semi-rigid limit. Therefore, the $C_{3v}$ configuration which is similar to the ground state $CH_3Cl$ is naturally chosen for the reference semi-rigid limit, because this *exact* prolate top structure provides the exact physical meanings to the $K_a$ stacks in each semi-rigid vibrational state.

Now, we begin to consider such a correlation between these two particularly chosen limits. With the $NH_3$ inversional motion quenched, under $C_{3v}(M)$ only the dimeric stretch and internal rotation, hindered or not, can be involved in the intermolecular motions. However, it has been shown that the zero-order dimeric stretching wave function with any stretching quantum number $v_s$ is totally symmetric (Section

3.6.1). Therefore, in order to derive the correlation in terms of the quantum numbers and symmetry species, only the evolution of the *pure* internal rotational states into the semi-rigid limit needs to be examined, because this correlation can be duplicated for each value of $v_s$. On the other hand, being equivalent to an extremely hindered $NH_3$ internal rotation, the semi-rigid bending vibration, without any internal vibration in the $NH_3$ subunit, of the reference $C_{3v}$ semi-rigid configuration is worth particular attention for the correlation purpose. Due to the $C_{3v}$ structural symmetry, this bending vibration *mode* must be doubly degenerate, and thus should have E as its symmetry species because E is the only two dimensional species available under $C_{3v}(M)$. The same result can be obtained if a rigorous symmetry analysis is performed for the corresponding vibrational displacement vectors. In the semi-rigid limit, this doubly degenerate vibration corresponds to a two dimensional (2-D) isotropic harmonic oscillation [38], which can be exactly specified by the bending quantum number ($v_b$) and the associated angular momentum ($l_b$).

Therefore, more accurately speaking, the correlation being sought for is between free internal rotational quantum numbers $j$, $k_c$ and the semi-rigid bending vibrational quantum numbers $v_b$, $l_b$ through the symmetry species in $C_{3v}(M)$ and the near prolate top $K_a$ quantum numbers.

The symmetry species of the free internal rotation states as a function of $j$ and $k_c$ can be readily derived from Table 3.4.4.1-2 along with the $C_{3v}(M)$-$D_{3h}(M)$ symmetry correlation table (Appendix Table 4). (Of course, it can also be derived by using the standard symmetric top

wave functions under $C_{3v}(M)$, as in Section 3.4.4.1 under $D_{3h}(M)$.) The results are summarized in Table 3.7.4-1.

On the other hand, the symmetry species of the semi-rigid bending states as a function of $v_b$ and $l_b$ can be deduced as follows: As can be found in almost any standard textbook on quantum mechanics [38], the energy of a 2-D isotropic harmonic oscillator can be expressed as $(v_b+1)\hbar\omega$, where $\omega$ is the fundamental angular frequency; each $v_b$ level is $(v_b+1)$-fold degenerate to account for the $v_b+1$ different signed vibrational angular momentum quantum numbers (or number) $\pm l_b$ with $l_b=v_b$, $v_b-2$, $v_b-4$, ..., 0 or 1. As a direct result of the fact that angular momentum (along the axis perpendicular to the 2-D vibrational plane) operator $L_z$ commutes with the Hamiltonian, the wave function corresponding to each $(v_b,l_b)$ should have *only* the multiplicative factor $\exp(i\pm l_b\varphi)$ that is dependent on $l_b$ and the corresponding angular coordinate $\varphi$. Therefore, in order to find the symmetry species of a $v_b$ *vibrational* level, we do not need to bother to employ the $v_b+1$ *complete* wave function expressions as the basis set in the symmetry reduction. Instead, the $v_b+1$ functions of the form $\exp(i\pm l_b\varphi)$ with $l_b=v_b$, $v_b-2$, $v_b-4$, ..., 1 or 0, will suffice the purpose. Furthermore, we do not need to derive the transformation properties of $\varphi$ under $C_{3v}$, required by the symmetry reduction; it is recognized that for the particular $C_{3v}$ semi-rigid configuration the transformation properties of $\varphi$ under $C_{3v}(M)$ are equivalent to those of $\chi_s$ listed in Table 3.4.3-2. (However, this by no means implies that these two coordinates have the same physical significance.)

The $C_{3v}(M)$ symmetry species as a function of $v_b$ and $l_b$ thus

Table 3.7.4-1
The $NH_3$ subunit internal rotational symmetry species under $C_{3v}(M)$ as a function of $j$ and $k_c$ quantum numbers.

| $k_c$ | | Symmetry species under $C_{3v}(M)$ |
|---|---|---|
| 0 | even $j$ | $A_1$ |
| | odd $j$ | $A_2$ |
| 1, $3n\pm1$[a] | | E |
| 3n | | $A_1 \oplus A_2$ |

[a]n: positive integer.

derived are summarized in Table 3.7.4-2. (In Herzberg (Vol.2, p.127) [34], the *point group* symmetry species under $C_{3v}$ is given as a function *only* of $v_b$. Since there exists the isomorphism [32] between the point group and the permutation-inversion group, in terms of $v_b$, the results derived in this work need be consistent with those listed in Herzberg.)

In order to facilitate the discussion, as opposed to the notation $S_o(v_s;v_l;j,k_c)$ for the zero-order intermolecular vibrational states in the free internal rotor limit, the notation

$$[S](v_b,l_b)$$

will be introduced for the semi-rigid bending vibrational states, listed in Table 3.7.4-2. Here, S is the symmetry species of the vibrational state corresponding to one set of $(v_b,l_b)$; the square brackets are used to remind that it is in the semi-rigid limit. Although this definition makes all the states with $l_b$=3n (n:positive integer.) denoted by $[A_1 \oplus A_2](v_b,3n)$, with its reducible double degeneracy emphasized, it must be recognized that this single notation corresponds to two vibrational *levels* if any anharmonicity is introduced.

Due to the invariance of the symmetry species associated with each state and thus those with the $K_a$ rotational manifolds (the evolving units) throughout the whole evolution, to make the correlation, the $K_a$ symmetry species should be derived not only as a function of $j$ and $k_c$ (Section 3.7.3) but also of $v_b$ and $l_b$. Because the rotational symmetry species of a semi-rigid vibrational state with

Table 3.7.4-2
$C_{3v}(M)$ symmetry species, as a function of the bending quantum numbers ($v_b$ and $l_b$), of the semi-rigid *bending* vibrational states of Ar-$NH_3$ with a $CH_3Cl$-like exact symmetric top configuration.

| | $l_b$ | | | | | | |
|---|---|---|---|---|---|---|---|
| | 0 | 1 | 2 | 3 | 4 | 5 | 6 |
| .... | | ... | | ..... | | ... | |
| $v_b$=6 | [$A_1$][a] | | [E] | | [E] | | [$A_1 \oplus A_2$] |
| $v_b$=5 | | [E] | | [$A_1 \oplus A_2$] | | [E] | |
| $v_b$=4 | [$A_1$] | | [E] | | [E] | | |
| $v_b$=3 | | [E] | | [$A_1 \oplus A_2$] | | | |
| $v_b$=2 | [$A_1$] | | [E] | | | | |
| $v_b$=1 | | [E] | | | | | |
| $v_b$=0 | [$A_1$] | | | | | | |

[a]Square brackets are used to remind that the species inside is the *semi-rigid* vibrational, instead of rovibrational or zero-order intermolecular vibrational, symmetry.

symmetry [S] are the direct product of the well understood ground state rotational symmetry species [32] and S, the $K_a$ symmetry species can be readily obtained under $C_{3v}(M)$, as tabulated in Table 3.7.4-3. [32] As a result, the bending state $K_a$ symmetry species in the semi-rigid limit can then be deduced, from Tables 3.7.4-2 along with -3, as a function of $K_a$ (or $K_a(\pm)$) and $[S](v_b,l_b)$, where ± denote the sign for $l_b$ associated with the $K_a$ rotational manifold.

By combining Table 3.7.3 (the splittings of the free internal rotational states into the $K_a$ rotational manifolds) and Tables 3.7.4-2, -3 (the $K_a$ rotational manifolds contained in the semi-rigid bending vibrational states), the correlation under $C_{3v}(M)$ between the $S_o(v_s;v_l=0;j,k_c)$ states (with $v_s$ fixed) in the free internal rotor limit and the $[S](v_b,l_b)$ states in the semi-rigid limit can be established. There are two different frameworks for this correlation; one is in the format of $j$ vs. $k_c$, as depicted in Table 3.7.4-4, the other is of $v_b$ vs. $l_b$. It is the former that will be employed in the following discussion. This is because we definitely do not think that the complex is close to the semi-rigid limit.

Under this choice, the symmetry species $S_o$ are arranged in an array of $j$ vs. $k_c$, with all free internal rotor states of the same $j$ aligned horizontally to indicate the generality of this correlation for either a prolate or oblate top as the internal rotor; the $S_o(v_s=0;v_l=X;j,k_c)$ notation is not used, but is inherent in such an array. For convenience of finding the numerical regularities among different quantum numbers, the $K_a$ rotational manifolds, represented in the format of $K_a$, or $K_a(\pm)$, are put in the order of increasing $K_a$.

Table 3.7.4-3
$C_{3v}(M)$ symmetry species of the $K_a$ rotational manifolds in the semi-rigid limit as a function of $K_a$, the sign for $l_b$, and the symmetry species [S] of the bending vibration.

| | $K_a$ | | | |
|---|---|---|---|---|
| [S] | 0 | 3n+1[a] | 3n+2 | 3n+3 |
| $[A_1]$ | $A_1$ | E | E | $A_1 \otimes A_2$ |
| $[A_2]$ | $A_2$ | E | E | $A_2 \otimes A_1$ |
| [E] | E | $A_1 \otimes A_2$ (+)<br>E (−) | E (+)<br>$A_1 \otimes A_2$ (−) | E (+)<br>E (−) |

[a]n: nonnegative integer.

Table 3.7.4-4

Quantum number correlation, under $C_{3v}(M)$, between the zero-order intermolecular vibrational states $S_o(v_s;v_i=0;j,k_c)$, with $v_s$ fixed, in the free internal rotor limit and the bending vibrational states $[S](v_b,l_b)$ in the semi-rigid limit.

(The symmetry species $S_o$ are arranged in an array of $j$ vs. $k_c$; the symbol $S_o(v_s;v_i=0;j,k_c)$ itself is not used. The evolution units, the $K_a$ rotational manifolds, are represented in the format of $K_a$, $K_a(+)$, and $K_a(-)$, where (+) and (−) denote the sign for $l_b$. Basically, these $K_a$ symbols are inserted between $S_o$ and $[S](v_b,l_b)$ to indicate their roles as the evolving units. [AA] is an abbreviation for $[A_1 \otimes A_2]$.)

| | $k_c=0$ | $k_c=1$ | $k_c=2$ | $k_c=3$ |
|---|---|---|---|---|
| $j=4$ $A_1$ | 4(+),[E](4,4)<br>3, [AA](5,3)<br>2(−),[E](6,2)<br>1(+),[E](7,1)<br>0, [$A_1$](8,0) | 4, [AA](3,3);(−),[E](5,5]<br>3(−),[E](4,2);(+),[E](6,4)<br>2(+),[E](5,1); [AA](7,3)<br>1, [$A_1$](6,0);(−),[E](8,2)<br>E 0, [E](7,1) | 4(−),[E](2,2); [AA](6,6)<br>3(+),[E](3,1);(−),[E](7,5)<br>2, [$A_1$](4,0);(+),[E](8,4)<br>1(−),[E](5,1); [AA](7,3)<br>E 0, [E](6,2) | 4(+),[E](1,1);(+),[E](7,7)<br>3, [$A_1$](2,0); [AA](8,6)<br>2(−),[E](3,1);(−),[E](7,5)<br>1(+),[E](4,2);(+),[E](6,4)<br>$A_1 \oplus A_2$ 0, [AA](5,3) |
| $j=3$ $A_2$ | 3, [AA](3,3)<br>2(−),[E](4,2)<br>1(+),[E](5,1)<br>0, [$A_1$](6,0) | 3(−),[E](2,2);(+)[E](4,4)<br>2(+),[E](3,1); [AA](5,3)<br>1, [$A_1$](4,0);(−)[E](6,2)<br>E 0, [E](5,1) | 3(+),[E](1,1);(−),[E](5,5)<br>2, [$A_1$](2,0);(+),[E](6,4)<br>1(−),[E](3,1); [AA](5,3)<br>E 0, [E](4,2) | 3, [$A_1$](0,0); [AA](6,6)<br>2(−),[E](1,1);(−),[E](5,5)<br>1(+),[E](2,2);(+),[E](4,4)<br>$A_1 \oplus A_2$ 0, [AA](3,3) |
| $j=2$ $A_1$ | 2(−),[E](2,2)<br>1(+),[E](3,1)<br>0, [$A_1$](4,0) | 2(+),[E](1,1); [AA](3,3)<br>1, [$A_1$](2,0);(−),[E](4,2)<br>E 0, [E](3,1) | 2, [$A_1$](0,0);(+),[E](4,4)<br>1(−),[E](1,1); [AA](3,3)<br>E 0, [E](2,2) | |
| $j=1$ $A_2$ | 1(+),[E](1,1)<br>0, [$A_1$](2,0) | 1, [$A_1$](0,0);(−),[E](2,2)<br>E 0, [E](1,1) | | |
| $j=0$ $A_1$ | 0, [$A_1$](0,0) | | | |

Basically, these $K_a$ symbols are inserted between $S_o$ and $[S](v_b, l_b)$ to indicate their roles as the evolving units. When two semi-rigid bending states are put in a row of the same $K_a$, the left one is chosen to be of lower $v_b$ and $l_b$ value, and thus is associated with the lower $K_a$ rotational manifold in the actual spitting. [AA] is an abbreviation for $[A_1 \otimes A_2]$. Instead of $[A_1] \otimes [A_2]$, $[A_1 \otimes A_2]$ emphasizes (1) that these two states share the same bending vibrational quantum numbers in the semi-rigid limit, and (2) the connection between Tables 3.7.4-2 and -4.

This correlation, starting from the free internal rotor limit, can be concisely summarized as follows: (1) the $j$ value determines the allowed range for $K_a$ to be $[0, j]$ (Section 3.7.3), (2) for each $K_a$ value, $j$ and $k_c$ determine the correlated $v_b$ and $l_b$, i.e.

$$(v_b, l_b) = (|2j - |K_a \pm k_c||,\ |K_a \mp k_c|) \qquad (3.7.4\text{-}1)$$

(When $K_a > 0$ and $k_c > 0$, there exist two sets of $(v_b, l_b)$.), (3) $K_a$ and $k_c$ determine the correlated vibrational symmetry [S], i.e.

$$[S] = \begin{cases} [A_1] \\ [A_1 \otimes A_2], \\ [E] \end{cases} \text{for } |K_a \mp k_c| = \begin{cases} 0 \\ 3n \quad (n\text{: positive integer.}), \\ 3n \pm 1 \end{cases} \qquad (3.7.4\text{-}2)$$

and (4) if arranged as in Table 3.7.4-4, with the [E] states always appearing in pair vertically, the lower [E] in each pair will be associated with (+) and the upper [E] with (−) when $K_a > 0$; no sign will be attached when $K_a = 0$.

Several features of the correlation that greatly facilitated its

derivation will be discussed in the following.

*Classically* speaking, due to the fact that J=j+l, where the e-o-e l is perpendicular to the a principal axis of the complex, the projection $J_a$ of J (with $K_a$ as the projection magnitude) on this axis can be ascribed to that of the $NH_3$ internal rotation j. Because j is basically the sum of two different angular momenta: one ($k_c$) associated with the $NH_3$ internal rotation along the $C_3$ axis of the subunit, the other with the rotation of the subunit $C_3$ axis itself. In the $C_{3v}$ semi-rigid limit, the former will coincide with the a axis of the complex, while the projection vector of the latter on the same axis will correspond to the bending angular momentum $l_b$. In other words, in this limit, the projection vector $J_a$ should be accounted for by the collinear vectorial sum of $k_c$ and $l_b$. This implies that

$$l_b = |K_a \mp k_c|, \qquad (3.7.4\text{-}3)$$

which is contained in Equation (3.7.4-1). Based on this equation, the expression for $v_b$ in Equation (3.7.4-1) becomes a necessary result if the symmetry species of the evolving $K_a$ manifolds are considered.

In terms of $K_a$ symmetry, there are several paradoxes. The first one is that all the $K_a$=0 manifolds in the $k_c$=0 column correlate to the bending states only with $[A_1]$ symmetry, irrespective of the symmetry, $A_1$ or $A_2$, of the free internal rotor states the $K_a$ manifold originate from. This is a unique feature if compared with other $K_a$=0 manifolds which always connect the $[S_o]$ bending states to the free internal rotor state of the same symmetry $S_o$. Another paradox is that the *nondegenerate* $[A_1]$ bending states can actually correlate to a *doubly*

*degenerate* E or *two nondegenerate* A free internal rotor states.

As reflected by the similarity between the two upside-down half-pyramidal state distributions in Tables 3.7.4-2 and 3.7.4-4, if only $K_a$=0 manifolds are concerned with, there is a *one-to-one* correspondence between the semi-rigid bending states and the free internal rotor states.

It is also interesting to examine how all the $K_a$ manifolds (stacks) belonging to a semi-rigid bending state distribute themselves among the free internal rotor states. It is found that Table 3.7.4-2 is basically an infinitely many upward repetitions of the [S] symmetry distribution along the slanted lower right edge of the table. This implies that the $K_a$ distributions, on Table 3.7.4-4, of all of the bending states on this lower right edge of Table 3.7.4-2 can be treated as a repetitive unit on Table 3.7.4-4. Of course, according to the alternately state missing feature in each $l_b$ stack of Table 3.7.4-2, there should be an increment of $v_b$ by *two* accompanied with each upward increment of the unit distribution.

In finding this unit correlation distribution in Table 3.7.4-4, we will start from $[A_1](0,0)$ and follow the state ordering along the lower right edge of Table 3.7.4-2. The correlation scheme is simply, under the condition of Equation (3.7.4-3), always connect the currently lowest available $K_a$ in the semi-rigid limit to the currently lowest available $K_a$ of the same value in the free internal rotor limit. (This scheme necessarily consists with the requirement that the symmetry species of each rovibrational state is invariant throughout the whole evolution between the two limits.) This makes

the $K_a$ manifold distribution of [A](0,0) propagate in a single direction, following the slanted edge of the free internal rotor state distribution. However, all the $K_a$ distributions of other bending states with $l_b>0$ have *two* branches, corresponding to $\pm l_b$, respectively. The right branch still follows the lower right edge of the free internal rotor state distribution; the right branch generally propagates downward first, and eventually deflected to become parallel with its right branch at the same $J$ value as its origin, the $K_a=0$ location. If $v_b$ is odd, then the left branch corresponds to $+l_b$ and the right one to $-l_b$; if $v_b$ is even, then the above relations are reversed.

The resultant correlation table indicates an important fact that, within a semi-rigid bending state, a lower $K_a$ manifold is not necessarily lower in the free internal rotor limit. It is noted that the $K_a>0$ manifold(s) in the right branch *before* the "deflection point" have to be lower in energy than the $Ka=0$ manifold of the same bending state; the intercrossing (but not necessarily the symmetry and $J$ dependent interaction) between these (this) $K_a>0$ manifolds (or manifold) and the $K_a=0$ manifold becomes a necessity in the evolution. (Another energy level reversing phenomenon could occur is when the internal rotor is a prolate top, which is not our case. This is because, on the same $J$ level in the free internal rotor diagram, the $K_a=0$ manifold with a higher $k_c$ (more to the right of the same $J$ level) corresponds to a lower $v_b$ in the semi-rigid limit (see Table 3.7.4-4); however, the higher the $k_c$, the higher the corresponding energy level in the free internal rotor limit.)

Generally, when the semi-rigid limit does not have a $C_{3v}$ configuration, the bending vibration loses the 2-D isotropy of the corresponding harmonic oscillation, although, according to the definition of "semi-rigid", each vibrational direction still has the harmonicity (harmonic force constant) of its own. In such a case, $v_b$ and $l_b$ are no more exact good quantum numbers; as a result, *no direct or exact* $(j,k_c)$-$(v_b,l_b)$ quantum number correlation, as shown in Table 3.7.4-4, can be made between the free internal rotor limit and any interested non-$C_{3v}$ semi-rigid limit. This is true even when the 2-D isotropy accidentally remains for such a non-$C_{3v}$ semi-rigid configuration. The reason is that the (classical) $k_c$ vector is *not collinear* with the principal a axis of the complex, which is the figure axis for the $C_{3v}$ semi-rigid limit; although $v_b$ and $l_b$ still happen to be good quantum numbers, no simple quantum number relationship, such as Equation (3.7.4-3), exists. Of course, if it is insisted to establish an evolving picture like table 3.7.4-4 starting from the free internal rotor limit to a non-$C_{3v}$ semi-rigid limit, we should remove all the $v_b$ and $l_b$ quantum numbers from the table, only with the symmetry species ($S_o$ and [S]) and the $K_a$ splittings from each free internal rotor state left. It is noted that the symmetry [S] of the semi-rigid bending state should be maintained although the bending quantum numbers are removed. This is because that, for correlations *within* semi-rigid limit, the evolving unit is basically each vibrational state with its rovibrational structure, the inside $K_a$ stacks, "moving" as a whole; the semi-rigid vibrational symmetry [S] should be invariant. This reflects the fact that the $C_{3v}$ semi-rigid

limit used in Table 3.7.4-4, plays the central role as a "relay station", which can be used to start a secondary correlation to any other configuration within semi-rigid limit.

### 3.7.5 $K_z$ Correlation under $D_{3h}(M)$ between the Two Limits

The correlation relationship under $D_{3h}(M)$ between the free internal rotor limit and the semi-rigid limit can be generalized from its analogue under $C_{3v}(M)$. (However, care must be taken because it is *not* a straightforward matter of duplicating the $C_{3v}(M)$ correlation table (Table 3.7.4-4) for even and odd $v_i$, respectively, and replacing all symmetry species by those of $D_{3h}(M)$.) First of all, it is noted that the $NH_3$ inversional motion, that extends the molecular symmetry group to $D_{3h}(M)$, is *not* allowed in the semi-rigid limit. Therefore, it is again the *inversion-free* semi-rigid bending vibrational states, as used in Table 3.7.4-4 under $C_{3v}(M)$, that are to be correlated to the free internal rotor states, which are now the $NH_3$ rotation-*inversion* states. In other words, the number of the bending states in the semi-rigid limit remains the same, while the number of the intermolecular vibrational states in the free internal rotor limit is doubled. Since this correlation should be duplicable for any pair of $v_i$=2n and 2n+1 (n: nonnegative integer) and any stretching quantum number $v_s$, the following discussion will be made only for $v_i$=0, 1 and $v_s$=0.

The *natural* schematic $C_{3v}(M)$-to-$D_{3h}(M)$ *ro*··'*rational* correlations for the lowest three free internal *rotation* states, shown in Table 3.7.4-4, are depicted in Figures 3.7.5 (a)-(c), respectively. That

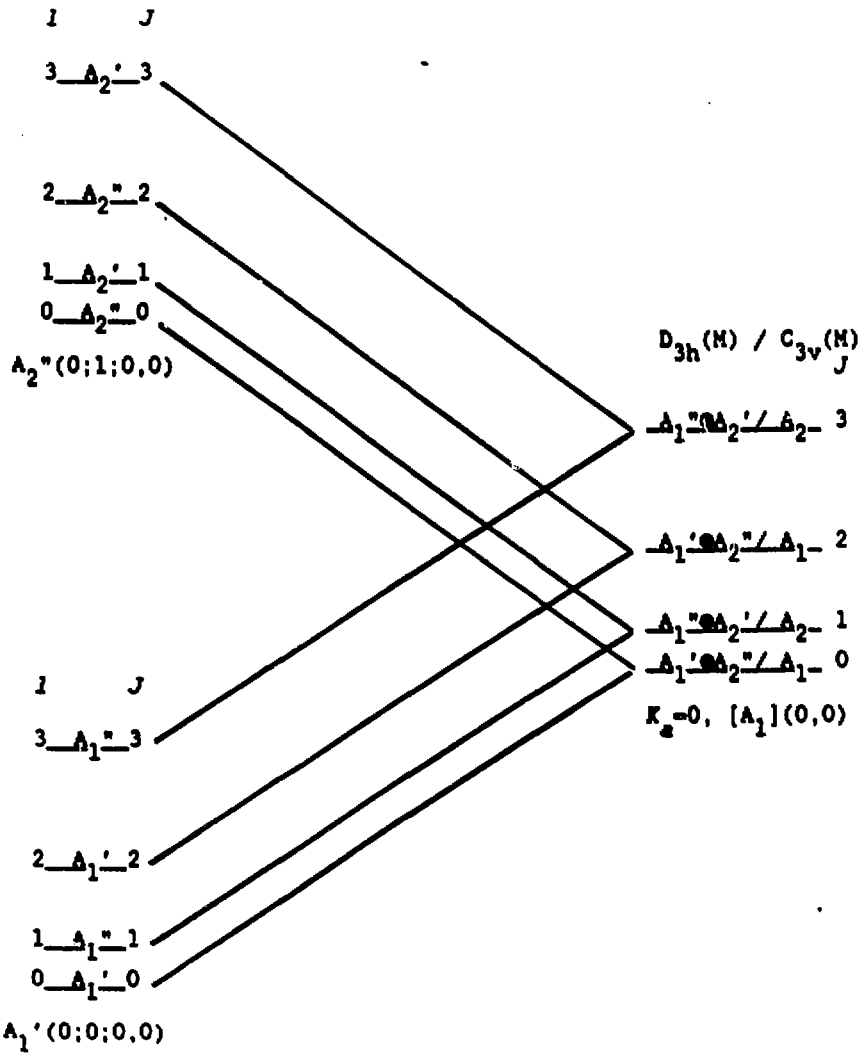


(a) $(j,k_c)=(0,0)$.

Figure 3.7.5
The $C_{3v}(M)$-to-$D_{3h}(M)$ rovibrational correlations for the lowest three lowest three free internal rotor states shown in Table 3.7.6-4 for: (a) $(j,k_c)=(0,0)$, (b) $(j,k_c)=(1,0)$, and (c) $(j,k_c)=(1,1)$.

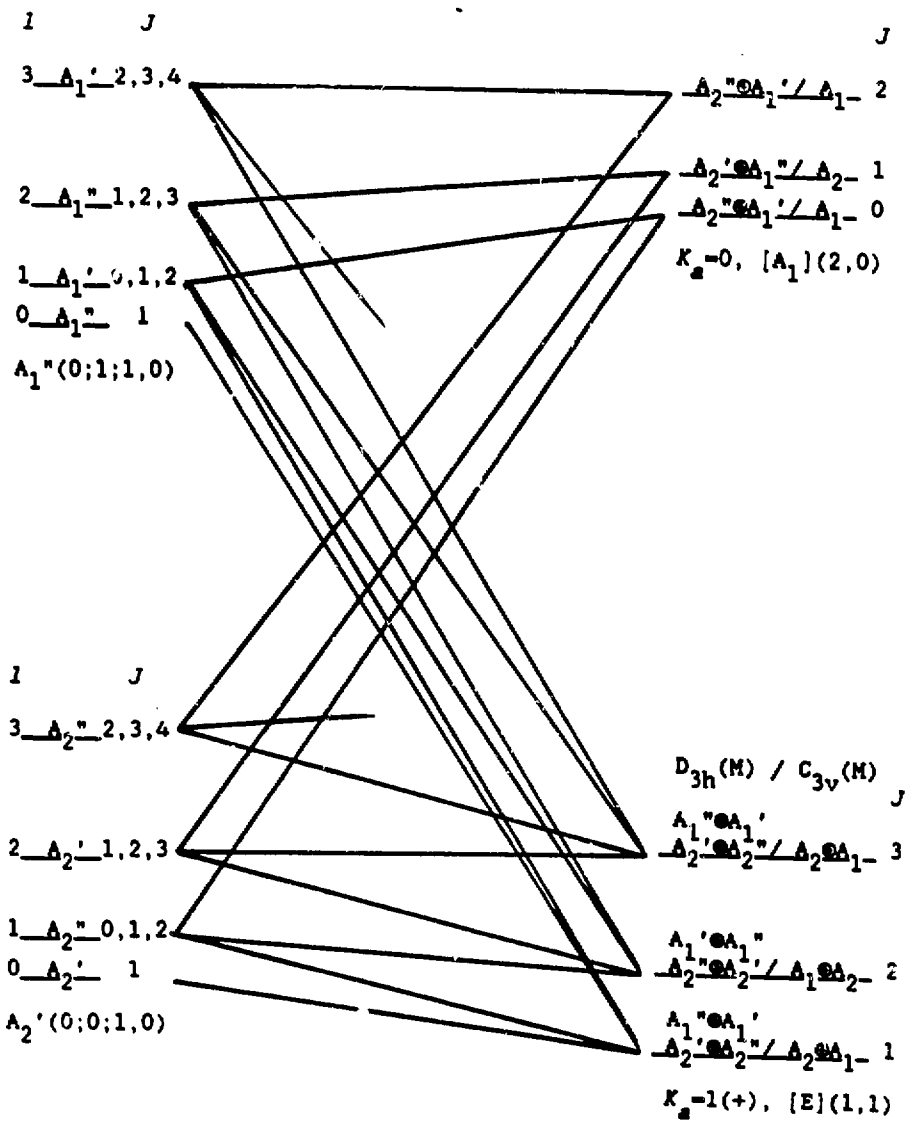


Figure 3.7.5 (b) $(j,k_c)=(1,0)$.

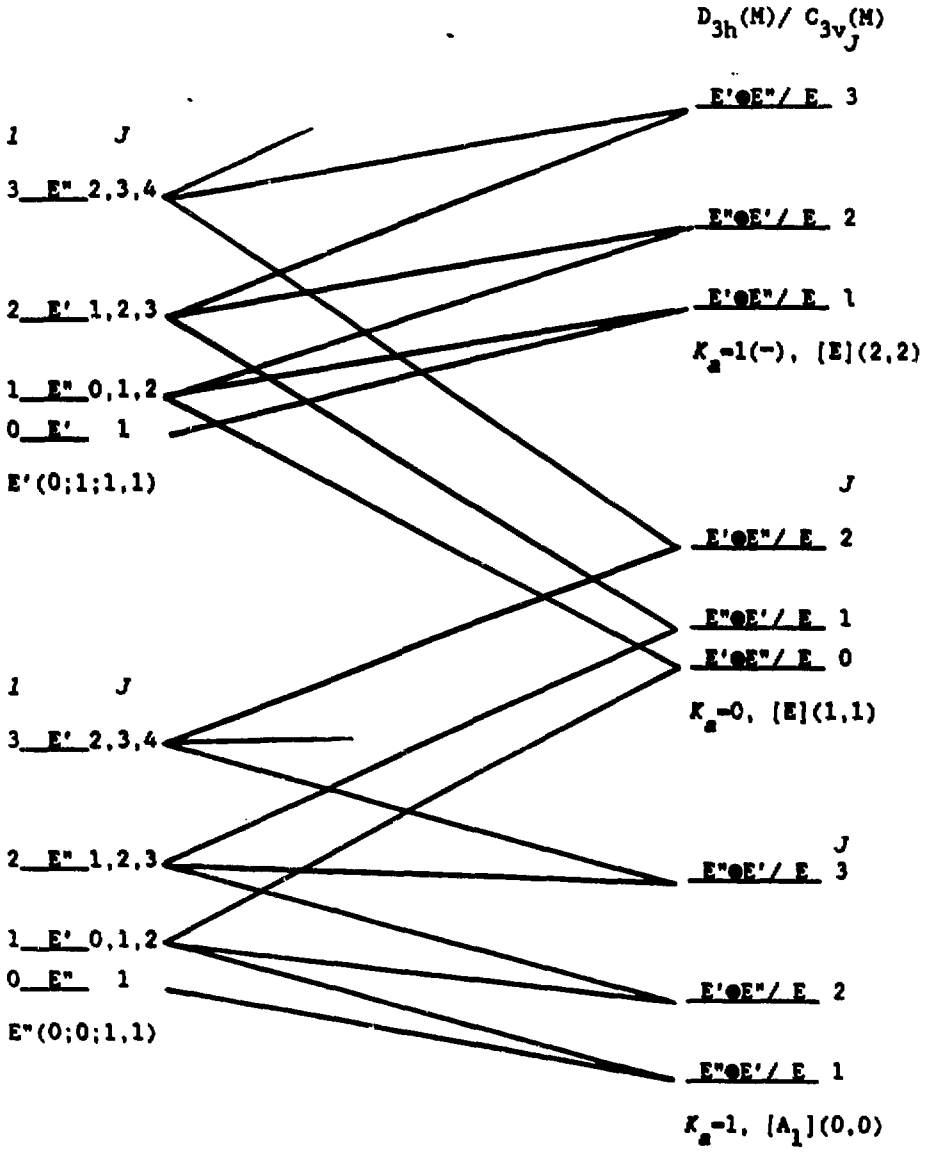


Figure 3.7.5 (c) $(J,k_c)$=(1,1).

they are "natural" is based on the following operational phenomenon. Assume that in the beginning such correlations are made arbitrarily, and the only rule followed is that levels of the same symmetry and same $J$ on both sides are connected (with straight *lines)*. However, Figures 3.7.5 (a)-(c) will always be the final schematic correlations, if the following two steps are performed: (1) according to the same-symmetry-same-$J$ interaction selection rule, create a "noncrossing intersection" (similar to those in Figure 3.7.2-1) for each pair of *mutually interacting* correlation lines that intercross each other, and (2) straighten all such resultant noncrossing correlation *curves*. (Of course, such straightening is unnecessary only for the rovibrational correlation purpose. However, it helps us to visualize the resultant $K_a$ manifolds under $D_{3h}(M)$, which are to be defined.)

Because $K_a$ is a quantum number purely of rotational motion, not of the inversional motion that extends the molecular symmetry group to $D_{3h}(M)$, the definition of the $K_a$ manifolds under $D_{3h}(M)$ needs to be clarified. (Since more rovibrational levels are generated under $D_{3h}(M)$, usually there are more than one way to conceptually group them into manifolds. For example, two well separated manifolds might be considered as a superposition of two *internally* split manifolds.) By looking at Figures 3.7.5 (a)-(c), one may naturally choose each rotational manifold that apparently evolves as a whole to be *one* $K_a$ manifold under $D_{3h}(M)$, no matter how many superimposed rotational $J$-stacks are included in such a $K_a$ manifold. The $K_a$ value is chosen to be the same as its correlated value under $C_{3v}(M)$ because, in principal, the inversional motion should not change the value of any

rotational quantum number. For example, in Figure 3.7.5 (c), there are two $K_a$=0 and two $K_a$=1 manifolds under $D_{3h}$(M), as opposed to the correlated one $K_a$=0 and two $K_a$=1 manifolds under $C_{3v}$(M). (Although this is purely for convenience for the moment, this definition for $K_a$ can actually be physically justified, as will be shown later.)

It is noted in Figures 3.7.5 (a)-(c) that each *rovibrational* state in either limit, except the $I$=0 states in the free internal rotor limit, is *degenerate*: in the free internal rotor limit, it is the *accidental* $J$-degeneracy due to the j-1 vectorial addition; in the semi-rigid limit, it is the degeneracy caused by the inversional motion. (However, the latter does not necessarily correspond to the inversional degeneracy of $v_I$=0 and 1, respectively, as will be explained in the following.) Therefore, *both* limits of this correlation consist of many divergent sources of the rovibrational levels and thus the $K_a$ manifolds under $D_{3h}$(M), as opposed to the corresponding correlation under $C_{3v}$(M) (Table 3.7.4-4) in which only the free internal rotor limit contains the divergent sources.

As can be imagined according to Figures 3.7.5 (a)-(c), it is the inversional splitting in the free internal rotor limit that "dissociates" each $C_{3v}$(M) rovibrational level into two $D_{3h}$(M) levels. However, the inversional motion does *not* always split each $C_{3v}$(M) $K_a$ manifold into two $D_{3h}$(M) $K_a$ manifolds thus defined; as exemplified by Figure 3.7.5 (c), the inversional motion "turns on" only the e-o-e rotational splitting in each of the two $K_a$=1 manifolds. Such phenomena for the lowest six $(j,k_c)$'s are summarized in the schematic representation shown in Table 3.7.5, in which the $D_{3h}$(M) $K_a$

Table 3.7.5
Schematic representation of the $D_{3h}(M)$ correlation building blocks, associated with the lowest six $(J,k_c)$'s in Table 3.7.4-4. (The notation formats: $S_o(v_s;v_i;J,k_c)$ for the free internal rotor states; $[S](v_b,l_b)$ for the semi-rigid bending states; $K_a$ and $K_a$(sign for $l_b$) for the $K_a$ manifolds.)

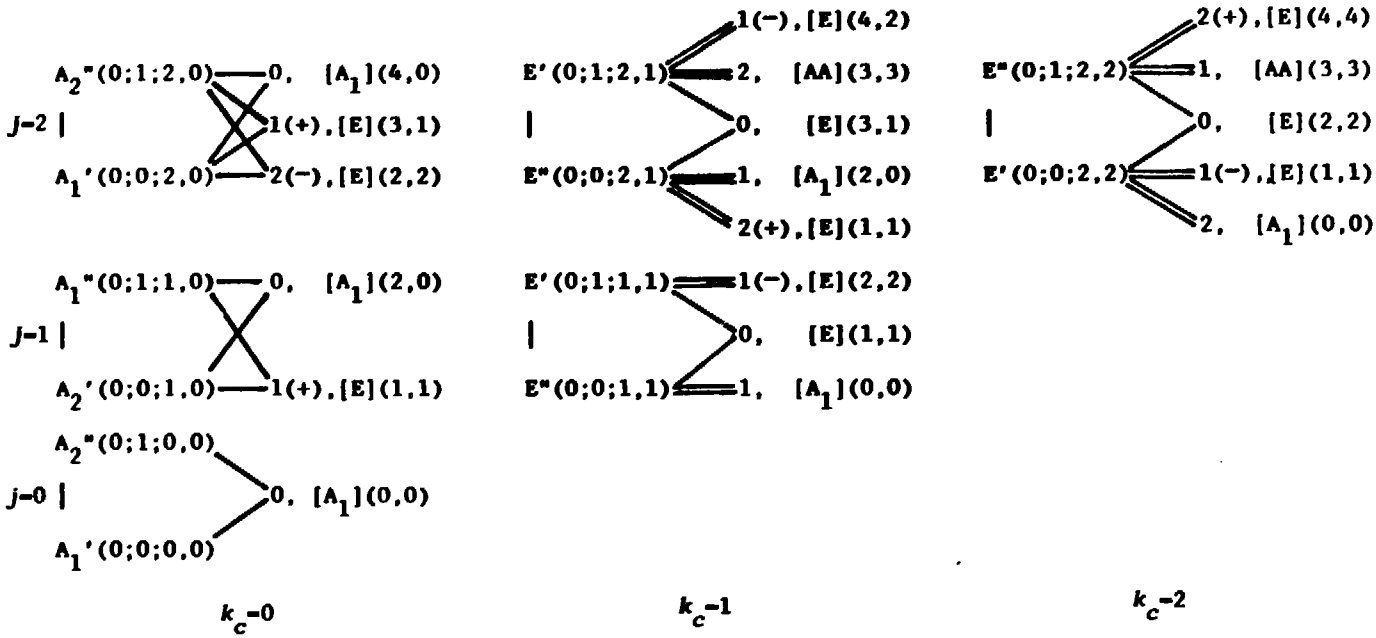

correlations are represented by different segments. According to the actual energy scales for the inversional motion and the e-o-e rotation, this table shows the following important facts: (1) each $C_{3v}(M)$ $K_a$=0 manifold of the ($j,k_c$>0) states and all $C_{3v}(M)$ $K_a$ manifolds of the ($j,k_c$=0) states will *inversionally* split into two $D_{3h}(M)$ $K_a$ manifolds belonging to $v_i$=0 and 1, respectively, and (2) each $C_{3v}(M)$ $K_a$>0 manifold of the ($j,k_c$>0) states only *shifts* as a whole into one $D_{3h}(M)$ $K_a$ manifold, but associated with small e-o-e rotational splittings, as reminded by the double-segments in Table 3.7.5.

The use of segments in Table 3.7.5 also indicates how the (2$j$+1)2 degeneracy of each internal ($j,k_c$) state is removed in the perturbed cases under $D_{3h}(M)$; 2$j$+1 is due to the internal rotation, 2 to the internal inversion. Importantly, this result under $D_{3h}(M)$ is consistent with the physical picture of a "miniature Stark effect", previously applied under $C_{3v}(M)$ (see Section 3.7.3.). Since each free internal rotation-*inversion* state under $D_{3h}(M)$ has defined-parity, each of them should split into $j$+1 "Stark" component states. Our choice for one $K_a$ manifold under $D_{3h}(M)$ is thus physically justified.

Like Table 3.7.4-4, Table 3.7.5 is also applicable to the cases in which the semi-rigid configuration does not have $C_{3v}$ point group symmetry if *only* the bending quantum numbers $v_b$ and $l_b$ are ignored. (See the last paragraph of Section 3.7.4.)

### 3.7.6 Intermolecular Vibrational Transitions

As indicated by the ($j,k_c$)-($v_b,l_b$) quantum number correlation

tables (Tables 3.7.4-4 and 3.7.5), the $K_a$ manifolds originating from the same intermolecular vibrational state actually belong to different semi-rigid bending vibrational states, respectively. Therefore, each single zero-order intermolecular vibrational level will eventually be "delocalized" by the limiting anisotropic potential into an energy scale that covers several semi-rigid bending states, which is typically few hundred to several thousand $cm^{-1}$. For similar reasons, the spacings among the intermolecular vibrational states (if always artificially defined by their singly correlated $K_a$=0 manifolds) will also follow the same trend. This is consistent with the inter-state "repulsions" required by the same-symmetry-same-$J$ interaction selection rules when further anisotropic potential is introduced. As a result, the actual inter-$K_a$ transitions should have higher frequencies than predicted by the zero-order picture. In other words, in Figure 3.6.1, the internal $NH_3$ inversion-rotation energy scales serve as the lower bounds for the corresponding transitions; however, this is *not* true for the stretching scale, which has not been determined by experiment conclusively.

Given in Section 3.6.3.1 were the *most unrestrictive* rovibrational optical selection rules, which allow many transitions forbidden by some approximate selection rules for the semi-rigid limit. Among these approximate rules, we are concerned particularly with $\Delta K_a$. The $\Delta K_a$=0 pure *rotational* selection rule and $\Delta K_a$=0, ±1 *rovibrational* selection rule [39] for the semi-rigid (exact or highly near) prolate top should be relaxed for this highly near prolate but floppy complex. This is because these classical $\Delta K_a$ rules are based

on the restrictive assumption that the molecular dipole, or its averaged effective vector, is collinear with the top axis. However, this is unnecessarily true for the current case, in which the $NH_3$ dipole moment is allowed to move away from the complex a axis to a large degree. Therefore, we expect this near prolate top complex to follow the rules followed by the semi-rigid *asymmetric* top [39], although it is not semi-rigid at all; in other words, $\Delta K_a$ should be *even* for the a type transitions, and *odd* for the b or c type transitions. The "a, b and c type" refer either to the averaged dipole direction of a given intermolecular vibrational state or to the direction of an intermolecular vibrational transition moment, or generally to a mixture of both. As a result, the associated intensities are highly dependent on the internal dynamics of the complex. If it is close to the free internal rotor limit, the $NH_3$ inversion-rotation selection rules

$$\Delta k_c = 0 \text{ and}$$
$$\Delta v_i : \text{odd}$$

might still play a dominant role in determining the stronger intermolecular vibrational transitions. (This implies that bands with a q branch should be stronger when near this limit.)

Since the $K_a$ manifolds are the evolving units between the two limits under either $C_{3v}(M)$ or $D_{3h}(M)$, the discussion will be focused on the qualitative aspects of the transitions *between* different $K_a$ manifolds originating from either the *same* or *different* intermolecular vibrational states. (It could be misleading to call the transitions

between the $K_a$ manifolds related to the *same* intermolecular vibrational state "overall rotational" transitions because of the state mixing and the actual energy scale involved.) Without introducing any conceptual bias, these transitions will generally be called "inter-$K_a$ transitions".

In order to facilitate the application of the $\Delta J$ selection rule, we define "$J$-stack(s)" to exist within a $D_{3h}(M)$ $K_a$ manifold as follows (see Figures 3.7.5 (a)-(c)): Each $K_a$=0 manifold consists of a *single* $J$-stack; however, each $K_a$>0 manifold consists of *two* $J$-stacks, i.e. a lower one ($J_l$-stack) and an upper one ($J_u$-*stack) basically superimposing on each other*, both starting from $J$=$K_a$. (Of course, "upper" or "lower" is determined by the relative positions of their $J$ level origins in the free internal rotor limit, because their relative positions could be switched during the evolution between the two limits.) This might not seem to be a necessary definition before examining the ($j$,$k_c$=3n) states (n:positive integer). This is because, for such states, each $J$ in a $K_a$=0 manifold corresponds to two, instead of one, irreducible symmetry species, and each $J$ in a $K_a$>0 manifold to four, instead of two; each $J$ in these $J$-stacks thus defined therefore corresponds to *two* independent symmetry species ($A_1'\otimes A_2'$ or $A_1''\otimes A_2''$), instead of one. Such a same-$J$-doublet of a $J$-stack defined for the ($j$,$k_c$=3n) states evolves basically as a small unit; as can be indicated by a correlation, similar to Figure 3.7.5, such a same-$J$-doublet must correlate to a *single* level in *both* limits; its splitting induced by the same-symmetry-same-$J$ interactions with other states should generally be small.

Importantly, within each $J$-stack thus defined, there is a parity alternation associated with each increment of $J$ by one; for the $(j,k_c=3n)$ states, the two irreducible symmetry species of a same-$J$-doublet must have the same parity. The symmetry species of such a $J$-stack will be defined to be that (or those) associated with the lowest $J$ in the stack. This is similar to the symmetry definition for the $K_a$ manifolds, which is the *total* symmetry corresponding to the lowest $J(=K_a)$. This makes the symmetry of a $K_a>0$ manifold under $D_{3h}(M)$ be the direct sum of the symmetry of $J_u$-stack and that of the $J_l$-stack.

Once we know the symbol $S_o(v_s;v_i;j,k_c)$ of the zero-order intermolecular vibrational state, as those shown in Figure 3.6.1, the $D_{3h}(M)$ symmetry of any rovibrational level originating from it can then be quickly deduced as follows: The $S_o(v_s=0;v_i;j,k_c)$ state can split into $j+1$ $K_a$ manifolds under $D_{3h}(M)$ with $K_a=j$, $j-1$, $j-2$, ..., 2, 1, 0. The symmetry species of the nonzero $K_a$ manifolds with *even* $j-K_a$ are all $\{S_o\}\otimes\{(S_o)''\}$; those of the rest with *odd* $j-K_a$ are all $\{(S_o)''\}\otimes\{S_o\}$. Here, the symbol ()" denotes a parity switching operation. The symmetry notation is in the format of

$$\{J_l\text{-stack symmetry}\}\otimes\{J_u\text{-stack symmetry}\};$$

otherwise, a single $J$-stack is implied. (For example, the differences in the number of stack(s) implied should be made among $\{A_1''\}\otimes\{A_1'\}$, $A_1''\otimes A_2''$, and $\{A_1'\otimes A_2'\}$.) The symmetry of $K_a=0$ manifold ($J$-stack) is affected also only by the evenness or oddness of $j$: $S_o$ for *even* $j$, $(S_o)''$ for *odd* $j$. Because of the parity alternation feature of the

$J$-stacks, the symmetry of any rotational level can then be readily determined by the symmetry of the stack thus derived. For example, the symmetry of the $K_a$=3 manifold originating from the $A_1''\otimes A_2''(0;0;j=3,3)$ zero-order intermolecular vibrational state should be $\{A_1''\otimes A_2''\}\otimes\{(A_1''\otimes A_2'')''\}$ because $j-K_a$ is even; the symmetry of the $J_u$-stack is thus the second term $(A_1''\otimes A_2'')''=A_1'\otimes A_2'$, which is the symmetry of its lowest $J$ ($=K_a=3$) and all other odd $J$'s in the $J_u$-stack; all even $J$'s can only be $A_1''\otimes A_2''$.

The above scheme provides an efficient and systematic method to figure out the symmetry of each rovibrational state without referring to any correlation diagram like Figures 3.7.5 (a)-(c). The $D_{3h}(M)$ symmetry species of the $J$-stacks, thus derived, for the lowest seven $(J,k_c)$'s are shown in Figure 3.7.6. Since the transitions between two different $K_a$ manifolds can generally be "decomposed" into few inter-$J$-stack transitions, the $J$-stack symmetry species, shown in Figure 3.7.6, are thus useful in determining the existence of P, Q, R branches involved in an inter-$K_a$ transition.

Because a $K_a$ manifold can consist of a $J_l$-stack and a $J_u$-stack, we have to specify which $J$-stack of the $K_a$ manifold is involved in the P, Q, R branches. To do this, symbol like $P_u^l$ will be employed; the subscript and superscript *position* are used for the lower and upper $K_a$ manifold, respectively; the subscript and superscript themselves ($l$ or $u$) denote which $J$-stack of the $K_a$ manifold is involved. Therefore, $P_u^l$ represent a $\Delta J=-1$ branch connecting the $J_u$-stack of the lower $K_a$ manifold to the $J_l$-stack of the upper $K_a$ manifold. Other symbols like $Q_l$, $R^u$, etc. can be understood similarly.

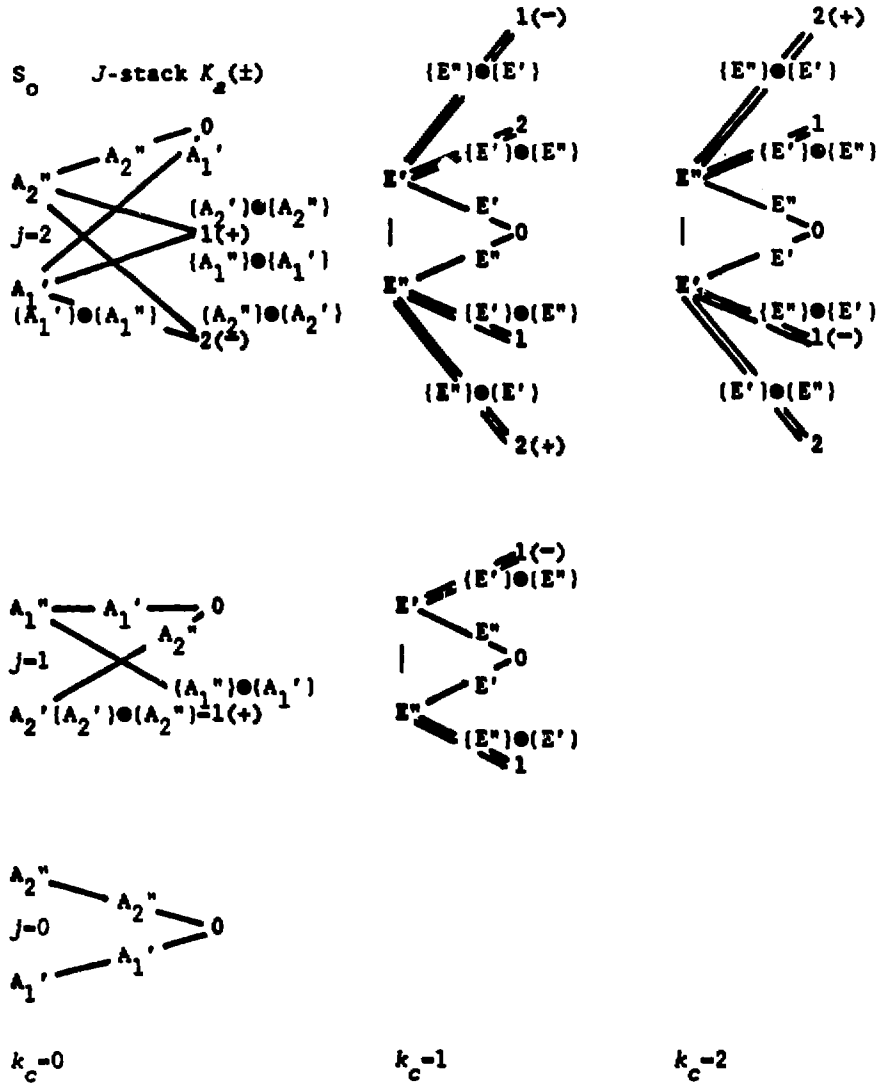


Figure 3.7.6
The $D_{3h}(M)$ symmetry species of the $J$-stacks for the lowest seven $(j,k_c)$'s. (See Table 3.7.5 for semi-rigid bending quantum numbers.)

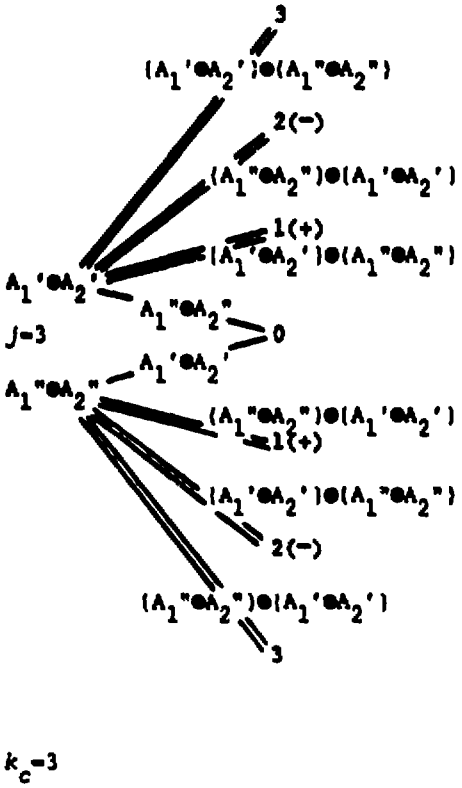


Figure 3.7.6 (Continued)

Since only the parity selection rule and $\Delta J$ rule are required t determine the rotational fine structure for an *allowed* inter-$K_a$ transition, in deducing the general rule for the existence of certain P, Q, R branches we can ignore the parity independent part of the symmetry symbol, which is predetermined by the inter-$K_a$ transition considered. The existence of the P, Q, R branches as a function of the $J$-stack parities and $\Delta K_a$ involved in an inter-$K_a$ transition is given in Table 3.7 6-1. It is noted that when this table is applied to an inter-$K_a$ transition with the two $K_a$ manifolds each originating from a $S_o(vs;v_i;j,k_c=3n)$ state (n:positive integer), we should double the number of each type of branch shown on the table if all the same-$J$-doublets split.

A special feature indicated by Table 3.7.6-1 is that a *unique* Q branch is allowed without being "accompanied" by a P and R branch, as opposed to the familiar semi-rigid polyatomic vibrational bands, in which only the Q branch has ever been found to be missing. This is because the $\Delta J=\pm 1$ selection rules are overridden by the parity requirement under $D_{3h}(M)$. Such anomalous unique Q branch transitions connect only the $K_a=0$ manifolds either *between or within* the $(j,k_c>0)$ states, but *not* the $(j,k_c=0)$ states (see Figure 3.7.6). It should be noted that for the $(j,k_c=3n>0)$ states such a Q branch band is likely to slightly split into two if the same-$J$-doublets in the $J$-stacks are slightly split. (These unique Q branches are surprisingly entire *vibrational* bands.) It is noted that if these unique Q branch bands occur in the case of $\Delta k_c=0$ and $\Delta v_i$:odd, they are not only rovibronically but also *vibronically* allowed. Of course,

Table 3.7.6-1
The existence of the P, Q, R branches as a function of the $J$-stack parities and $\Delta K_a$ involved in an inter-$K_a$ transition.
(Z: an arbitray $J$-stack symmetry)

| | | |
|---|---|---|
| upper $J$-stack | Z' | Z" |
| lower $J$-stack | Z' | Z' |
| $\Delta K_a$ | even / odd | even / odd |
| P,Q,R type | P,R / Q | Q / P,R |

| | | |
|---|---|---|
| upper $J$-stack | Z'⊗Z" (Z"⊗Z') | Z' (Z") |
| lower $J$-stack | Z' | Z'⊗Z" |
| $\Delta K_a$ | even / odd | even / odd |
| P,Q,R type | $P^l,Q^u,R^l$ / $P^u,Q^l,R^u$ ($P^u,Q^l,R^u$ / $P^l,Q^u,R^l$) | $P_l,Q_u,R_l$ / $P_u,Q_l,R_u$ ($P_u,Q_l,R_u$ / $P_l,Q_u,R_l$) |

| | | |
|---|---|---|
| upper $J$-stack | Z'⊗Z" | Z"⊗Z' |
| lower $J$-stack | Z'⊗Z" | Z'⊗Z" |
| $\Delta K_a$ | even / odd | even / odd |
| P,Q,R | $P_u^u,Q_u^l,R_u^u$ / $P_u^l,Q_u^u,R_u^l$ | $P_u^l,Q_u^u,R_u^l$ / $P_u^u,Q_u^l,R_u^u$ |
| type | $P_l^l,Q_l^u,R_l^l$ / $P_l^u,Q_l^l,R_l^u$ | $P_l^u,Q_l^l,R_l^u$ / $P_l^l,Q_l^u,R_l^l$ |

"vibronically allowed" implies the intensities of these bands must be strong.

If such a unique Q branch band occurs *within* one ($J,k_c>0$) state, or, equivalently, between the associated $v_i=0$ and 1 zero-order state, it can be assigned to a first approximation as a pure inversional transition (see Figure 3.7.6). However, such pure internal inversional transitions, with $K_a=0 \leftarrow 0$, within the ($J,k_c=0$) states are forbidden by symmetry, even if the $A_1'$ and $A_1''$ symmetry are also allowed. This suggests that classically the $NH_3$ inversion must be "triggered" by an internal rotation about the $C_3$ axis of the subunit. This is reasonable because such an internal rotation tends to increase the H–N–H bond angle by the associated centrifugal distortion force, which makes the $NH_3$ more planar and thus closer to the other inverted configuration; however, if the internal rotation is about an axis perpendicular to the $C_3$ axis, then the H–N–H will be decreased. (As an aside, it is reminded that *not* all the free internal rotor limit q branches correlate to such unique Q branch vibrational bands.)

To estimate the complexity of some low lying intermolecular vibrational transitions, we first take the perturbed E'(0;1;1,1) ← E"(0;0;1,1) transition as an example, which was observed in microwave but hardly rotationally assigned [14,15]. According to Table 3.7.6-1, the four $K_a$ manifolds (Figure 3.7.6, Table 3.7.5) and thus six inter-$K_a$ transitions involved in this case should result in totally nineteen branches, including six P, six R and *seven* Q branches. (The extra Q is due to the previously explained inversional transition.) In other words, the Q branch like cluster observed at about 20 GHz

could be either of the seven branches. (Of course, which one is a big question.) It is also remembered that, as can be generalized from the discussion in Section 3.6.4, the zero frequency should serve as a branch reflection point and thus a necessary pseudo-bandhead for the extremely low lying vibrational bands. (It is "pseudo" because the vibrational band still can have its real bandhead, which is caused by the noninertial forces.) Although this is not a general complication for the intermolecular vibrational transitions, the reflected spectral distribution definitely further complicates the current band patterns, according to the sample temperature.

We now examine, as another example, the FIR $A_2'(0;0;1,0) \leftarrow A_2''(0;1;0,0)$ transition in the perturbed cases. (The microwave transition between the $K_a$=0 and 1 manifolds originating from the $A_2'(0;0;1,0)$ state will not be considered.) Based on Figure 3.7.6 and Table 3.7.6-1, the $K_a$=0 ← 0 transition will have P and R branch; the $K_a$=1 ← 0 transition will have all $P^l$, $Q^u$ and $R^l$ branch. (If $A_1'$ and $A_1''$ symmetry species are also allowed, such as in the case of Ar-$ND_3$, then the P, Q, R branch for this intermolecular vibrational transition will be doubled.)

Of course, these examples represent the lowest and thus the simplest cases for the microwave and FIR transitions, respectively; according to Figure 3.7.6, the distribution density of the P, Q, R branches (themselves) will increase "exponentially" for higher FIR transitions.

Since $\Delta K_a$ can be any feasible signed integer, the minimum lower $J$ ($J''_{min}$) of the P, Q, R branch and the P-R branch gap should be

affected by the lower $K_a$ ($K_a$") and $\Delta K_a$ value. These relations are given in Tables 3.7.6-2(a) and (b), respectively, as a reference. (The P-R branch gap given is for the cases where the rotational structureis characterized dominantly by the rotational constant $B$ and the lower and upper $B$ are close in value.) However, we should not take the regularity of the spectroscopic rotational structure for granted; if the complex is close to the free internal rotor limit, each P, Q, R branch should be distorted into the regular "framework" of the $\Delta l$ (o, q, s, ..., or n, p, r, t, ...) branches. This can be manifested, as an example, by the o-q-s to P-Q-R branch evolution relationship (Table 3.7.6-3) for the $A_2'(0;0;1,0) \leftarrow A_2''(0;1;0,0)$ intermolecular vibrational transition. In this case, the o and s branch evolve into a $P^1$ and R branch, respectively, with the rotational line spacings shrinking from $4B$ ($=2B|\Delta l|$) to $2B$; more dramatically, a single q branch diverges into three distinct branches, interestingly, belonging to *two* inter-$K_a$ transitions in the semi-rigid limit. Since the q branch divergence cannot be achieved all at once, in most of the perturbed situations both the $K_a = 1 \leftarrow 0$ and $0 \leftarrow 0$ transition bands must be *asymmetrically* distributed about its own band center. In other words, the regularities, in the equal spectral line spacing, of both $\Delta l$ and $\Delta J$ branch patterns can never be available simultaneously, even when no interactions among different $K_a$ manifolds are seriously involved.

## 3.8 Intermolecular-Vibrational Assignment of Observed Spectrum

It will be shown that the observed band centered at 26.470633(17)

Table 3.7.6-2(a)
The minimum lower $J$ ($J''_{min}$) of the P, Q, R branch as a function of the $\Delta K_a$ value and lower $K_a$ ($K_a''$).

| | $J''_{min}$ of P branch | Q branch | R branch |
|---|---|---|---|
| $\Delta K_a>0$ | $K_a''+\Delta K_a+1$ | $K_a''+\Delta K_a$ | $K_a''$ |
| $\Delta K_a=0$ | $K_a''+1$ | $K_a''$ | $K_a''$ |
| $\Delta K_a<0$ | $K_a''$ | $K_a''$ | $K_a''$ |

Table 3.7.6-2(b)
The P-R branch gap as a function of the $\Delta K_a$ value and lower $K_a$ ($K_a''$) when (1) the rotational structure is characterized dominantly by the rotational constant $B$ and (2) the lower and upper $B$ are close in value.

| | P-R branch gap |
|---|---|
| $\Delta K_a>0$ | $2B(2K_a''+\Delta K_a+2)$ |
| $\Delta K_a=0$ | $2B(2K_a''+2)$ |
| $\Delta K_a<0$ | $2B(2K_a''+1)$ |

Table 3.7.6-3
The o-q-s to P-Q-R branch evolution for the $A_2'(0;0;1,0) \leftarrow A_2''(0;1;0,0)$ intermolecular vibrational transition.

| free internal rotor limit | | semi-rigid limit | |
|---|---|---|---|
| o branch | $\Longrightarrow$ | $P^1$ branch | |
| q branch (one peak) | $\Longrightarrow$ | $Q^u$ branch | $K_a=1 \leftarrow 0$ |
| | | $R^1$ branch | |
| s branch | $\Longrightarrow$ | P branch | $K_a=0 \leftarrow 0$ |
| | | R branch | |

$cm^{-1}$, reported in this work, can correlate *only* to one of the following two zero-order transitions: (1) $A_2''(v_s=1;v_i=1;0,0) \leftarrow A_2''(0;v_i=1;0,0)$, the fundamental dimeric stretching band for the $A_2$ states with $v_i=1$, (2) the $K_a=0 \leftarrow 0$ subband of $A_2'(0;0;j=1,0) \leftarrow A_2''(0;v_i=1;0,0)$, the lowest internal-rotation-inversion difference band (see Figure 3.6.1). It is noted in Table 3.7.5 that the second transition does *not* correlate to the fundamental bending transition but to its second harmonic in the semi-rigid limit. Since this measured $K_a$ subband is the first FIR data on Ar-$NH_3$ and therefore no reliable semiempirical potential showing principal global features for the complex can have been synthesized to test the assignment, further determination between the two possibilities will be made only tentatively at the end of the section.

Similar to the ortho and para $H_2$ molecule [36], it is expected that the $A_2$ and E states, with different nuclear spin statistical weights (see Section 3.6.3.1), transform into each other extremely slowly in collisional process, such as in the free jet expansion. (The symmetry species used in the following are those of $D_{3h}(M)$. They might look like those of $C_{3v}(M)$ when the superscripts, denoting different parities, are removed for abbreviation.) Therefore, it is meaningful to consider the overall energy level distribution as a superposition of two independent distributions, viz., one for the $A_2$ states and the other for the E states. Each of the two distributions has its own "pseudo-ground" state. They are pseudo because none of the two ground states, viz., the $A_2''(0;1;0,0)$ and $E''(0;0;1,1)$ state, has all intermolecular vibrational quantum numbers zero.

According to the 35 $cm^{-1}$ fundamental stretching frequency estimated *roughly* from the ground state centrifugal distortion constant [13], we can reasonably assume for the *zero-order* picture that the states with the stretching quantum number $v_s$=1 are at least 10 $cm^{-1}$ higher than their counterpart states with $v_s$=0; column two and four ($v_s$=1) in Figure 3.6.1 should be shifted upward by at least 10 $cm^{-1}$ with respect to column one and three ($v_s$=0). In other words, the first intermolecular-vibrationally excited state in the *zero-order* $A_2$ state distribution and the second excited state in the zero-order E state distribution are at least 10 $cm^{-1}$ higher than their individual pseudo-ground state. Since the typical effective rotational temperature of the free jet is about 5 K (kT≈100 GHz≈3 $cm^{-1}$), only three intermolecular vibrational states should be significantly populated: viz., the two pseudo-ground states and the E'(0;1;1,1) state, which is only about 20 GHz (~0.2 kT) above and thus should be approximately equally populated as the E pseudo-ground state. In the zero-order picture, the population of any other higher intermolecular vibrational state should thus be less than few percent of those of the three states.

The population among the intermolecular vibrational $K_a$ component states in the perturbed cases will be examined as follows: According to the $(j,k_c)$-$(v_b,l_b)$ quantum number correlation under $D_{3h}(M)$ (Table 3.7.5), the more the intermolecular anisotropy is introduced, the more the energy level splitting features are dominated by the semi-rigid limit high frequency bending vibrations, as indicated by the correlated $v_b$ quantum numbers. Importantly, it is noted that the

accompanied quenching of the inversional splittings (only 24 GHz [35]) is on a much smaller energy scale and should be "swamped" easily by the above principal splitting features. As a result, to a first approximation, the $K_a$ manifolds basically tend to evolve *upward* with respect to the ground intermolecular vibrational state. This is apparent for the $K_a$ manifolds correlating to a *nonzero* $v_b$ because of the necessity of approaching the corresponding *high* frequency vibrational states of the semi-rigid limit. On the other hand, same trend for the $K_a$ manifolds correlating to $v_b$=0 can be found readily if the semi-rigid limit $K_a$ manifolds distribution, specified by Equation 3.7.2, is considered; it is noted that the large rotational constant $A$ (~6.3-9.9 $cm^{-1}$, see Section 3.7.1) of the complex will dominantly characterize the relative distribution among the $K_a$ manifolds in this limit. Therefore, if only states of the same stretching quantum number $v_s$ are considered and no perturbation due to states of other $v_s$ is involved, all the excited intermolecular vibrational $K_a$ component states, possibly except the four correlating to the E"(0;0;1,1) and E'(0;1;1,1) state, should have less population than in the zero-order limit.

However, the barely rotationally assigned and vibrationally unassigned *irregular* Q branch observed at ~19-20 GHz *and* other microwave transitions scattered between 13-21 GHz [14,15] should belong to the six possible inter-$K_a$ transitions among the four $K_a$ component states originating from the E"(0;0;1,1) and E'(0;1;1,1) state. This "finalist" assignment is based on (1) the quantum number correlation (Table 3.7.5), (2) the predicted distribution complexity

among these E states (Section 3.7.6), (3) the electric dipole selection rules (Section 3.6.3.1), and (4) the typical beam temperature. This spectroscopic evidence confirms that at least the lower three of the four $K_a$ component states should be close together within few tens GHz and thus significantly populated in the actual perturbed system. This should not be considered as a trivial assignment because these four $K_a$ component states do correlate to three different semi-rigid bending quantum numbers, $v_b$=0, 1, and 2.

When perturbations between states of different $v_s$'s (0 and 1 for the current case) are considered, certain states might "accidentally" have a higher population than in the zero-order state. However, that is not a general trend for most of the $K_a$ component states. Consequently, the most possible lower intermolecular vibrational component state of the observed band should still be those that correlate to the lowest three zero-order intermolecular vibrational states.

Since the 26.470633(17) $cm^{-1}$ band is composed of very regular P and R branch transitions, as indicated by the small number of rotational constants required to obtain a 1 MHz standard deviation in the fit, it is impossible that this band could have one of the four irregular $K_a$ manifolds, belonging to the two E states, as its lower state. Furthermore, the rotational constants of the lower state of this band match fairly well with those of a regular ground state observed in microwave [13]. In other words, the lower state of this band can be conclusively assigned to be the lowest $K_a$=0 component state, the only $K_a$ manifold originating from the zero-order

$A_2''(0;1;0,0)$ state.

According to the optical selection rules $A_2 \leftrightarrow A_2$ and $A_2 \not\leftrightarrow E$ (see Section 3.6.3.1), we can then focus the discussion only on the $A_2$ state. The next higher $A_2$ state in the actual perturbed system can correlate only either to $A_2'(0;0;j=1,0)$ or to $A_2''(v_s=1;v_i=1;0,0)$ in the zero-order limit, depending on the fundamental stretching frequency. The upper state of the observed band is thus most likely to correlate to one of these two zero-order states. This is because (1) as previously explained, the $K_a=0$ and 1 manifold of the $A_2'(0;0;1,0)$ state should basically evolve upward (>19 $cm^{-1}$) (unless there is "accidental" perturbation due to other states, for example, of the same $A_2$ symmetry but with different $v_s$), and (2) the energy of the $A_2''(1;1;0,0)$ state is essentially contributed by the dimeric stretching motion, whose frequency is estimated to be higher than 10 $cm^{-1}$. For similar reasons, all other excited $A_2$ intermolecular vibrational states in perturbed cases seem to be too high for the observed 26.5 $cm^{-1}$ band center. In other words, the observed band could be correlated to either of the following three transitions:

for $A_2'(0;0;1,0) \leftarrow A_2''(0;1;0,0)$:

$K_a=0 \leftarrow 0$,

$1 \leftarrow 0$;

for $A_2''(1;1;0,0) \leftarrow A_2''(0;1;0,0)$:

$K_a=0 \leftarrow 0$.

All these transitions have P and R branches; in addition, the $K_a=1 \leftarrow 0$ transition also exhibits a Q branch (see Tables 3.7.5, 3.7.6-1 and

Figure 3.7.6). Although both the $K_a$=0 ← 0 and 1 ← 0 transitions have R branches starting with R(0), there is a difference between their P branches; for $K_a$=0 ← 0, it begins with P(1), whereas for $K_a$=1 ← 0, it starts with P(2). Because of the confirmed existence of P(1) in the 26.470633(17) $cm^{-1}$ band (Figure 3.3), we can eliminate the possibility of the $K_a$=1 ← 0 transition. Thus we are left two possible assignments which are both $K_a$=0 ← 0 and different only in the upper $K_a$ component state.

As previously explained, the upper state assignment will be made only tentatively between the two possibilities. Three apparently supportive evidences for the $A_2''(1;1;0,0)$ state as the upper state will be presented below.

For this tentative assignment $A_2''(1;1;j=0,0) \leftarrow A_2''(0;1;j=0,0)$, neither of the two intermolecular vibrational states involved should have complication due to the rotational coupling with j; each rotational state is nondegenerate with $J=1$. In terms of the spectral line spacings, even the corresponding p and r branch structure in the free internal rotor limit would be similar to the correlated P and R branch structure in the semi-rigid limit. This band structure should also exhibit distortion relatively *insensitive* to the potential variation because there are no accidentally degenerate zero-order rovibrational states as in the $A_2'(0;0;j=1,0)$ state (see Section 3.6.2). This is consistent with the high degree of regularity in the observed band pattern.

Another supporting evidence for the tentative intermolecular vibrational assignment is obtained from the calculated change in the

effective distance between Ar and $NH_3$ in the lower and upper state. If a pseudo-diatomic model is assumed, the effective distance can be calculated directly from the $(B+C)/2$ rotational constant for each state. [13] The results are:

3.8358Å for lower state ($A_2''(0;1;0,0)$),

3.8723Å for upper state.

As indicated, there is about a one percent increase in distance for the observed band. Of course, such an increase is only a necessary condition for the fundamental stretching transition. However, we do not rule out the possibility that in other nonstretching transitions the upper state could also exhibit a longer effective distance than the lower state, especially when an accurate potential surface is not available for the system. In other words, this is relatively weak evidence for the tentative assignment.

However, it is noted that these two effective distances are essentially consistent with the free internal rotor model; both values are longer than any combination of the atomic vdW radii taken from standard inorganic textbooks [2] if the only structural requirement is that two H's of $NH_3$ are at equal distance and closer than the third H with respect to Ar.

Additional supporting evidence for this assignment is provided by the estimated polar angle index, derived from the measured $eqQ_{aa}$ of the upper state. If the perturbation of the electronic environment of the N atom due to the Ar atom is small and can be neglected, $eqQ_{aa}$ can be expressed in the usual way [13]

$$eqQ_{aa} = eqQ_{NH3}\langle P_2(\cos\theta)\rangle$$
$$= (-4.09\ \text{MHz})\langle(3\cos^2\theta-1)/2\rangle.$$

The polar angle index can then be defined as

$$\theta_2 = \cos^{-1}[\langle\cos^2\theta\rangle^{1/2}],$$

where the subscript 2 is a reminder that it is related to $\langle P_2(\cos\theta)\rangle$. For reasonably small bending amplitude, $\theta_2$ approximates $\langle\theta\rangle$. However, for large amplitude motion, $\theta_2$ will lose this physical meaning as $\langle\theta\rangle$ and become a characteristic index for different internal rotational states in the free internal rotor limit. Since the Ar-$NH_3$ system is close to this limit, the internal rotational wave function can be approximated by the standard symmetric top rotational function $|J,m,k\rangle$, with $J=j$, $m=\pm\Lambda$, and $k=\pm k_c$, where the nonnegative quantum number $\Lambda$ represents $K_a$ of the complex. Simply speaking, the rotational wave function of the $NH_3$ symmetric top is described in a coordinate system fixed with the complex pseudo-diatomic frame. With this wave function, the $\theta_2$ index can then be calculated. The calculated results for some low lying internal rotational states is given in Table 3.8-1.

As expected, $\theta_2$ is dependent only on $j$ and $\Lambda$, but not on $k_c$. Consequently, the same results can be applied to the free internal rotor limit atom-diatom systems, which have zero equivalent $k_c$. It is noted that these calculated $\theta_2$ indices are well separated and thus could be used for internal rotational state identification to some extent. The $\theta_2$ indices of the ground states, low lying bending (or

Table 3.8-1
Theoretical free rotor limit of the $\theta_2$ indices for low lying internal rotational states of an atom-symmetric-top system.

| $\theta_2$ | internal rotational state | $\lvert J,\pm\Lambda,\pm k_c\rangle$ |
|---|---|---|
| $54.7^\circ$ | $S_o(v_s;v_i;0,0)$, a $K_z$=0 state | $\lvert 0,0,0\rangle$ |
| $39.2^\circ$ | $K_z$=0 component of $S_o(v_s;v_i;1,0)$ | $\lvert 1,0,0\rangle$ |
| $39.2^\circ$ | $K_z$=0 component of $S_o(v_s;v_i;1,1)$ | $\lvert 1,0,\pm 1\rangle$ |
| $63.4^\circ$ | $K_z$=1 component of $S_o(v_s;v_i;1,0)$ | $\lvert 1,\pm 1,0\rangle$ |
| $63.4^\circ$ | $K_z$=1 component of $S_o(v_s;v_i;1,1)$ | $\lvert 1,\pm 1,\pm 1\rangle$ |
| | | $\lvert 1,\pm 1,\mp 1\rangle$ |

internal rotational) states of some binary vdW complexes, and the upper state of the intermolecular stretching band of this work are listed in Table 3.8-2. We find that even the relatively more hindered Ar-HCl, the worst example in the table, still exhibits values of $\theta_2$ that are quite different for the lowest $K_a$=0 and 1 bending states; importantly, these values are not too different from the their theoretical values. The deviation of the $\theta_2$ for Ne-HCl, a nearly free internal rotor system, is within 3.5°. Therefore, the $\theta_2$ values, 58.3° and 52°, obtained for the two states involved in the Ar-$NH_3$ stretching band support the $S(v_s;v_i;0,0) \leftarrow S(v_s;v_i;0,0)$ assignment, which is in agreement with the tentative assignment.

Since this is the first time that the $\theta_2$ index is used to identify the $K_a$ value for a highly near prolate complex in the nearly free internal rotor limit, the generality of this method still needs to be further examined. Hopefully, the answer can be improved by one more step when a reliable potential surface for Ar-$NH_3$ is available.

Although the above evidences might seem more supportive to the $K_a$=0 manifold of the $A_2''(1;1;0,0)$ state than of the $A_2'(0;0;1,0)$ state as the upper state, we cannot rule out the possibility that these evidences are just *accidentally* more in favor of this tentative assignment. It should be emphasized again that we need to measure more FIR intermolecular vibrational bands to initiate the iteration between the spectroscopic investigation and the semiempirical synthesis of the potential, and such an iteration is the only way to rigorously test the intermolecular vibrational assignments of the observed bands.

Table 3.8-2
The measured $\theta_2$ indices of the ground states and low lying bending (or internal rotational) states of some dimers. The values in parentheses are the free rotor limits of $\theta_2$ indices taken from Table 3.8-1.

| Ar-HCl | Ne-HCl | Ar-$NH_3$ |
|---|---|---|
| ground [42] | ground [42] | ground [13] |
| $42^{\circ a}$ ($54.7^{\circ}$) | $52^{\circ}$ ($54.7^{\circ}$) | $58^{\circ}$ ($54.7^{\circ}$) |
| lowest $\Sigma$ ($K_a$=0) bend [40] | | upper state of this work (ground state)[b] |
| $41^{\circ}$ ($39.2^{\circ}$) | | $52^{\circ}$ ($54.7^{\circ}$) |
| lowest $\Pi$ ($K_a$=1) bend [41] | | |
| $58^{\circ}$ ($63.4^{\circ}$) | | |

[a]The discrepancy is not surprising, because the ground state is deep in the potential well.

[b]It is in the ground internal rotational state, if in the free internal rotor limit.

References

1. G.C. Pimentel and A.L. McClellan, 'The Hydrogen Bond' (Freeman, San Francisco, 1960).

2. J.E. Huheey, 'Inorganic Chemistry', 2nd ed. (Harper & Row Publishers, New York, 1978), p.262.

3. D.D. Nelson, Jr., G.T. Fraser, and W. Klemperer, Science 238, 1670 (1987) and references therein.

4. G.T. Fraser *et al*, J. Chem. Phys. 80, 3073 (1984).

5. E.J. Goodwin, N.W. Howard, A.C. Legon, Chem. Phys. Lett. 131, 319 (1986).

6. N.W. Howard and A.C. Legon, J. Chem. Phys. 86, 6722 (1987).

7. P. Herbine and T.R. Dyke, J. Chem. Phys. 83, 3768 (1985).

8. G.T. Fraser, K.R. Leopold, W. Klemperer, J. Chem. Phys. 80, 1423 (1984).

9. G.T Fraser, F.J. Lovas, R.D. Suenram, D.D. Nelson, Jr., W. Klemperer, J. Chem. Phys. 84, 5983 (1986).

10. G.T Fraser, K.R. Leopold, W. Klemperer, J. Chem. Phys. 81, 2577 (1984).

11. G.T. Fraser, D.D. Nelson, Jr., G.J. Gerfen, W. Klemperer, J. Chem. Phys. 83, 5442 (1985).

12. G.T. Fraser, D.D. Nelson, Jr., K.I. Peterson, W. Klemperer, J. Chem. Phys. 84, 2472 (1986).

13. D.D. Nelson, Jr., G.T. Fraser, K.I. Peterson, K. Zhao, and W. Klemperer, F.J. Lovas and R.D. Suenram, J. Chem. Phys. 85, 5512 (1986).

14. D.D. Nelson, Jr., Ph.D. dissertation, Harvard University.

15. G.T. Fraser, D.D. Nelson. Jr., A. Charo, and W. Klemperer, J. Chem. Phys. 82, 2535 (1985).

16. D.D. Nelson, Jr., G.T. Fraser, and W. Klemperer, J. Chem. Phys. 83, 6201 (1985).

17. D.D. Nelson, Jr. and W. Klemperer, G.T. Fraser, F.J. Lovas, and Suenram, J. Chem. Phys. 87, 6364 (1987).

18. R.C. Cohen, K.L. Busarow, K.B. Laughlin, G.A. Blake, M. Havenith, Y.T. Lee, and R.J. Saykally, J. Chem. Phys. 89, 4494 (1988).

19. A.D. Buckingham, P.W. Fowler, J.M. Hutson, Chem. Rev. 88, 963 (1988), and references therein.

20. Z. Latajka and S. Scheiner, J. Chem. Phys. 84, 341 (1986).

21. K. Sagarik, R. Ahlrichs, and S. Brode, Mol. Phys. 57, 1247 (1986).

22. M.J. Frisch, J.A. Pople, J.E. Del Bene, J. Phys. Chem. 89, 3664 (1985).

23. M.J. Frisch, J.E. Del Bene, J.S. Binkley, H.F. Schafer III, J. Chem. Phys. 84, 2279, (1986).

24. S. Liu, C.E. Dykstra, K. Kolenbrander, J.M. Lisy, J. Chem. Phys. 85, 2077 (1986)

25. D.D. Nelson, Jr. and W. Klemperer, J. Chem. Phys. 87, 139 (1987).

26. M. Ignuscio, G. Moruzzi, K.M. Evenson, and D.A. Jennings, J. Appl. Phys. 60, R161 (1986).

27. M. Havenith, D.-H. Gwo, K.L. Busarow, R.C. Cohen, R.J. Saykally. In preparation.

28. J.T. Hougen, "Methane symmetry operations", MTP International Review of Science, Physical Chemistry (Editor: D.A. Ramsey), Series Two, Vol. 3, Spectroscopy (Butterworth, London 1976).

29. E.B. Wilson, Jr., J.C. Decius and P.C. Cross, 'Molecular vibrations, The Theory of Infrared and Raman Vibrational Spectra' (Dover Publications Inc., New York, 1980), p.285.

30. G. Arfken, 'Mathematical Methods for Physicists', 3rd ed. (Academic Press, Orlando, Florida, 1966), chapter 1.

31. J.B. Marion, 'Classical Dynamics of Particles and Systems', 2nd ed. (Academic Press, New York, 1970).

32. P.R. Bunker, 'Molecular Symmetry and Spectroscopy' (Academic Press, New York, San Francisco, London, 1979), and references therein.

33. D. Papousek and M.R. Aliev, 'Molecular Vibrational-rotational Spectra' (Elsevier Scientific Publishing Company, Amsterdam, Oxford, New York, 1982), and references therein.

34. G. Herzberg, 'Infrared and Raman Spectra' (Van Nostrand, New York, 1945), and references therein.

35. C.H. Townes and A.L. Schawlow, 'Microwave Spectroscopy' (Dover, New York, 1975), and references therein.

36. G. Herzberg, 'Spectra of Diatomic Molecules' (Van Nostrand, New York, 1945).

37. K.T. Tang and J.P. Toennies, J. Chem. Phys. 76, 2524 (1982) and references therein.

38. C. Cohen, B. Diu, F. Laloe, 'Quantum Mechanics', Vol.1 (John Wiley & Sons, New York, 1977).

39. G. Herzberg, 'Electronic Spectra and Electronic Structure of Polyatomic Molecules' (Van Nostrand, New York, 1966).

40. R.L. Robinson, Ph.D. dissertation, University of California,

Berkeley (1987).

# Chapter 4

## Concluding Remarks

The first high resolution vibration-rotation-tunneling transitions of Ar-$NH_3$ and $(NH_3)_2$ were identified in the dense spectra of a $NH_3$-in-Ar mix in a continuous planar supersonic jet measured by the Berkeley tunable far infrared (FIR) laser spectrometer. Among the seven *rotationally* assigned bands, the one centered at 26.470633(17) $cm^{-1}$ was identified in this work to be of Ar-$NH_3$. [1] (The other six bands belong to $(NH_3)_2$. Their analyses and study will be presented in M. Havenith's Ph.D. dissertation [2] and Reference 3.) However, approximately 250 spectral lines over the ~7 $cm^{-1}$ wide spectrum still remain rotationally unassigned; they could belong either to these two or to other higher complexes. The promising probing capability of this state-of-the-art technique for small van der Waals complexes was once again confirmed.

Since so far no semiempirical synthesis of the potential surface for Ar-$NH_3$ has ever been proposed, it is natural to start with a group theoretical study. In order to facilitate the intermolecular vibrational assignment, a basic dynamics study aided by a rigorous permutation-inversion group theoretical treatment was made on the *rovibrational* levels. According to this study, the zero-order picture, viz., the free internal inverting rotor limit, of the complex was carefully defined. The rovibrational quantum number correlation (see Section 3.7.5) between this and the classical semi-rigid limit

was then established for this highly near prolate binary complex. This correlation not only provides a basic (nonnumerical) physical picture of the evolution of its intermolecular vibrational component states ($K_a$ manifolds) between the two limits, but also predicts qualitatively the high complexity in its spectrum.

According to the spectral range probed so far and the results of the group-theory-aided dynamics study, an intermolecular vibrational assignment was made; the observed band centered at 26.470633(17) $cm^{-1}$ can correlate *only* to one of the following two zero-order transitions (see Figure 3.6.1): (1) the fundamental dimeric stretching band for the $A_2$ states with the $NH_3$ inversional quantum number $v_i$=1, viz., $A_2''(v_s=1;v_i=1;0,0) \leftarrow A_2''(0;v_i=1;0,0)$, (2) the $K_a=0 \leftarrow 0$ subband of the lowest internal-rotation-inversion difference band, $A_2'(0;0;j=1,0) \leftarrow A_2''(0;v_i=1;0,0)$. Although based on several factors, particularly the measured nuclear quadrupole coupling constant, a tentative assignment was made in favor of the first possibility, a definitive determination is currently impossible for the following reasons.

Because the complex is closer to the nearly free internal rotor limit, the group-theory-aided high barrier limit treatment, introduced in Hougen's classic work on $(H_2O)_2$ [4], is definitely inappropriate. Therefore, to initiate the iteration between the spectroscopic investigation and the semiempirical synthesis of the potential is the only resort. Since this intermolecular vibrational band is the only assigned FIR data on Ar-$NH_3$, no reliable semiempirical potential for the complex has been synthesized. It is essential to obtain a minimum amount of spectroscopic data on the potential along each of the four

intermolecular rovibrational coordinates, viz., one for the dimeric stretch, one for the $NH_3$ inversion, and two for the internal $NH_3$ rotation. In other words, more FIR spectroscopic study will be required before a trial potential showing *principal global features* can be proposed and tested against further FIR spectroscopic data; only further verification of the spectroscopic predictions from such a potential model can determine whether the tentative assignment can be justified.

Currently the most interesting and most badly needed transitions are the following three FIR $K_a$ subbands (see Figure 3.6.1): $K_a$=0 ← 0, $K_a$=1 ← 0 of $A_2'(v_s=0;v_i=0;j=1,k_c=0) \leftarrow A_2''(0;1;0,0)$, and $K_a$=0 ← 0 of $A_2''(1;1;0,0) \leftarrow A_2''(0;1;0,0)$. The former two subbands reflect the potential basically along the internal rotation coordinates, whereas the last reflects that along the dimeric stretching coordinate. In terms of state population in a ~5 K jet expansion, these transitions are the most accessible ones; in terms of the intermolecular vibrational assignment, they are also the simplest because of the small numbers of $K_a$ subbands originating from their zero-order intermolecular vibrational states. It is expected for Ar-$NH_3$ that an internal rotation transition-moment should be larger than a stretching transition-moment *if* both motions are not strongly mixed; the relative intensities between the two $K_a$=0 ← 0 subbands *might* constitute a spectroscopic evidence for their intermolecular vibrational assignments and thus provide a clue for the first potential synthesis.

On the other hand, further investigation of the six $K_a$ subbands of the $E'(0;v_i=1;1,1) \leftarrow E''(0;v_i=0;1,1)$ transition in the few tenths

$cm^{-1}$ to few $cm^{-1}$ region should in principle be crucial to the understanding of the potential along the $NH_3$ inversional coordinate. However, conventional microwave spectroscopy, probing approximately 1 $cm^{-1}$ and below, can hardly cover the whole structure of an intermolecular vibrational band, which is typically a few $cm^{-1}$ wide at the low jet temperatures. This is true even when the bend center is located below 1 $cm^{-1}$ and the pseudo-bandhead at zero frequency is "forced" to occur. In addition, according to the derived quantum number correlation, we do expect at least some of these $K_a$ subbands to have a band center a little higher than 1 $cm^{-1}$. However, the spectroscopic technique in the 1-10 $cm^{-1}$ region is still immature and under development. As a result, the tunable FIR spectroscopy is still indispensable to investigate these two E states, which have to be involved as the lower states of the FIR transitions. However, the complexity in their rotational level distributions, as has been theoretically predicted and partially revealed in the microwave study, could pose a problem for the spectroscopic rotational $J$ assignment. The Stark tuning at low field and microwave-FIR double resonance are suggested to diagnose the $J$ values.

In the future FIR investigation of Ar-$NH_3$, the definition of the intermolecular vibrational band pattern needs to be broadened. Interestingly, by using the quantum number correlation derived in this work and the optical selection rules under the molecular symmetry group and the three dimensional pure rotational group, the first *vibronically* (not rovibronically) allowed *unique Q branch* vibrational band [5] was theoretically predicted to exist for such a binary

complex with an inverting subunit. This anomalous spectroscopic phenomenon, hopefully experimentally confirmed, should revise the more than half-century old conventional concept about the vibronically allowed band pattern. There could have been spectroscopic evidences from our lab for such a special phenomenon. The rotational *J* assignments for these "candidates" are still in progress.

In view of the fact that a symmetric top can be correlated to either an asymmetric top (distorted symmetric top) or a linear system (with symmetric top *K* quantum number equal to zero), Ar-$NH_3$, an atom-*symmetric-top* complex, should be considered as the next prototypical van der Waals complex after Ar-HCl. In addition, since structurally Ar-$NH_3$ behaves like half of a $(NH_3)_2$ complex, which has recently been a controversial topic, the study of Ar-$NH_3$ will definitely teach us certain aspects of the $(NH_3)_2$ dynamics. Therefore, further study of the tremendously interesting Ar-$NH_3$ complex is highly encouraged.

References

1. D.H. Gwo, M. Havenith, R.C. Cohen, K.L. Busarow, R.J. Saykally. In preparation.

2. M. Havenith, Ph.D. dissertation, University of Bonn. In preparation.

3. M. Havenith, D.H. Gwo, K.L. Busarow, R.C. Cohen, R.J. Saykally. In preparation.

4. L.H. Cordert and J.T. Hougen, J. Mol. Spectrosc. 130, 86 (1988), and references therein.

5. D.H. Gwo, J.T. Hougen, R.J. Saykally. In preparation.

Appendix Table 1
Character table of the $D_{3h}(M)$ molecular symmetry group.[a]

| $D_{3h}(M)$ | E | (123) | (23) | E* | (123)* | (23)* |
|---|---|---|---|---|---|---|
| number of class element(s) | 1 | 2 | 3 | 1 | 2 | 3 |
| $A_1'$: | 1 | 1 | 1 | 1 | 1 | 1 |
| $A_2'$: | 1 | 1 | −1 | 1 | 1 | −1 |
| E': | 2 | −1 | 0 | 2 | −1 | 0 |
| $A_1''$: | 1 | 1 | 1 | −1 | −1 | −1 |
| $A_2''$: | 1 | 1 | −1 | −1 | −1 | 1 |
| E": | 2 | −1 | 0 | −2 | 1 | 0 |

[a]Adapted from P.R. Bunker, 'Molecular Symmetry and Spectroscopy' (Academic Press, New York, San Francisco, London, 1979).

Appendix Table 2
Multiplication table between the symmetry species of $D_{3h}(M)$ group.

| | $A_1'$ | $A_2'$ | E' | $A_1''$ | $A_2''$ | E" |
|---|---|---|---|---|---|---|
| $A_1'$ | $A_1'$ | $A_2'$ | E' | $A_1''$ | $A_2''$ | E" |
| $A_2'$ | $A_2'$ | $A_1'$ | E' | $A_2''$ | $A_1''$ | E" |
| E' | E' | E' | $A_1'\oplus A_2'\oplus E'$ | E" | E" | $A_1''\oplus A_2''\oplus E''$ |
| $A_1''$ | $A_1''$ | $A_2''$ | E" | $A_1'$ | $A_2'$ | E' |
| $A_2''$ | $A_2''$ | $A_1''$ | E" | $A_2'$ | $A_1'$ | E' |
| E" | E" | E" | $A_1''\oplus A_2''\oplus E''$ | E' | E' | $A_1'\oplus A_2'\oplus E'$ |

Appendix Table 3
Character table of the $C_{3v}(M)$ molecular symmetry group.[a]

| $C_{3v}(M)$ | E | (123) | (23)* |
|---|---|---|---|
| number of element(s) in the class | 1 | 2 | 3 |
| $A_1$: | 1 | 1 | 1 |
| $A_2$: | 1 | 1 | −1 |
| E: | 2 | −1 | 0 |

[a]Adapted from P.R. Bunker, 'Molecular Symmetry and Spectroscopy' (Academic Press, New York, San Francisco, London, 1979).

Appendix Table 4
The $C_{3v}(M)$-$D_{3h}(M)$ symmetry correlation table.[a]

| $C_{3v}(M)$ | $D_{3h}(M)$ |
|---|---|
| $A_1(12)$[b] | $A_1'(0) \oplus A_2''(12)$ |
| $A_2(12)$ | $A_2'(12) \oplus A_1''(0)$ |
| E(12) | $E'(6) \oplus E''(6)$ |

[a]From P.R. Bunker, 'Molecular Symmetry and Spectroscopy' (Academic Press, New York, San Francisco, London, 1979).

[b]The number in parentheses is the nuclear spin statistics for Ar-$NH_3$.

Appendix Table 5
Observed spectral lines which have not rotationally assigned.

| Frequency[a] (GHz) | Relative Intensity[b] | FIR Laser #[c] |
|---|---|---|
| 520.488 | 15 | 4 |
| 531.462 | 500 | 4 |
| 531.666 | 35 | 4 |
| 562.418 | 26 | 4 |
| 573.070 | 26 | 4 |
| 573.163 | 70 | 4 |
| 573.281 | 10 | 4 |
| 573.287 | 10 | 4 |
| 593.546 | 160 | 4 |
| 595.952 | 17 | 4 |
| 605.765 | 20 | 4 |
| 616.996 | 55 | 4 |
| 626.0793 | 19 | 1 |
| 626.1885 | 7 | 1 |
| 626.1913 | 43 | 1 |
| 626.4381 | 44 | 1 |
| 626.6093 | 17 | 1 |
| 627.1473 | 190 | 1 |
| 627.4393 | 22 | 1 |
| 627.9589 | 15 | 1 |
| 628.5501 | 16 | 1 |
| 628.8633 | 36 | 1 |
| 629.0737 | 10 | 1 |
| 629.0765 | 156 | 1 |
| 629.3393 | 20 | 1 |
| 629.5781 | 290 | 1 |
| 629.6561 | 63 | 1 |
| 629.7993 | 47 | 1 |
| 630.3269 | 52 | 1 |
| 630.8049 | 10 | 1 |
| 630.8065 | 290 | 1 |
| 631.5293 | 144 | 1 |
| 631.5425 | 61 | 1 |
| 631.6277 | 33 | 1 |
| 631.7265 | 64 | 1 |
| 632.0133 | 33 | 1 |
| 632.3265 | 15 | 1 |
| 632.7253 | 295 | 1 |
| 633.8457 | 19 | 1 |
| 634.7985 | 19 | 1 |
| 635.4661 | 210 | 1 |
| 635.6993 | 10 | 1 |
| 635.7421 | 12 | 1 |
| 636.0553 | 18 | 1 |

Appendix Table 5 (continued)

| Frequency (GHz) | Relative Intensity | FIR Laser # |
|---|---|---|
| 636.3021 | 15 | 1 |
| 636.8277 | 25 | 1 |
| 636.8313 | 7 | 1 |
| 637.0713 | 45 | 1 |
| 637.1221 | 10 | 1 |
| 637.2725 | 53 | 1 |
| 637.2761 | 28 | 1 |
| 637.4621 | 140 | 1 |
| 637.5573 | 43 | 1 |
| 637.6321 | 90 | 1 |
| 637.7773 | 28 | 1 |
| 637.9053 | 50 | 1 |
| 637.9953 | 8 | 1 |
| 638.0673 | 84 | 1 |
| 638.3413 | 60 | 1 |
| 638.4513 | 26 | 1 |
| 638.5753 | 78 | 1 |
| 638.6425 | 41 | 1 |
| 638.7033 | 335 | 1 |
| 638.9145 | 40 | 1 |
| 641.4093 | 16 | 1 |
| 642.5205 | 13 | 1 |
| 643.1369 | 24 | 1 |
| 643.2493 | 13 | 1 |
| 643.4761 | 23 | 1 |
| 643.6125 | 17 | 1 |
| 644.599 | 210 | 4 |
| 644.651 | 30 | 4 |
| 652.0717 | 60 | 1 |
| 653.2469 | 156 | 1 |
| 653.4633 | 370 | 1 |
| 654.7707 | 21 | 1 |
| 654.8253 | 16 | 1 |
| 655.5969 | 24 | 1 |
| 655.644 | 20 | 1 |
| 656.0979 | 375 | 1 |
| 656.3439 | 570 | 1 |
| 656.3751 | 24 | 1 |
| 656.9277 | 20 | 1 |
| 657.2393 | 19 | 1 |
| 657.6353 | 38 | 1 |
| 658.3173 | 29 | 1 |
| 658.6399 | 390 | 1 |
| 658.6463 | 36 | 1 |
| 658.6887 | 38 | 1 |
| 659.1113 | 18 | 1 |

Appendix Table 5 (continued)

| Frequency (GHz) | Relative Intensity | FIR Laser # |
|---|---|---|
| 659.3637 | 96 | 1 |
| 659.5461 | 45 | 1 |
| 659.6633 | 71 | 1 |
| 660.0993 | 84 | 1 |
| 660.6253 | 104 | 1 |
| 660.6539 | 53 | 1 |
| 660.7023 | 138 | 1 |
| 661.2793 | 70 | 1 |
| 661.3117 | 76 | 1 |
| 661.5799 | 26 | 1 |
| 661.8883 | 36 | 1 |
| 661.9661 | 40 | 1 |
| 662.1023 | 295 | 1 |
| 662.7037 | 70 | 1 |
| 663.6177 | 38 | 1 |
| 663.1233 | 48 | 1 |
| 664.2093 | 19 | 1 |
| 664.2513 | 25 | 1 |
| 664.3003 | 21 | 1 |
| 664.9023 | 425 | 1 |
| 665.8333 | 94 | 1 |
| 667.1913 | 39 | 1 |
| 667.8943 | 40 | 1 |
| 668.1913 | 36 | 1 |
| 668.7758 | 50 | 1 |
| 669.3213 | 47 | 1 |
| 670.5823 | 464 | 1 |
| 672.5513 | 61 | 1 |
| 672.7923 | 153 | 1 |
| 673.3053 | 100 | 1 |
| 673.3078 | 564 | 1 |
| 773.5073 | 28 | 1 |
| 674.8453 | 93 | 1 |
| 677.5263 | 60 | 1 |
| 678.0088 | 220 | 1 |
| 678.9157 | 250 | 1 |
| 678.9266 | 114 | 1 |
| 680.2733 | 24 | 1 |
| 680.8640 | 17 | 1 |
| 681.5693 | 50 | 1 |
| 681.5733 | 285 | 1 |
| 681.7573 | 53 | 1 |
| 683.7043 | 36 | 1 |
| 684.1283 | 70 | 1 |
| 686.1348 | 34 | 1 |
| 687.1158 | 120 | 1 |

Appendix Table 5 (continued)

| Frequency (GHz) | Relative Intensity | FIR Laser # |
|---|---|---|
| 687.1233 | 24 | 1 |
| 687.7344 | 93 | 1 |
| 689.3083 | 16 | 1 |
| 689.7113 | 34 | 1 |
| 690.0343 | 41 | 1 |
| 690.1053 | 133 | 1 |
| 694.023 | 70 | 2 |
| 695.1907 | 70 | 2 |
| 695.8543 | 20 | 2 |
| 697.2167 | 36 | 2 |
| 697.3703 | 74 | 1 |
| 697.7307 | 116 | 2 |
| 697.9467 | 16 | 2 |
| 698.2767 | 16 | 2 |
| 698.5719 | 60 | 2 |
| 699.8195 | 33 | 2 |
| 702.0443 | 40 | 1 |
| 702.1327 | 17 | 2 |
| 702.1727 | 9 | 2 |
| 702.2379 | 38 | 2 |
| 702.3567 | 14 | 2 |
| 703.0167 | 10 | 2 |
| 703.1047 | 13 | 2 |
| 703.1307 | 18 | 2 |
| 703.1533 | 154 | 1 |
| 703.4047 | 15 | 2 |
| 704.1939 | 26 | 2 |
| 704.3075 | 9 | 2 |
| 704.7773 | 24 | 1 |
| 705.102 | 20 | 2 |
| 705.3688 | 66 | 1 |
| 705.3903 | 134 | 1 |
| 705.6443 | 166 | 1 |
| 706.5287 | 14 | 2 |
| 706.5293 | 100 | 1 |
| 706.9163 | 68 | 1 |
| 707.4636 | 105 | 1 |
| 709.0207 | 54 | 1 |
| 710.1567 | 16 | 2 |
| 710.6513 | 50 | 1 |
| 711.0123 | 126 | 1 |
| 713.4583 | 96 | 1 |
| 715.9513 | 120 | 1 |
| 716.3793 | 61 | 1 |
| 716.9843 | 40 | 1 |
| 717.6163 | 26 | 1 |

Appendix Table 5 (continued)

| Frequency (GHz) | Relative Intensity | FIR Laser # |
|---|---|---|
| 718.7773 | 116 | 1 |
| 719.3371 | 20 | 2 |
| 720.7847 | 18 | 2 |
| 721.1826 | 17 | 2 |
| 725.4953 | 95 | 1 |
| 726.482 | 30 | 3 |
| 727.4487 | 13 | 2 |
| 728.3559 | 22 | 1 |
| 728.8333 | 50 | 1 |
| 730.092 | 40 | 1 |
| 730.9193 | 12 | 1 |
| 731.4393 | 14 | 1 |
| 735.1747 | 37 | 2 |
| 736.414 | 30 | 2 |
| 737.9697 | 22 | 2 |
| 738.8187 | 18 | 2 |
| 738.8207 | 15 | 2 |
| 739.1607 | 54 | 2 |
| 739.5567 | 13 | 2 |
| 739.6687 | 33 | 2 |
| 743.1157 | 16 | 2 |
| 743.5637 | 13 | 2 |
| 744.9997 | 32 | 2 |
| 746.7677 | 32 | 2 |
| 747.0197 | 33 | 2 |
| 747.1337 | 26 | 2 |
| 748.0913 | 7 | 1 |
| 749.2229 | 20 | 1 |
| 749.2289 | 15 | 1 |
| 749.8447 | 19 | 2 |
| 750.4433 | 9 | 1 |
| 755.9567 | 15 | 2 |
| 764.3817 | 46 | 2 |
| 765.2587 | 36 | 2 |
| 766.6687 | 100 | 2 |
| 768.8017 | 36 | 2 |
| 769.7097 | 15 | 2 |
| 774.669 | 50 | 3 |
| 774.8261 | 9 | 2 |
| 774.8279 | 16 | 2 |
| 776.8806 | 35 | 2 |
| 776.9967 | 420 | 2 |
| 778.4607 | 88 | 2 |
| 779.3507 | 68 | 2 |
| 779.5647 | 16 | 2 |
| 779.6587 | 8 | 2 |

Appendix Table 5 (continued)

| Frequency (GHz) | Relative Intensity | FIR Laser # |
|---|---|---|
| 779.7827 | 10 | 2 |
| 779.8567 | 9 | 2 |
| 780.4117 | 16 | 2 |
| 787.4307 | 210 | 2 |
| 788.1447 | 46 | 2 |
| 788.7527 | 30 | 2 |
| 793.7407 | 14 | 2 |
| 796.3867 | 30 | 2 |
| 797.9567 | 112 | 2 |
| 803.1847 | 12 | 2 |
| 809.204 | 20 | 2 |
| 809.227 | 20 | 2 |
| 810.177 | 45 | 3 |
| 816.3667 | 17 | 2 |
| 816.5607 | 15 | 2 |
| 817.8807 | 10 | 2 |
| 819.0207 | 9 | 2 |
| 819.2087 | 20 | 2 |
| 820.7447 | 19 | 2 |
| 823.8031 | 15 | 2 |
| 825.4075 | 13 | 2 |
| 825.5567 | 48 | 2 |
| 827.0767 | 14 | 2 |
| 827.3567 | 10 | 2 |
| 828.7747 | 20 | 2 |
| 829.8895 | 32 | 2 |
| 844.608 | 30 | 3 |

[a]The frequencies shown were obtained in the search mode of the experiment, and have not been measured to their best accuracy (<1 MHz) available. Although most frequencies listed have four digits after the decimal point, their typical accuracy is estimated to be ±1 MHz.

[b]The reference for the relative intensity is arbitrarily chosen. It is remembered that the uncertainty in the intensity is considerably large.

[c]The laser numbers, 1-4, represent the following FIR laser lines:

1: 692.9514 GHz, HCOOH
2: 761.6083 GHz, HCOOH
3: 787.7555 GHz, DCOOD
4: 584.3882 GHz, HCOOH